RICE UNIVERSITY

Biophysical Interactions of the OHC Motor Protein Prestin: A Study at the Single Molecule Level

by

Ramsey I. Kamar

A Thesis Submitted
in Partial Fulfillment of the
Requirements for the Degree

Doctor of Philosophy

Approved, Thesis Committee:

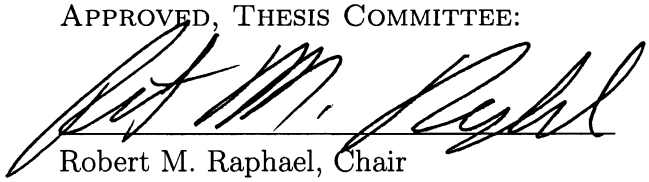

Robert M. Raphael, Chair
Associate Professor of Bioengineering

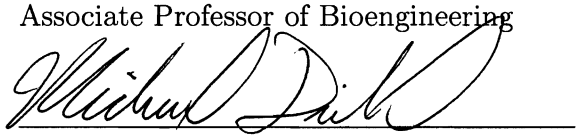

Michael R. Diehl,
Assistant Professor of Bioengineering and Chemistry

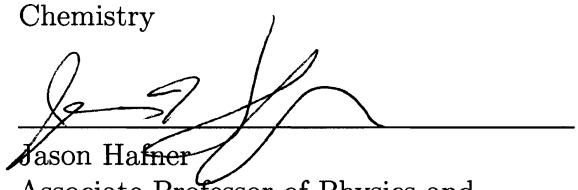

Jason Hafner
Associate Professor of Physics and Astronomy

Houston, Texas

February, 2011

ABSTRACT

Biophysical Interactions of the OHC Motor Protein Prestin: A Study at the Single Molecule Level

by

Ramsey I. Kamar

The exquisite frequency selectivity and amplification characteristics of mammalian hearing intimately depend on the fast electromechanical motion of the outer hair cells in the cochlea. This membrane based process, termed electromotility, is driven by the protein prestin which is uniquely present in the OHC lateral wall. Voltage dependent motility, in OHCs and mammalian cells expressing prestin, is accompanied by intramembranous charge movement which is widely considered a signature of electromotility and prestin function.

How prestin converts changes in membrane potential into axial length changes of OHCs is currently not understood at the molecular level. Many electromotility models predict that prestin conformational changes are the underlying mechanism connecting charge movement and motility. Currently, however, only indirect evidence for a prestin conformational change is available.

Various experiments have indicated that the oligomeric states of prestin may be an important determinant of function. Numerous reports have provided varying estimates of prestin oligomeric state. However, estimates have been based on measure-

ments performed outside the membrane making, firm biophysical conclusions difficult.

Biophysical studies of prestin function have demonstrated its dependence on membrane properties. Alterations of membrane cholesterol affect voltage dependence of charge movement and motility. In addition cholesterol manipulations cause spatial redistribution of prestin and possibly change prestin oligomeric state. However, the underlying cause for prestin sensitivity to cholesterol and its relation to membrane distribution is unknown.

We have applied single molecule fluorescence (SMF) imaging, single particle tracking (SPT), and Förster resonance energy transfer (FRET) to investigate prestin interactions at the molecular level. The results of our SMF experiments have suggested that prestin forms mainly tetramers and dimers in the cell membrane. Using SPT to map the trajectories of prestin in the membrane, we have found that prestin undergoes diffusion in and hops between membrane confinements of varying size. In addition, we have found that cholesterol affects the size and confinement strength of the compartments but does not affect the diffusivity within the compartments. Finally, using a combination of electrophysiology and FRET we have demonstrated that prestin undergoes voltage dependent structural changes. In total, our results refine our molecular understanding of prestin function.

Acknowledgments

There are many people who I need to thank for their help and support along the way. First and foremost, I need to thank my advisor Robert Raphael. Rob, you took me into your lab and gave me a chance to prove myself and I will always be thankful to you for that. I only hope that my work has paid you justice. I don't think I will ever know your true opinions on Middle East politics but I think that is by design.

I also need to thank the other members of my thesis committee: Professors Mike Diehl and Jason Hafner. Thank you for the time put in reading and thinking about my thesis and for the constructive criticism at my defense. I have learned quite a lot from the process and my thesis has improved as a result of your input.

In particular I need to specially thank Professor Diehl and his lab members. Mike, I came into Rob's lab barely knowing what a plasmid is, and I owe a large chunk of my knowledge to you and the Diehl Lab. Thank you for "showing me the ropes" on single molecule techniques. Even though I didn't end up using your TIRF scope for my experiments, I learned a lot of the basics by playing around with it. Your enthusiasm for experimental science — specifically, science done right — is inspiring and I have great respect for you as a result. Thanks for making your lab like a second home and letting me "hang around". Hopefully, I didn't wear out my welcome. Also thank you for the SNAP plasmid. It saved a lot of time and money. Rusty and Pam, all your help and expertise on molecular biology have been invaluable. Dzifa, I had fun working with you on the TIRF scope and watching you fend off Pouyan. Schweller, "hey there kid". Always enjoyed our goofing around and coffee breaks. To the rest

of the lab, Kenneth, Jonathan and Nic — and everyone really — thanks for making me feel so welcome in your lab.

Laurent Cognet came to Rice from France for a short sabbatical that the Gods seemed to have planned perfectly with me in mind. I say short, but in the few months that he was here he managed to put out a paper in Science in quite impressive fashion. I owe Laurent a lot for his advice and assistance including software. Without his help I would have had to do a lot of wheel reinventing. Thank you Laurent for taking the time out of your schedule.

I also need to thank the former and current members of Rob's lab. In particular I need to thank Ryan McGuire. Ryan, thanks for spending 12 hours a day with me on the voltage FRET experiment. How many times did we spend all day and get like one cell — You're a trooper! Your help was invaluable to the experiment. You're a true workhorse and a good friend. Louise, always a great thing writing down PDEs and boundary conditions on the board with you. I might have forgotten my math otherwise. Thanks for making me feel so welcome upon joining Rob's lab. You (and Jenni) made me feel included very quickly. Which brings me to Jenni. I can't believe we went to high school together and didn't know each other. Crazy! I'll always miss us just randomly breaking out into song in the office...or me trying to scare the life out of your guinea pig by "welcoming it to the jungle" and informing it that it was "going to die". Poor pig. Dan, I have great respect for your seemingly endless knowledge of the history of Christianity. You are a great conversationalist and an even better tether puller. Yong Zhou, Imran Quraishi, Jeff Triffo, Chance Mooney and Guillaume Duret have also been great colleagues and added to my experience in the Raphael Lab.

Thanks to the Drezek lab for allowing me to use your lab space where I did my experiments on the TIRF scope. Without it I would not have been able to complete

my experiments. Hopefully I wasn't too much of a pest or overly territorial about its use.

There have been a slew of undergraduates coming in and out of the Raphael lab who have contributed to my research. Lisa and Ken, thanks for making the prestin-citrine and positive control constructs and for being pretty good about documenting your work. Charlie, thanks for helping with FRET imaging. Peter, thanks for your help tracking those little spots moving around — I hope you didn't get any seizures doing so. Amanda, thanks for making the prestin-SNAP construct and for pretending to like my cooking. I'm waiting for you to call me and inform me that your music career has blossomed. In addition I need to thank Ericka Lawson who is definitely not an undergraduate. However her expertise helped Amanda efficiently create the SNAP tag construct.

To the members of the Hulet Lab, some of whom I overlapped with, I thank you too. You have always been good friends and have given me a reason (other than Valhalla of course) to come onto the main campus. Dan, it was always a pleasure to have worked with you and to have known you and Sara. Guthrie, working with you made me a better scientist and animal sound specialist. James, thanks for starting the Scotch Club. Best idea ever. To the rest of the Hulet Lab members of old and new, thanks for being good friends and for always letting me borrow a phododiode or power meter when I needed one.

My lifelong friends from Moses Hall also deserve a lot of thanks. Some I keep up with more than others, but I can always count on it being just like old times when we do catch up. A number of my Moses Hall friends should really be referred to as Brothers and deserve special recognition. A few who have lived in Houston with me, during my time in graduate school, deserve special recognition. Grant, Alan,

Snarf, Marshall, and Travis: you guys are like a second family — and thanks for the shirt. Alan, thanks for always talking me up to everyone (generally with more praise than I deserve). You are one of the best storytellers I know. Marshall, I can always count on you show me how to do a choke hold when I need to, or to amuse me by getting on Snarf's nerves, or to join me in doing the neurotic Woody Allen impression/stereotype. It is rare for me not to be the loudest guy in the room — but not when Marshall is around! Snarf, thanks for being my cooking buddy and impressing me with your music skills, and thanks for cooking for us when we get home drunk and hungry and unable to drive to Whataburger. Travis, you were a great college roommate and just an all-round stand up guy. You also have a great kid — hopefully we get to see more of him. We can always count on Grant to be the cooler head and share his wisdom. The rule is as follows: When Grant speaks you listen because it *is* going to be important (with very few exceptions).

I have to give a special thanks to my family who have been so supportive along the way. Thanks for always being on my side. Mom, thank you for teaching me how to be a good person and for fostering my love of music. To the extend that I have a "right brain" I got it from you. Dad, thank you for fostering my curiosity in how things work when I was little and for kicking my rear into gear my senior year of high school. Nadia, you are cool. Thanks for being younger than me and yet making everyone think you are older by being more mature and more of an adult. Sorry I picked on you when we were little. Just always be cool like you are, yeah. Last but not least, I thank my wife Bahar...now Dr. Sharafi. Azizam, you helped me get through some rough times and you've always been there to help me enjoy the good times. I can't imagine life without you. Without you, who would point out that I am too chubby, that I have an ugly mole, a funny brain, wooden feet, etc. And without you, who would let me be their sous-chef and who would make sure that I dress properly, that I animate my slides, and that I get a present for my birthday, and who would shave

the back of my neck when it gets too scruffy, and who would teach me about how awesome dark chocolate is, and who would make me the best fish in the world with mashed potatoes, and who would buy me a new laptop bag, and who would watch the X-files with me while clenching to my arms in fear that Scully is going to die — and most importantly, who would put their hand on my neck to calm me down when I get frustrated? Thanks for being an awesome wife and companion and for sharing your life with me. I love you so much. IMYA!

List of Abbreviations

AFM	Atomic Force Microscopy
BG	Benzylguanine
BM	Basilar Membrane
CDF	Cumulative Distribution Function
DRM	Detergent Resistant Membrane
eCFP	Enhanced Cyan Fluorescent Protein
eYFP	Enhanced Yellow Fluorescent Protein
FP	Fluorescent Protein
FRAP	Fluorescence Recovery After Photobleaching
FRET	Förster Resonance Energy Transfer
FWHM	Full Width Half Maximum
HEK	cell Human Embryonic Kidney cell
IHC	Inner Hair Cell
IMP	Intra-Membraneous Particles
MβCD	Methyl-β-Cyclodextrin
MSD	Mean Squared Deviation
NA	Numerical Aperture
NLC	Nonlinear Capacitance
OHC	Outer Hair Cell
PMT	Photo Multiplier Tube
SMF	Single Molecule Fluorescence
SPT	Single Particle Tracking
STAS	Sulfate Transporters and Anti-Sigma factor Antagonist
TEM	Transmission Electron Microscopy
TIRF	Total Internal Reflection Fluorescence
TMR	Tetramethylrhodamine

Contents

Illustrations

Chapter 1

Introduction

1.1 Motivation

It is particularly telling that some of the major principles underlying the current modern understanding of mammalian hearing were proposed some 60 years ago by the astrophysicist Thomas Gold, and well over a century ago by the physicist for whom the Helmholtz coil, Helmholtz free energy, and the Helmholtz equation are named — and who is regarded as advancing the modern acceptance of the conservation of energy as a general principle of physics. Hermann von Helmholz was the first to propose how the basilar membrane could act as a frequency analyzer for sound [von Helmholtz, 1912], and Thomas Gold was the first to propose that hearing should require a source of active amplification in the cochlea to account for the observed frequency tuning and amplification of acoustic energy [Ashmore, 2008, Gold, 1948]. This aspect of hearing has been termed the cochlear amplifier and somehow accounts for the ability of the cochlea to discern between frequencies different by 0.1% [Gummer, 2003] and to provide $40 - 60\,dB$ amplification of sounds over an $8 - 9$ octave bandwidth [Ashmore, 2008].

Cochlear amplification is intimately dependent on a unique form of cellular motion, termed electromotility, that is coupled to membrane voltage in the outer hair cells (OHC) of the cochlea [Brownell et al., 1985]. The membrane protein prestin pro-

vides the critical component driving electromotility by electro-mechanically coupling membrane voltage into axial $4-5\%$ length changes of OHCs [Ludwig et al., 2001, Zheng et al., 2000]. Measurable voltage-evoked membrane charge movement is found to accompany motility [Ashmore, 1990] and is widely considered to be a signature of function and a surrogate to measurement of electromotility. In addition, since the charge movement is similar to that in the voltage gated ion channels, it is widely considered to be the result of a conformational change that moves charged species into the membrane [Dallos et al., 1993]. However, direct experimental evidence confirming a voltage-dependent conformational change is lacking and therefore a clear molecular picture of prestin function is currently unavailable.

Previous experimental evidence has demonstrated that interactions with the membrane environment critically tune prestin function. Manipulations of membrane cholesterol concentration reversibly affect prestin associated charge movement and motility [Rajagopalan et al., 2007, Sfondouris et al., 2008, Sturm et al., 2007]. Changes in membrane cholesterol also reversibly affect both the distribution of prestin in the membrane [Organ and Raphael, 2007, Rajagopalan et al., 2007, Sturm et al., 2007] and, based on biochemical and optical microscopy studies, possibly the distribution of prestin stoichiometries [Greeson, 2008, Rajagopalan et al., 2007, Sturm et al., 2007]. In addition, local variations in nonlinear capacitance have been found in OHCs suggesting the existence of functional domains in the lateral wall [Santos-Sacchi, 2002]. These previous observations, along with other reported studies that suggest prestin oligomeric state can affect its function [Bian et al., 2010, Detro-Dassen et al., 2008], demonstrate that changes in membrane cholesterol may affect prestin function by either modifying its oligomeric state or by changing its association with membrane

microdomains containing cholesterol.

Measuring the lateral mobility of a protein is a common method that is used to understand its organization in the membrane especially when considering the effects of membrane confinements. Previous methods employed to study prestin diffusion, such as fluorescence recovery after photobleaching (FRAP) [Organ and Raphael, 2007] and indirect electrophysiological means [Santos-Sacchi and Zhao, 2003, Takahashi and Santos-Sacchi, 2001], were unable to clearly differentiate between multiple modes of diffusion or discern sub-micron sized confinements. While the studies which utilized FRAP did point to non-simple diffusion of prestin as a possibility, its exact nature could not be determined. The use of single particle tracking (SPT) has become a widely used method for characterizing membrane fluidity, protein diffusion, protein-membrane interactions, and overall membrane structure in great detail since it circumvents the ensemble averaging inherent to FRAP.

That defining the functional unit of prestin has been recognized as an important goal is reflected by counting the number of groups that have applied a multitude of methods to determine the distribution of prestin oligomeric states [Bian et al., 2010, Detro-Dassen et al., 2008, Mio et al., 2008, Pasqualetto et al., 2008, Rajagopalan et al., 2007, Sturm et al., 2007, Wang et al., 2010, Z. et al., 2006]. Since prestin is a membrane protein, the interactions with the membrane are a crucial determinant to its folded structure, function, and native stoichiometry. However, none of the methods previously employed to determine prestin oligomeric state distribution were performed in the cell membrane, which may affect the results and possibly explain the widely varying estimates of prestin oligomeric state. Therefore, a careful charac-

terization of prestin oligomeric state requires that it be done *in situ* and with single molecule resolution.

While it is generally agreed that prestin is the crucial component underlying OHC electromotility and NLC, little is understood about how prestin functions at the molecular level. Much work has been done to better understand the molecular mechanism of prestin function, but the methods employed have generally not been sensitive to individual prestin motion or distribution in the membrane. The general theme of the work in this thesis is to take an approach that tries to obtain information on prestin structure and interactions with the membrane environment at the level of single prestin molecules or single aggregates of prestin. The following unanswered questions have motivated the experiments reported in this thesis. While each study performed was primarily geared towards answering a specific question, there is overlap between the experiments and there are conceptual connections between the questions.
(1) What is(are) the functional unit(s) of prestin? A prerequisite to answering this question is what forms of prestin actually reside in the cell membrane. Specifically, what is the distribution of oligomeric states in the membrane?
(2) How does the membrane environment affect prestin function? To answer this question it must first be determined how prestin molecules are organized in the membrane.
(3) Of fundamental importance is the question of how prestin responds to changes in the membrane electric field. How do these changes relate to nonlinear charge movement? What is it that modifiers of prestin function do to the molecule to result in changes in its function?
By their nature, these questions necessitate the approaches used in our study which

are sensitive at the single molecule level and nanometer length scales.

1.2 Structure of thesis

The overarching goal of this thesis is to improve the current characterization of prestin interactions with itself and the interactions of prestin with the membrane environment in order to better understand its function at a molecular level that has so far not been achieved in current studies of prestin. Ch. 2 provides a background for understanding mammalian hearing and how it depends on prestin function. A discussion of cell membrane heterogeneity and current models describing how the membrane is compartmentalized are also provided. In addition, a brief introduction to the experimental techniques that have been employed in this work to study prestin at the level of single molecules and nanometer length scales is outlined.

Ch. 3 applies single molecule fluorescence (SMF) microscopy and diffraction limited signal brightness analysis [Brameshuber et al., 2010, Harms et al., 2001a, Schmidt et al., 1996b] to quantify the distribution of fluorescent stoichiometries from aggregates of prestin-citrine with the goal of determining the distribution of prestin oligomeric states in the cell membrane. A comparison of our results to a probabilistic model that we developed suggests that prestin forms mainly tetramers and dimers in the cell membrane. We also use the method to test whether modifications of membrane cholesterol affect prestin oligomerization.

In order to understand how cholesterol manipulation affects prestin function, Ch. 4 uses a combination of SMF microscopy and site directed labeling with a photostable dye to perform live cell SPT of prestin. We found that prestin undergoes hop-diffusion

in confinements of a broad size range with an average area of $\sim 1\,\mu m^2$. Depletion of membrane cholesterol increased the average confinement area and produced a large gap in the distribution of confinement sizes. In addition, our observation that cholesterol depletion decreases the confinement strength explains cholesterol dependent alterations in the punctate distribution of fluorescence observed for cells expressing prestin-GFP. Our results allowed us to narrow the possible ways that cholesterol may affect prestin charge movement and confirmed the growing view that the membrane environment directly affects prestin function.

In Ch. 5 using a combination of Förster resonance energy transfer (FRET) and the whole-cell patch clamp technique to control membrane voltage, we measure the self-interactions of prestin genetically fused to either CFP or YFP FRET reporters as a function of membrane voltage in live cells. We find that prestin-prestin FRET decreases with depolarization over a voltage range that is biophysically relevant to prestin function. The width of the FRET/voltage relationship is consistent with the width of the charge/voltage relationship. In addition, we are able to inhibit the FRET versus voltage trend with the introduction of salicylate which destroys both prestin associated charge movement and motility. Finally, we also measure voltage dependent FRET of prestin genetically tagged with tandem FRET pairs. Our results provide one of the first confirmations of voltage dependent structural changes in prestin, and support the view that a prestin conformational change is the underlying mechanism of electromotility. We demonstrate that the voltage-dependent structural changes in prestin could either be changes in oligomerization or changes in conformation of prestin oligomers that result in reduced distance between C-terminal tags when the membrane is depolarized. In addition, we show compelling evidence that a confor-

mational change in prestin involves a reorientation of the C-terminus relative to the cell membrane.

Finally, in Ch. 6 we summarize our results and specific conclusions for each experiment described in this thesis. We address how our conclusions have improved our understanding of prestin function. We also highlight relevant connections and implications between the results of the three studies. In concluding, we point out the limits of our results and remaining unanswered questions. Finally, we suggest future studies that are motivated by the remaining unanswered questions.

Chapter 2

Background

2.1 Mammalian hearing

A basic description of mammalian hearing describes the process by which acoustic energy, in the form of air pressure waves, is collected, processed, and ultimately transmitted to the brain where it is perceived as sound. Acoustic waves must first be efficiently transmitted from air to the fluids in the cochlea, residing in the inner ear, where it can mechanically stimulate the appropriate sensory cells. However, the process is not simply a passive relay of sound. A crucial element of mammalian hearing involves a unique and only partially understood method of active amplification.

2.1.1 Auditory pathway

The outer and middle ear

The first element of the ear is the pinna, the cartilaginous outer tissue which directs sound into the auditory canal. The auditory canal tapers in diameter until reaching the tympanic membrane or eardrum. The purpose of the taper in the auditory canal is to provide an initial amplification of sound before reaching the middle ear. Vibrations of the tympanic membrane are transmitted into motion of the three ossicles or middle ear bones which couple to the oval window of the fluid filled cochlea. Their purpose is to impedance match the air within the ear canal to the fluid of the cochlea (Fig. 2.1).

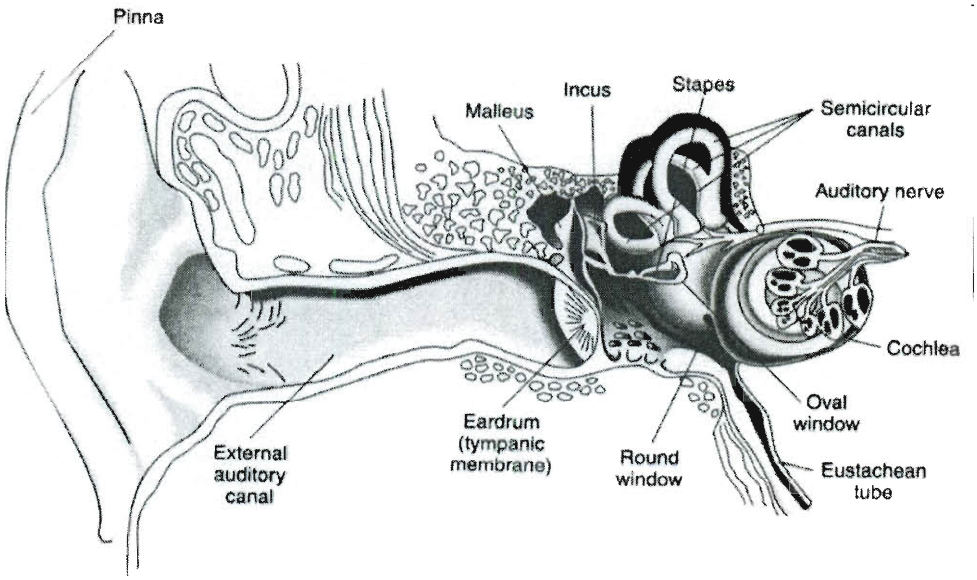

Figure 2.1 : Anatomy of mammalian auditory system. Image source: http://www.skidmore.edu/~hfoley/Perc9.htm.

The cochlea

The cochlea is a snail shaped, fluid filled duct that comprises the inner ear. It is coiled into two to three turns around the modiolus which is the bony central core of the cochlea housing the spiral ganglion which transmits auditory nerve impulses to the brain. If the cochlea were unraveled into a linear form, it would be $35mm$ long (in humans) from base to apex [Geisler, 1998]. Pressure waves, entering the cochlea via the oval window, are transmitted to the fluid (perilymph) within the scala vestibuli which is the upper-most of three compartments comprising a cross-section of the cochlea (Fig. 2.2). The other two compartments are the scala tympani — the lowest compartment, also filled with perilymph and connected at the helicotrema to the scala vestibuli — and the scala media (or cochlear duct), the middle compartment, which is filled with endolymph. The three compartments are separated from each other by a number of membranes, each one of which carries its own function. The Reissner's membrane is a two cell layer thick membrane separating the endolymph of the scala media from the perilymph of the scala vestibuli. The Reissner's membrane is effectively transparent to sound [Geisler, 1998], making the scala vestibuli and scala media effectively one compartment acoustically. However it does allow each compartment to maintain separate ionic compositions allowing for preservation of the endocochlear potential. Within the scala media, along most of its outer wall, is the stria vascularis, a specialized cellular structure that acts as a potassium (K^+) pump keeping the endolymph potassium concentration high thus generating the endocochlear potential. The basilar membrane (BM) defines the boundary between the scala media and the scala tympani. It is of central importance to the auditory system since it defines the basic platform of the cochlear partition. Much of the acoustic energy entering the cochlea is transmitted as a traveling wave along the BM. On top of the BM rests the

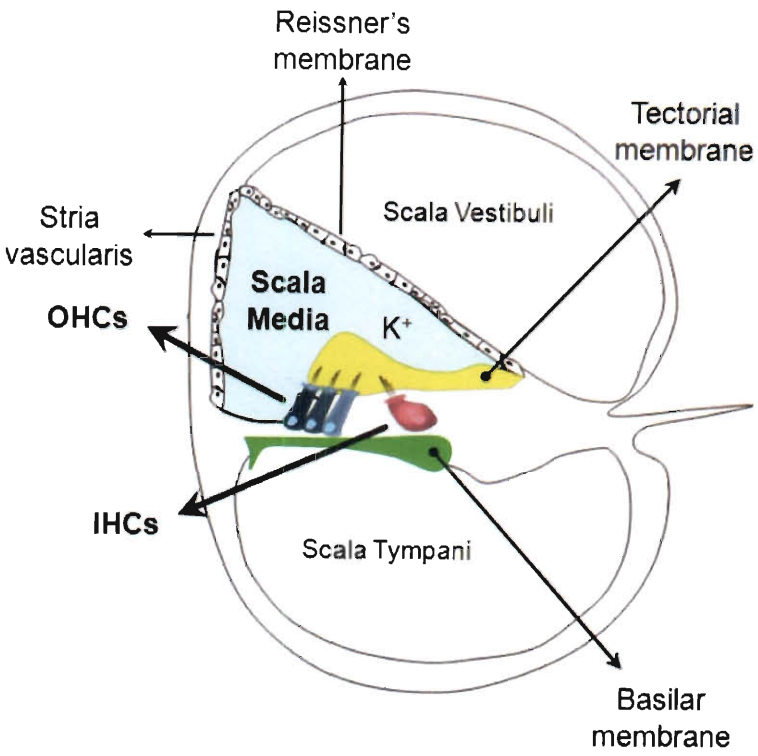

Figure 2.2 : Cross section of cochlear turn. Image source: [Podgorski, 2009].

organ of Corti where the sensory cells of the cochlea reside.

The organ of Corti

The organ of Corti is an intricate series of substructures that spectrally analyze, amplify, and convert mechanical energy into neural signals (Fig. 2.3). The organ of Corti is partially bounded on its apical surface by the tectorial membrane (TM) which is a gelatinous structure covering the sensory cells. Most of the organ of Corti is bathed with perilymph and is separated from the endolymph of the scala media by a series of tight junctions (reticular lamina). At the base of the organ of

Corti is the previously mentioned BM. Along the BM, the amplitude of the traveling wave is sharply dependent on position for each frequency entering the cochlea. High frequencies produce the largest amplitude near the base and low frequencies near the apex. This is due to variations in the lateral breadth and vertical thickness of the BM that change the resonant frequency along its length. In this sense the BM acts roughly as a Fourier spectrum analyzer for sound. Also along the BM reside two sets of ciliated hair cells which sit in supporting cells called Deiters' cells. The stereocilia protrude above the reticular lamina into the endolymph filled space between the tectorial membrane and the reticular lamina. Inner hair cells (IHC) run along the BM closer to the modiolus and are the true sensory cells of the auditory system in the sense that they provide the final signal to the brain. Motion of the endolymph relative to the BM laterally displaces the stereocilia allowing the modulation of the influx of predominantly K^+ ions, thereby depolarizing or hyperpolarizing the cell. It is the endocochlear potential that drives the influx of K^+. These shifts in membrane potential result in neurotransmitter release into the afferent innervations of the IHCs to fire signals to the brain. Laterally further from the modiolus reside three rows of outer hair cells (OHC) running along the length of the BM. OHCs are also sensory cells for sound, however they are predominantly efferently innervated. They play a unique role that is central to the mechanics of the cochlea and mammalian hearing characteristics.

2.1.2 Cochlear amplification

Outer hair cells

The stereocilia of the OHCs (in contrast to IHCs) do make contact with the tectorial membrane (Fig. 2.3a). Relative displacement of the TM membrane and the reticular

lamina shears and deflects the OHC stereocilia causing mechano-electrical transduction and cell depolarization (Fig. 2.3a). Unlike IHCs, however, OHCs undergo whole cell length changes in response to changes in membrane potential [Ashmore, 1987, Brownell et al., 1985]. Membrane depolarization results in axial contraction and hyperpolarization results in axial elongation. This process has been termed electromotility (Fig. 2.4). The resting axial length of OHCs increase along the length of the BM from $\sim 10 - 20\,\mu m$ near the basal end of the cochlear to $\sim 80\mu m$ near the apex [He et al., 2006]. Since the BM changes stiffness by more than 100-fold [Dallos et al., 1996] along its path through the cochlea, the OHCs are selectively excited. High frequency sounds excite hair cells at the base of the cochlea and low frequency sounds at the apex.

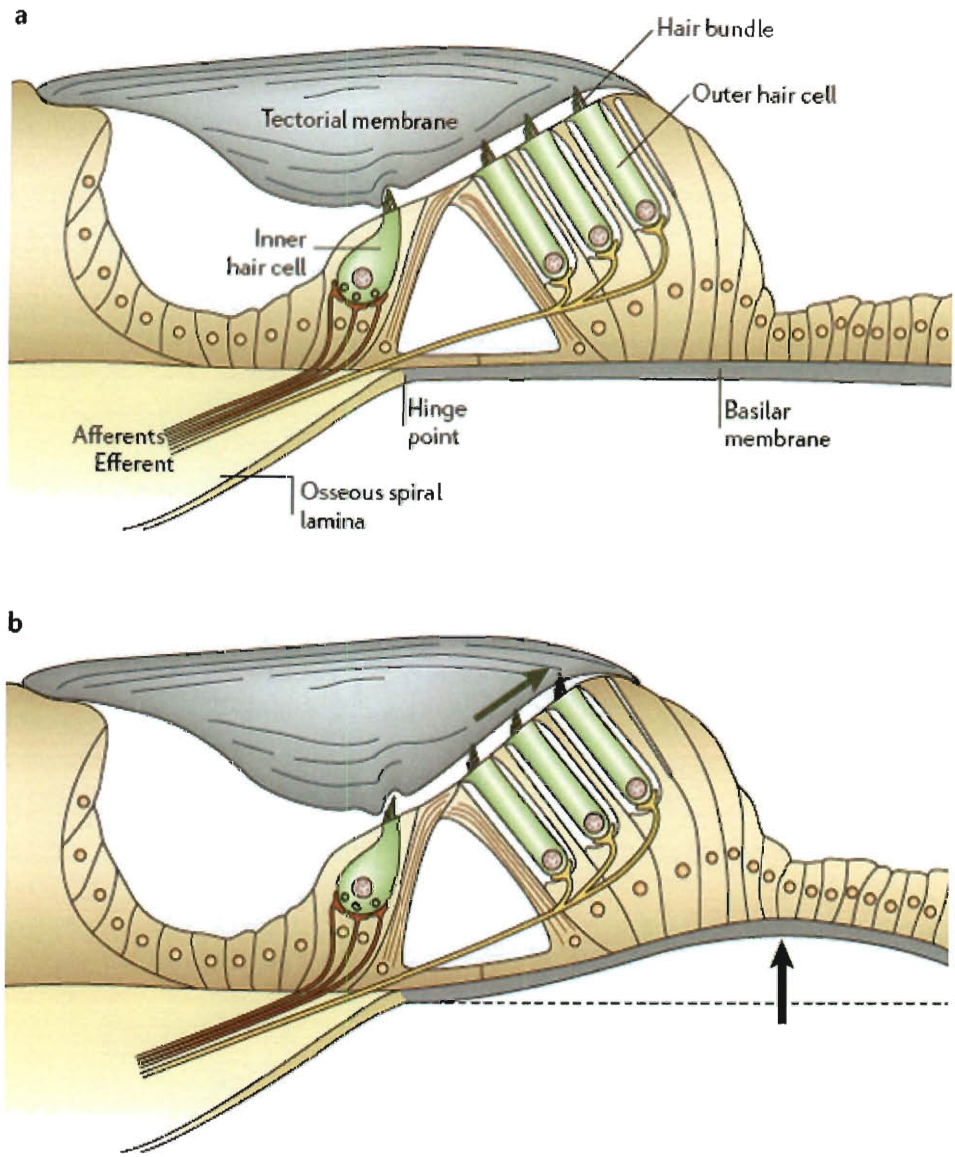

Figure 2.3 : Cross section of organ of Corti. Image source: [Fettiplace and Hackney, 2006].

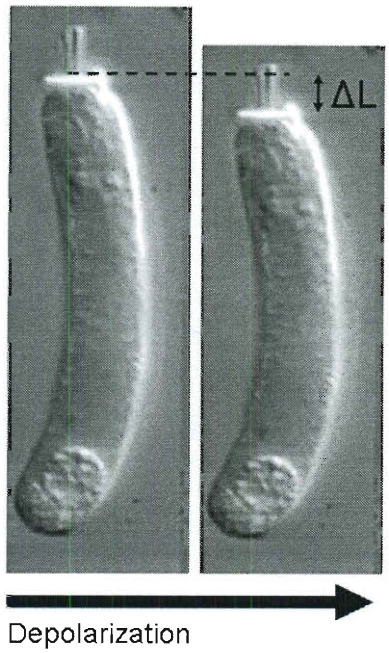

Figure 2.4 : Outer hair cells. OHC depolarization causes cell shortening. Image adapted from: [Frolenkov et al., 1998].

The cochlear amplifier

Voltage evoked changes in length of OHCs feed mechanical energy back into the motion of the BM boosting the amplitude and frequency response of the system (see Fig. 2.5), and they do so up to rates at least as high as $79kHz$ [Frank et al., 1999]. In this sense the OHCs act as both sensors and local amplifiers of BM motion. This mechanism of active amplification, using the endocochlear potential as a battery supplying the necessary voltage, is termed the cochlear amplifier. Cochlear amplification is thought to account for the exquisite frequency discrimination and sensitivity of

mammalian hearing [Ashmore, 2008]. While it was suggested for some time that OHC motility is crucial to cochlear amplification due to the piezo-electric like properties of OHCs and that the motor element resided in the membrane [Kalinec et al., 1992], it was not until the discovery of the membrane protein prestin [Zheng et al., 2000] that the likely candidate was revealed.

2.1.3 Prestin as a membrane motor and nonlinear capacitance

Electro-mechanical coupling

In addition to their motile properties, OHCs under voltage clamp using patch recording pipettes show a voltage dependent membrane capacitance [Santos-Sacchi, 1991] similar to that observed in the voltage gated ion channels [Villalba-Galea et al., 2008] (Fig. 2.6). Depolarization and hyperpolarization of the OHC results in the coupling of net positive charge into and out of the membrane, respectively. Since the amount of charge moved per unit step of membrane potential depends on the membrane voltage, this effect is termed nonlinear capacitance (NLC). In addition, the charge/voltage and OHC-length/voltage relationships are found to parallel each other since they both are well fit by a sigmoidal two-state Boltzmann function with similar shape parameters and voltages of half-maximal charge movement or length change (Fig. 2.6, middle panel). As a result, the measured NLC in OHCs is a bell shaped curve since it is the derivative of the sigmoidal charge/voltage relationship. Due to the tight functional correspondence between the two, measurement of NLC in OHCs is generally considered a surrogate measure of electromotility [Dallos and Fakler, 2002]. It is generally believed that the membrane protein prestin, which is highly expressed only in OHCs, provides the molecular basis for both nonlinear capacitance and electromotility in OHCs.

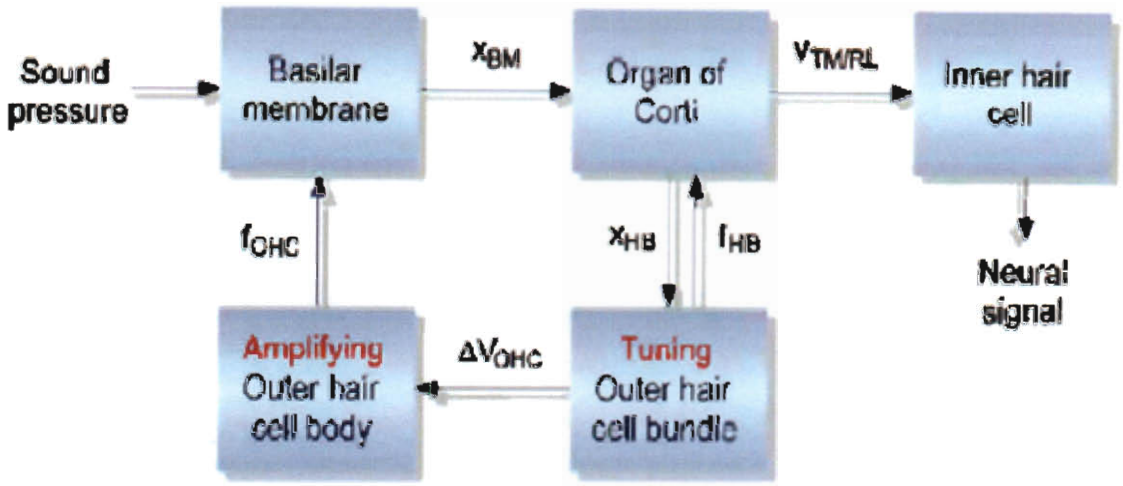

Figure 2.5 : Cochlear amplification diagram. Image source: [Ashmore et al., 2010].

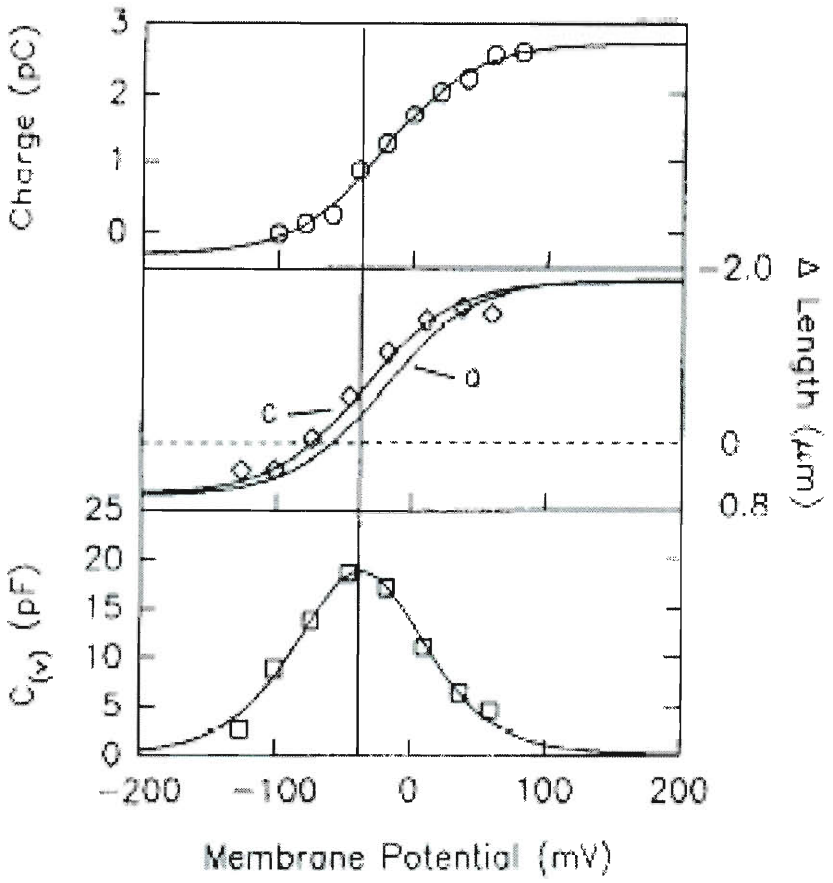

Figure 2.6 : Electromotility. Image adapted from: [Santos-Sacchi, 1991].

Prestin functional characteristics

Prestin was discovered in 2000 by subtractive cloning of IHC and OHC cDNA libraries [Zheng et al., 2000]. Prestin was found to be highly expressed in the OHC lateral membrane, but not in the IHC. It was found to consist of 744 amino acids [Zheng et al., 2000] with both N-terminus and C-terminus situated intracellularly [Zheng et al., 2001]. Prestin has 10-12 transmembrane domains forming a hydrophobic core in the membrane portion [Dallos and Fakler, 2002, Deák et al., 2005], and a large

C-terminal portion consisting mostly of a STAS (sulfate transporters and anti-sigma factor antagonist) domain common to all the members of the SLC26 anion exchanger family to which prestin belongs (see Fig. 2.7) [Pasqualetto et al., 2010].

A wide array of evidence supports prestin as the motor protein underlying electromotility. Heterologous expression of prestin in mammalian cells confers all the hallmarks of electromotility observed in OHCs [Chambard and Ashmore, 2003, Deák et al., 2005, Iida et al., 2005, Zhang et al., 2007, Zheng et al., 2000]. Prestin transfected TSA201 kidney cells displayed NLC, and when pulled into a microchamber followed by stimulation with sinusoidal driving signals, displayed voltage dependent motility [Zheng et al., 2000]. Knock-in mice, with an impaired function prestin mutant, lack normal sensitivity and frequency selectivity indicating that prestin is required for cochlear amplification [Dallos et al., 2008]. The observation of NLC in mammalian cells heterologously expressing prestin is therefore widely regarded as a direct signature and metric of prestin function in those systems, and supports the use of mammalian cells as a model system for the OHC.

Generally, prestin is assumed to operate by undergoing a conformational change in response to sensing changes in transmembrane potential [Ashmore, 2008]. Presumably, a conformational change in prestin both exerts force on the membrane, explaining OHC axial length changes, and couples charged species into the membrane thereby evoking NLC (Fig. 2.8). A detailed molecular picture of the conformational change has yet to be experimentally observed, however a number of phenomenological models exist. Most notable are the area motor models [Dallos et al., 1993, Iwasa, 1994, Oliver et al., 2001] and the membrane bending model [Raphael et al., 2000,

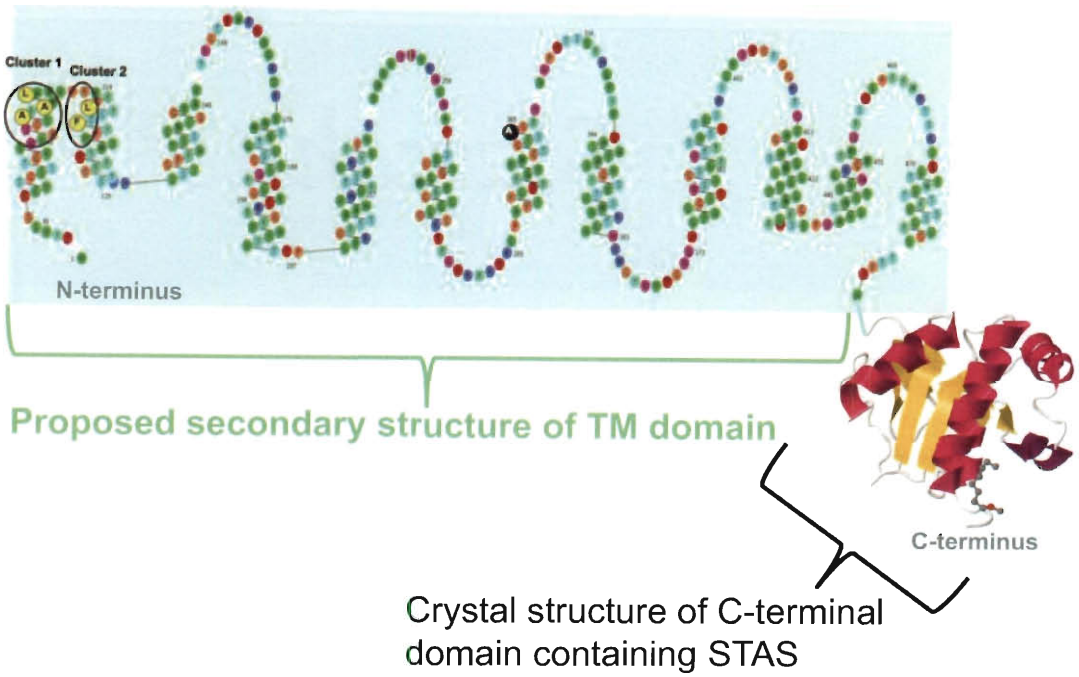

Figure 2.7 : Summary of prestin structural knowledge. Mammalian prestin is 744 amino acids with both N- and C-termini located intracellularly [Zheng et al., 2000]. The structures of the N-terminal and transmembrane domains are unknown, however there are predicted structures posing 10-12 transmembrane $\alpha-$helices for the transmembrane domain. Shown is a predicted structure for the transmembrane domain based on hydrophobicity calculations and evolutionary trace analysis [Rajagopalan et al., 2006]. The prestin C-terminal domain crystal structure has been solved and shows that the C-terminal domain of prestin has an ovoid shape containing a central core with a β-sheet, composed of 6 β-strands, surrounded by 5 α-helices [Pasqualetto et al., 2010]. The C-terminal domain is mostly comprised of the STAS domain and is about 240 amino acids. The crystal structure excludes a variable loop comprising amino acids 564 through 636 and also excludes the extreme C-terminal region (residues 719 through 744) which is predicted to be a flexible disordered region, however the structure as a whole is tightly held together by multiple hydrogen bonds [Pasqualetto et al., 2010].

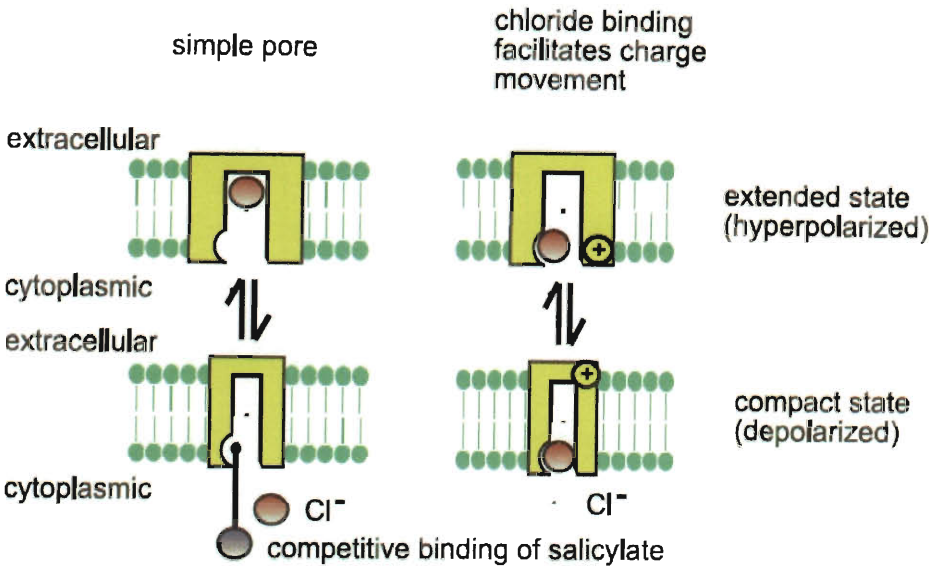

Figure 2.8 : Area motor models of prestin. Image adapted from: [Ashmore, 2008].

Spector et al., 2006]. The area motor model assumes that a prestin conformational change involves changes in cross-sectional area of the motor within the membrane while simultaneously coupling charged species into the membrane. The membrane bending model proposes that local electrically-induced curvature changes of flexoelectric membrane elements, resulting from membrane dipole reorientation, produce cell length changes via membrane-cytoskeletal coupling. While the model does not specifically construct a mathematical formalism on how nonlinear charge movement occurs, NLC could easily be incorporated into the model since it allows for the possibility of a membrane protein conformational change as either the source or the result of membrane curvature changes.

Several pieces of experimental evidence provide important clues on the nature of a conformational change in prestin. It has been shown that intracellular anions are required for NLC and electromotility [Oliver et al., 2001]. The observation that application of salicylate inhibits NLC charge movement in a dose dependent manner suggests that salicylate competes with Cl^- for binding to prestin. This initially lead to the hypothesis that Cl^- acts as an extrinsic voltage sensor for prestin [Oliver et al., 2001]. However, according to another model, Cl^- allosterically effects prestin allowing it to undergo conformational changes [Rybalchenko and Santos-Sacchi, 2008]. Both these models suggest that prestin contains a binding pocket for chloride. The crystal structure of the C-terminal STAS domain has recently been solved and shows the structure to be rigidly held together by multiple hydrogen bonds [Pasqualetto et al., 2010]. This suggests that a conformational change in prestin probably does not involve shape changes in the C-terminus. Furthermore, reversal of charged residue clusters in the C-terminal domain do not affect the shape factor of NLC but do in some cases shift NLC [Bai et al., 2006] or reduce total charge movement. While this suggests that the C-terminus may play a role in affecting allosteric modulation of prestin by anions, it also suggests that these residues remain outside the membrane electric field in a conformational change. Finally, an intriguing recent report shows convincing evidence that a 3-state or a modified version of the common two-state model may be required to describe the electro-mechanical coupling of a conformational change in prestin [Homma and Dallos, 2011].

Prior to the discovery of prestin, a dense array of 8-10 nm particles were found on the cytoplasmic leaflet of OHC plasma membranes [Gulley and Reese, 1977, Kalinec et al., 1992] and were purported to be the motor. Subsequent to the discovery of the

prestin gene, it was initially assumed that prestin was probably a tetramer since the predicted size of the protein was too small to account for the 8-10 nm particles [Ashmore, 2008], and an initial report suggested that prestin forms at least a dimer, formed by two monomers cross-linked with a disulfide bond, and possibly a tetramer based on PFO-PAGE and SDS-PAGE gels [Z. et al., 2006]. Further experiments demonstrated that prestin oligomeric state might affect prestin function [Bian et al., 2010, Detro-Dassen et al., 2008, Rajagopalan et al., 2007, Sturm et al., 2007, Wang et al., 2010]. Subsequently much interest has been placed on determining the oligomeric state(s) of prestin motivated by what constitutes the functional unit(s) and by the possibility that oligomerization could play an import role in motor function. Numerous conflicting reports have touched on this question [Bian et al., 2010, Detro-Dassen et al., 2008, McGuire et al., 2010, Mio et al., 2008, Murakoshi et al., 2006, Rajagopalan et al., 2007, Sturm et al., 2007, Wang et al., 2010, Z. et al., 2006] (see Discussion in Ch. 3), however a clear description of prestin oligomeric state distribution and its relevance to electromotility and prestin associated charge movement remains ambiguous.

It has become increasingly evident that the membrane environment of prestin is crucial to its function. Various drug treatments and membrane manipulations have been shown to alter prestin associated charge movement and motility. Amphiphilic drugs known to alter membrane curvature shift NLC [Fang and Iwasa, 2007, Greeson and Raphael, 2009]. Substitution of lipids with differing acyl-chain lengths shift the operating point of NLC due to changes in membrane thickness [Fang et al., 2010]. Arguably the most important membrane manipulation that affects prestin function — and, unfortunately, often ignored in functional models — is modification of membrane cholesterol concentration. Membrane cholesterol has been shown to be functionally

important for hearing. OHC cholesterol levels decrease during maturation of hearing in mice, and manipulation of cholesterol levels in live adult mice affect cochlear amplification [Rajagopalan et al., 2007]. Furthermore, hypercholesterolemia has been linked to reduced cochlear amplification in human patients [Preyer et al., 2001]. For both OHCs and prestin transfected cells, depletion of membrane cholesterol reversibly shifts the NLC curve [Rajagopalan et al., 2007, Sturm et al., 2007]. Specifically, the peak of NLC shifts toward depolarized potentials for depletion and towards hyperpolarized potentials for cholesterol loading. Furthermore, cholesterol concentration and total charge movement were demonstrated to have a linear relationship [Sfondouris et al., 2008]. Numerous studies demonstrate that prestin may associate into cholesterol rich microdomains. Images of fluorescently labeled prestin in transfected cells show a qualitatively punctate prestin distribution in the membrane [Organ and Raphael, 2007, Rajagopalan et al., 2007, Sturm et al., 2007]. Depletion of membrane cholesterol reversibly eliminates puncta. Punctate prestin fluorescence also colocalizes with known lipid raft markers [Rajagopalan et al., 2007, Sturm et al., 2007], and prestin from membrane fractions of transfected cell lysate also colocalizes with lipid raft markers on Western blots [Rajagopalan et al., 2007]. It should be stressed that the cholesterol induced shifts in NLC are as large as $150\,mV$ in OHCs [Rajagopalan et al., 2007], easily exceeding shifts due to any other known drug treatment. All these studies highlight the importance of understanding the functional significance of prestin microdomain localization on motor function.

2.2 Membrane protein environment

2.2.1 Cell membrane is heterogenous

Early descriptions of the cell's lipid membrane described it as predominantly a passive solvent for proteins in the membrane [Simons and Ikonen, 1997, Singer and Nicolson, 1972]. However, in recent decades experimental evidence has lead to a paradigm shift in describing the cell membrane in order to explain the slower diffusion of molecules in the cell membrane compared to model membranes and to explain the apparent slowing of molecules upon oligomerization [Kusumi et al., 2005]. Current models, driven by recent advances in experimental technology, characterize the membrane as a heterogeneous environment that is compartmentalized by lipid-lipid, lipid-protein, and protein-protein interactions. Differing views exist on how the membrane is compartmentalized, each with considerable experimental support and some apparent inconsistencies. Nonetheless, it is clear that domains or confinements of membrane molecules do exist even if the underlying cause for them is not completely clear. While some controversy remains on the exact nature of the compartmentalization of the membrane, the different views may not be mutually exclusive and it is probably fair to say that most researchers in the field agree that multiple types of membrane confinements exist [Dietrich et al., 2002, Lingwood and Simons, 2010] and that they play important roles in facilitating interactions between membrane constituent molecules [Eggeling et al., 2009].

2.2.2 Compartmentalization of the cell membrane

Lipid rafts and microdomains

The membranes of mammalian cells contain countless types of lipids and a wide array of proteins depending on cell type. The main lipids are the glycerophospholipids, the sphingolipids, and sterols. The predominant type of glycerophospholip is phosphadidylcholine, which is the predominant lipid overall, and the main sphingolipid is sphingomyelin with 10-20% composition of most membranes [Munro, 2003]. Cholesterol is the most predominant and important sterol comprising 30-40% of most lipid membranes [Munro, 2003]. Glycerophospholipids are characterized by generally having unsaturated acyl chains (at least one double bond in the hydrocarbon tail chain) and sphingolipids are characterized by predominantly saturated acyl chains [Munro, 2003]. Cholesterol interacts with the hydrophobic tails of both types of lipids but predominantly with sphingolipids due to their straight saturated tails [Silvius, 2003].

The original raft hypothesis derived from mainly two observations: detergent resistant membrane (DRM) fractions, and the observation that lipids are asymmetrically distributed in cells. It has been observed that when plasma membrane components are solubilized with the non-ionic detergent Triton-X for extraction, a portion is resistant to solubilization. The resistant portion (DRM) is also observed to be enriched in sphingolipids, cholesterol and glycosylphosphatidylinositol(GPI)-anchored proteins [Simons and Ikonen, 1997]. This observation was then used to propose the lipid raft hypothesis in order to explain how the GPI-anchored proteins were selectively transported to the apical outer leaflet of membranes which are enriched in sphingolipids. The hypothesis is that domains, containing sphingolipids and cholesterol, form on the

outer leaflet of the membrane and exist in a liquid ordered phase surrounded by a phospholipid rich liquid disordered phase. The formation of rafts is also aided by the ability of cholesterol to order lipids with saturated tails. Lipid rafts have been proposed to be involved in signalling, facilitation of membrane protein oligomerization, and membrane trafficking [Munro, 2003]. Membrane anchored proteins and transmembrane proteins would reside in the rafts due to associations with raft related lipids, interactions with raft proteins, or due to hydrophobic interactions [Lingwood and Simons, 2010]. Although the observation of DRM fractions supports the existence of rafts, it has been demonstrated that the presence of a protein in a DRM fraction cannot be used to prove that it is raft associated [Munro, 2003] — and in fact Triton X can even be used to form rafts in model membranes [Heerklotz, 2002]. However, the observation that membrane rafts can indeed be formed in model membranes [Lingwood and Simons, 2010] makes the existence of rafts in real cell membranes plausible.

Some controversy exists on whether lipid rafts can exist in cell membranes [Munro, 2003]. Although rafts can form in model membranes, they may not be able to form in cell membranes due to their greatly increased heterogeneity [Munro, 2003]. Recent ultra high speed single particle tracking studies of gold colloid labeled lipids have offered an alternative to the raft hypothesis [Kusumi et al., 2005]. DOPE, an unsaturated phospholipid probe (which should not be involved in lipid rafts), was found to undergo hop diffusion in $230\,nm$ sized compartments in rat kidney cells [Fujiwara et al., 2002, Murase et al., 2004]. Cholesterol did not affect the size of the compartments but cytoskeletal disrupting agents did. In addition the diffusion of GPI-anchored proteins, which should associate with lipid rafts, were found to undergo hop diffusion in compartments of roughly equal size to DOPE [Umemura et al., 2008].

A number of studies utilizing advanced microscopy techniques have provided considerable evidence for rafts of varying size. Electron microscopy of lipid raft markers in membrane patches displayed cholesterol-dependent clustering in microdomains with a mean diameter of 44 nm that occupy 35% of the cell surface [Prior et al., 2003]. Using fluorescence correlation spectroscopy, nanoscale organizations of sphingolipids, cholesterol, and proteins were found on both the inner and outer leaflets of live cells [Lasserre et al., 2008]. Eggeling et al. have found fairly clear evidence of small ($\sim 20\,nm$) shortlived ($\sim 10-20\,ms$) domains using STED to obtain improved spatial resolution [Eggeling et al., 2009]. In contrast, fairly large domains, in muscle cells, of size $700\,nm$ that survived for at least $13\,s$ were found for DMPE, which is a saturated lipid probe, while DOPE, a mono-unsaturated lipid probe, was found to diffuse with predominantly free diffusion [Schütz et al., 2000]. Recent definitions of membrane domains have been characterized less restrictively, and describe larger stable rafts that form from coalesced small dynamic rafts [Lingwood and Simons, 2010]. Dietrich et al. found transient confinement zones (TCZ) to GM1 (a glycosphingolipid), Thy-1 (a GPI-linked protein), DPPE (a fully saturated lipid analogue), and DOPE (an ununsaturated phospholipid) [Dietrich et al., 2002]. All were found in transient confinement zones, but GM1, Thy-1, and DPPE had more abundance of and longer residence in TCZs than did DOPE as would be expected if the confinement zones represented lipid rafts. Also, depletion of cholesterol with MβCD strongly affected the size of the confinement zones for GM1, Thy-1, and DPPE also consistent with the raft hypothesis. The long residence times ($\sim 5\,s$) and the fact that DOPE which is an unsaturated lipid was also confined suggested the possible involvement of the cytoskeleton [Dietrich et al., 2002]. Domains that depend on cholesterol have even

been found to coexist with cholesterol-independent domains [Sharma et al., 2004, Zacharias et al., 2002] perhaps indicating a needed redefinition of what a raft is.

Cytoskeletal fencing

Though it had long been suggested that the underlying cytoskeleton may be involved in interactions with membrane proteins and lipids [Sheetz et al., 1980], it was not until the experiments conducted in the last decade by the Kusumi group, alluded to above, that serious consideration was given to the concept as a general principle [Kusumi et al., 2005]. The basic line of evidence (but by no means the only evidence) comes from ultra-fast SPT of various membrane molecules, that have been conjugated to $\sim 30\,nm$ sized gold colloids that unlike fluorophores do not bleach and can therefore be tracked indefinitely and can be viewed with standard white light microscopy and therefore can be tracked at ultra-fast speeds ($25\,\mu s$ frame times) [Fujiwara et al., 2002, Murase et al., 2004, Suzuki et al., 2005, Umemura et al., 2008]. The molecules tested include saturated and unsaturated lipids, GPI-linked proteins, G-coupled proteins (which are linked to cytoplasmic leaflet lipids), and transmembrane proteins. The measurements were made in a wide array of cell types, each showing confinements to all types of molecules in the membrane with the size of the confinements varying between cell types. Confinement sizes were often modified by cytoskeletal inhibitors and only moderately depended on membrane cholesterol. Microscopic diffusion constants within the corrals are comparable to those within membrane blebs and model membranes. Lastly, the confinement sizes agree with independent estimates of the cytoskeleton mesh-size from optical trapping and electron microscopy experiments. These observations lead to the membrane-skeleton fence model and the anchored-protein picket model which pose that the membrane of all cells are compartmentalized

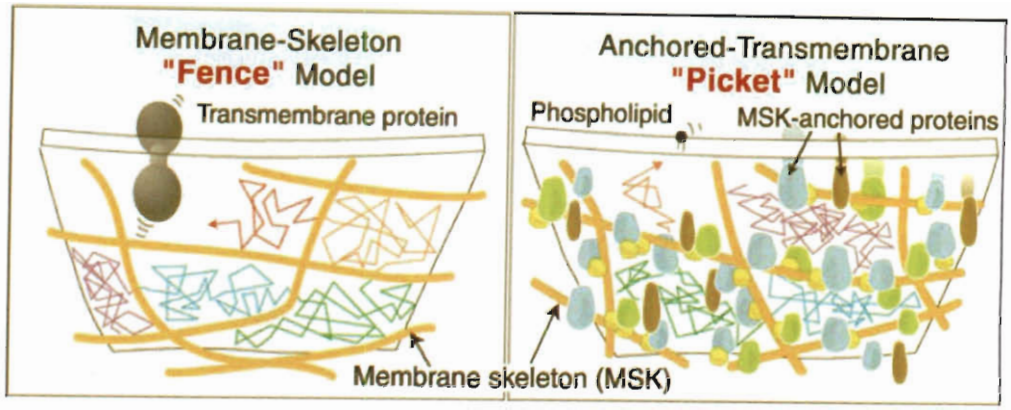

Figure 2.9 : Cytoskeletal membrane compartmentalization models. Image source: [Kusumi et al., 2005].

by the cytoskeleton as a general principle. In the membrane-skeleton fence model, the cytoplasmic portion of transmembrane proteins and G-protein coupled receptors are corralled by the cytoskeleton, and that proteins hop between corrals (Fig. 2.9, left picture). The anchored-protein picket model accounts for the confinements of lipids, on both inner and outer leaflets, and the GPI-anchored proteins: transmembrane proteins bound to the cytoskeleton form "pickets" that corral lipids and membrane proteins (Fig. 2.9, right picture). The models account for the long observed reduced macroscopic diffusion of membrane proteins and lipids in cells compared to in artificial membranes. For a detailed review see Ref. [Kusumi et al., 2005].

While the cytoskeletal corralling models appear promising, some controversy remains. Some experiments have given conflicting results. While in many cases this is due to misinterpretation of the data [Kusumi et al., 2005], some inconsistencies remain. For example, single molecule studies of a GPI-anchored protein in T24 cells using fluorescent labeling seemed to show no confinements [Wieser et al., 2007a]. In

contrast, gold colloid labeled lipid probes in T24 cells were found to be transiently confined in compartments as large as $120\,nm$ [Murase et al., 2004]. Much of the controversy on the experiments supporting the cytoskeletal corralling models has been due to the possibility that the use of functionalitized gold nanoparticles may cross-link to other entities in the membrane and affect the diffusion of the probe. Gold nanoparticles have been shown to affect diffusion in cells [Tomishige and Kusumi, 1999] and even in model membranes [Lee et al., 1991].

2.2.3 Protein-protein interactions

The ways in which protein-protein interactions affect protein function and cellular processes is too vast a subject to do justice to here. Protein-protein interactions are involved in signalling [Virkamäki et al., 1999], cell motility [Parsons et al., 2004], cargo trafficking [Yildiz et al., 2003], and maintaining cell shape [van den Ent et al., 2006] — these examples comprise a very short list of physiological roles for which protein-protein interactions are important. Various disease states are the result of altered interactions between proteins [Gray, 2004]. Often, the functional unit of a protein is an oligomer [Cuff et al., 1998], and in some cases, different oligomeric states of a protein have distinct functions [Hebert and Carruthers, 1992]. For an overview of the importance of protein-protein interactions, see the introduction to the review by [Phizicky and Fields, 1995].

2.3 Background on techniques

At their fundamental level, basically all biological processes in living organisms involve the motions and interactions of small objects — such as proteins, lipids, and small molecules — over length scales as short as nanometers. Modern advances in optical

microscopy instrumentation and techniques have revolutionized the study of cellular function by allowing researchers the opportunity to obtain information on sub-cellular events with single molecule and nanometer resolution.

2.3.1 Single molecule fluorescence

Principles of single molecule detection

Single molecule detection allows the possibility of obtaining the full distribution and time-evolution of a population of events in a heterogeneous environment. Ensemble measurements, on the other hand, by their nature average over a large population of events and therefore typically mask important details. However, just like measuring the probability of getting "heads" in a coin toss experiment requires flipping a coin many times, single molecule experiments require the acquisition of an ensemble of events to obtain the full distribution.

A common single molecule detection technique used for studying the motion and localization of proteins, and the one used in this thesis, is single molecule fluorescence (SMF) microscopy. An ensemble of proteins are somehow labeled with a fluorescent molecule (serving as a reporter for their localization), excited with resonant light, and the resulting photons are subsequently collected (using a microscope, Fig. 2.10) with sufficient efficiency that once they are sent to a detector the individual nature of the proteins are apparent. The concept is simple, however a number of requirements must be met for SMF microscopy to (a) allow the protein to be detected, (b) preserve the individual nature and identity of each protein, and (c) do so in a way that does not perturb the aspect of the protein you are trying to study.

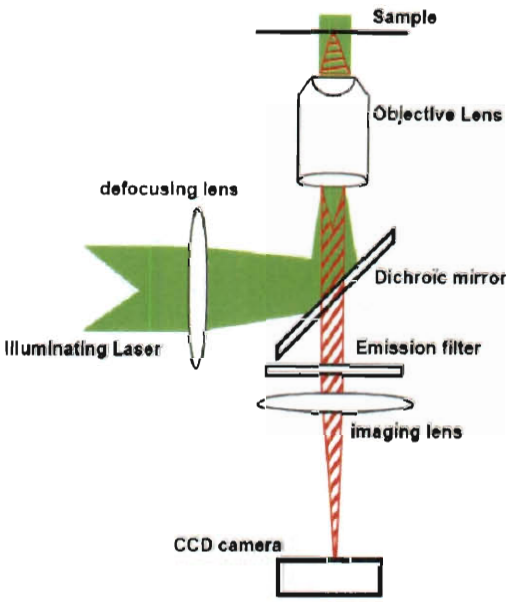

Figure 2.10 : Diagram of a typical wide-field SMF microscope. Image source: [Cognet et al., 2002].

Detecting SMF requires collecting sufficiently many photons from the fluorescent tag such that its fluorescence is detectable above sources of noise. Obtaining high photon detection efficiencies requires minimizing losses along the path of the microscope. This typically entails a high numerical aperture objective to maximize photon collection efficiency and a high quantum efficiency detector to detect as many of the collected photons as possible. Furthermore, a fluorophore must be chosen that has a quantum yield that is as high as possible to maximize the number of emitted photons. In addition, the light from the fluorescent tag must be spectrally separated from other sources of stray light when possible. The most important sources of stray light in SMF experiments are the excitation laser light, cellular autofluorescence, and out of focus fluorescence from the fluorophore of interest [Cognet et al., 2002]. Stray laser light and cellular autofluorescence can be minimized by appropriate choice of dichroic and emission filters and by use of red-shifted fluorophores [Harms et al., 2001b]. Out of focus fluorescence may be reduced by either minimizing the expression level of fluorescently labeled protein or, if possible, using total internal reflection (TIR) to minimize the excitation volume to a $\sim 100 - 200\,nm$ region from the coverslip [Axelrod et al., 1984]. If one is interested in knowing the excitation intensity of the laser at the location of the fluorophore, then TIR is not advisable. This is because of the exponentially decaying electromagnetic field perpendicular to the coverslip and the fact that the membrane topology of a cell can have a large variance from its substrate ($\sim 150\,nm$) [Giebel et al., 1999, Stock et al., 2003] complicating an analysis of fluorophore brightness [Cognet et al., 2002]. A high background level can also be reduced by a photobleaching treatment with intense laser light to bleach autofluorescence and reduce out of focus fluorescence.

If the area density of fluorophores is too high, single molecule detection becomes impossible even if an experimental setup has excellent light collection efficiency. This is because for single molecules to be identified, the individual diffraction limited signals of the molecules must be sufficiently separated so that they do not overlap. This typically requires area densities of $\lesssim 1$ fluorescent molecule per μm^2 [Schmidt et al., 1996a]. Depending on the application, there are a number of ways of accomplishing this criteria. If one is only interested in the location of molecules (for example in single particle tracking) then one may again use photobleaching to reduce the area density to an appropriately low level. However if precise quantification of single molecule fluorescence is desired, TIR is not ideal for the reasons described above. Another option, in cases involving site directed labeling, is to reduce the concentration of fluorescent substrate [Schmidt et al., 1996a]. Also, one may take advantage of stable expression systems under inducible control to limit the expression level of the protein of interest [Bian et al., 2010]. Controlled expression allows for reduced area density while avoiding the need for a photobleaching step.

The use of single molecule detection has increasingly been applied in live cells allowing researchers to maximize the biological significance of the results. Care must be taken so that the experimental procedures (*e.g.* acquisition and fluorescent labeling) do not affect the biological function of the protein or the physical characteristic of the protein that is being measured. There are always trade-offs in the choice of procedure which must be maximized for each experiment. In SPT experiments, long trajectories of the moving particle are required to characterize the motion with statistical confidence [Kusumi et al., 2005]. The use of fluorescent labels for SPT limit the length of trajectories due to photobleaching but offer the best chance of minimizing

influence on the motion. The probe must not crosslink proteins to itself or to other membrane molecules which can affect a particle's diffusion or apparent aggregation. Specificity of labeling is also important especially when measuring protein oligomerization. In this case the probe must label only the protein of interest and not other molecules in the membrane. When measuring protein colocalization by accounting for the fluorescence in a diffraction limited area, one must also be sure that the probe labels the protein in a 1:1 ratio.

Fluorescent labeling considerations

The characteristics of the ideal fluorophore are photostability, small size, high quantum yield, specificity, 1:1 labeling stoichiometry, and ease of use. No fluorescent labeling strategies contain all these characteristics, but some characteristics are exemplified in individual strategies. Often experiments conducted *in vitro* can utilize special binding chemistries with highly stable fluorophores and achieve excellent specificity. However, for experiments performed in cells it is often more difficult to maximize all these characteristics. Also, depending on the parameter one wishes to study, the best in-cell labeling strategy may differ. For example, obtaining accurate trajectories using SPT does not critically depend on a 1:1 labeling stoichiometry, and in fact multiple labels per protein could actually be an advantage that allows for observing tracks longer [Cai et al., 2007].

The use of the fluorescent proteins (FP), especially the use of green fluorescent protein (GFP) [Tsien, 1998] and its variants, have become ubiquitous in the biosciences. The fluorescent proteins offer a great advantage for studies in cells since they can be genetically tagged to a protein of interest providing perfect labeling specificity

(for a nice review see [Cognet et al., 2002]). Furthermore, one can be assured that the FPs provide a 1:1 labeling stoichiometry making possible accurate "counting" of the protein of interest. In most cases fusion proteins constructed with the FPs retain their function in the cell. However, compared to the synthetic fluorophores such as Cy3, Cy5, tetramethylrhodamine (TMR), and the Alexa dyes, the FPs suffer reduced brightness and poor photostability. Nonetheless, the FPs provide ease of use since they can be expressed in mammalian cells by simple transfection methods without requiring a separate labeling step which can lead to non-specific labeling.

Often an experiment, most notably SPT experiments, will require fast time resolution and long observation times. In this case the critical characteristics are fluorophore brightness and photostability. As stated above, the synthetic organic dyes are superior to the FPs as far as brightness and photostability are concerned. Essentially unlimited observation times are provided by labeling with antibody-functionalized nano-particles [Fujiwara et al., 2002, Ritchie et al., 2005, Umemura et al., 2008]. However, nano-particles for use in SPT are generally tens of nanometers in size and therefore risk crosslinking to other proteins or sterically hindering native interactions with other macromolecules. Synthetic dyes are small but always require engineering a labeling chemistry. Fluorescent antibiodies or biotin-streptavidin chemistries are but two examples of methods that can be used to label proteins of interest with synthetic dyes. To prevent crossliking, Fab fragment antibodies against the protein can be used [Wieser et al., 2007b], or if using biotin-streptavidin chemistry a monovalent form of streptavidin has been developed [Howarth et al., 2006]. Antibodies are not always available or the generation of a binding site for fluorophore attachment at the surface of the cell may not be possible. In such cases a recognition sequence to a fluorescent

substrate may be introduced genetically at either N- or C-termini, but the fluorescent substrate must be membrane permeable if the binding site is intracellular. We have used this last method in Ch. 4 to label prestin at its C-terminus with a substrate fluorescently tagged with TMR.

2.3.2 Förster resonance energy transfer

Utility of FRET

Förster resonance energy transfer (FRET) was first fully formulated by German chemist Theodor Förster in 1948 [Förster, 1948]. FRET is the transfer of energy from an excited state donor molecule to an acceptor molecule via coupling between their transition dipole moments. The utility of FRET derives from its sharp dependence on distance and has therefore been characterized as a "ruler" for detecting proximity between molecules [dos Remedios and Moens, 1995]. As a result, FRET is commonly used to determine when two molecules are close to each other and when performed carefully can provide information on structural changes. The length scale is on the order of nanometers. The use of FRET and related techniques have become widely used in the field of biophysics. FRET has been employed to detect protein-protein interactions [Kenworthy, 2001], study conformational changes within proteins [Blunck et al., 2004] and DNA [Klostermeier and Millar, 2001], and study protein folding [Schuler and Eaton, 2008] and protein structure [Nazarov et al., 2007].

Theory of energy transfer

FRET is a quite general photophysical effect that can occur between any two molecules if they share spectral overlap and are within a characteristic distance R_o of each other called the Förster radius. Förster first treated FRET phenomenologically as the ra-

diationless transfer between two molecules [Andrews, 1989]. However since then it has been shown using a more general standard quantum electrodynamics calculation that Förster's result is the short distance limit of the full interaction hamiltonian incorporating radiative and radiationless Coulombic interactions [Andrews, 1989, Andrews and Bradshaw, 2004]. The mathematical theory is most often referenced from [Lakowicz, 1999].

The rate of energy transfer $k_T(r)$ depends on the overlap J_λ of the donor emission spectrum $F_D(\lambda)$ and acceptor absorption spectrum $\varepsilon_A(\lambda)$, the distance r between the molecules, the quantum efficiency of the donor Q_D, the index of refraction of the medium n, the inverse radiative decay rate of the donor τ_D in the absence of the acceptor, and a factor κ^2 which depends on the relative orientations of the two molecules [Lakowicz, 1999]. The rate of energy transfer can be parameterized in terms of the Förster radius R_o as

$$k_T(r) = \frac{1}{\tau_D}\left(\frac{R_o}{r}\right)^6 \tag{2.1}$$

which defines R_o as the distance for which the rate of energy transfer is equal to the decay rate τ_D^{-1}. The Förster radius is expressed in terms of the overlap integral J_λ as

$$R_o^6 = 8.79 \times 10^{-25}\left(\kappa^2 n^{-4} Q_D J_\lambda\right) \tag{2.2}$$

where

$$J_\lambda = \left(\int_0^\infty d\lambda F_D(\lambda)\right)^{-1} \int_0^\infty d\lambda\, \lambda^4 F_D(\lambda)\varepsilon_A(\lambda)\,. \tag{2.3}$$

Rarely is the orientational factor κ^2 completely known (see Lakowicz for κ^2 depen-

dence on orientation angles). However, often precise knowledge of κ^2 is not needed if only changes in FRET are desired. Often an orientation factor of $\kappa^2 = 2/3$ is assumed which is what the value would be for donors and acceptors that undergo randomized relative orientational diffusion [Lakowicz, 1999]. The efficiency of energy transfer E is given by $E = 1/(1 + (r/R_o)^6)$ and can be determined experimentally by measuring relative changes in donor fluorescence or lifetime in the presence and absence of acceptor.

Chapter 3

Use of single molecule fluorescence to explore prestin oligomerization

3.1 Introduction

Prestin is the motor protein that provides the molecular basis for outer hair cell (OHC) electromotility which is responsible for amplification in the mammalian cochlea [Zheng et al., 2000]. It is generally accepted that prestin undergoes a conformational change [Dallos et al., 1993, Iwasa, 1994, Oliver et al., 2001] that couples mechanical force in the cell membrane, evoking whole cell length changes in OHCs [Brownell et al., 1985], with charge movement that is routinely measured as a nonlinear capacitance (NLC) in both OHCs [Huang and Santos-Sacchi, 1993, Santos-Sacchi, 1991, Tunstall et al., 1995] and mammalian cells exogenously expressing prestin [Chambard and Ashmore, 2003, Deák et al., 2005, Iida et al., 2005, Zheng et al., 2000]. Much interest has been placed on how prestin functions at the molecular level and in particular on what constitutes the functional unit of prestin. Initially it was purported that prestin is a tetramer since electron micrograph and freeze fracture images of OHCs [Gulley and Reese, 1977, Kalinec et al., 1992] and AFM images of prestin transfected mammalian cells [Murakoshi et al., 2006] displayed a high density of 8-11 nm sized intramembranous particles (IMP), thought to be prestin, that are roughly four times larger than the predicted size of prestin based on its primary structure. However, since the discovery of prestin numerous studies have given conflicting estimates of

prestin oligomeric state focusing mainly on dimer [Bian et al., 2010, Detro-Dassen et al., 2008, Pasqualetto et al., 2008] and tetramer [Mio et al., 2008, Pasqualetto et al., 2008, Z. et al., 2006].

Several lines of evidence point towards an important role for oligomerization in prestin function. NLC recordings on transfected cells co-expressing two prestin mutants with distinct voltage-dependent capacitances showed functional characteristics that could not be described in terms of a simple sum of the two mutants alone indicating that interaction of the mutants alters function [Detro-Dassen et al., 2008]. Correlation of electrophysiological recordings to biochemical measurements, on a cell line under inducible expression of prestin, shows evidence of a dominant negative effect of two unknown forms of monomer [Bian et al., 2010]. It has been well established that manipulations of membrane cholesterol significantly alter prestin function [Rajagopalan et al., 2007, Sfondouris et al., 2008, Sturm et al., 2007]. In addition, membrane cholesterol manipulations affect the observed distribution of prestin oligomeric states on biochemical assays further suggesting a connection between oligomerization and prestin function [Rajagopalan et al., 2007, Sturm et al., 2007].

While multiple studies have demonstrated the tendency of prestin to oligomerize using a number of methods such as gel electrophoresis [Rajagopalan et al., 2007, Sturm et al., 2007, Z. et al., 2006] and protein purification [Mio et al., 2008, Pasqualetto et al., 2008], the methods employed cannot be done *in situ* and are often prone to effects that can affect protein-protein interactions. Biochemical assays such as BN-PAGE electrophoresis are useful tools to glean information on protein oligomerization, however the results are often ambiguous due to the sensitivity on the conditions employed

that can cause complexes to dissociate. Studies that have purified prestin from cell lysate have either required expression of prestin in an expression system showing compromised function [Mio et al., 2008] or required expression of truncated forms of prestin [Pasqualetto et al., 2008] calling into question the accuracy of the inferred oligomeric states. Since prestin is a membrane protein, its folded structure and protein interactions will be sensitive to the membrane environment. Therefore, rigorous determination of prestin oligomeric state distribution ultimately requires a method that can discern the native oligomeric structure *in situ* with a resolution at the level of single prestin molecules.

An experimental method utilizing single molecule fluorescence (SMF) detection to determine the local stoichiometries of individual fluorescent molecules has been described by Schmidt et al. [Schmidt et al., 1996b]. By using SMF, one can gain *a priori* knowledge of the average unitary fluorescence intensity $\bar{I}_1$ and its probability density $\varrho_1(I)$ as a reference for assigning a stoichiometry to n colocalized fluorophores. The authors point out that the distribution of fluorescent intensities of n colocalized fluorophores are n recursive convolutions of the single molecule distribution if the fluorophores are statistically independent. The convolutions can be used as a basis for determining the distribution of stoichiometries in an experimental sample. This method has been employed in a handful of studies to measure protein oligomerization or to measure changes in oligomerization. Clustering of the L-type Ca^{2+} channel was observed by Harms et al. in live cells [Harms et al., 2001a] in one of the first applications of the technique. Zhang et al. have used the technique to demonstrate that activation of TβR-II with TGF-β induces dimerization [Zhang et al., 2009]. Brightness analysis has also been used to demonstrate cholesterol dependent partitioning

of the fluorescent lipid probe Bodipy-GM1 and cholesterol dependent clustering of GPI [Brameshuber et al., 2010]. In this study we use SMF to show that brightness analysis can be used to demonstrate oligomerization of prestin tagged with the fluorescent protein citrine in the HEK cell. The use of a fluorescent protein offers the advantage of a 1:1 fluorescent tag to prestin ratio which simplifies the analysis of determining prestin stoichiometries. Our results suggest that prestin tends to form oligomers in the cell membrane, in states composed predominantly of tetramers followed by dimers. We make an initial attempt to use brightness analysis to observe whether changes in prestin oligomerization occur upon membrane cholesterol manipulation. We further conclude that SMF brightness analysis is a potentially powerful tool that could be employed to detect membrane cholesterol dependent changes in prestin oligomerization.

3.2 Materials and methods

3.2.1 Prestin expression and cell culture

A plasmid encoding for a fusion protein of prestin and enhanced yellow fluorescent protein (EYFP) (gerbil-prestin gene, accession number AF230376, was previously sub-cloned into the multiple cloning site of pEYFP-N1 [Greeson et al., 2006]) was genetically modified to create a plasmid encoding for monomeric prestin-citrine via the point mutations Q69M [Griesbeck et al., 2001, Heikal et al., 2000] and A206K [Zacharias et al., 2002] of the YFP gene using quick change mutagenesis. Citrine was chosen due to a factor of $\sim$2 improved photostability over eYFP [Cognet et al., 2002, Griesbeck et al., 2001].

HEK293 cells were grown in 6-well plates containing culture media consisting of phenol-red free DMEM supplemented with 10% BCS, 1% penicillin-streptomycin, 14.3 mM HEPES, 16.1 mM $NaHCO_3$, and 4 mM L-glutamine at 37°C, 5% CO_2. Cells below passage 30 were transfected with prestin-citrine plasmid using Fugene 6 transfection reagent (Roche, Indianapolis, IN) according to product instructions. Eight hours post transfection, cells were trypsinized and replated onto #1.5 coverslips that were cleaned using an RCA washing procedure [van Dam, 2005] to remove potentially fluorescent organic impurities. At 24-36 hours post transfection, cells adherent to coverslips were fixed using 4% paraformaldehyde for 10 min and rinsed several times with PBS. In some cases cells were treated with 10 mM methyl$-\beta-$cyclodextrin (MβCD) in serum free DMEM for 10 min prior to fixation. Coverslips were then mounted onto a viewing chamber with vacuum grease to form a leak proof seal, bathed in PBS imaging buffer, and then mounted on an inverted microscope for viewing (Fig. 3.1).

3.2.2 Single molecule fluorescence microscopy

A schematic summarizing the experimental configuration and sample is depicted in Fig. 3.1. Fixed HEK cells expressing prestin-citrine were imaged on a Zeiss Axiovert inverted microscope. Prestin-citrine was excited using 514 nm light from a fiber coupled Ar^+ laser made circularly polarized with a $\lambda/4$ waveplate placed at 45° to the polarization axis of the laser to reduce the dependence of citrine fluorescence on excitation dipole orientation. The laser power P, measured directly after the objective, was either 10-11 mW or ~ 5 mW and the beam waist at the sample is estimated at $\omega_o = 80.6 \pm 0.9\,\mu m$ (statistical error only) as measured using a razor blade at the focus (see Sec. 3.3.6). Prestin-citrine fluorescence was collected from the basal portion of the cells with a 100X, 1.45NA objective using immersion oil with index

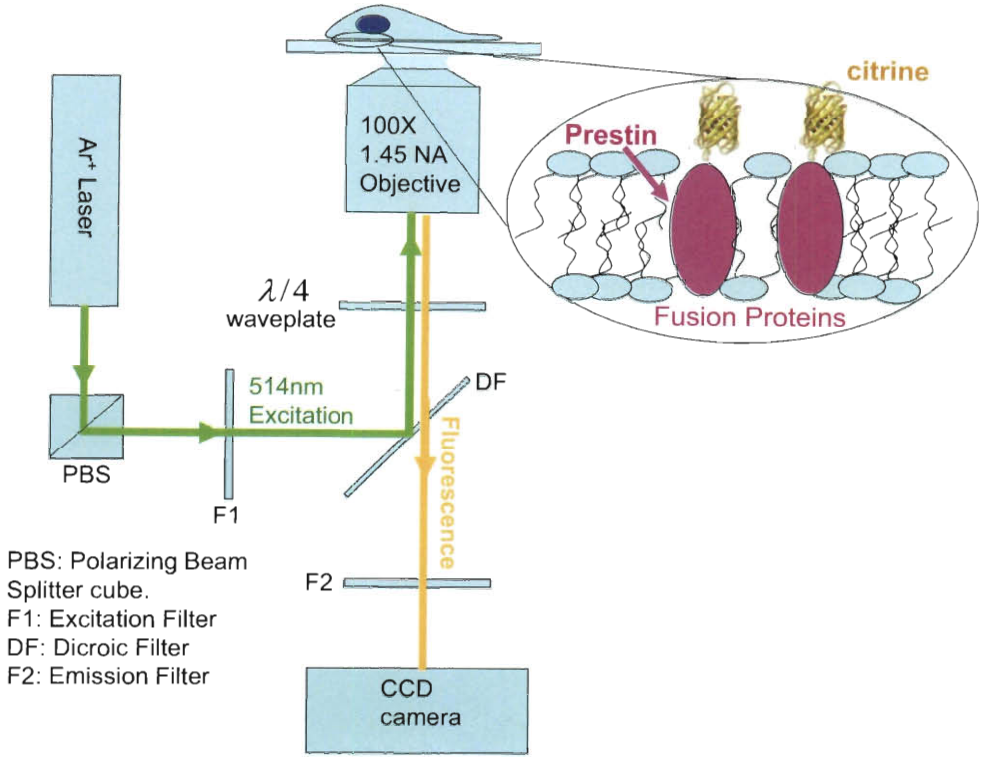

Figure 3.1 : Block diagram of single molecule fluorescence experimental setup. Filter set is from Zeiss (part number 488053). Excitation filter (F1) is BP 514/10, dichroic filter (DF) is FT 540, and emission filter (F2) is BP 575/50. The emission filter is required to select the $514\,nm$ line of the laser and reject the 488, 476, and $458\,nm$ lines. To reduce signal brightness dependence on laser polarization a $\lambda/4$ waveplate (Thorlabs) is placed in the excitation beam path to circularly polarize excitation laser (514 nm, green). Sample consists of fixed HEK293 cells expressing prestin (depicted as pink ovals) C-terminally fused with citrine (yellow) in the cell membrane. Citrine has an excitation maximum of $516\,nm$ and an emission maximum of $529\,nm$ [Griesbeck et al., 2001]. The prestin-citrine molecules are excited using epi-illumination configuration, as opposed to total internal reflection (TIR), to reduce variation of citrine signal brightness that would occur due to variations in height of the citrine molecules from the coverslip and due to the exponentially decaying evanescent wave that would be present were TIR to be used. The use of a high numerical aperture (NA=1.45) objective was critical for collecting sufficient photons for single molecule detection.

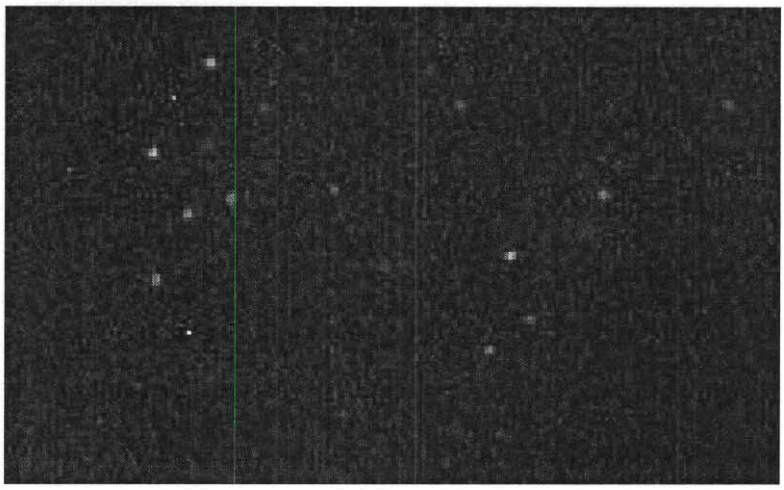

Figure 3.2 : Fluorescence image of single prestin-citrine molecules in a cell. Laser intensity is $\sim 93\, W/cm^2$ and integration time is 500 ms.

of refraction $n = 1.518$ and filtered in a band from 550-600 nm. The peak intensity of the laser is given by $I_o = 2P/\pi\omega_o^2$ [Demtröder, 1998]. We detected prestin-citrine fluorescence, which appears as diffraction limited spots (Fig. 3.2) with spatial size $s \approx 255 \pm 34\, nm\ FWHM$ in agreement with the point spread function of the microscope, using the Zeiss Axiocam MRm CCD camera (12 bit bins, 60% quantum efficiency). The camera is operated using Zeiss Axiovision software to acquire 200 frame image stacks or movies with exposure time either 500 ms or 250 ms. A multiplicative camera gain of 8 is used. The camera pixels are binned 2×2 to a magnified size of $a = 125.3 \pm 0.5\, nm$ in the object plane. Frame sizes varied between experiments but were roughly $20\, \mu m \times 20\, \mu m$ and were centered in the field of view of the microscope. This limits reduction in the excitation intensity, from the center of the Gaussian beam profile, to a few percent at the edges of the frame.

3.2.3 Image analysis

Files containing images in movies are analyzed using custom made Matlab analysis software. The early frames of the movies are discarded both because the MRm camera gain is seen to vary at early times (first 6-7 frames for 500 ms exposure data) before it stabilizes and because there is excessive background fluorescence at early times due to high expression of prestin-citrine. The frame at which the analysis begins is chosen to correspond to when individual molecules become clearly apparent with sufficient separation from each other to allow discrimination of spots. The frame in the stack chosen varies from cell to cell, and between experiments, based on expression level and frame rate. In some experiments, the excitation laser is set at the intensity used for the experiment during focusing of the cell which results in a certain amount of pre-bleaching of prestin-citrine. Details of pre-bleaching and image stack cropping are specifically given for each set of experimental conditions in the Results. To maximize performance of the analysis software, image stacks of each cell are cropped into multiple sub-image stacks, chosen around regions where the background signal is fairly uniform, and pooled together for final analysis.

The analysis software fits each fluorescent spot intensity profile $\Psi(x, y)$ (detected by a peak finding algorithm) in every frame to a 2-D Gaussian of the form

$$\Psi(x,y) = \frac{4I\ ln2}{\pi s^2} exp\left\{\frac{-4\ ln2}{s^2}\left[(x-x_o)^2 + (y-y_o)^2\right]\right\} + b \tag{3.1}$$

where I is the background subtracted spot intensity, s is the full-width at half-maximum of the point spread function, b is the background level, and (x_o, y_o) is the position of the spot using nonlinear least squares regression [Bevington, 1992].

The fitting uncertainty of each parameter is also recorded for every spot (Fig. 3.3). The spot intensities are determined with better than $\sim 20 - 25\%$ precision.

Elimination of spurious signals is efficiently accomplished by finding an appropriate value for a parameter that defines a thresholding condition for detection of spots in the image stack. It is adjusted to find a compromise between allowing detection of all the existing spots in the images while remaining restrictive enough to avoid detecting spurious fluorescence. Any remaining signal profiles detected that have a width s that falls out of a reasonable range of the point spread function (an interval as wide as 1.5-2.5 pixels $\sim$ $200 - 300\,nm$ was typical) is discarded since anything smaller cannot have been a diffraction limited object and anything larger is likely to be either a spurious object or two partially overlapping diffraction limited signals. This criteria is justified by Monte Carlo simulations (see Fig. 3.18) of signals added to real background noise. Also spots near the edge of a frame are discarded to avoid errors due to incomplete spatial detection of an intensity profile. Finally, any signals detected with a precision worse than 25-30% are discarded. A set of data was deemed to be of appropriate enough quality for analysis if the signal to noise ratio was high enough such that the post processing data elimination removed only a small fraction of detected signals.

3.2.4 Statistical analysis of brightness

The measured intensities of spots from multiple cells are binned on a histogram for fitting to theoretical distributions $\rho_n(I)$. Alternatively, the data was smoothed by presenting it as a probability density distribution of intensity calculated from the

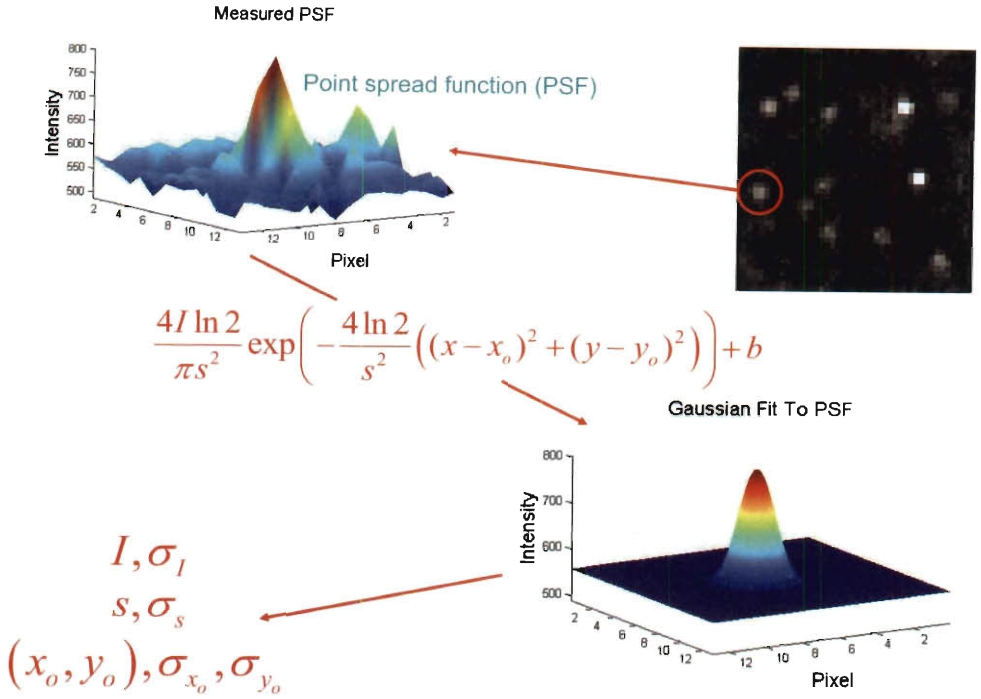

Figure 3.3 : Characteristics of point spread function from fitting diffraction limited signals. Diffraction limited signals are fit to Eq. 3.1 from which signal brightness I, width s (FWHM), and position (x_o, y_o) are obtained. From the fit, the uncertainties in all the parameters are estimated. Shown is an example of a fluorescent signal and the Gaussian fit to the signal. The expected width (FWHM) of the signals based on diffraction from the equation $s = .514\lambda/NA$ is $204\,nm$ ($NA = 1.45$ and $\lambda \approx 575\,nm$ since fluorescence is collected in a band from $550 - 600\,nm$). In practice we measure a slightly larger width of $s \approx 255\,nm$.

following equation [Schmidt et al., 1995]

$$\rho(I) = \frac{1}{\sqrt{2\pi}N} \sum_{i}^{N} \frac{1}{\sigma_{I,i}} exp\left(-\frac{(I - I_i)^2}{2\,\sigma_{I,i}^2}\right). \tag{3.2}$$

The probability density distribution represents on a histogram each measured signal i as a Gaussian of unit area centered at its measured intensity I_i with standard deviation equal to the uncertainty in its determination $\sigma_{I,i}$. The factor of N is the number of spots in the histogram and normalizes the distribution to unit area. To normalize $\rho(I)$ to the total number of spots, the factor of N is left out.

To generate theoretical distributions $\rho_n(I)$ that correspond to the data with high noise level and minimal bleaching (i.e. data with potentially multimeric populations), we first measured the signature of the single molecule distribution $\varrho_1(I)$ in a low noise environment. This is accomplished by bleaching the transfected cell sample for an extended time until only single citrine fluorescence signals remain. From $\varrho_1(I)$, the $\varrho_n(I)$ are calculated recursively via the following convolution integral [Schmidt et al., 1996b]

$$\varrho_n(I) = \int dI' \varrho_1(I') \varrho_{n-1}(I - I') \tag{3.3}$$

where we have assumed that colocalized fluorophore intensities are statistically independent (see Fig. 3.4). In a higher noise environment, where each distribution would be broader and perhaps distorted (Sec. 3.3.2), the $\varrho_n(I)$ would not be the correct distributions. To find the correct distributions $\rho_n(I)$ from $\varrho_n(I)$, the effect of the experimental noise on the $\varrho_n(I)$ is determined separately for each stoichiometry by a Monte Carlo simulation detailed in Sec. 3.3.2. Briefly, fluorescent signals sampled from $\varrho_1(I)$ and its convolutions $\varrho_n(I)$ are each added to real background noise taken

from images used in the analysis. The generated images are then analyzed just like the real data to obtain the $\rho_n(I)$. Experimental histograms and measured probability density distributions of prestin-citrine signal brightness are fitted to a linear combination of theoretical distributions

$$\rho(I) = \sum_n \alpha_n \rho_n(I) \tag{3.4}$$

to obtain the apparent number α_n of each prestin-citrine stoichiometry detected in the cells. If the fit is done correctly $\sum_n \alpha_n$ should equal the total number of detected spots N. Each fitted weight α_n is corrected for the measured detection efficiency η_n of its corresponding distribution $\varrho_n(I)$ to obtain the corrected weights $\alpha_{n,cor} = \alpha_n/\eta_n$ (η_n is determined in the Monte Carlo simulation).

3.3 Results

3.3.1 Histogram of detected signal displays equally separated peaks

We first measured the brightness of prestin-citrine molecules in the portion of membrane near the coverslip of untreated HEK cells to see if we could discriminate distinct stoichiometries of colocalized prestin (Fig. 3.5, wide bins and black curve). During focusing of the microscope on the basal portion of some of the cells, the laser intensity was set to the same value used during data acquisition. For these cells, this resulted in a certain amount of photobleaching (up to ~5 seconds) before recording the image stack. The earliest portion of the image stack was removed (number of frames removed ranged from 7 to 40 corresponding to ~4 to 21 seconds) for each cell based on the amount of background fluorescence. A starting frame was chosen individually for each cell to be as early in the image stack as possible, to minimize

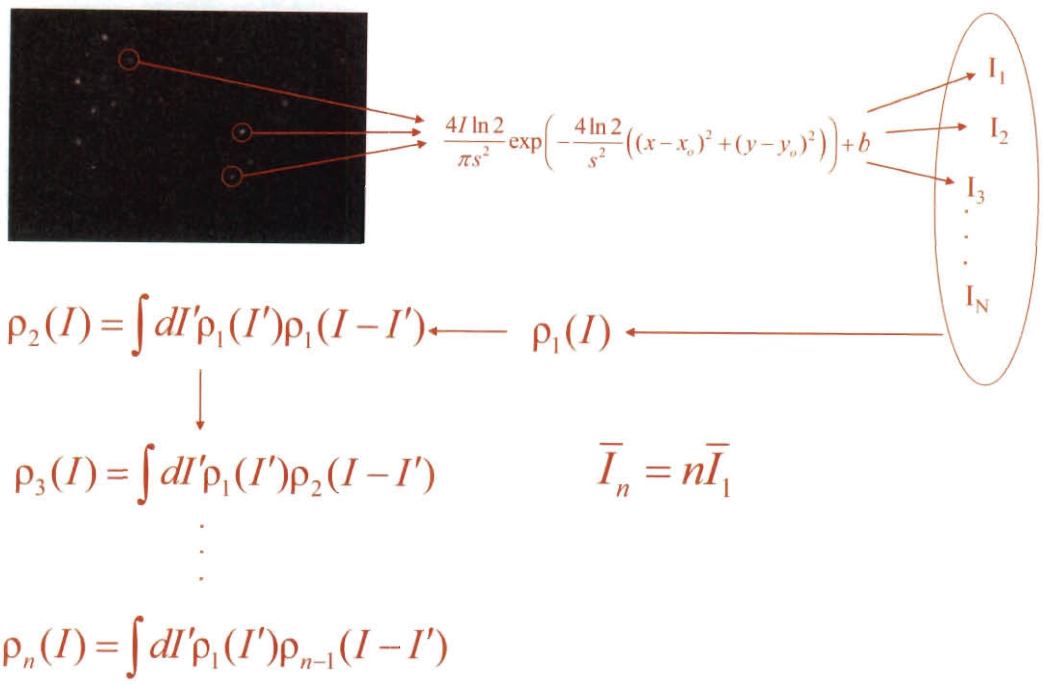

Figure 3.4 : Principle of brightness analysis. By measuring an ensemble of signal brightness values from a prestin-citrine transfected cell, that has been bleached extensively, the brightness distribution of single citrine molecules $\varrho_1(I)$ is determined. This measurement serves as a reference for assigning a stoichiometry to a distribution of n colocalized citrine molecules. From $\varrho_1(I)$, the $\varrho_n(I)$ are calculated recursively via Eq. 3.3. The brightness of a distribution of n colocalized citrine molecules $\bar{I}_n$ is $n\bar{I}_1$ with the width of each successive distribution scaling as $\sqrt{n}$ [Schmidt et al., 1996b].

photobleaching of colocalized prestin-citrine, while still allowing for clear discrimination of diffraction limited signals. Shown in Fig. 3.5 is pooled signal intensity data from all the cells corresponding to the first 30 frames after the chosen starting frame. Also shown is the distribution of signal intensities of single prestin-citrine molecules ($\varrho_1(I)$, Fig. 3.5, narrow bins) excited with the same laser intensity and integration time but are measured in a low noise background obtained by prolonged bleaching. In both the signal brightness histogram and calculated probability density function, we observed 3 clear peaks in the distribution at various positions along the intensity axis indicating local accumulation of probability for certain intensities. To locate the positions of the peaks we fit a portion of the distribution to the sum of 3 Gaussians (Fig. 3.6, left panel). The positions of the peaks are plotted in Fig. 3.6 (right panel) along with the mean ($\bar{I}_1 = 898 \pm 317\, counts/500\, ms$, mean±SD) and most probable value $I_{1,peak} = 730\, counts/500\, ms$ of the single molecule distribution $\varrho_1(I)$. The mean and most probable intensity of $\varrho_1(I)$ differ because of its asymmetric shape [Mutch et al., 2007]. The obtained positions of the Gaussians were fit to a line through the origin (Fig. 3.6, right panel) and gave a slope of $846\, counts/500\, ms$ in agreement with the mean and peak value of the single molecule distribution. It should be noted that a fitting function composed of greater than 3 Gaussians consistently failed to describe the data at low intensities as did extending the fit using only 3 Gaussians to cover intensities from zero to $1000\, counts/500\, ms$. This was due to limited detection efficiency of the monomeric population in the level of background noise that exists prior to extensive bleaching.

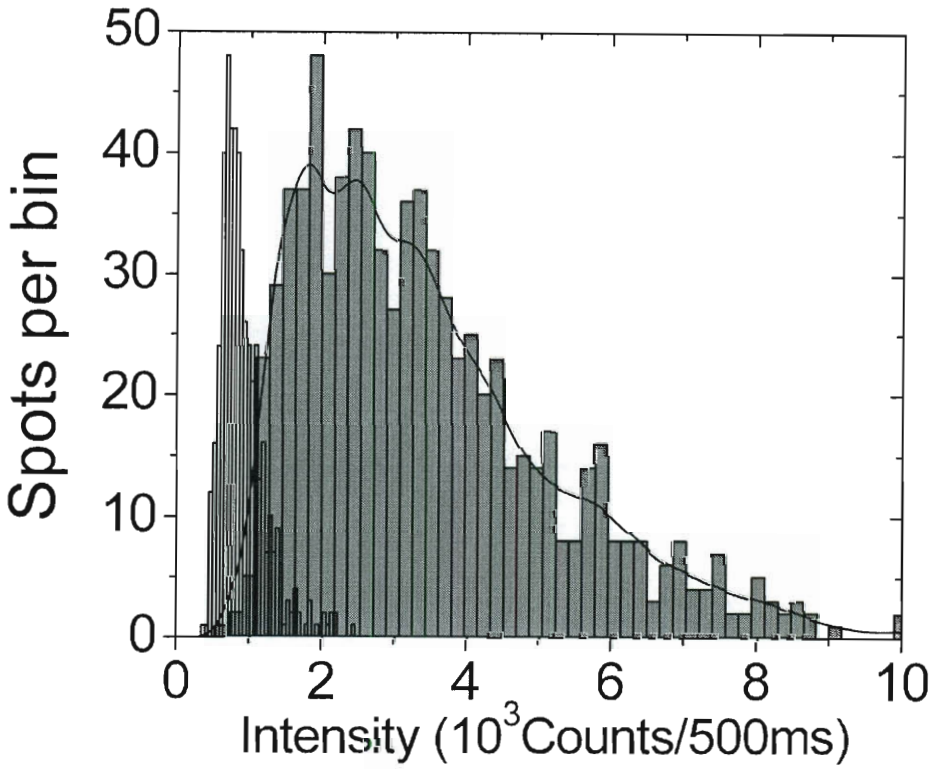

Figure 3.5 : Histogram of 802 measured prestin-citrine fluorescence intensities measured from 3 cells (wide bins, bin size is 180 counts/500 ms) and includes the data from the earliest 30 frames of the image stack for each cell. The thin curve is the calculated probability density of the data (see Sec. 3.2.4 and Eq. 3.2). The frame rate for this exposure time is $(531ms)^{-1}$. The best estimate for the laser intensity is $45-50W/cm^2$. The solid curve is the calculated probability density distribution using Eq. 3.2. Also shown is the measured single molecule distribution $\varrho_1(I)$ at the same illumination conditions (narrow bins, bin size is 50 counts/500 ms). Single molecule distribution measurement contains 487 individual spots from a transfected cell that was bleached for an extended period to reduce the background fluorescence to a low level (bleached until brightness distribution of spots remained constant).

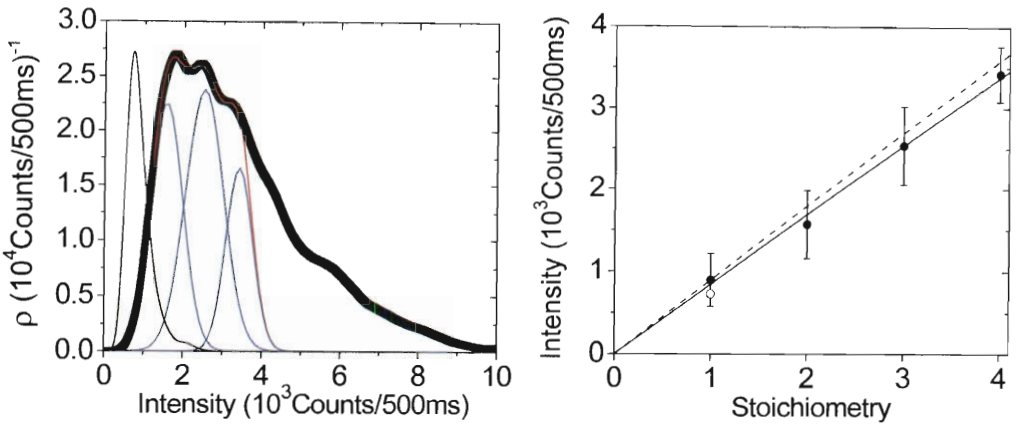

Figure 3.6 : Centroid location of aggregates in multimodal histogram. Left: Probability density distribution (thick black curve) of the data in Fig. 3.5 is fit to the sum of 3 Gaussians (total fit shown as red curve, individual components are blue curves). We restrict the fit from 1000 to 3400 counts/500 ms. The widths of the Gaussians and their separation on the abscissa are left as free parameters. Also shown is the probability density of the single molecule distribution ($\varrho_1(I)$, thin black curve) from Fig. 3.5. Right: Plot of the positions of the Gaussian fits versus stoichiometry 2,3, and 4. The error bars represent the fitted standard deviations of the Gaussians. Also shown for a stoichiometry of 1 is the mean $\pm$ standard deviation (black point with error bar), and most probable value (open circle) of the measured single molecule distribution. Solid line is a linear fit to the position of the Gaussians and corresponds to a separation of 846 counts/500 ms. Dotted line has slope equal to the mean of the single molecule distribution (898 counts/500 ms).

3.3.2 Determination of theoretical higher order distributions

Using the measured single molecule distribution as a template, we simulated the effect of noise on the distributions corresponding to stoichiometries $n = 1$ through $n = 8$ (Fig. 3.7). We first found convolutions $\varrho_n(I)$ of the measured single molecule distribution $\varrho_1(I)$ which are given by Eq. 3.3. These represent the brightness distribution of n colocalized fluorescent citrine molecules given that single molecules of citrine have intensities distributed as $\varrho_1(I)$ which is measured. To generate a sample population of intensities that are distributed according to $\varrho_n(I)$ $(8 \geq n \geq 2)$, we first assign

a uniformly distributed random number r ($r = 0..1$) to each of the 487 measured intensity values contained in $\varrho_1(I)$ and randomize the order by sorting the intensities according to r; this is repeated $n-1$ more times to generate n lists each containing 487 randomly ordered intensities. We then randomly pick n of those intensities (one intensity from each of the n lists) based on its assigned r value and sum them to generate an intensity value that is distributed as $\varrho_n(I)$. For each stoichiometry n, 2435 signals are added one at a time at random positions to an image stack containing experimental noise to generate an image stack 2435 frames long. Each added signal consists of a 2D-Gaussian of the form in Eq. 3.1 with intensity randomly sampled from $\varrho_n(I)$ and width s equal to the experimentally measured point spread function. The signals on the image stacks are analyzed in the same way as experimentally measured image stacks. The distribution functions $\rho_1(I) - \rho_8(I)$ are then assigned to the histograms of intensity values from fitting the simulated signals in the noisy background. The obtained histograms are shown in Fig. 3.7 (left panel) and demonstrate that the distribution of intensities for a stoichiometry of $n = 1$ is not fully detected at the low brightness end of the distribution. The detection efficiency η_n of each stoichiometry is given by $\eta_n = \#\,detected \div 2435$ and is plotted in Fig. 3.7 (right panel).

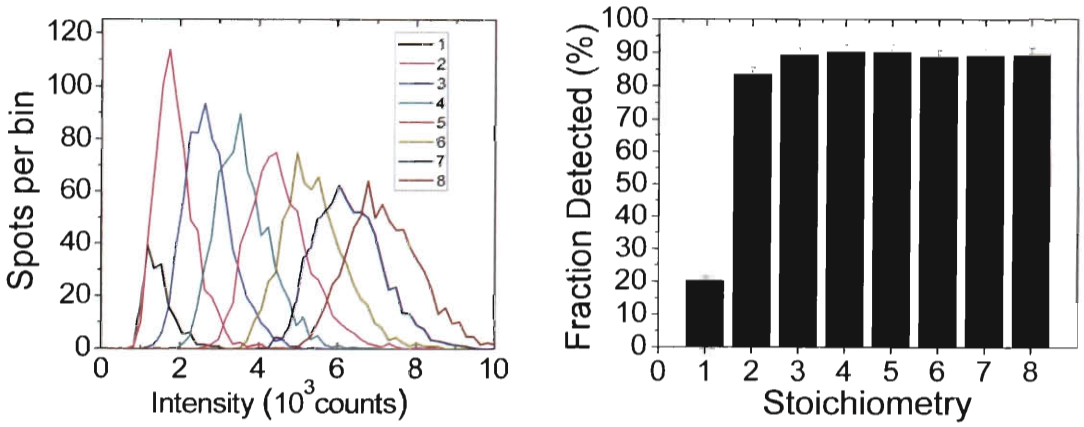

Figure 3.7 : Theoretical distributions in high noise environment. Left: Simulated histograms representing distribution of colocalized fluorophores in an environment consisting of real background noise from a real image (frame 15 of one of the cells) corresponding to the data in Fig. 3.5. Distribution for stoichiometries of n=1 to 8 colocalized signals are depicted. Each simulation was analyzed with the Matlab analysis software in identical manner as done for the real data. For each stoichiometry n, a total of 2435 intensities drawn from each $\varrho_n(I)$ were simulated at random positions in the image to obtain each $\rho_n(I)$. Right: The number of simulated points detected (out of 2435) for each stoichiometry 1-8 are: 494, 2038, 2177, 2202, 2200, 2165, 2174, and 2181, respectively. Solid bars depict the detection efficiency of the intensity distribution for each simulated stoichiometry.

3.3.3 Fitting of colocalization data at low intensity and long exposure time with generated distributions

Linear combinations of the generated fitting functions $\rho_1(I) - \rho_8(I)$ are used to fit the measured probability density of signal brightness using Eq. 3.4 (Figs. 3.8 and 3.9). From the fits, the number α_n of detected colocalized prestin-citrine signals corresponding to each stoichiometry n were determined (Fig. 3.8, figure legend). The weights $\alpha_{n,corr}$, corrected for the detection efficiency of the nth stoichiometry, are plotted in Fig. 3.12 (open bars). Due to photobleaching over the long 30 frame period,

which continuously removes fluorescent prestin-citrine from colocalized aggregates, the occupancy α_n of each stoichiometry n is a decreasing function of n.

To avoid averaging over a long period, we binned a subset of the same data (132 out of 802 signals) over a narrower time window (frames 13-17 as opposed to 1-30). We chose to center the range of frames around frame 15 both because frame 15 is the midpoint of the range analyzed above and because the background noise image used in the calculation of the $\rho_n(I)$ came from that frame. The probability density of the signals is shown in Fig. 3.10 and the corresponding histogram of the signal brightness is displayed in Fig. 3.11. The probability density is fit with a linear combination of $\rho_1(I) - \rho_6(I)$ (Fig. 3.10) and shows a pronounced weight to a stoichiometry $n = 4$. The fitted weights corrected for detection efficiency are plotted in Fig. 3.12 (open bars) again showing a pronounced weight for $n = 4$.

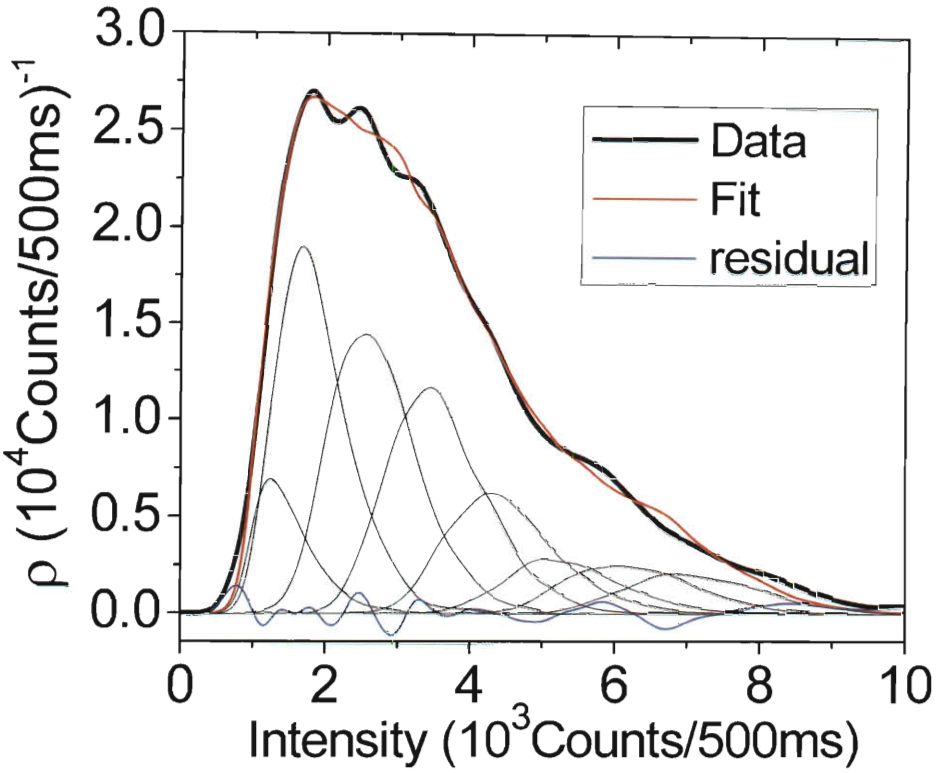

Figure 3.8 : Fitting of probability density $\rho(I)$ with calculated theoretical distributions. Data is fit by Eq. 3.4 using probability density of theoretical distributions to find the relative weights α_n for n 1 to 8. The fitting functions $\rho_n(I)$ (thin black curves) calculated from Fig. 3.7 are normalized to unit area. The fitted α_n values are (in number of detected spots): 51.74, 182.69, 177.73, 156.1, 92.607, 44.822, 44.845, and 38.863 with $\sum_n \alpha_n = 789$ which is 13 spots short of the actual number of detected signals of 802. Correcting for the efficiency of detection for each species, the fitted number in each population $\alpha_{n,cor}$ is: 255.04, 218.28, 198.79, 172.62, 102.5, 50.412, 50.229, and 43.389. $\sum_n \alpha_{n,cor} = 1091$ spots. The apparent fractions $\alpha_{n,cor}/\sum_n \alpha_{n,cor}$, corrected for the efficiency of detection for each species, are: 0.23371, 0.20003, 0.18217, 0.15818, 0.093927, 0.046196, 0.046029, and 0.03976.

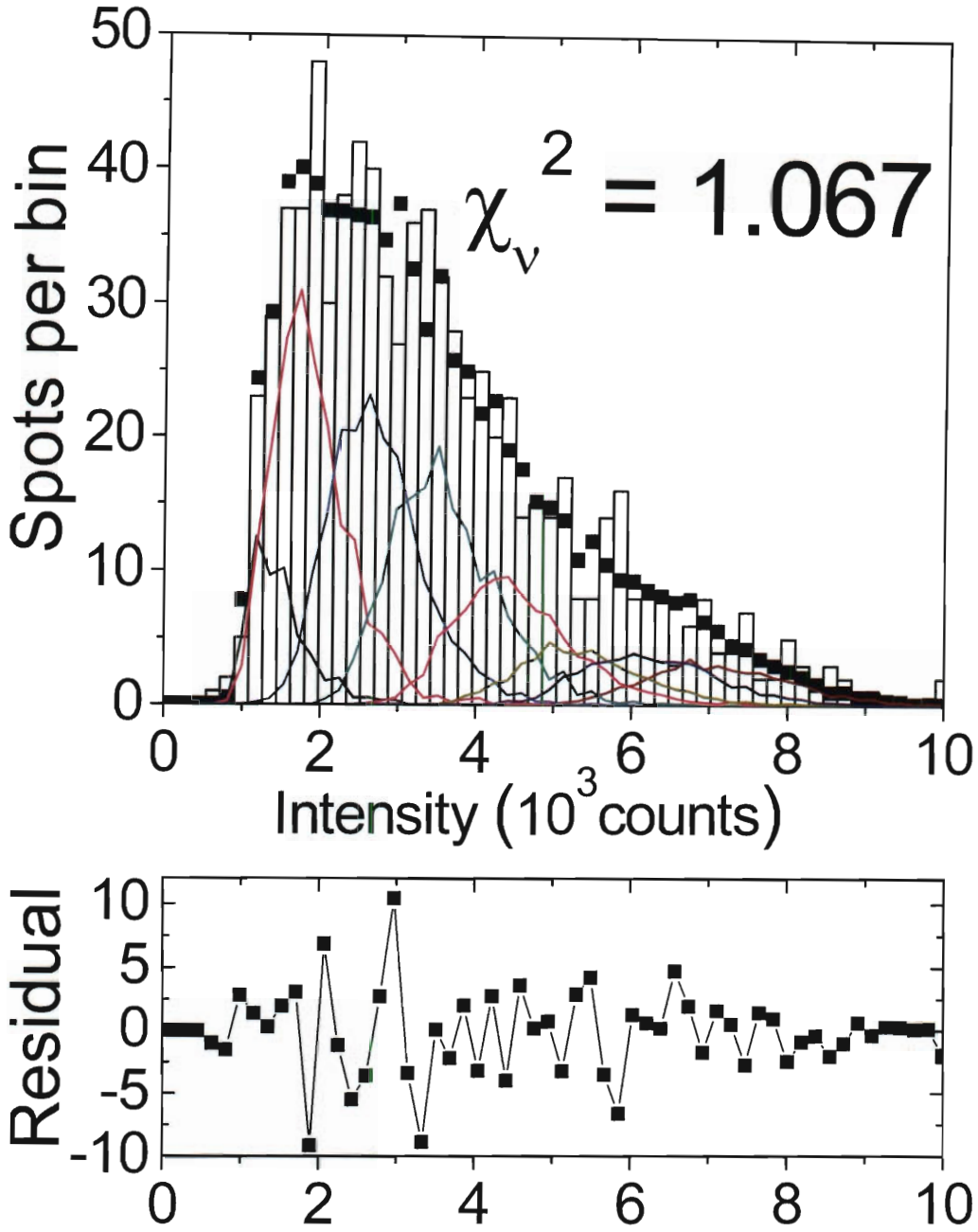

Figure 3.9 : χ^2-test of fit to signal intensity distribution. The weights α_n, obtained from fitting the probability density distribution (Fig. 3.8), are multiplied by the theoretical histograms obtained in the Monte Carlo simulation (Fig. 3.7) and summed according to Eq. 3.4. A comparison of the fit (black squares) with the measured histogram (open bars) yields a $\chi^2_\nu = 1.067$ corresponding to a χ^2 probability $> 30\%$. Poisson statistics are assumed for each bin.

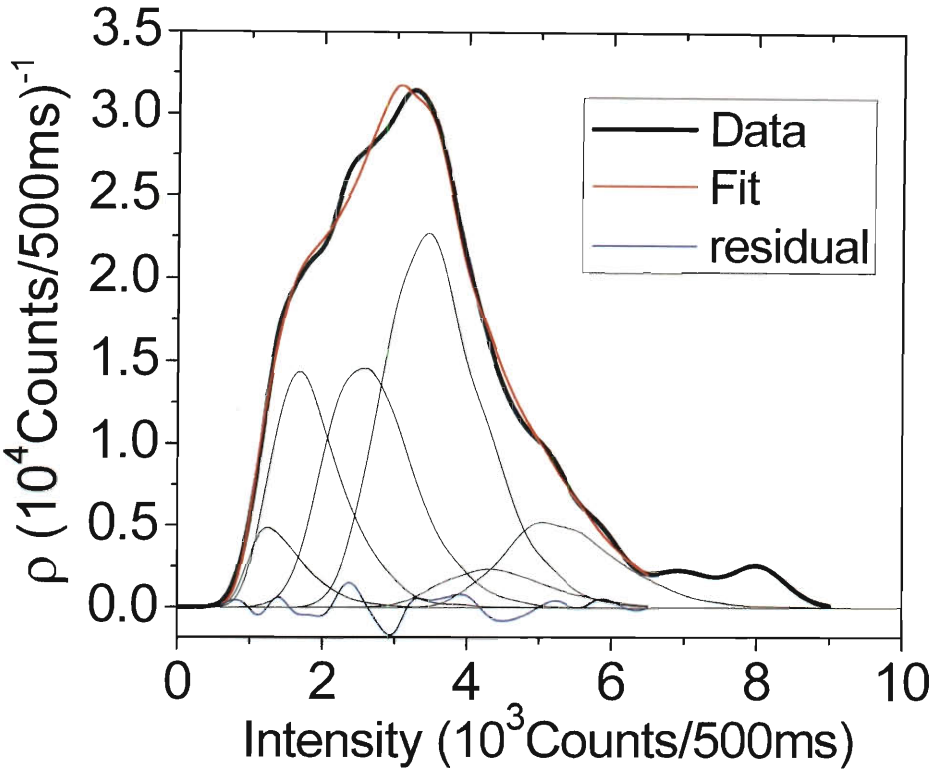

Figure 3.10 : Fit to 5 frame subset of multimeric data. Probability density of 132 measured signal intensities, from frames 13-17 of the 30 frames used in Fig. 3.5, are fit to Eq. 3.4 for n from 1 to 6. Frame 15 corresponds to the background noise image used to generate the $\rho_n(I)$. Individual components are shown as thin black curves. The fit is cut off at 6500 counts/500 ms, beyond which there are only 6 signals, due to low statistics. Fitted α_n values are (in number of signals): 5.9871, 22.719, 29.552, 49.889, 5.6594, and 13.509, with $\sum_n \alpha_n = 127$ which is 5 spots short of the actual number of detected signals. Correcting for the efficiency of detection, $\alpha_{n,cor}$ values are (number of signals): 29.511, 27.145, 33.054, 55.167, 6.2639, and 15.194, with $\sum_n \alpha_{n,cor} = 166$. This gives corrected apparent fractions $\alpha_{n,cor} / \sum_n \alpha_{n,cor}$: 0.17742, 0.16319, 0.19872, 0.33166, 0.037658, and 0.091344.

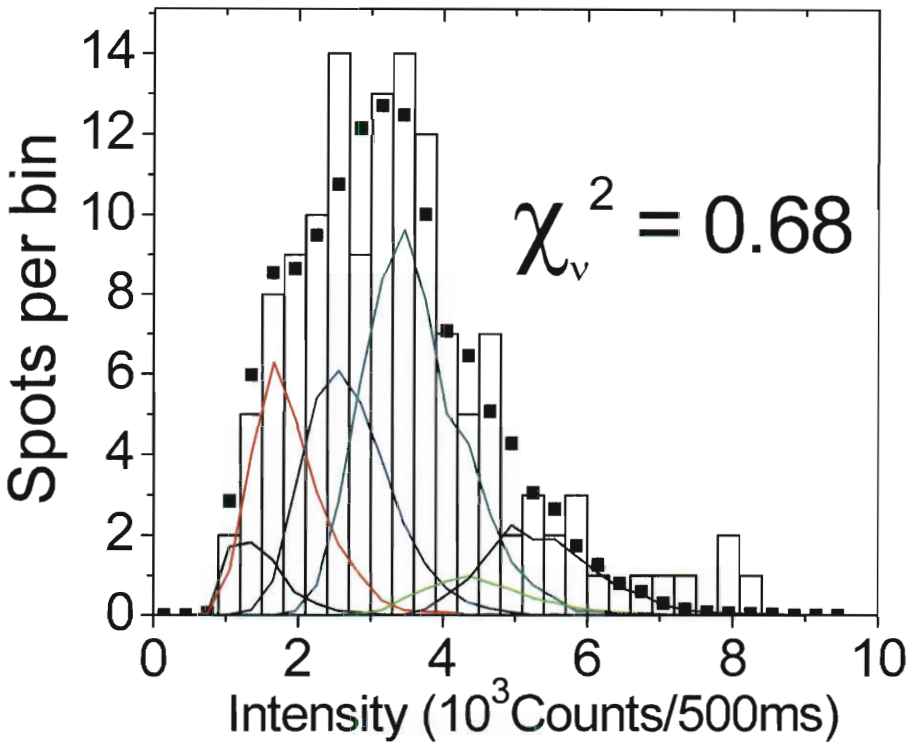

Figure 3.11 : χ^2-test of fit to narrow time window data. Histogram of signal intensities from frames 13-17 (Bin size is 300 counts/500 ms). The weights $\alpha_1 - \alpha_6$ are multiplied by histograms generated in Monte Carlo simulation and summed (fit: black squares; individual components: thin colored curves; data: open bars). A reduced-chi-squared of $\chi^2_\nu = 0.68$ is obtained corresponding to a χ^2 probability $> 80\%$.

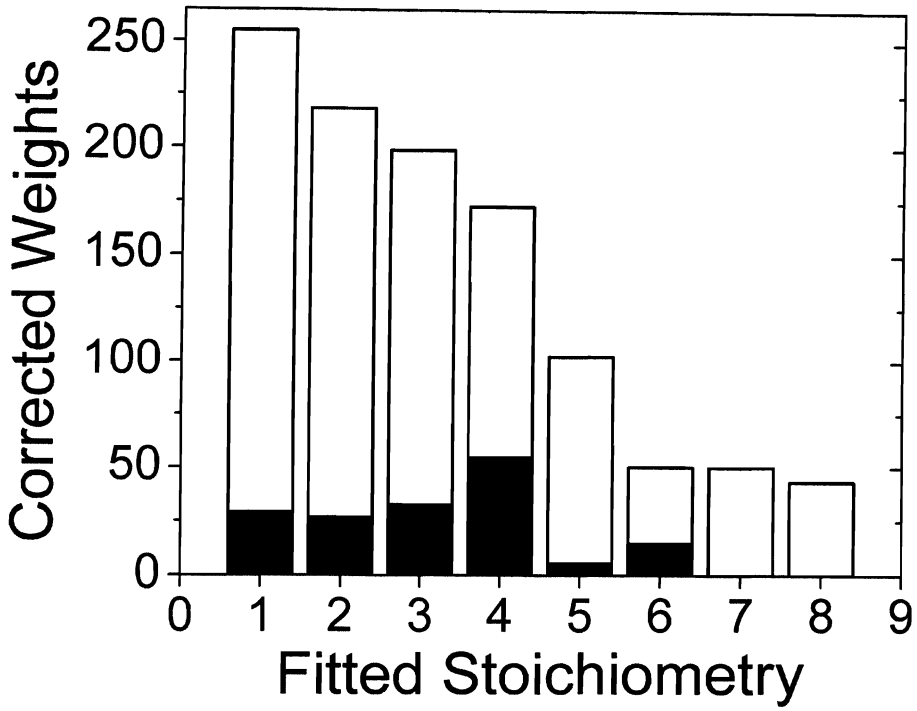

Figure 3.12 : Summary of fits to 500 ms data. Open bars represent corrected weights for data averaged over 30 frames. Solid bars represent corrected weights for data averaged over middle 5 frames.

3.3.4 Effect of cholesterol manipulations on prestin-citrine brightness histogram

We repeated the measurement of prestin-citrine signal brightness in untreated cells and cells depleted of membrane cholesterol (see Fig. 3.13). We increased the laser intensity to $I_o = 108 \pm 10\, W/cm^2$ and decreased the exposure time to 250 ms with a frame rate of $(297\, ms)^{-1}$. For this experiment, an equal amount of photobleaching occurred before acquisition of the image stack for each cell. Analysis of the image

stacks begins at frame 100 which corresponds to $\sim 30\,s$ after the turn on of the laser. Histograms of the fitted signal brightness over the first 6 frames (frames 100-106) are shown in Fig. 3.13 for both groups. For each cell imaged, the single molecule distribution of intensities $\varrho_1(I)$ is also measured after another prolonged photobleaching period, and the signal intensities are pooled together into one histogram (Fig. 3.13). The effects of noise on the convolutions of the single molecule intensity were determined in the same manner as before and were used to generate the fitting functions $\rho_n(I)$ in the same way. Due to the longer photobleaching step before data acquisition, the background level is lower compared to the data acquired with a lower power and 500 ms integration time. This resulted in an improved detection efficiency for the monomeric population in the observed noise level ($\eta_1 \approx 60\%$). The probability density $\rho(I)$ was fitted to linear combinations of $\rho_1(I)$ and $\rho_2(I)$ using Eq. 3.4 (Fig. 3.14). The obtained corrected weights $\alpha_{n,corr}$ corresponded to stoichiometric populations of 80% $n = 1$ and 20% $n = 2$ for both groups. Within the error of our measurement, the distribution of prestin-citrine signal brightness in untreated and MβCD treated cells are identical. We expect that any differences that may have been present in the distribution of oligomeric states of prestin between untreated and MβCD groups have been masked by excessive photobleaching.

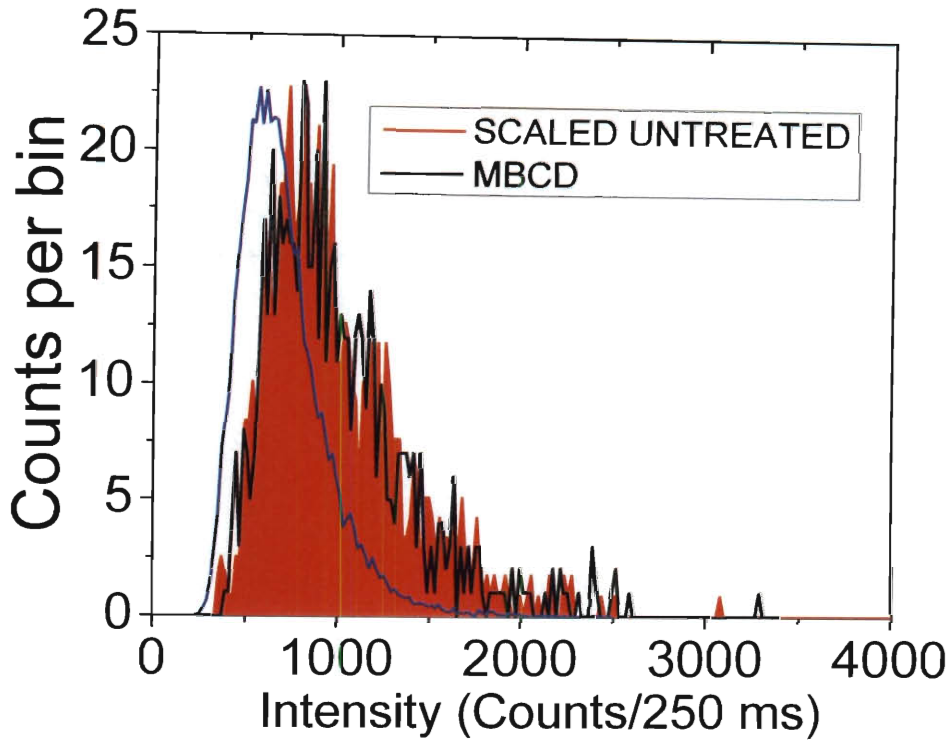

Figure 3.13 : Effect of cholesterol on signal brightness histogram. Shown are histograms of signal intensity for both untreated cells (red, N=795) and cells treated with 10 mM MβCD (black, N=669). The histogram for untreated group is scaled by the number of detected signals in MβCD treated group to allow a visual comparison. Bin size is 20 counts/250 ms. Data is acquired from the first 6 frames, after the chosen starting frame, for both groups. A total of 16 and 19 cells were included for untreated and MβCD treated cells, respectively. The exposure time is 250 ms and the frame rate is $(297ms)^{-1}$. Each cell analyzed includes an equal amount of pre-bleaching prior to the frame for which the analysis begins. The excitation intensity for both sets is $I_o = 108 \pm 10\, W/cm^2$. Also shown is the measured single molecule distribution (N=20280, blue histogram) of signal intensities derived from the same cells used to acquire the untreated and MβCD treated data by exposing the cells to further bleaching for an extended period prior to duplicate acquisition. The single molecule histogram is divided by a large factor to place it on the same scale as the untreated and MβCD histograms. The single molecule distribution has a mean of $\bar{I}_1 = 699 \pm 239 counts/250\, ms$ and a peak value of $603\, counts/250\, ms$.

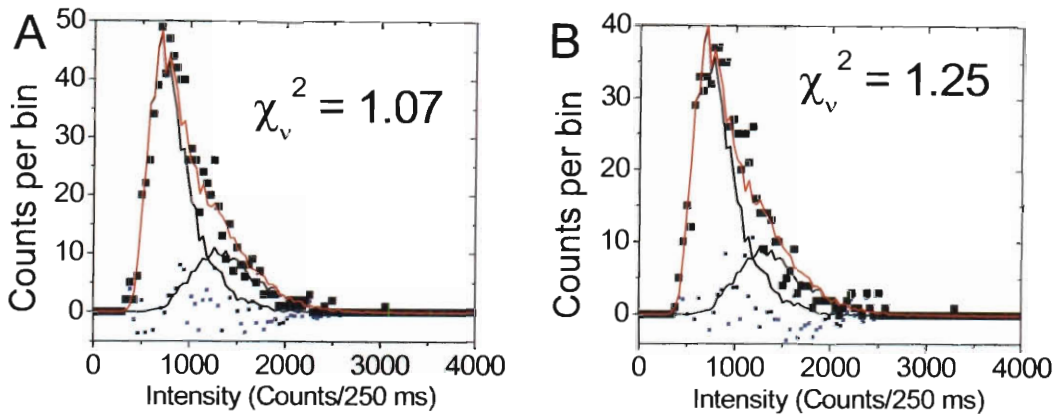

Figure 3.14 : Fits to cholesterol manipulation histograms. (A) Data from untreated cells. (B) Data from cells treated with 10 mM MβCD. Data are solid squares. Both groups are fit to the sum of an n=1 component and an n=2 component according to Eq. 3.4 where the components are derived from a Monte Carlo simulation described in the text. Fits are displayed as red histograms and individual components are black histograms. We obtain the following parameters: for untreated group (A) α_n values are 587.69 and 217.16 with $\sum_n \alpha_n = 805$ (different by 10 from the actual number of detected spots); $\alpha_{n,corr}$ values are 993.28 and 241.38 with $\sum_n \alpha_{n,corr} = 1235$; and corrected fractions $\alpha_{n,cor}/\sum_n \alpha_{n,cor}$ are 0.8045 and 0.1955; for cholesterol depleted group (B) α_n values are 487.58 and 185.81 with $\sum_n \alpha_n = 673$ (different by 4 from the actual number of detected spots); $\alpha_{n,corr}$ values are 824.07 and 206.54 with $\sum_n \alpha_{n,corr} = 1031$; and corrected fractions $\alpha_{n,cor}/\sum_n \alpha_{n,cor}$ are 0.7996 and 0.2004. The reduced χ^2-test statistic for (A) untreated group $\chi^2_\nu = 1.07$ and (B) MβCD treated group $\chi^2_\nu = 1.25$ correspond to χ^2 probabilities of >30% and >10% respectively.

3.3.5 500 ms data with nearly equal prior photobleaching

The previously described analysis of the 500 ms data was a pooling of prestin-citrine signals from 3 cells exposed to different amounts of bleaching prior to analysis. To allow the possibility of determining the actual relative content of prestin oligomeric species that produced the observed brightness distribution, a separate subset of the data in Fig. 3.5 was analyzed a third time such that the analysis begins after a nearly equal amount of pre photobleaching of each cell. It was possible to find a starting

frame for two of the three cells such that the starting frame for each cell corresponded to the equal bleaching condition ($\sim 13\,s$ of pre photobleaching). The histogram of signal brightness is shown in Fig. 3.15. In addition, a new noise background image was chosen to correspond to the level of noise of the new starting frame. The noise image was employed in a Monte Carlo simulation, as describe above, to generate the $\rho_n(I)$ for stoichiometries $n = 1 - 9$. The histogram was fit to Eq. 3.4 (Fig. 3.15) as before using various linear combinations of the generated distributions $\rho_n(I)$. Many linear combinations were attempted, and the resulting fits compared to each other using χ^2 and F-tests. The fitting results can be summarized as follows. There is a robust population of stoichiometries $n = 1$ through 4 with about 15% of signals with stoichiometry $n > 4$. Of all possible five parameter fits that include stoichiometries $n = 1$ through 4 and one with $n > 4$, the one that includes $n = 8$ is by a significant margin the best fit. A fit including a linear combination of all states ($n = 1 - 9$) yields a nearly zero population for stoichiometries $n = 5$ and 6 with a roughly equal population distributed between stoichiometries $n = 7$ through 9. Since a fit using all nine fitting parameters gave the same results as including only stoichiometries $n = 1-4$ and $7-9$, the fit with fewer fitting parameters is displayed in Fig. 3.15 since it resulted in lower estimates of the standard deviation in the parameters. Modeling the possible composition of prestin oligomeric species that could have produced the obtained fitted weights is presented in the Discussion (Sec. 3.4.5).

3.3.6 Calibration of system and validation of measurements

We performed a series of measurements to test the consistency of various measured and assumed parameters. As mentioned in Sec. 3.2.2, we measured the beam waist of the excitation laser to be $80.6 \pm 0.9\,\mu m$ in the object plane by translating a razor blade that was mounted onto a micrometer stage into the beam profile. By measuring the laser power as a function of razor position, one can extract the $1/e^2$ radius which is the beam waist. This assumes a Gaussian profile of the laser and allows estimation of the laser intensity at the location of the prestin-citrine molecules in the object plane. A separate, less accurate measurement of the beam waist was performed by imaging the intensity of a high concentration of fluorescent beads in solution on a coverslip. Fitting the profile along the coverslip to a 2-D Gaussian of the form $\sim exp\,(-2r^2/\omega_o^2)$ yielded a beam waist of $\omega_o = 87 \pm 5\,\mu m$ roughly in agreement with the more precise razor blade measurement. To test our estimation of I_o, we measured the mean time until photobleaching τ_{on} which is itself a quantity of interest and depends on laser intensity I_o via [Cognet et al., 2002]

$$\tau_{on} = \tau_{on}^{\infty}(1 + \frac{I_s}{I_o}) \tag{3.5}$$

where τ_{on}^{∞} is the mean time it takes the citrine fluorophore to bleach at infinite excitation intensity and I_s is the saturation intensity. In Fig. 3.16 we plotted histograms of observed lifetimes at excitation powers of $\sim 11\,mW$ corresponding to intensities of $\sim 100\,W/cm^2$. We estimated $\tau_{on}^{\infty} = 6.96\,ms$ and $I_s = 7\,kW/cm^2$ from published reports (See Fig. 3.17 legend for details), and using Eq. 3.5 predicted an average "on" time of $459\,ms$ in agreement with the doubly measured mean lifetimes of $469\,ms$ and $504\,ms$ in Fig. 3.16. Using Eq. 3.5, we predict that τ_{on} for the previous data, taken

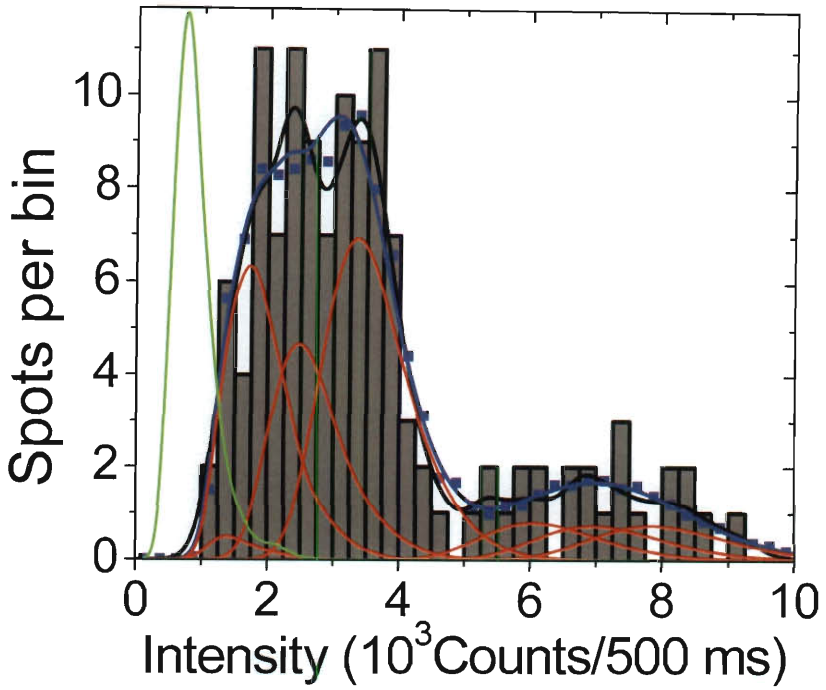

Figure 3.15 : Fit to brightness histogram of 500 ms data with equal bleaching among cells. Data includes two of the three cells that are contained in Figs. 3.5 and 3.10. The standard deviation in the background fluorescence for both cells at the chosen starting frame are nearly equal ($\sigma_b = 40\,counts/500\,ms$). Histogram and probability density of brightness data are represented by grey bars and black curve respectively. Histogram contains 123 measured individual signal brightness values and is binned at $250 counts/500 ms$. Blue curve is fit to probability density and blue squares are the fit using the same fitting parameters but instead use the histogram form of the $\rho_n(I)$. Red curves are the individual components $\alpha_n \rho_n(I)$ of the fit. Several fits corresponding to different linear combinations of the $\rho_n(I)$ were performed, the one displayed being for stoichiometries $n = 1$ through 4 and 7 through 9. Also shown as the green curve is the measured single molecule distribution $\varrho_1(I)$.

with a laser intensity of $45 - 50\,W/cm^2$, would be $1066\,ms$.

We next measured the detected signal from single prestin-citrine molecules, which is proportional to the number of detected photons $S_{det}(I_o, \Delta t)$, as a function of excitation intensity and camera integration time (Fig. 3.17). This measurement allows a separate testing of consistency between the measured lifetime τ_{on} and laser intensity. The predicted dependence of $S_{det}(I_o, \Delta t)$ on laser intensity and integration time is given by

$$S_{det}(I_o, \Delta t) = \eta_{det} k_\infty \tau_{on}^\infty \left[1 - exp\left(\frac{-\Delta t}{\tau_{on}^\infty (1 + \frac{I_s}{I_o})}\right)\right] \tag{3.6}$$

where Δt is the integration time, η_{det} is the overall detection efficiency of the experiment for citrine fluorescence, and k_∞ is the emission rate at infinite excitation. The factor of $1 - exp(\frac{-\Delta t}{\tau_{on}^\infty (1+\frac{I_s}{I_o})})$ accounts for citrine photobleaching but does not take into account blinking during the acquisition time. All quantities in Eq. 3.6 are independently estimated parameters determined either by measurement or reference to published values except η_{det} which was estimated by finding the multiplicative scaling factor that matched the data acquired at $250ms$. The detected signal $S_{det}(I_o, \Delta t)$ shows the correct time and laser intensity dependence and predicts an overall photon detection efficiency of $\sim 1 - 1.5\%$.

3.4 Discussion

3.4.1 Observable features of the distribution

One of the goals of the first portion of this study was to demonstrate that we could resolve populations of colocalized prestin-citrine molecules using brightness as an indicator of the stoichiometry of colocalization. The histogram of spot intensities in

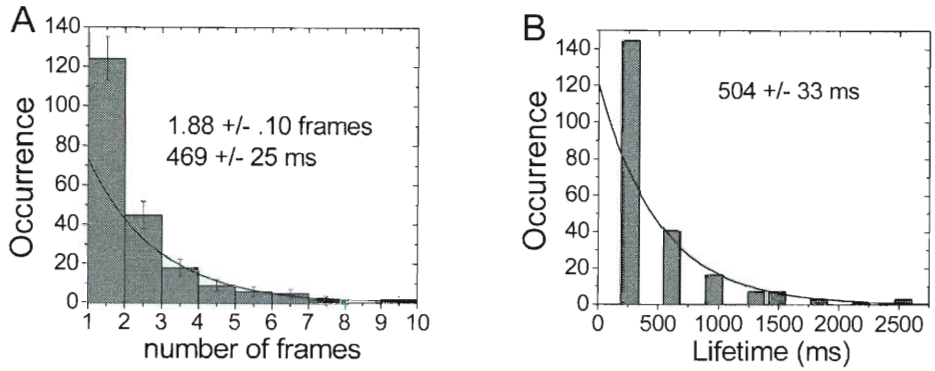

Figure 3.16 : Measurement of average time until photobleaching. Laser excitation intensity for (A) $I_o = 110 \pm 4\, W/cm^2$ and (B) $I_o = 108 \pm 8\, W/cm^2$ is the same, within the error, as in Figs. 3.13 and 3.14. Individual prestin-citrine fluorescence signals are monitored, and the time until bleaching is recorded on a histogram. (A) Data is acquired on a Cascade II EMCCD camera with exposure time 250 ms. The time delay between frames is negligible. $\langle \tau_{on} \rangle = 469 \pm 25\, ms$ (B) Data is acquired on the same MRm camera used throughout this study. Exposure time is 250 ms and frame rate is (328 ms)$^{-1}$. $\langle \tau_{on} \rangle = 504 \pm 33\, ms$.

Fig 3.5 showed a qualitative discreteness of at least three populations. Gaussian fits to a portion of the distribution (Fig. 3.6) provided the positions of the peaks in the distribution $\rho(I)$. The linear relationship between the positions of the peaks and stoichiometry (and that the separation matches the intensity of the measured single molecule distribution) is consistent with colocalization of prestin and supports the statistical independence of colocalized fluorophores required for brightness analysis. However the Gaussian fitting functions are not correct in that they are not based on convolutions of the measured single molecule distribution $\varrho_1(I)$, as described in [Schmidt et al., 1996b], and thus do not have the correct widths and shape. Yet early attempts to fit data with direct convolutions of $\varrho_1(I)$ (Eq. 3.3) failed to describe the low intensity portion of the distribution since the extent of $\varrho_1(I)$ covered more low intensities than found in the data (fit not shown). We found that taking into account

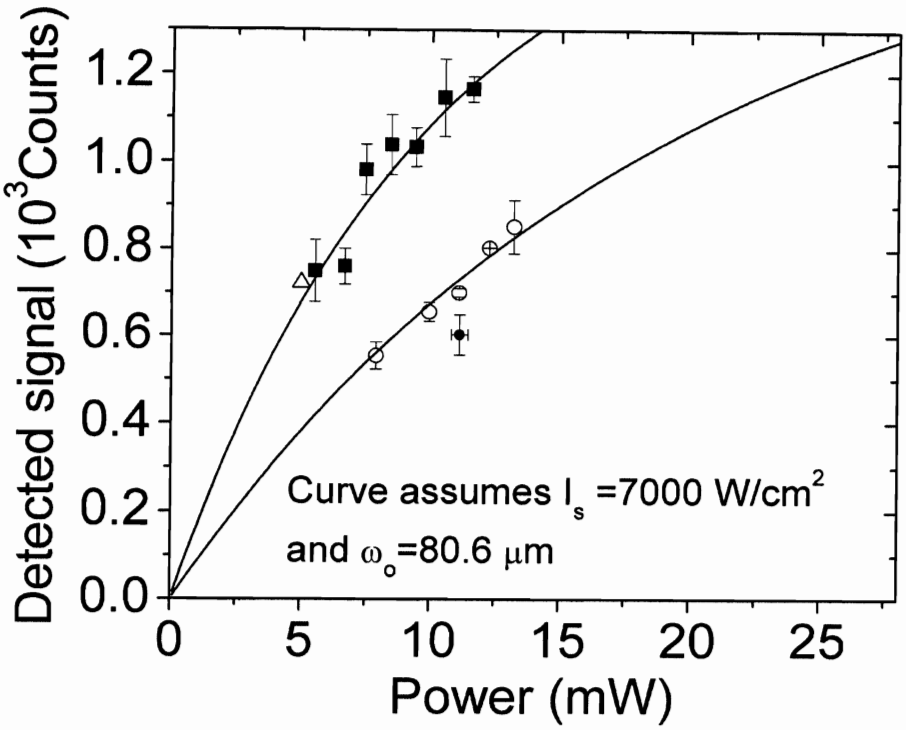

Figure 3.17 : Signal brightness versus laser intensity. Laser intensity is varied and peak value of signal brightness distribution for single molecules is measured. Camera exposure time is either 250 ms (open circles) or 500 ms (solid squares). Solid curves are a plot of Eq. 3.6 assuming $I_s = 7\,kW/cm^2$ (average of reported values for eYFP [Harms et al., 2001b, Steinmeyer et al., 2005]), $k_\infty = 3100\,photons/ms$ (assumed equal to reported value for eYFP and eGFP [Harms et al., 2001b]), and $\tau_{on}^{\infty} = 6.96\,ms$ (inferred from comparison of relative photobleaching quantum yield of citrine to eYFP [Heikal et al., 2000] and τ_{on}^{∞} for eYFP of 3.2 ms [Steinmeyer et al., 2005]). A multiplicative camera gain of 8 is incorporated into the equation and we assume a conversion factor between produced photoelectrons and analog to digital units (ADU) of $1e^-$/ADU (personal communication with Zeiss company). The only completely unknown parameter is the overall detection efficiency of the experimental setup η_{det} which is inferred by finding the correct scaling of the curve (overall multiplicative factor) to match the data acquired with a 250 ms integration time. A detection efficiency of ~1.5% is inferred from the scaling. The same detection efficiency is applied to the upper curve for 500 ms data. Also shown is the peak value of $\varrho_1(I)$ for data in Fig. 3.6 (open triangle) and the average and standard deviation of the peak values of $\varrho_1(I)$ for the cells used in Fig. 3.13 (solid circle).

the fluctuations of the background fluorescence provided an explanation of the issue.

Treating higher order distributions as direct convolutions of the measured single molecule distribution ϱ_1 in the presence of higher noise is not completely correct. This can be understood by considering two prestin-citrine molecules, labeled a and b, of real intensities I_a and I_b. If signal a is colocalized with b, and we neglect photon shot noise, a single signal of brightness $I_{a+b} = I_a + I_b$ would be observed on a noiseless background. On a noisy background the spatially separated signals a and b may or may not be detected and the probability of their detection is a sharply varying function of their brightness (see Fig. 3.18A). Furthermore, if they are detected the measured intensities I'_a and I'_b will in general be different than I_a and I_b (see Fig. 3.18B). If we now consider a and b to be colocalized within a noisy environment, the measured intensity I'_{a+b} will *not* in general be equal to the sum $I'_a + I'_b$ but will be equal to the effect that the noise has on $I_{a+b} = I_a + I_b$. Specifically, $I'_{a+b} = \hat{N}(I_a + I_b)$ where $\hat{N}$ represents the action of the background. Since on a noisy background the effect of noise does not act independently on each colocalized fluorophore, Eq. 3.3 would not be correct. This demonstrates that background noise must be treated differently than other effects that would also broaden the width and affect the shape of the observed single molecule brightness distribution. This second category of effects includes a varying orientation of citrine with respect to the laser polarization, photophysical effects such as blinking, finite camera integration time, photon shot noise, and fluctuations in laser excitation intensity. These effects would, in contrast to background noise, act independently on colocalized non-interacting fluorophores.

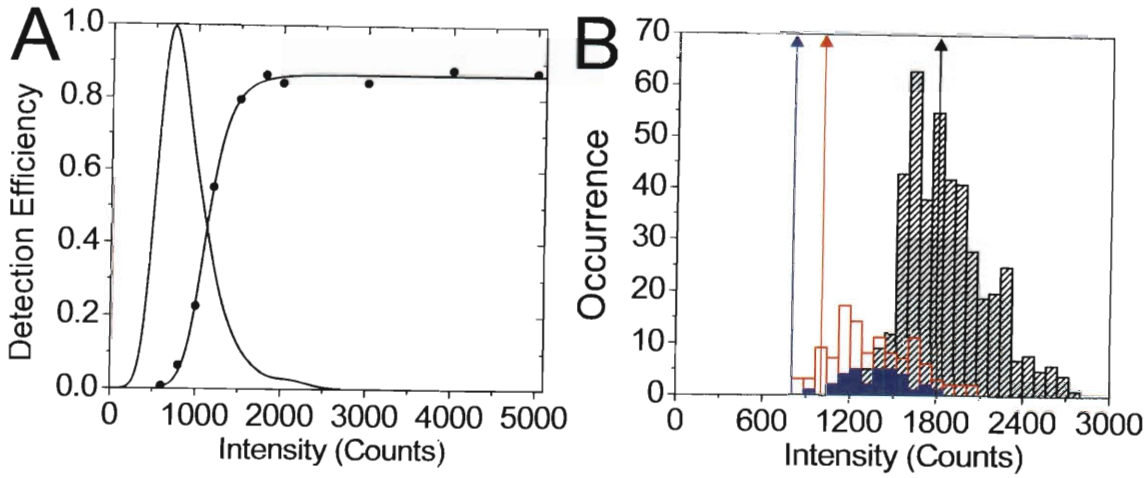

Figure 3.18 : Effects of background noise on signal brightness distribution. A simulation is conducted to measure the effect of background noise on the fitting of diffraction limited signal of varying intensity. Signals described by Eq. 3.1 are added to random positions within a measured background noise image. The background noise image was obtained by cropping a portion of the 15th frame of one of the image stacks containing a subset of the data in Fig. 3.5. We ensured that the cropped portion contained no detected signals. The standard deviation in the background signal σ_b of the cropped image is $65\,counts$. For each simulated intensity I_{sim}, a 500 frame image stack is created by adding one signal of the same intensity to each frame at random positions within the noise background. The image stacks are analyzed in the same manner as the real data as describe in the Methods. (A) Detection efficiency as a function of signal intensity was measured by counting how many out of the 500 simulated spots are detected. Simulated intensity ranged from $I_{sim} = 600 - 5000\,counts$. Intensities below $600\,counts$ were not detected. The fit to the data has no theoretical relevance and serves only a guide for the eye. Also shown is the measured single molecule distribution $\varrho_1(I)$ obtained from a transfected cell that was bleached with the laser until the background noise attained a low level of $\sigma_b = 16\,counts$ and imaged under the same conditions as minimally bleached cells. (B) Results of the simulation for selected intensities are displayed. The lines with up pointing arrows represent the input distributions which are delta functions ($500\,spots \times \delta(I - I_{sim})$) placed at the simulated intensity. The effects of the noisy background on the input distributions are demonstrated as histograms of the resulting intensities obtained by fitting the simulated signals. The histograms are colored the same as the delta functions. The displayed intensity inputs are 800 counts (blue), 1000 counts (red), and 1800 counts (black). The means of the resulting distributions are (in the same order) 1376.2 (blue), 1355.8 (red), and 1873.5 (black) counts. As I_{sim} is increased, the mean of the resulting distribution gets closer to the simulated intensity. The fitted intensity uncertainties and widths of the signals were in a range consistent with our post processing rejection criteria.

The weights obtained from fitting the data in Figs. 3.8 and 3.9 include corrections for the effects of background noise and pixelation noise, but do not correspond to the real distribution of brightness stoichiometires due to the effects of photobleaching, blinking, and long off times observed for the fluorescent proteins [Moerner et al., 1999, Schwille et al., 2000]. To obtain the real fractions, the photophysics of citrine would have to be taken into account. In addition, what we measure is a cumulative time average of the brightness distribution over a long period of 30 frames, corresponding to ~16 seconds, and therefore does not describe the distribution at a particular moment in time. Furthermore, independent of citrine photophysics, a portion of a population of N monomers placed randomly on a finite area will statistically have a nonzero probability to be colocalized. Therefore, the degree of colocalization observed for N detected prestin-citrine particles must be compared to the number of times one would expect two or more particles to be colocalized by random coincidence within a diffraction limited area (for the given particle density) assuming no interactions between prestin molecules.

Analysis of the 500 ms data over a narrower time window of five frames ($\sim 2.6\,s$) in Figs. 3.10 and 3.11 provides an improvement in our ability to interpret the results since doing so minimizes averaging the observed brightness distribution over an extended period during which the distribution is changing. In other words, analyzing a narrow time window provides more of a "snapshot" of the apparent distribution. Furthermore, since the analysis time window is centered around the frame that includes the background noise image utilized in the Monte Carlo simulation, the calculated fitting functions are more accurate since the background noise is representative of the experimental conditions. Also, over a five frame time window the background will

vary less than over a 30 frame window further improving the accuracy of the fitting functions. In the case where we averaged over 30 frames, the standard deviation in the background of the images decreased exponentially over the 30 frames making the fitting functions less accurate.

While the accuracy of an analysis of signal brightness to infer the distribution of prestin oligomeric states suffers from the effects of citrine photophysics, it nonetheless does provide a precise accounting of the experimentally observed brightness distribution. By including considerations for the effects of noise, our fitting method correctly describes measured historgrams of signal intensities with reasonable accuracy. In Figs. 3.8 and 3.9 we demonstrated that the fit to the data using Eq. 3.4 accounted for all but 13 of the 802 detected signals. Furthermore, the theoretical distributions for $\rho_n(I)$, generated from the measured brightness distribution of single citrines including noise effects, are found to be centered close to the peaks of the observed structure in the measured histogram. As shown in Figs. 3.10 and 3.11, the fit to the narrow time window data accounted for all but five of the 132 detected signals and the component distributions generated from the Monte Carlo simulation faithfully reside at intensity positions corresponding to aggregates observed in the experimental distribution. Since the fitting function Eq. 3.4 used to fit the data using least squares is linear in the fitting parameters α_n, a χ^2-test of fit is appropriate [Bevington, 1992]. All fits showed χ^2_ν statistics near unity, and corresponded to reasonable χ^2 probabilities indicating that the model applied appropriately describes the data.

Our observation of a pronounced weight to the $n = 4$ population over all lower stoichiometries (Fig. 3.12), even after taking into account the reduced detection ef-

ficiency for monomers, provides strong evidence that prestin tends to colocalize in the cell membrane. This is because all photophysical effects (bleaching, blinking, and long off times) will tend to bias the observed distribution of stoichiometries toward lower numbers. The only effect that could erroneously lead to apparent colocalization when none is actually present is incidental colocalization within a diffraction limited area as discussed above. This statistical problem has been treated by Chandrasekhar. In a given area A with N randomly distributed individual particles, what is the probability $C(n)$ that some n particles are randomly located in *any given* sub-region of diffraction limited area a_{dl}? The average value of n, $\langle n \rangle$, is given by

$$\langle n \rangle = N(a_{dl}/A) \equiv \nu. \tag{3.7}$$

The probability $C(n)$ is given by the Bernoulli distribution [Chandrasekhar, 1943]

$$C(n) = \frac{N!}{n!(N-n)!} \left(\frac{\nu}{N}\right)^n \left(1 - \frac{\nu}{N}\right)^{N-n}. \tag{3.8}$$

This is well approximated by a Poisson distribution [Chandrasekhar, 1943]

$$C(n) = \nu^n e^{-\nu}/n!\,. \tag{3.9}$$

Looking at the observed weights from fitting the data in Figs. 3.10 and 3.11, and taking into account the stoichiometry of each weight, we obtain an estimate of the total number N_{total} of individual detectable (i.e. fluorescent) prestin-citrine molecules contained in the 5 frame time interval which is given by

$$N_{total} = \alpha_1 + 2\alpha_2 + 3\alpha_3 + \cdots + 6\alpha_6. \tag{3.10}$$

This gives a total of $N_{total} = 465$ individual prestin molecules (or about $N = 465/5 = 93$ per frame). To get the mean number of particles per diffraction limited area ν, we use Eq. 3.7 with $a_{dl} = \pi(\frac{.61}{.514}s)^2$ where $s = 255\,nm$ (Sec. 3.2.2). The ratio multiplying s comes from the fact that we measure the FWHM of the point spread function (which is theoretically $.514\frac{\lambda}{NA}$), but the Raleigh criterion is defined in terms of the first minimum of the Airy pattern ($d_R = .61\frac{\lambda}{NA}$). The total plasma membrane area analyzed is $354\,\mu m^2$ giving an average number of prestin per diffraction limited area of $\nu = .07$. Applying Eq. 3.8 (or Eq. 3.9 giving nearly identical results) we find that the probability for random colocalization of two fluorescent prestin-citrine molecules is about 3.4% and the probability for randomly having 3 prestin colocalized is 0.08%. Even taking into account the observed maximum fluctuation in density ($\nu = .18$) predicts probabilities of 8% and .5% for random colocalization of two and three fluorescent prestin-citrine molecules respectively. This result demonstrates that random colocalization of the observed density of fluorescent prestin-citrine cannot account for the observed degree of colocalization in Fig. 3.12. Our results so far tend to suggest that prestin molecules in the plasma membrane are more likely to colocalize with other prestin molecules with stoichiometry corresponding to $n \geq 4$ than they are to form stoichiometries of either $n = 1$, 2, or 3.

Our observation that prestin might form higher order oligomers is in agreement with the suggestions of biochemical observations (showing oligomeric populations of prestin on PAGE gels [Detro-Dassen et al., 2008, McGuire et al., 2010, Rajagopalan et al., 2007, Sturm et al., 2007, Z. et al., 2006] and from yeast two-hybrid experiments [Z. et al., 2006]), and from electrophysiological studies [Detro-Dassen et al., 2008]. It is commonly proposed that prestin has a tetrameric quaternary structure

([Mio et al., 2008, Wang et al., 2010, Z. et al., 2006]) with one report suggesting prestin is a dimer [Detro-Dassen et al., 2008] since predominantly monomer and dimer bands were observed on BN-PAGE gels in contrast to the observations of Z. et al., Rajagopalan et al., and McGuire et al.. The latter study [Detro-Dassen et al., 2008] further reports that the dimer is a single functional unit, as opposed to a dimer of independent functional monomers, based on electrophysiology of cells cotransfected with two different functionally altered prestin mutants. This conclusion was based on the observation that NLC recordings required a fitting function composed of a sum of three NLC curves, two corresponding to each mutant individually and one corresponding to a heterodimer. While this provides strong evidence that oligomerization affects prestin function, it does not prove that the functional unit is a dimer. Even if the dimer is functional, it does not rule out the existence of functional higher order states that may exist natively in the cell membrane. Indeed the authors provide the caveat that solubilization of prestin before BN-PAGE might dissociate weak protein-protein interactions that could form higher order oligomers. Furthermore, Detro-Dassen et al. do not perform BN-PAGE gels on the heterodimer or on any of the mutants individually to show whether they form oligomers. This missing information is important since it is possible that the dimer and monomer may each have independent functions. This idea is supported by a recent report correlating the maturation of NLC to prestin expression assayed with biochemical measurements using an inducible prestin cell line [Bian et al., 2010]. The authors show evidence of a dominant negative effect of a lower weight monomer on a higher weight monomer. In addition, they observe a rapid early increase in the valence of charge movement and shift in voltage of peak capacitance, the saturation of which correlates with the first observation of prestin dimers on Western blots. Mio et al. have shown that

prestin purified from Sf9 cells has four-fold symmetry and that multiple antibodies bind to prestin as shown by electron microscopy images [Mio et al., 2008], however indications for prestin function in Sf9 cells are weak and show a thousand fold less charge movement than in HEK cells. Subsequently, the authors presented evidence of prestin degradation in the Sf9 expression system [Tadenuma et al., 2008]. One report [Wang et al., 2010] proposes a somewhat different conclusion on what comprises the functional unit. Based on comparison of measured prestin charge density in OHCs with published densities of the IMPs in freeze fracture images, they conclude that prestin forms tetramers since the charge density they measure is four times higher than the IMP density. However, they propose that prestin subunits function independently in the tetrameric aggregates since the slope factor of motility and charge movement are equal. While this is a possible scenario, their analysis is problematic since estimates of charge per functional unit from NLC is highly model dependent. They assume the common two-state Boltzmann model for prestin function and they assume that each prestin subunit carries one electron charge. However, it has been shown that estimates of motor charge from NLC could vary by a factor of 3 going from a two-state to a continuous model, and that since it is unknown whether the total charge of the motor is moved fully within the membrane electric field gradient, estimates of total charge are problematic [Scherer and Gummer, 2005]. Finally, one group [Pasqualetto et al., 2008] has reported that a purified variant of prestin tends to aggregate in ratios ranging from 2 to 4 in various buffer solutions as determined by dynamic light scattering. Clearly, the question of what oligomeric states of prestin exist and which of them is functional remains an open one.

In light of these studies it is tempting to interpret the results of Figs. 3.10, 3.11,

and 3.12 as indicating that prestin is predominantly a tetramer since the fitted weight corresponding to a stoichiometry of $n = 4$ is pronounced over lower *and* higher values. However, since the analysis does not take into account the effects of bleaching over the time course of the image stack and other photophysical effects like blinking and long off times, the conclusion of a tetramer cannot be conclusively reached from the data presented so far. This is because higher order oligomeric states (n>4) could have bleached to a stoichiometry of 4; and due to blinking and the statistics of the interplay between multiple dark states and the fluorescent state of the citrine tag [Moerner et al., 1999, Schwille et al., 2000], an observed stoichiometry of 4 could correspond to any number of higher order oligomeric states where one or more of the citrines are non-fluorescent. This point will be explored in Sec. 3.4.5 where specific models of prestin oligomeric content will be compared to the observed distribution of brightness.

3.4.2 Cholesterol dependence of prestin oligomerization

Previous studies have demonstrated that membrane cholesterol manipulations can reversibly tune prestin function [Rajagopalan et al., 2007, Sfondouris et al., 2008, Sturm et al., 2007]. Decreases in native concentration of membrane cholesterol shift the voltage of half maximal charge movement (V_{pkc}) in the depolarized direction in both the native OHC and in transfected mammalian cells. Likewise, increases in membrane cholesterol hyperpolarize V_{pkc} from its original position. However, the molecular mechanism of cholesterol dependent NLC tuning is unknown. Previous biochemical evidence suggests that changes in membrane cholesterol concentration affect prestin oligomerization [Rajagopalan et al., 2007]. Rajagopalan et al. have reported that lysate of prestin transfected HEK cells, having undergone membrane

cholesterol manipulations and run on PAGE gels, showed decreased or increased intensity dimer bands for membrane cholesterol depletion and loading respectively [Rajagopalan et al., 2007]. Furthermore, they report that transfected cells treated with MβCD required increased levels of crosslinker to see dimer formation. The notion that cholesterol could affect prestin function by affecting changes in prestin oligomerization is indirectly supported by the above mentioned electrophysiological study [Detro-Dassen et al., 2008] since it was demonstrated that oligomerization can affect prestin function. This is further supported by previous work in our lab that showed a significant decrease in ensemble averaged FRET in cells cotransfected with CFP and YFP prestin fusions [Greeson, 2008, Rajagopalan et al., 2007].

Having shown that we can detect the fluorescence from single prestin-citrine molecules and that we can discriminate colocalized populations corresponding to specific stoichiometries, we reasoned that we should be able to use the technique to test whether cholesterol depletion affects prestin oligomerization as suggested by Rajagopalan et al.. As discussed above, the photophysics of the fluorescent tags greatly complicate an accurate determination of the real, absolute fractions in multiple stoichiometries. However if those effects are kept constant between two treatment groups this technique could in principle allow observation of relative changes in the stoichiometric distribution of colocalized populations [Brameshuber et al., 2010, Schmidt et al., 1996b, Zhang et al., 2009]. We therefore decided to repeat the measurement of prestin-citrine signal brightness histograms for both untreated cells and cells treated with MβCD to reduce membrane cholesterol. This time, however, care was taken to ensure an equal exposure to the excitation laser prior to the frame in the image stacks where analysis begins. This ensures that in any given frame the photobleach-

ing probability for prestin-citrine molecules is the same from sample to sample and allows a relative comparison between groups.

We observed that the brightness distribution of untreated cells and cells treated with MβCD had identical brightness distributions (Figs. 3.13 and 3.14). The corrected weights from fitting the data using Eq. 3.4 for each group were fractionally identical and corresponded to 80% single and 20% double copies of prestin-citrine (Fig. 3.14). An analysis of incidental colocalization of the observed concentration of detected bright fluorophores again could not account for a 20% population of stoichiometries with $n = 2$.

The requirement of equal photobleaching prior to analysis requires that the frame for which the analysis begins is suitable for all cells imaged. Variations in expression level from cell to cell will yield a different optimal frame for each cell. Therefore, a starting frame number had to be chosen that was early enough to "catch" the colocalization of prestin-citrine before citrine photobleached, yet long enough to allow low background noise and sparse spatial density of detected signals for all cells imaged. This requirement resulted in a chosen starting frame for the comparative experiment that corresponded to a longer time after initial laser turn-on compared to the prior experiment done with a 500 ms integration time. This resulted in a greater amount of initial photobleaching in the 250 ms experiment even though the time per frame is shorter. If depletion of membrane cholesterol does result in changes of prestin oligomerization or colocalization, it is likely that the degree of photobleaching employed in this study masked any differences in the observed brightness histograms. However, the observation of identical histograms between the two treatment groups

demonstrates that if care is taken to ensure an equal amount of prebleaching, repeatable results can be obtained.

3.4.3 Measured quantities are self consistent

The measured average time before photobleaching τ_{on} of citrine (Fig. 3.16) is in agreement with published photophysical parameters of citrine and eYFP (see Fig. 3.17) [Heikal et al., 2000, Schwille et al., 2000, Steinmeyer et al., 2005]. This provides a consistency check on our measurement of the laser beam waist, which is required to know the laser intensity, with the advantage that the measurement is independent of the overall detection efficiency η_{det}. Our measurement of the detected fluorescence signal from single molecules $S_{det}(I_o, \Delta t)$ versus laser intensity, for two separate integration times, demonstrates that the signal has the expected dependence on I_o and Δt. It also provides another consistency check on the calibration of the apparatus. In particular it is consistent with our estimate of the laser power and allows an estimate of the overall detection efficiency of 1-1.5%. While this may seem low, it is not at all uncommon to find reports of η_{det} ~1% in published single molecule studies [Blab et al., 2004, Enderlein et al., 1997, Thompson et al., 2002]. An estimate of light collection efficiency losses from considerations of the experimental equipment (camera quantum efficiency, objective acceptance angle, filters etc.) gave a calculated upper limit of ~4.4% but did not take into account index of refraction mismatch between sample buffer and immersion oil and effects of the coverslip sample buffer interface on the angular distribution of fluorophore fluorescence [Enderlein, 1999]. Furthermore, our estimate of the number of detected photons is consistent with the observed uncertainties in the signal intensity and with the localization accuracy (Fig. 3.19) [Thompson et al., 2002].

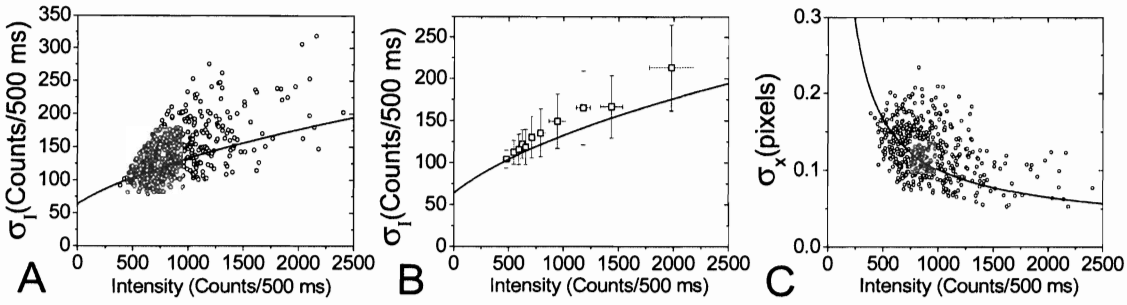

Figure 3.19 : Comparison of experimental photon counting precision and position accuracy with theory. We compare the fitting errors of collected photons I and position x from measured signals contained in $\varrho_1(I)$ for data acquired with $500\,ms$ integration time (Fig. 3.5) with analytic calculations by Thompson et al.. (A) Uncertainty in fitted intensity, which is proportional to the number of detected photons S_{det}, versus intensity I. Solid curve is the equation $\sigma_I = 1.3{\times}8{\times}\left(\frac{I}{8} + \frac{4\pi\sigma_\Psi^2(\sigma_b/8)^2}{a^2}\right)^{1/2}$ where $\sigma_\Psi = s/2\sqrt{2\,ln2}$ is the standard deviation of the point spread function, a is the pixel size, and σ_b is the standard deviation in the background. The factors of 8 take into account an arbitrary camera gain. A photoelectron to count conversion of $1e^-/count$ is assumed (Zeiss personal communication). The factor of 1.3 is a correction factor reported in Thompson et al. (B) Same data in (A) is binned in various intervals. Error bars are the standard deviation in data points for each bin. (C) Plot of fitted localization error versus I. Solid curve is the equation $\sigma_x = (\frac{\sigma_\Psi^2+\frac{a^2}{12}}{I/8} + \frac{8\pi\sigma_\Psi^4\sigma_b^2}{a^2I^2})^{1/2}$ where the factor of 8 dividing I in the first term is again an arbitrary camera gain factor.

3.4.4 Downfalls of method and difficulties in interpretation

The previous discussion has predominantly focused on correctly accounting for the observed distribution of signal brightness which is a required first step in determining the real distribution of prestin stoichiometries. To determine the stoichiometric distribution of prestin colocalization that leads to the observed distribution of brightness stoichiometries, the photophysical properties of the fluorescent tag has to be taken into account. Specifically, if the probability $p(t)$ of citrine being in a fluo-

rescent state at any time t after the laser has been turned on is known, the actual distribution of oligomeric states can be inferred from the observed distribution of brightness stoichiometries. If there are N colocalized prestin-citrine molecules in a diffraction limited area (whether the prestin are colocalized by chance or whether they are bound together in an aggregate or otherwise actively colocalized by membrane compartments), and each one of them has a probability $p(t)$ to be fluorescent, then the observed distribution $W^N_{p(t)}(n)$ of brightness stoichiometries $n = 0, 1, 2, \ldots, N$ is given by a binomial distribution

$$W^N_{p(t)}(n) = \frac{N!}{n!(N-n)!} p(t)^n (1 - p(t))^{N-n}. \tag{3.11}$$

In other words, the probability to observe n of the N prestin citrine molecules fluorescent is $W^N_{p(t)}(n)$. It is also important to note that even in the case that prestin does not form oligomers or actively colocalize, if there is a high enough expression level there could still be several prestin colocalized per diffraction limited area and give the appearance of colocalization simply by probability considerations. If in a cell expressing only prestin monomers there is in reality an average of ν_{real} prestin monomers per diffraction limited area, after some amount of bleaching there will be an average of $\nu = p(t)\nu_{real}$ fluorescent prestin per diffraction limited area. This would give rise to a broad apparent distribution of stoichiometris according to Eq. 3.9. So in principle, if $p(t)$ is known and there is a high expression level, the real distribution of oligomeric states can be determined by taking into account Eq. 3.11 and by also accounting for a high expression level using Eq. 3.9. However such an analysis that takes into account random colocalization is by no means trivial since an estimate of the "on" probability is difficult. Especially when one allows for the fact that there

could be random colocalization of multiple oligomeric states the analysis quickly becomes unwieldy. Therefore control over the expression level would greatly facilitate oligomerization analysis since then the concentration of prestin could be kept low enough that Eq. 3.9 ensures the probability of random colocalization is negligible (i.e. $\frac{C(2)}{1-C(n>0)} \approx 0$). If the concentration of prestin were low enough, only the photophysical effects would have to be taken into account using linear combinations of Eq. 3.11. Just as important, control of expression would allow for a lower background fluorescence noise level requiring less bleaching and thus maximizing $p(t)$. The closer $p(t)$ is to 1, the more representative the observed stoichiometries are of the real distribution of oligomeric states.

A comparison of the data acquired with $45 - 50\,W/cm^2$ laser excitation with a $500\,ms$ integration time and a $(531\,ms)^{-1}$ frame rate and the data acquired with $108\,W/cm^2$ laser intensity with a $250\,ms$ integration time and a $(297\,ms)^{-1}$ frame rate shows that the experimental conditions of the former data set allowed for capturing colocalization of higher stoichiometries before photobleaching. This can be partially accounted for from a consideration of the expected bleaching for the laser intensities and frame rates employed in each case. We measured the "on" time of citrine to be $468\,ms$ when illuminated with $108\,W/cm^2$ and we can infer using Eq. 3.5 that the "on" time would be $1066\,ms$ using $\sim 50\,W/cm^2$. Even though a faster frame rate was used in the former case, the ratio of the "on" time to the inverse frame rate is larger in the latter case ($1066/531 \approx 2 > 468/297 = 1.58$) by almost 30%. However a longer "on" time in relation to the camera speed is only part of the reason for the improvement. Numerous reports have been made showing the existence of one or more long-lived dark states of the fluorescent proteins with lifetimes up to $50\,s$ which are observed

during continuous laser illumination in single molecule experiments [Dickson et al., 1997, Garcia-Parajo et al., 2000, Moerner et al., 1999, Peterman et al., 1999]. The exact nature of these dark states is as yet unknown with some attributing it to photo-isomerization of the chromophore [Weber et al., 1999]. However, most report that the lifetime of the dark state does not depend on excitation intensity. A longer "on" time by a factor of two would then correspond to an increase in $p(t)$ by an amount that would approach a factor of two if the "off" time is large compared to the "on" time. In hindsight using the lower excitation intensity with a slower frame rate would have been a superior set of conditions for evaluating the effects of cholesterol depletion on oligomerization state since they better allow for "catching" the oligomers before they go into a dark state for the reasons just described.

3.4.5 Quantitative estimate of prestin oligomeric content

Despite the fact that the expression level in our experiments is large enough that the coincident localization probability of prestin-citrine oligomers is too high to ignore (as discussed in Sec. 3.4.4), we were able to develop a model that fully incorporates coincident localization with photobleaching to describe the experimentally observed brightness stoichiometries. For the sake of simplicity in the subsequent analysis we make the assumption that any degree of colocalization that cannot be accounted for by coincident localization is due to oligomerization of prestin. The validity of this assumption will be discussed in Ch. 6 Sec. 6.5.3. We found that the minimal number of oligomeric species required to account for the observed brightness stoichiometries included populations of prestin-citrine monomers, dimers, and tetramers. The calcu-

lated probability model is given by

$$P(n) = \sum_{N} W^{N}_{p(t)}(n) \sum_{n_1\ n_2\ n_4} \delta_{N,n_1+2n_2+4n_4} \frac{\nu_1^{n_1} e^{-\nu_1}}{n_1!} \frac{\nu_2^{n_2} e^{-\nu_2}}{n_2!} \frac{\nu_4^{n_4} e^{-\nu_4}}{n_4!} \tag{3.12}$$

where $W^{N}_{p(t)}(n)$ is the conditional probability, defined in Eq. 3.11, that given there are N prestin-citrine in an aggregate n of them are fluorescent; $p(t)$ is the "on" probability; and ν_1, ν_2, and ν_4 are the densities per diffraction limited area of prestin-citrine monomer, dimer and tetramer respectively. The Kronecker delta function has been employed to constrain the number of prestin-citrine molecules N in any diffraction limited region to be linear combinations of multiples of monomer, dimer, or tetramer. Specifically, the function $P(n)$ is the calculated probability to find a signal in any given diffraction limited area to be of stoichiometry n given the concentrations of each oligomeric species and the probability $p(t)$ for any individual prestin-citrine molecule to be fluorescent. The inner sum is over all possible configurations of n_1, n_2, and n_4 such that the Kronecker delta is nonzero. The outer sum in principle runs over N from zero to infinity, however in practice it is cut off at a suitable N_{max} such that the probability of getting N_{max} prestin localized to any randomly chosen diffraction limited area is essentially zero for the given densities of each oligomeric state. This probability is given by the inner sum in Eq. 3.12, so the condition on a suitable N_{max} is mathematically written $\sum_{n_1\ n_2\ n_4} \delta_{N \geq N_{max}, n_1+2n_2+4n_4} C(n_1)C(n_2)C(n_4) \approx 0$. To allow comparison with the measured weights α_n, the probabilities $P(n)$ are renormalized by the probability $1-P(n=0)$ to observe at least one fluorescent particle in a diffraction limited area and also multiplied by the total number of fluorescent particles (N_{total}, Eq. 3.10) via

$$P_\alpha(n) = N_{total} \frac{P(n)}{1 - P(n=0)}. \tag{3.13}$$

This renormalization of probabilities is required since in the experiment we do not actually measure the population of aggregates in which *all* of the prestin-citrine molecules in the aggregate are non-fluorescent nor do we measure the probability for any diffraction limited area to be vacant of prestin molecules (i.e. we do not measure $\alpha_{n=0}$). Using the definition in Eq. 3.13, $P_\alpha(n)$ represents the number of observable signals with stoichiometry n, out of the total number of signals N_{total}, that would be expected to be produced from a prestin-citrine population with spatial densities of ν_1 monomers, ν_2 dimers, and ν_4 tetramers given that the probability for any prestin-citrine molecule to be fluorescent is $p(t)$. Once the set of concentrations ν_i of each species i is found that describes the observed distribution of signal brightness stoichiometries, the fractional content of each oligomeric species f_i is found from

$$f_i = \frac{\nu_i}{\sum_i \nu_i}. \tag{3.14}$$

The model is easily generalized to include additional prestin-citrine oligomeric species. While a model including only monomer, dimer and tetramer was sufficient to model the data (Figs. 3.20 and 3.21), a model including an small additional population of 8-mers was able to model the results more closely (Figs. 3.22 and 3.23). The probabilistic model including the 8-mer population is given by

$$P(n) = \sum_N W^N_{p(t)}(n) \sum_{n_1\ n_2\ n_4\ n_8} \delta_{N,n_1+2n_2+4n_4+8n_8} \frac{\nu_1^{n_1} e^{-\nu_1}}{n_1!} \frac{\nu_2^{n_2} e^{-\nu_2}}{n_2!} \frac{\nu_4^{n_4} e^{-\nu_4}}{n_4!} \frac{\nu_8^{n_8} e^{-\nu_8}}{n_8!} \tag{3.15}$$

where ν_8 is the concentration of prestin-citrine 8-mers per diffraction limited area. The first model (Eq. 3.12 and Figs. 3.20 and 3.21) accounts for the observed stoichiometries greater than $n = 4$ in Fig. 3.15 assuming only coincident localization of prestin-citrine tetramers. The second model (Eq. 3.15 and Figs. 3.22 and 3.23)

account for the stoichiometries greater than $n = 4$ using both coincident localization and a possible real population of prestin-citrine 8-mers. However, the results of comparing both models to the data imply that the distribution of prestin oligomeric states is composed predominantly of tetramers followed by dimers ($25.4 \pm 0.9\%$ dimer and $65.7 \pm 2.7\%$ tetramer for the first model and $28.4 \pm 2.5\%$ dimer and $61.6 \pm 5.1\%$ tetramer for the second model). Furthermore, for both models the relative fractions of each oligomeric state came out fairly robust. The main differences in the model including an 8-mer population, compared to the simpler model, is a reduction in the amount of monomer that is balanced by the 8-mer population and a slight decrease in the ratio of tetramer to dimer. Clearly distinguishing whether the observed stoichiometries with $n > 4$ are truly due to an 8-mer population is difficult without reducing the expression level as discussed in Sec. 3.4.4 so as to make the probability of coincident localization negligible. Since fitting of the brightness data in Fig. 3.15 suggested that the most appropriate stoichiometry to describe the signals at the high intensity portion of the histogram corresponded to $n = 8$, it is possible that prestin tetramers sometimes aggregate to form 8-mers. If the experiment were repeated with low expression and stoichiometries with $n > 4$ remained, it would indicate that prestin oligomers with order larger than tetramer actually exist.

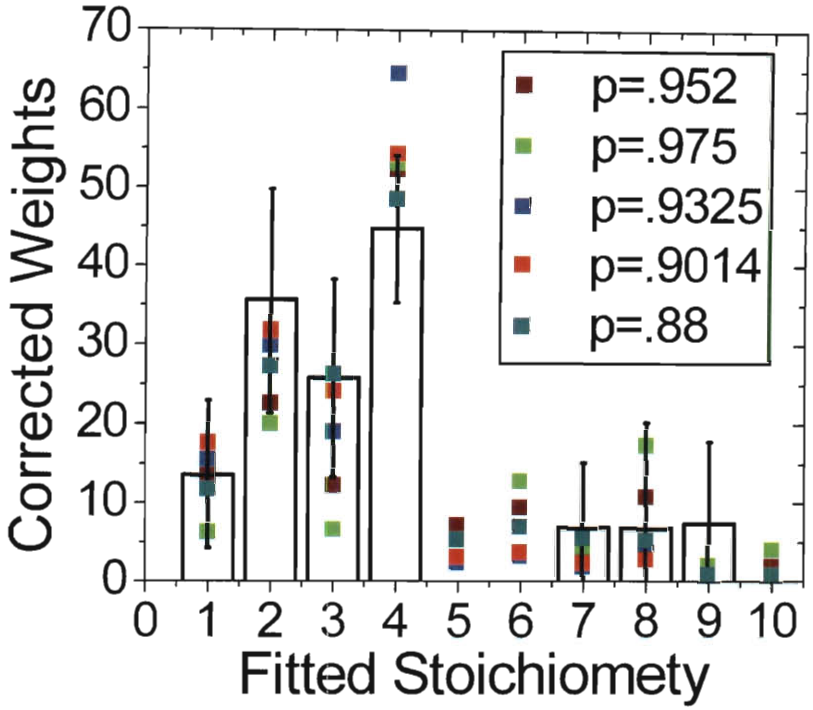

Figure 3.20 : Comparison of fitted weights to monomer/dimer/tetramer model. Bars represent the weights $\alpha_{n,corr}$ obtained from fitting data in Fig. 3.15 to Eq. 3.4 with $n = 1, 2, 3, 4, 7, 8, 9$. Error bars are the estimated standard deviation in the fitting parameters. The standard deviation in each alpha is taken to be the square root of the diagonal elements of the error matrix [Bevington, 1992]. Legend: colored squares are manual fits of the obtained weights $\alpha_{n,corr}$ using probabilistic model described by Eqs. 3.12 and 3.13 for various trial values of the "on" probability $p(t)$. For each trial value of $p(t)$, ν_1, ν_2, and ν_4 are manually adjusted until $P(n)$ matches the distribution of weights $\alpha_{n,corr}$ as closely as possible.

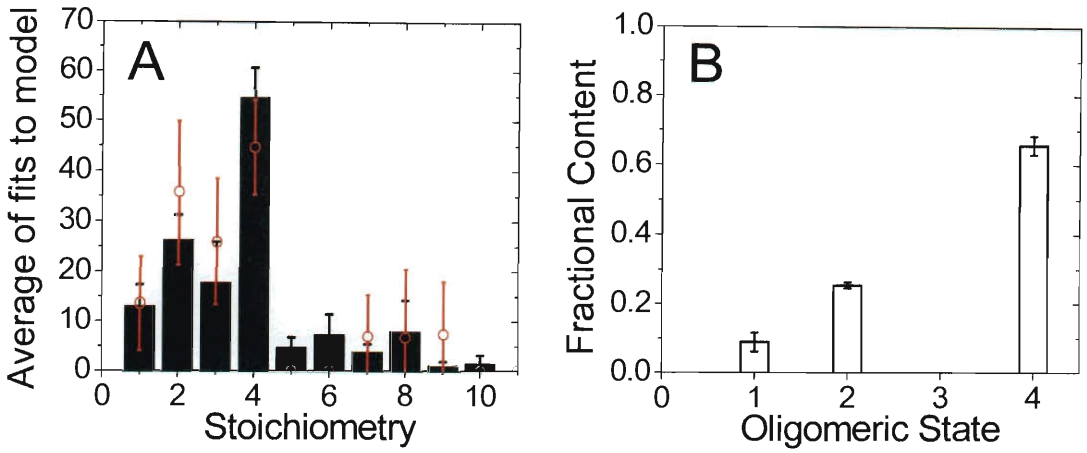

Figure 3.21 : Results of fit to monomer/dimer/tetramer model. (A) The average and standard deviation of the trial fits in Fig. 3.20 are shown as solid bars. The fitted weights are re-displayed as red open circles. (B) The fractional content f_i of each prestin oligomeric state i implied by the monomer/dimer/tetramer model is displayed. Each open column is the average fractional content $\langle f_i \rangle$ of the five trials and the error bar is the standard deviation. The fractional content for each oligomeric state is 8.9 ± 2.8, 25.4 ± 0.9, and $65.7 \pm 2.7\%$ for monomer, dimer, and tetramer respectively. The error bars do not represent the overall estimate of the error in each fractional population, but instead represent its sensitivity to $p(t)$ over the range of trail values of $p(t)$.

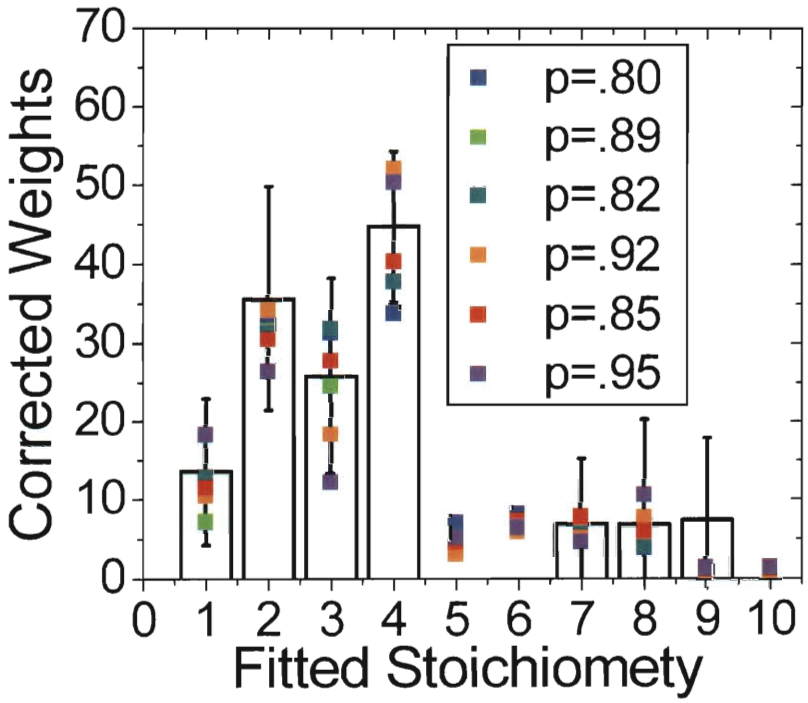

Figure 3.22 : Fits of weights to monomer/dimer/tetramer/8-mer model. Same procedure as in Fig. 3.20 except a possible population of 8-mers is included in the model. In this case, six trial values of $p(t)$ were performed (colored squares, see Legend).

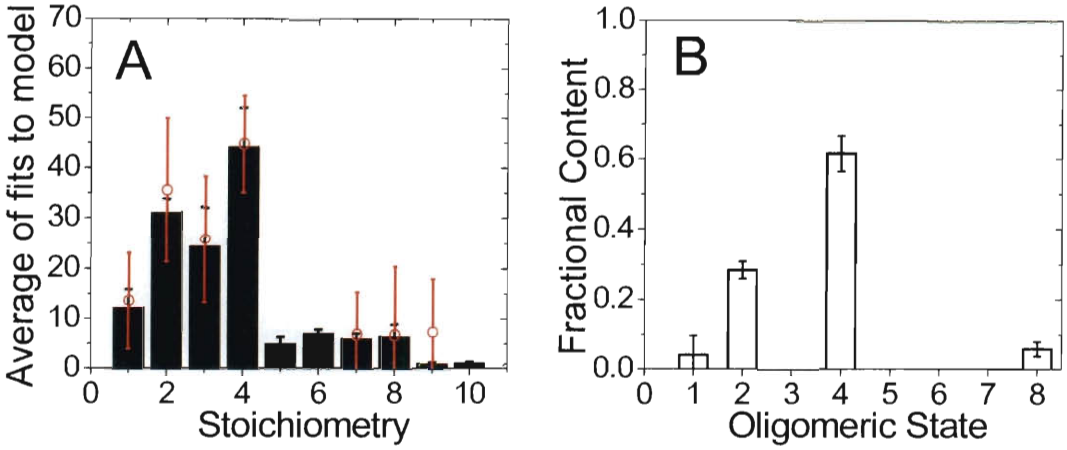

Figure 3.23 : Prestin oligomeric structure based on monomer/dimer/tetramer/8-mer model. (A) Same procedure as in Fig. 3.21 with the inclusion of a population of 8-mers. (B) The average fractional content for each prestin oligomeric state is 4.1 ± 5.5, 28.4 ± 2.5, 61.6 ± 5.1, and $5.9 \pm 2.1\%$ for monomer, dimer, tetramer, and 8-mer respectfully.

Another difference between the models concerns the implied overall prestin expression level for the trial values of "on" probability or, more relevant to the oligomeric models, the average total number of prestin per diffraction limited area given by $\nu_{real} = \nu_1 + 2\nu_2 + 4\nu_4$ for the first model and $\nu_{real} = \nu_1 + 2\nu_2 + 4\nu_4 + 8\nu_8$ for the second model (the average is over trial values of $p(t)$). While for both models the average total prestin density per diffraction limited area is similar ($\nu_{real} \sim 1.5$) and the relative fractions of each oligomeric species are robust to variations in $p(t)$, the implied prestin density in the model including an 8-mer population had far less sensitivity to $p(t)$ than did the first model (see Fig. 3.24) for the range of $p(t)$ values tolerated by each model (roughly, $p(t)$ could range from $0.8 - 1.0$). Nevertheless for both models the implied total expression densities of prestin-citrine seem low (the highest implied density was ~ 3.3 prestin per diffraction limited area or $12 \frac{1}{\mu m^2}$) compared to what would be expected from an over-expression system using a CMV promoter as we

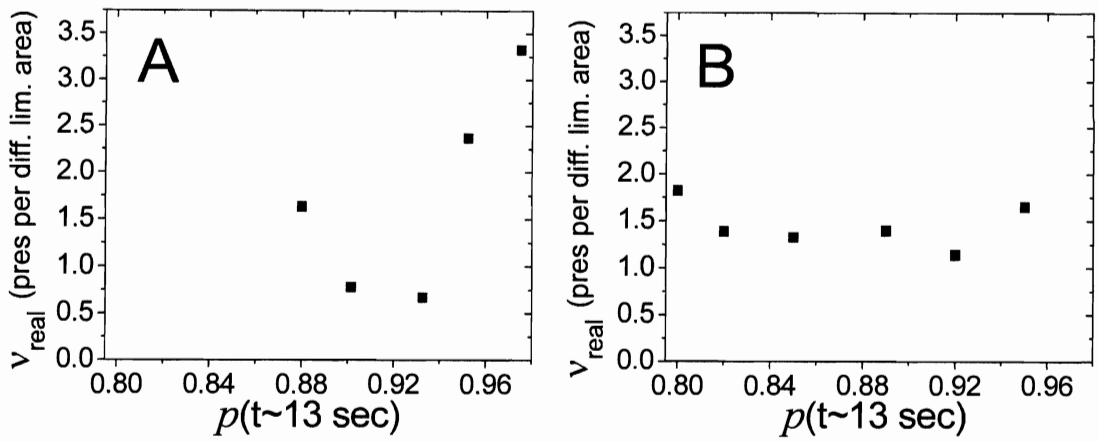

Figure 3.24 : Sensitivity of expression density per diffraction limited area ν_{real} to "on" probability for models of prestin oligomeric content. (A) Monomer/dimer/tetramer model. (B) Monomer/dimer/tetramer/8-mer model.

have here (at least $\sim 50-100\,\frac{1}{\mu m^2}$, see Refs. [Knowles et al., 2010] and [Brameshuber et al., 2010]). Furthermore, the range of "on" probabilities that allowed reasonable agreement with the data were unreasonably high in relation to an estimate stemming from a consideration of the known photophysics (estimate comes from assuming "on" probability is $p = \frac{\tau_{on}}{\tau_{on}+\tau_{off}}$ where $\tau_{on} = 1066\,ms$ is estimated from our experiments as discussed above, and $\tau_{off} \sim 1-1.7s$ is assumed to be what was measured for GFP in published studies [Dickson et al., 1997, Garcia-Parajo et al., 2000, Moerner et al., 1999]). The low estimates of total prestin expression might be explained by the fact that much of the background fluorescence is due to in focus spots that are not detected due to overlapping point spread functions. However, at the moment the high model-derived estimates of "on" probability are difficult to reconcile even with estimates biased toward high probability.

While the values of $p(t) \geq 0.8$ are difficult to reconcile with the photophysics of the

fluorescent proteins, the high values we obtain are almost exactly consistent with values derived in other studies that measure the stoichiometry of various EGFP tagged receptors using a complementary method of counting GFP photobleaching steps. One study microinjected NMDA-EGFP fusion protein mRNA into oocytes and used the photobleaching step method to determine subunit stoichiometry [Ulbrich and Isacoff, 2007]. They estimated a probability of 79.5% for EGFP to be fluorescent by fitting the distribution of observed stoichiometries to a probability model analogous to the one we have here. Nakajo et al. estimated a probability of $p(t)=64-70\%$ for GFP tagged KCNQ1 ion channel complexes with a tetrameric stoichiometry [Nakajo et al., 2010]. A dimeric subunit stoichiometry for the EGFP tagged Hv1 voltage gated proton channel was determined by Tombola et al., and a fluorescent probability of 80% was deduced. Finally, the technique was used to show that the TRPP2/PKD1 complex is composed of three TRPP2 and one PKD1 domains, and an "on" probability of 83% was calculated - again in close agreement with the value determined in this study. Given the near ubiquitous reporting of an "on" probability of $\sim 80\%$ for EGFP, we tend to believe the resulting ratios of dimer and tetramer obtained in this study. However, this reflects the fact that we have a poor understanding of the factors (photophysical or otherwise) that determine $p(t)$.

A natural question arises upon reference to these published reports. Namely, why has the method of counting photobleaching steps not been employed in our study as was done in the reports cited above? While an additional analysis of prestin-citrine photobleaching steps could add information improving the likelihood of correctly assigning stoichiometries to fluorescent spots, the method would not be suitable as a replacement for brightness analysis in this study. Since the mean time until pho-

tobleaching of citrine is only about two frames long, there is a high occurrence of multiple bleaching events within one or two frames. This is particularly true of spots containing multiple fluorescent prestin-citrine molecules (see Fig. 3.25 B). In fact, Ulbrich and Isacoff specifically report difficulty in discriminating bleaching steps as a limiting factor for bleaching events corresponding to stoichiometries above 5, and they further suggest an analysis of brightness as a solution even though their average bleaching time ($\tau_{on} \sim 5s$ corresponding to 150 frames in their study) is significantly longer than in our study [Ulbrich and Isacoff, 2007]. Also clear is that citrine fluorescence traces are often non-ideal (i.e. showing random fluctuations in fluorescence) and blinking does not always occur in clearly defined digital steps making an analysis based on step-bleaching problematic. It is for these reasons that we chose the technique of analyzing the brightness of the signals. However, we did analyze bleaching steps in a few cases, three of which are displayed in Fig. 3.25. The traces make clear a number of important points. Firstly, the bleaching of the signals often *do* occur in a digital manner further supporting that we are indeed observing prestin-citrine fluorescence at the single molecule level (Figs. 3.25A and C). Secondly, the bleaching step size is consistent with the mean brightness of the measured single molecule distribution $\varrho_1(I)$ as should be the case if the distribution of brightness is reflective of single citrine copies. Furthermore, some of the signals (Fig. 3.25C) display the blinking behavior of the fluorescent proteins often cited as the signature of single molecules in SMF studies using GFP and its variants.

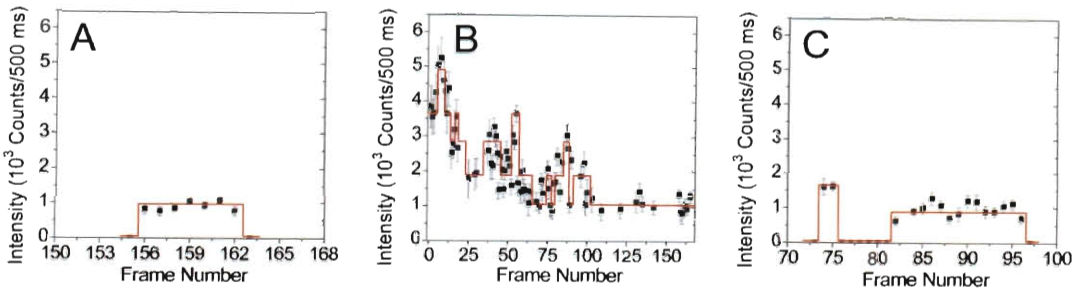

Figure 3.25 : Examples of bleaching steps for three observed signals. The fitted intensity of three separate spots are plotted versus frame number. The chosen spots were atypically long-lived. Error bars are the uncertainty determined from fitting. Red steps represent likely stoichiometric assignments and are not evenly spaced due to effects that cause a broadening of the brightness distribution. Integration time is $500\,ms$ and frame rate is $(531\,ms)^{-1}$ and excitation intensity is $45{-}50\,W/cm^2$. (A) One step bleach. Fluorescence abruptly disappears in a digital manner. (B) $\sim 5{-}6$ step bleach. For this signal, data points are missing from some frames either because the spot "blinked" or because the spot was not detected by the program. This was due either to poor signal to noise ratio for the spot in the given frame, or because another signal came in close proximity causing the program to fit the two signals as one. This spot displayed rapid fluctuations in fluorescence. (C) Example of "blinking". A signal digitally appears and goes into a dark state for period of $\sim 3\,sec$ before it regains fluorescence for $\sim 7.9\,sec$. All three time traces are plotted on the same vertical scale. The typical separation between bleach steps is in agreement with the mean of $\varrho_1(I)$ from Fig. 3.5 as expected.

Chapter 4

Diffusion of prestin using single particle tracking

4.1 Introduction

Mammalian hearing is intimately dependent on fast electro-mechanical coupling of transmembrane electric field to rapid length changes of the outer hair cells (OHC) of the inner ear [Ashmore, 1987, Brownell et al., 1985, Kachar et al., 1986]. This unique form of cellular motion, termed electromotility, has a distinct electrical signature in that voltage induced charge movement is coupled into the membrane [Santos-Sacchi, 1991]. Charge movement is measured electrophysiologically and is manifested as a bell shaped nonlinear capacitance (NLC) in the native OHC [Huang and Santos-Sacchi, 1993, Santos-Sacchi, 1991, Tunstall et al., 1995]. The transmembrane protein prestin, uniquely expressed in the OHC lateral wall, has been identified as the motor that drives electromotility [Zheng et al., 2000]. Measurement of NLC as a test of prestin function has become standard and is commonly characterized experimentally by measuring total charge movement and the voltage at peak capacitance V_{pkc}. Prestin is generally regarded to undergo a conformational change, coupling charge into the membrane, that exerts force on the OHC lateral wall [Oliver et al., 2001]. Mammalian cells exogenously expressing prestin gain NLC [Chambard and Ashmore, 2003, Deák et al., 2005, Iida et al., 2005] and have also been shown to exhibit voltage induced motion [Zheng et al., 2000] validating their use as a model system in place of the native OHC.

Numerous studies have demonstrated that an understanding of the interaction between prestin and the cell membrane is crucial to a full description of prestin function. Various manipulations to the plasma membrane environment have been shown to affect prestin function. For example, amphiphilic drugs which alter prestin function also alter membrane curvature and mechanical properties [Fang and Iwasa, 2007, Greeson and Raphael, 2009], and membrane substitution of lipids with differing acyl-chain lengths shift V_{pkc} due to changes in membrane thickness [Fang et al., 2010]. Anisotropic lipid diffusion has been measured in OHCs suggesting interactions of the OHC cytoskeleton with the membrane [de Monvel et al., 2006]. The OHC lateral wall, where prestin is functional, has lower membrane cholesterol levels than the basal or apical regions [Rajagopalan et al., 2007] where the motor is non-functional [Kalinec et al., 1992]. In both the OHC and in HEK cells, depletion of membrane cholesterol concentration shifts V_{pkc} in the depolarizing direction, and loading of membrane cholesterol causes hyperpolarizing shifts [Rajagopalan et al., 2007, Sturm et al., 2007]. Moreover, prestin confocal fluorescence images in transfected cells show punctate foci in the cell membrane [Organ and Raphael, 2007, Rajagopalan et al., 2007, Sturm et al., 2007]. Puncta reversibly disappear upon cholesterol depletion and reloading and co-localize with known lipid raft markers [Rajagopalan et al., 2007, Sturm et al., 2007]. Biochemical studies show the appearance of prestin in raft fractions of membrane lysate [Rajagopalan et al., 2007, Sturm et al., 2007] that decrease upon depletion of membrane cholesterol. Clearly, precise knowledge of prestin membrane organization in relation to domains dependent on cholesterol is important in order to understand these findings that together suggest an important role for cholesterol and microdomains in determining prestin function. Measurement of prestin diffusion in

the cell membrane could in principle allow a detailed map of interactions with such domains.

Early studies of prestin mobility were indirect electrophysiological measurements [Santos-Sacchi and Zhao, 2003, Takahashi and Santos-Sacchi, 2001]. Previous direct measurements of prestin diffusion employing fluorescence recovery after photobleaching (FRAP) suggested transient confinement of prestin as a possibility since immobile fractions remained after dual bleaches. However, since FRAP is an ensemble measurement, a detailed analysis of the size and character of the putative confinements was not possible, and other more complex modes of diffusion could not be ruled out [Organ and Raphael, 2007].

To study prestin diffusion at the finest level of detail requires the tracking of single prestin molecules. The use of single particle tracking (SPT) to study the diffusion of membrane proteins and lipids has become ubiquitous [Wieser and Schütz, 2008]. In recent years advancements have been made on correctly analyzing and interpreting the motion of molecules confined to membrane compartments [Ritchie et al., 2005, Wieser et al., 2007a, 2008]. In particular, the importance of the effects of detector averaging and time resolution on confined diffusion [Destainville and Salomé, 2006, Ritchie et al., 2005] and hop diffusion have been exposed, and methods for dealing with the effect have been published [Wieser et al., 2007a, 2008]. In this study we employ SPT of prestin, conjugated to a minimally invasive fluorescent tag, to measure prestin lateral mobility and explore cholesterol dependent changes to its diffusive behavior. We interpret our data using the analytical approximation to hop-diffusion developed by Wieser et al. and by a complementary statistical analysis of the full

distribution of squared displacements. We find that prestin undergoes hop-diffusion in relatively large confinements, and that its diffusive behavior is significantly affected by membrane cholesterol levels.

4.2 Materials and methods

4.2.1 Plasmid expression and cell culture

A plasmid encoding for prestin-SNAP-tag C-terminal fusion protein was created by PCR amplifying SNAP-tag from pSS26b plasmid (Covalys, now New England BioLabs, Ipswich, MA) using forward/reverse primers *5'-tttggtacccatggacaaagattgc-3'* and *5'-atatgcggccgcttatcccagacccggttta-3'*. Using restriction sites KpnI and NotI, we digested out the YFP gene fragment from a prestin-YFP plasmid (gerbil-prestin gene, accession number AF230376, previously sub-cloned [Greeson et al., 2006] into multiple cloning site of pEYFP-N1, Clontech, Mountain View, CA). SNAP-tag PCR fragments were finally ligated into digested prestin-YFP plasmid using the same restriction sites and then verified by sequencing.

HEK293 cells were grown in 6-well plates containing culture media consisting of phenol-red free DMEM supplemented with 10% BCS (Invitrogen, Carlsbad, CA), 1% penicillin-streptomycin, 14.3 mM HEPES, 16.1 mM $NaHCO_3$, and 4 mM L-glutamine at 37°C, 5% CO_2. Cells below passage 30 were transfected with prestin-SNAP-tag plasmid using Fugene 6 transfection reagent (Roche, Indianapolis, IN) according to manufacturer instructions. Cells were rinsed and aspirated with culture media 12-24 hours after transfection. Labeling solution containing 3μM SNAP-Cell TMR-Star substrate (derivative of benzyl-guanine (BG) conjugated to tetramethylrhodamine

(TMR))(New England BioLabs) in 400μL of culture media was added to cells in the 6-well dish and incubated at 37°C for 20 min to allow substrate to covalently bind to expressed prestin-SNAP-tag fusions. Cells were then rinsed once again in substrate-free culture media before being squirted off dish bottom and centrifuged in a 15 mL conical tube for three min per centrifugation. Natant media was aspirated from pelleted cells, and cells were resuspended and centrifuged twice more in culture media to remove excess fluorescent substrate. Cells were then incubated for 30 min in substrate-free media at 37°C and replaced with fresh media one more time to remove substrate that has leaked out of cells. Cells are then cultured on RCA cleaned [van Dam, 2005] #1.5 coverslips for 24 hours before imaging. For imaging, coverslips containing low density of adherent cells were first rinsed with HEPES buffered saline (HBS, contents in mM: dextrose 5.6, HEPES 21, KCl 5, NaCl 13.7, Na_2HPO_4 0.76, pH adjusted to 7.4, osmolarity 300 mOsm). Coverslips were finally mounted on a viewing chamber with vacuum grease and cells are bathed with HBS and mounted on microscope. In some cases, cells were given a 20 min treatment of 10 mM methyl$-\beta-$cyclodextrin (MβCD) in serum free media and washed prior to imaging in HBS. For control experiments, cells are fixed in 4% paraformaldehyde for 10 min before imaging.

4.2.2 Single molecule microscopy and trajectory calculation

Live HEK293 cells expressing prestin-SNAP-TMR (prestin-SNAP-tag labeled with BG-TMR) are imaged at room temperature on an inverted Zeiss Axiovert microscope using objective type total internal reflection (TIR) [Axelrod et al., 1984]. TMR fluorophores are excited using 10-11 mW of 514 nm light from an Ar^+ laser. Light is made circularly polarized with a $\lambda/4$ waveplate (Thorlabs, Newton, NJ) placed in

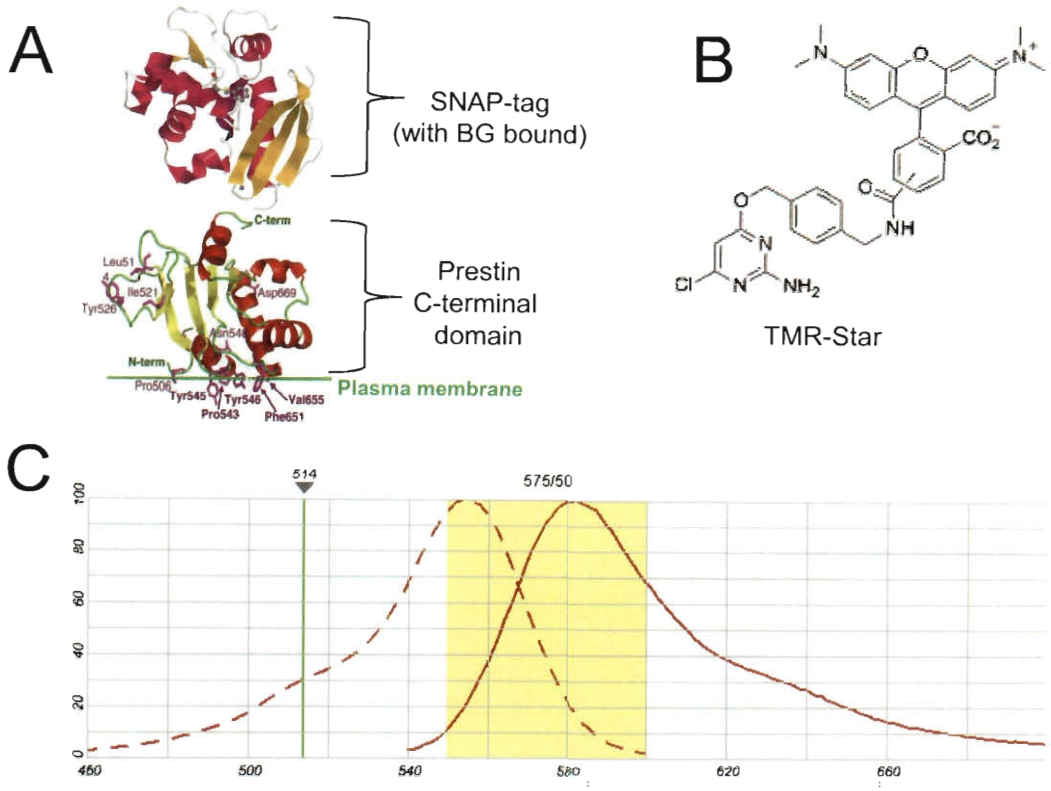

Figure 4.1 : Fluorescent labeling of prestin-SNAP-tag fusion protein. A) Cartoon of prestin-SNAP-tag fusion protein using crystal structures of each from Protein Data Bank. SNAP-tag is fused to C-terminus of prestin. SNAP-tag is based on mammalian O^6-alkylguanine-DNA-alkyltransferase (AGT) and can bind the substrate TMR-Star which is a derivative of benzylguanine (BG). When benzylguanine covalently binds AGT, a cysteine becomes benzylated releasing guanine. Shown fused to the C-terminal domain of prestin is human AGT with a benzyl group bound to it (grey ball and stick structure). AGT has a physical size of $\sim 2 \times 3.5 \times 4\,nm$ [Daniels et al., 2000]. B) Structure of TMR-Star which is benzylguanine conjugated to tetramethylrhodamine. C) Excitation (dashed curve, peak of $554\,nm$) and emission (solid curve, peak of $580\,nm$) spectrum of TMR-Star. Also shown as vertical green line is the excitation wavelength of $514\,nm$. The collection band ($550 - 600\,nm$) is shown highlighted.

the beam path at 45° to the polarization of the laser. Prior to placing laser in TIR configuration, we estimate the intensity to be $\sim$ 100 W/cm^2. Fluorescence is collected with a 100X, 1.45NA microscope objective and filtered in a band from 550-600 nm. Detection of TMR fluorescence, which appears as diffraction limited fluorescent spots, is captured on a force-air-cooled, back illuminated QuantEM EMCCD camera (Photometrics, Tucson, AZ) run with open source Micro-Manager plugin software to ImageJ. The experimental apparatus is depicted in Fig. 4.2. Prior to image acquisition sequence, a large fraction of prestin-SNAP-TMR molecules are bleached using the laser until the density of fluorescent molecules is low enough to preserve identification of fluorescent spots between frames. Image stacks 200 frames long are captured with a frame time Δt of 250.8 ms ($\sim$4 frames/s) and exposure time t_{ill} of 250 ms. Frame sizes are 256×256 pixels and, using a reticule to measure the magnification of the system, the height and width of each pixel is measured to correspond to 0.1569±0.0007 μm/pixel in the object plane.

Individual fluorescent spots in each frame are detected and analyzed using home-made analysis software in MATLAB (The MathWorks, Natick, MA). The position (x_o, y_o) (and uncertainty in position) of each spot in every frame is determined by fitting the spot intensity profile $\Psi(x, y)$ to Eq. 4.1

$$\Psi(x,y) = \frac{4I_o\, ln2}{\pi s^2} exp\left\{\frac{-4\, ln2}{s^2}\left[(x-x_o)^2 + (y-y_o)^2\right]\right\} + b \tag{4.1}$$

where I_o is the spot intensity, s is the full-width at half-maximum, and b is the background level. Trajectories are generated (Fig. 4.3) using a combination of software, which allows for correlation of spots between images, and correlation by

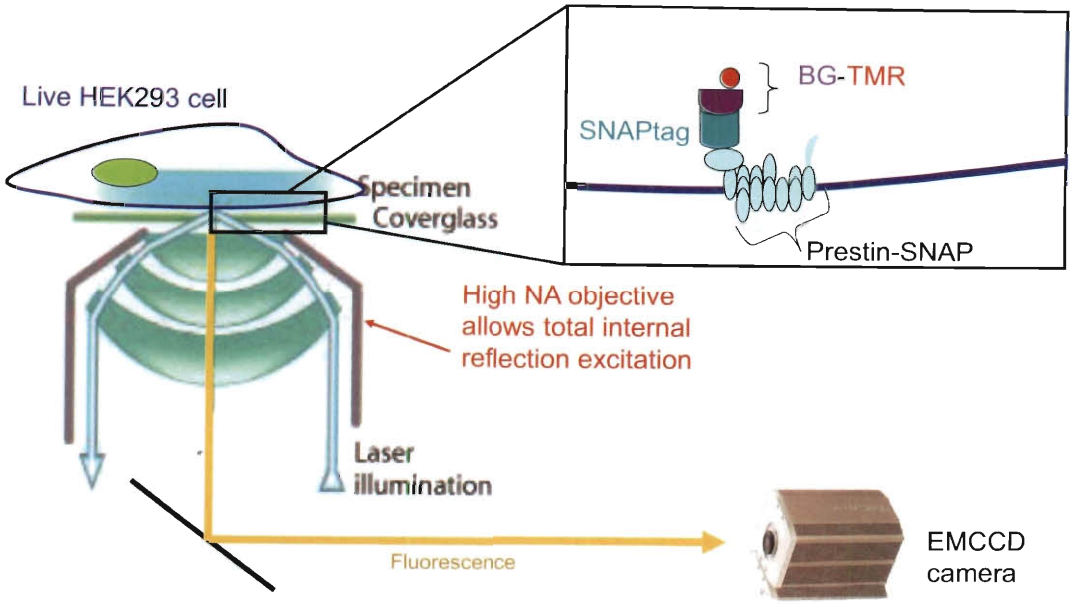

Figure 4.2 : Experimental setup for single particle tracking of prestin. Live HEK293 cells transfected with prestin-SNAP-tag fusion proteins are labeled with benzylguanine (BG) which is conjugated to tetramethylrhodamine (TMR). Cells are excited using objective type total internal reflection configuration which is possible due to the high NA objective (NA=1.45, 10x, α-PLAN-FLUAR, Zeiss) and allows for greatly improved signal to noise ratio compared to epi-illumination. Fluorescence from TMR is collected using the same objective onto the QuantEM EMCCD camera. The fluorescence appears as diffraction limited signals, and the spatial coordinates of the signals are determined by fitting them to a 2D Gaussian just like in Ch. 3. Image of objective adapted from: http://www.nikon.com/products/instruments/lineup/bioscience/biological-microscopes/application/tirf2/index.htm

hand. For each trajectory, the squared deviation $d^2(t_{lag})$ is calculated at every time $t_{lag} = (n-1)\,\Delta t$ (where n is the frame number, $n = 1$ referring to the first observation of the particle) according to

$$d^2(t_{lag}) = [x_o(t_{lag}) - x_o(0)]^2 + [y_o(t_{lag}) - y_o(0)]^2 \tag{4.2}$$

where $x_o(t_{lag})$ and $y_o(t_{lag})$ are the x and y coordinates of the particle at time t_{lag}, and $x_o(0)$ and $y_o(0)$ are the coordinates of the first observation of the particle. The mean-squared deviation $MSD(t_{lag})$ at time t_{lag} is calculated as an average of all the tracks according to

$$MSD(t_{lag}) = \left(\frac{1}{N_T(t_{lag})}\right) \sum_{i=1}^{N_T(t_{lag})} d_i^2(t_{lag}), \tag{4.3}$$

where the subscript i has been added to run over all $N_T(t_{lag})$ trajectories. The mean-squared deviation data is corrected for finite position accuracy σ_{xy} by subtracting from the *MSD* an offset Δ that the non-zero position uncertainty produces Martin et al. [2002] (see Fig. A.1 in Appendix A). Both σ_{xy} and Δ are determined by measuring the position of immobile prestin-SNAP-TMR molecules in fixed cells and using Eqs. 4.2 and 4.3 to calculate Δ, and ascribing the standard deviation in position to σ_{xy} (see Results).

4.2.3 Analysis of mean squared deviation

To describe the measured $MSD(t_{lag})$, we use the analytical hop-diffusion model developed by Wieser et al. [Wieser et al., 2007a]. They extend the exact calculation [Powles et al., 1992] of *MSD* for a particle totally confined to a domain or corral of size L to an array of partially permeable domains using an analytical approximation.

They find for the *MSD*

$$MSD_{hop}(t_{lag}) = \alpha \left\{ \frac{\alpha L^2}{3} - \frac{32\alpha L^2}{\pi^4} \sum_{k=1(odd)}^{\infty} \frac{1}{k^4} exp \left[- \left(\frac{k\pi}{L} \right)^2 \frac{D_{micro}}{\alpha} t_{lag} \right] \right\} + 4D_{macro}\, t_{lag}, \tag{4.4}$$

where D_{micro} is the microscopic diffusion constant the particle would have in the absence of confinement. D_{macro} $(= (1-\alpha)D_{micro} = \frac{1}{\hat{\tau}} D_{micro})$ is the macroscopic diffusion constant the particle appears to have over long observation times and describes the hopping between corrals, and α is the probability that the particle remains confined, which sets the macroscopic diffusion, and is related to the confinement strength $\hat{\tau} = D_{micro}/D_{macro}$ within the domains by $\hat{\tau} = \frac{1}{1-\alpha}$ (by definition, $\hat{\tau} \geq 1$ with $\hat{\tau} \to \infty/1$ signifying totally impermeable/permeable barriers). Eq. 4.4 is corrected [Wieser et al., 2007a] for the effects of detector time averaging [Destainville and Salomé, 2006, Goulian and Simon, 2000, Ritchie et al., 2005] over the finite exposure time t_{ill} to

$$MSD_{hop}(t_{lag}) = \alpha \left\{ \frac{\alpha L^2}{3} - \frac{32\alpha L^2}{\pi^4} \sum_{k=1(odd)}^{\infty} \frac{1}{k^4} exp \left[- \left(\frac{k\pi}{L} \right)^2 \frac{D_{micro}}{\alpha} t_{lag} \right] \right\} \times \frac{1}{1 + \frac{4D_{micro}t_{ill}}{L^2}} + 4D_{macro}(t_{lag} - \frac{1}{3}t_{ill}). \tag{4.5}$$

For fitting $MSD(t_{lag})$ data with the hop-diffusion model, we carried the summation in Eq. 4.5 out to 6 terms to define our fitting function $MSD_{fit}(t_{lag})$. We found estimates of the 3 fit parameters D_{micro}, L, and α by minimizing

$$\chi^2 = \sum_{t_{lag}} \left[\frac{1}{\sigma_{MSD}(t_{lag})} \Big(MSD(t_{lag}) - MSD_{fit}(t_{lag}) \Big) \right]^2, \tag{4.6}$$

where weighting factor $\sigma^2_{MSD}(t_{lag})$ is the variance of MSD at each t_{lag}, using least-squares fitting [Bevington, 1992] by the Levenberg-Marquardt method in Origin (Northampton, MA). Error in each fit parameter is the one-σ confidence interval determined by finding the range in that parameter, around the best fit value, that produces $\Delta\chi^2 = 1$ while allowing the other two parameters to vary. The confinement offset CO_{corr}, corrected for effects of detector averaging, is calculated from the fit parameters α and L according to $CO_{corr} = \alpha^2 L^2/3$ [Wieser et al., 2007a]. Error in CO_{corr}, using Gaussian error propagation [Bevington, 1992], is $\sigma_{CO_{corr}} = \frac{2}{3}\alpha L \left(L^2\sigma_\alpha^2 + \alpha^2\sigma_L^2\right)^{1/2}$ where σ_α and σ_L are the respective one-σ errors in α and L. Error in the confinement strength $\hat{\tau}$ is $\sigma_{\hat{\tau}} = \left(\frac{1}{1-\alpha}\right)^2 \sigma_\alpha$. Error in D_{macro} is $\sigma_{D_{macro}} = \left((1-\alpha)^2\sigma^2_{D_{micro}} + D^2_{micro}\sigma^2_\alpha\right)^{1/2}$.

4.2.4 Analysis of step-size distribution

The calculation of the squared step-size probability density distribution $p(\Delta r^2, t_{lag})$ was achieved by binning all measured individual squared-displacements Δr^2 for all trajectories combined, and normalizing the result to the total number of observed step-displacements. The cumulative distribution function (CDF) $P(\Delta r^2, t_{lag})$ was generated by cumulatively summing the $p(\Delta r^2, t_{lag})$ histogram [Schütz et al., 1997],

$$P(\Delta r^2, t_{lag}) = \int_0^{\Delta r^2} d\Delta r'^2 \, p(\Delta r'^2, t_{lag}). \tag{4.7}$$

Experimentally measured CDF was fit to a function describing one diffusive component

$$P(\Delta r^2, t_{lag}) = 1 - \varepsilon \, exp\left(\frac{-\Delta r^2}{r_o^2}\right) - (1-\varepsilon)\left(1 - F(\Delta r^2)\right), \tag{4.8}$$

with two free parameters r_o^2 and ε. The function $F(\Delta r^2)$ represents the CDF of apparent displacements measured for immobilized particles in fixed cells (see Results), and ε is the fraction of the diffusive component with characteristic squared diffusion length r_o^2. Detector time averaging effects [Goulian and Simon, 2000] and effects of positional uncertainty [Martin et al., 2002] are taken into account for r_o^2 by assuming $r_o^2 \approx 4D\,t_{lag} + \Delta - (4/3)D\,t_{ill}$.

4.3 Results

4.3.1 Characterization of position accuracy effects

Since a finite positional accuracy will introduce systematic errors into the measurement of *MSD* [Wieser et al., 2007a], it is important to characterize and understand the effects those errors produce. We therefore estimated the position error σ_{xy} by measuring the standard deviation in x-position σ_x of immobilized prestin-SNAP-TMR molecules over many frames. For each observed particle i, we also measure the apparent $d_i^2(t_{lag})$ which is a measure of the offset Δ_i the error σ_x produces. Shown in Fig. A.1A is Δ_i versus σ_x confirming the relationship $\Delta = 4\,\sigma_{xy}^2$ (see Appendix A). We measure the overall offset Δ that should be subtracted from the diffusion data by calculating the apparent *MSD* of the immobile particles in fixed cells using Eq. 4.3. The result is shown in Fig. A.1B giving $\Delta = 1.91 \pm 0.08 \times 10^{-3}\,\mu m^2$. Because the position uncertainty is dependent on the brightness [Thompson et al., 2002] of the particles, which varies between fluorescent spots, we measure a spread of uncertainties (Fig. A.1C). This effect is automatically taken into account in the measurement of Δ in Fig. A.1B since it is measured from an ensemble of particles that have a brightness distribution representative of that in live cell experiments.

4.3.2 Single particle tracking of prestin

We measured trajectories of prestin-SNAP-tag labeled with TMR-conjugated BG substrate which has the advantages of both preventing crosslinking of prestin due to one-to-one binding stoichiometry of BG to SNAP-tag, and long observation times due to photostability of TMR. Shown in Fig. 4.3 are sample prestin-SNAP-TMR trajectories (in untreated cells) that are relatively long, ranging from $\sim$ 8-48 s or $\sim$ 30-190 observed time steps, compared to the average trajectory length of around 9 s. The trajectories display what appear to be sub-regions of confinement varying in apparent size. Locations of the confinement zones in some of the examples appear to hop in position, and in others it appears to diffuse in a single localized region.

Since many tracks are too short to clearly observe the confinement of motion in a single trajectory [Suzuki et al., 2005], we calculated the *MSD* of all recorded tracks for each of two groups using Eq. 4.3. We first analyzed prestin motion in untreated cells depicted in Figs. 4.4A (solid circles) and 4.4B. The rise of $MSD(t_{lag})$ is clearly observed to change to a drastically shallower slope as t_{lag} increases consistent with confined diffusion. We also measured *MSD* of prestin in cells treated with 10 mM MβCD (Figs. 4.4A and C, open circles) which removes significant concentration ($\sim$60%) of cholesterol from the HEK cell plasma membrane [Sfondouris et al., 2008]. In this case we also see a decrease in slope of $MSD(t_{lag})$ at long t_{lag}, however the change in slope is more gradual. To obtain quantitative estimates of quantities relating to hop-diffusion, we performed fits (shown in Figs. 4.4A-C, red curves) of $MSD(t_{lag})$ for untreated and MβCD treated groups to the hop-diffusion model using Eq. 4.5 [Wieser et al., 2007a] described in Methods. Due to large variance in $MSD(t_{lag})$ at long t_{lag}, we restricted our analysis to $t_{lag} \leq 30$ s.

From the fit to the control group, we conclude that the average microscopic diffusion constant of prestin within confinement zones in the HEK plasma membrane is $D_{micro} = 0.0481^{+0.0029}_{-0.0027}\,\mu m^2/s$. We obtained fitted values for L and α of $1.215^{+0.057}_{-0.054}\,\mu m$ and $0.908^{+0.018}_{-0.016}$ respectively. Using the fitted values and uncertainties of L and α, we calculate the corrected confinement offset—the offset that is produced *only* by diffusion within (and hopping between) domains—to be $CO_{corr} = 0.406 \pm 0.041\,\mu m^2$. Instead of quoting the fitted value of L as our estimate for the average domain size, we make a more conservative estimate by calculating the full range in L implied by letting α and CO_{corr} vary by their maximum uncertainty ranges; this gives L in the interval $(1.13, 1.30)\,\mu m$. The value obtained for α implies the confinement strength is $\hat{\tau} = 11 \pm 2$ indicating strong confinement consistent with the nearly flat slope of $MSD(t_{lag} \to \infty)$ at large time lags (Fig. 4.4B).

Results from fitting the MβCD treated group indicate that, within the fitting error, the microscopic diffusion constant ($D_{micro} = 0.0499 \pm 0.0018\,\mu m^2/s$) is unchanged by depletion of membrane cholesterol. However, we found that the average domain size L is increased to be in a range $(1.85, 2.48)\,\mu m$. In addition, the MβCD treated group shows a marked decrease in the confinement strength (concomitantly a decrease in α) to $\hat{\tau} = 2.9 \pm 0.3$. This is reflected in the higher slope of $MSD(t_{lag} \to \infty)$ displayed in Fig. 4.4B.

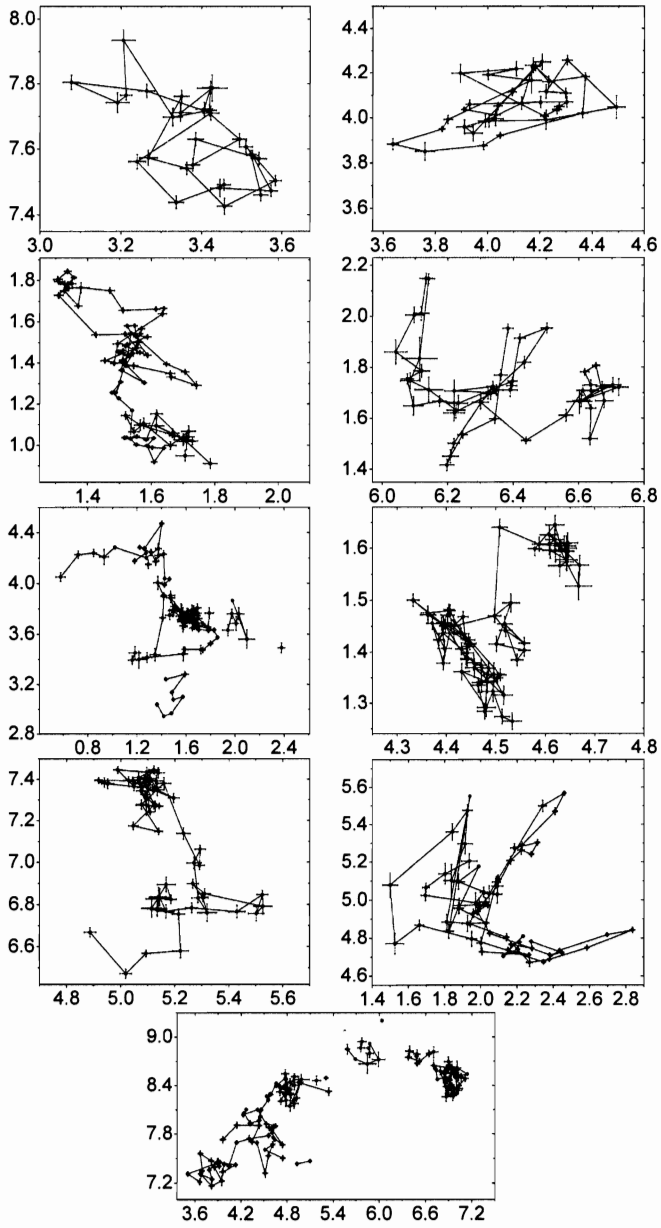

Figure 4.3 : Sample trajectories of BG-TMR labeled prestin-SNAP-tag molecules in untreated HEK cells. Coordinate axes are position in μm. Frame time is 250.8 ms for all trajectories. Error bars in position are fitting errors from Gaussian fits (Eq. 4.1) to spot intensity profiles. Displayed sample trajectories were chosen for presentation based on longer than average diffusion times before bleaching.

4.3.3 Cumulative distribution function of squared step-size

To explore prestin diffusion in greater detail requires full statistical knowledge of the step-size distribution. We therefore measured the probability density of squared step-size $p(\Delta r^2, t_{lag})$ at 250.8 ms, the shortest time lag measured, for both untreated and MβCD treated groups (Figs 4.5A and B insets). We also measured the cumulative distribution function (CDF) of squared step-size $P(\Delta r^2, t_{lag})$ (Figs. 4.5A-C) which gives the probability that after time t_{lag}, the particle will still be found within a squared-radius Δr^2 from where it started [Schütz et al., 1997]. For pure Brownian motion, the expectation is that $P(\Delta r^2) = 1 - exp(-\Delta r^2/r_o^2)$ where r_o^2 is the characteristic diffusive step. We initially reasoned that for a time step of 250.8 ms, the distribution should be approximately that of Brownian motion since on that timescale the average step-size would be $\approx (4D_{micro}t_{lag})^{1/2} = 220\,nm$ which is less than the average domain size [Wieser et al., 2008] obtained from *MSD* analysis for both treatment groups. However, we found that fits to a simple Brownian model significantly deviated from both untreated and MβCD CDFs (fits not shown). A look at the probability density distribution $p(\Delta r^2)$ for both groups reveals that the probability for short displacements rises quicker than an exponential rise explaining the poor fits (Figs. 4.5A and B).

We next explored possible effects that could cause deviations from a pure exponential. First we considered that if there is a broad distribution of domain sizes L, confined displacements within the smallest domains would appear immobile [Destainville and Salomé, 2006, Ritchie et al., 2005, Wieser et al., 2007a, 2008]. In particular, displacements within impermeable domains of an actual size $\ll \sim 95\,nm$ would appear to be less than $22\,nm$, below the position resolution, and hence indistinguishable

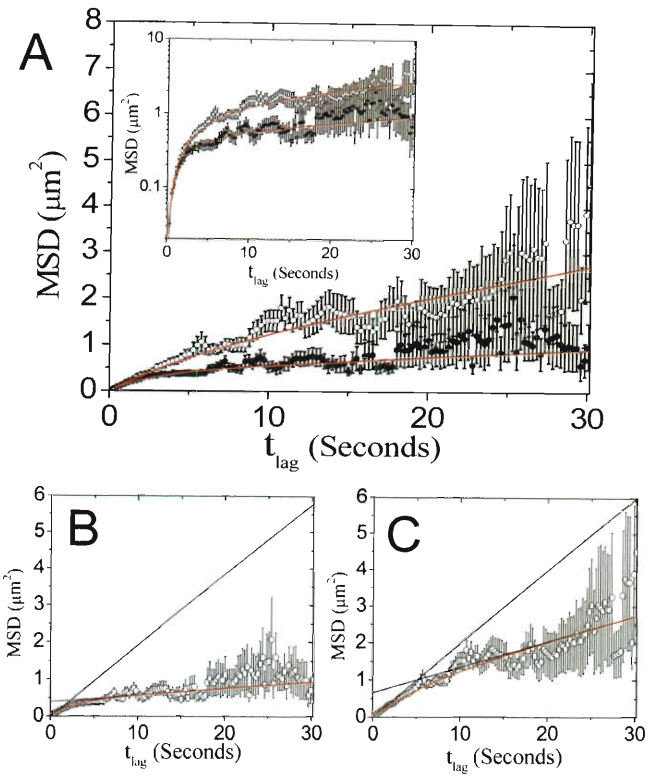

Figure 4.4 : Mean-squared deviation versus time for prestin-SNAP-TMR. (A) Measured *MSD* against t_{lag} in untreated (solid circles) and cholesterol depleted (open circles) cells. A total of 285 tracks were recorded for untreated cells, and 269 tracks were recorded for cells treated with 10 mM MβCD. Error bars are standard error of the mean. Increased variance at long t_{lag} result from decreased probability of observing long trajectories due to photobleaching of TMR. Both data sets are fit to hop-diffusion model (Eq. 4.5, solid curve). Inset: data is shown on a log scale to emphasize fit to early points. Resulting fitting parameters are: (for untreated cells) $\alpha = 0.908^{+0.018}_{-0.016}$, $L = 1.215^{+0.057}_{-0.054}\,\mu m$, and $D_{micro} = 0.0481^{+0.0029}_{-0.0027}\,\mu m^2/s$ with $\chi^2_\nu = 0.6$; (for cells treated with MβCD) $\alpha = 0.659^{+0.039}_{-0.039}$, $L = 2.15^{+0.14}_{-0.14}\,\mu m$, and $D_{micro} = 0.0499^{+0.0018}_{-0.0018}\,\mu m^2/s$ with $\chi^2_\nu = 0.67$. Asymptotic behavior (black curves) of MSD_{hop} for (B) untreated and (C) MβCD treated groups is shown superimposed on data and fit (red curves). According to hop-diffusion model, including averaging effects, $MSD_{hop}(t_{lag} \to 0) = 4D_{micro}(t_{lag} - \frac{1}{3}t_{ill})$ and $MSD_{hop}(t_{lag} \to \infty) = CO + 4D_{macro}\,t_{lag}$ where $CO = \frac{L^2\alpha^2}{3}(1 + \frac{4D_{micro}t_{ill}}{L^2})^{-1} - \frac{4}{3}(1-\alpha)D_{micro}t_{ill}$ is a confinement offset seen as the y-intercept in (B) and (C) [Wieser et al., 2007a]. Macroscopic diffusion constants D_{macro} are (B) $4.4 \pm 0.9 \times 10^{-3}\,\mu m^2/s$ and (C) $0.017 \pm 0.002\,\mu m^2/s$.

from immobile. We therefore characterized the apparent squared step-size distribution $f(\Delta r^2)$ for the immobile particle measurements and from it determined the CDF $F(\Delta r^2) = \int_0^{\Delta r^2} d\Delta r'^2 \, f(\Delta r'^2)$ (Fig. A.3). For a constant positional uncertainty σ_{xy}, $f(\Delta r^2)$ should be a monoexponential $f(\Delta r^2) \sim e^{-\Delta r^2/4\sigma_{xy}^2}$ which would give $F(\Delta r^2) = 1 - e^{-\Delta r^2/4\sigma_{xy}^2}$ (checked by simulation). However, not surprisingly, the experimentally measured $f(\Delta r^2)$ and $F(\Delta r^2)$ in Fig. A.3 do not fit to a monoexponential since, as demonstrated in Fig. A.1C, there is a distribution $g(\sigma_{xy})$ of standard deviations with spread $\sigma_{\sigma_{xy}}$ about the average $\bar{\sigma}_{xy}$ which we approximate by $g(\sigma_{xy}) \sim e^{-(\sigma_{xy}-\bar{\sigma}_{xy})^2/2\sigma_{\sigma_{xy}}^2}$. This will have the effect of smearing the exponential distribution in the following fashion:

$$f_{smear}(\Delta r^2) \sim \int_0^\infty d\sigma_{xy} f(\Delta r^2) g(\sigma_{xy}) \sim \int_0^\infty d\sigma_{xy} \, e^{-(\sigma_{xy}-\bar{\sigma}_{xy})^2/2\sigma_{\sigma_{xy}}^2} \, e^{-\Delta r^2/4\sigma_{xy}^2}. \quad (4.9)$$

To calculate this integral, we simulated $f_{smear}(\Delta r^2)$ numerically (Fig. A.2) with the measured parameters $\sigma_{\sigma_{xy}}$ and $\bar{\sigma}_{xy}$ and integrated to obtain $F(\Delta r^2)$. The result of the simulation is in excellent agreement with the measured CDF (Fig. A.3).

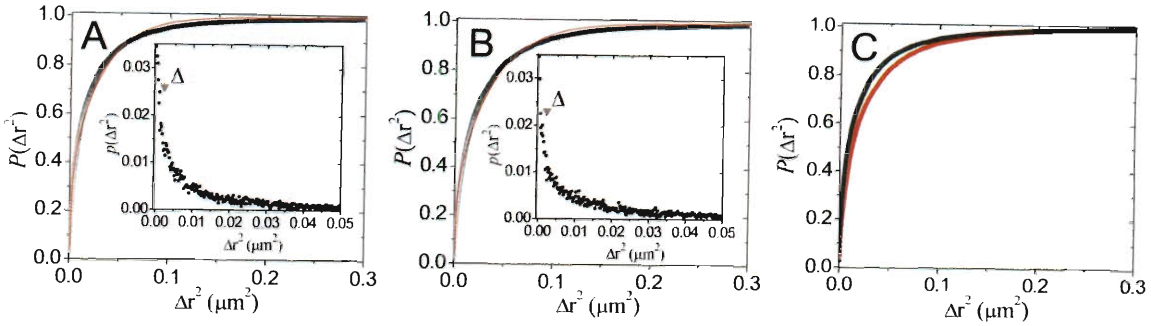

Figure 4.5 : Statistical distributions of squared step-size. CDF of (A) untreated (black circles appear like a thick line due to high density of points) and (B) MβCD treated groups. Fits of CDF using Eq. 4.8 are shown as red lines in (A) and (B). Insets show the original probability density (black circles) on a zoomed in scale; the position of the localization offset Δ is shown with gray arrows. (C) CDF of untreated (black circles) and MβCD (red circles) groups are re-plotted on the same graph for comparison.

Using Eq. 4.8 to fit the CDF of squared displacements with the inclusion of $F(\Delta r^2)$, accounting for the apparent immobility of displacements within small corrals, improved the fits considerably (Figs. 4.5A and B) although some slight deviations are still apparent. For the untreated group, the fitting gave $D = 0.0401\,\mu m^2/s$ and $\varepsilon = 0.6222$, and for MβCD we obtained $D = 0.0477\mu m^2/s$ and $\varepsilon = 0.684$. Apparently, according to our argument, depletion of membrane cholesterol decreases the apparent fraction $(1 - \varepsilon)$ of molecules confined to domains with size $\ll \sim$95 nm from 37.8 to 31.6% (an absolute difference of 6.2%) at a time lag of 250.8 ms consistent with a shift to larger domain sizes. The diffusion constant for the MβCD group is in reasonable agreement with that obtained from *MSD* analysis, however for the untreated group the diffusion constant is 17% lower.

We next considered that for long exposure times (as we have here) the CDFs

should not fit to an exponential due to detector averaging effects even for a constant domain size L. As reported in Wieser et al. [Wieser et al., 2008], the probability for apparent small displacements is enhanced for exposure times that are not short compared to t_{lag} (as observed in Figs. 4.5A and B, insets) since positional averaging biases the trajectory to the center of the domain causing a steeper increase of the CDF as shown in Fig. 4.5C. If, as we had originally assumed, there was a narrow domain size distribution peaked around the averages determined from *MSD* analysis ($\sim 1{-}2\,\mu m$), the effect would be minimal since $t_{ill} = 250\,\text{ms}$ is much less than the microscopic residence time [Destainville and Salomé, 2006] $\tau_{micro} = L^2/4D_{micro}$ which is 8 s for the untreated group and 23 s for MβCD treated group. However, since we have a range of domain sizes that extends toward small domains, as evidenced by both the large values of $(1-\varepsilon)$ and the observation in Fig. 4.3 of confinement regions of varying size, the effects of averaging time on the distribution of squared-displacements should enhance the probability for small displacements occurring within domains even somewhat larger than 95 nm (see Fig. 4.6A). To compare the relative effect on each treatment group, we subtracted the probability density distributions which is shown in Fig. 4.6B. We observe a peak in the difference distribution $\delta p(\Delta r^2) = p_{untreated}(\Delta r^2) - p_{M\beta CD}(\Delta r^2)$ out to Δr^2 of $\sim$0.01–0.02 μm^2 beyond which the difference is nearly flat. The sum of the probabilities out to Δr^2 of 0.02 μm^2 is $7 \pm 1\%$ in agreement with the difference of $(1-\varepsilon)$ between groups.

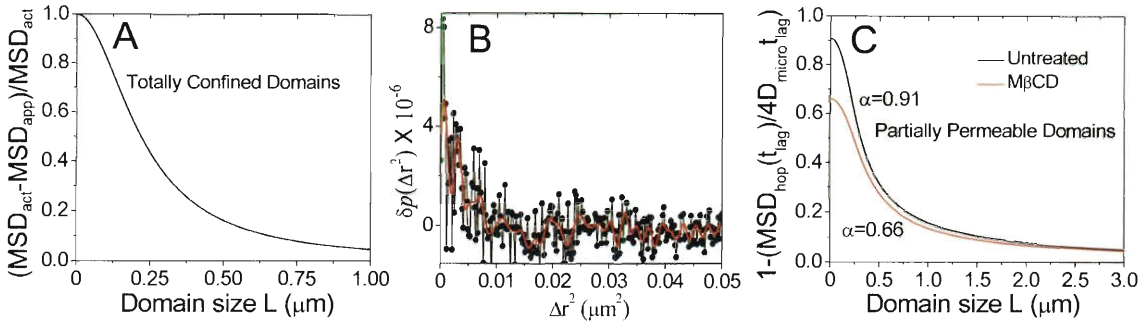

Figure 4.6 : Effect of positional averaging, L, and $\hat{\tau}$ on step-size distribution. (A) Plot of the error in $MSD(t_{lag} = 250.8ms)$ positional averaging over 250 ms would produce as a function of L for impermeable domains ($D_{micro} = 0.048\,\mu m^2/s$). (B) Difference of untreated and MβCD treated probability density distributions ($\delta p(\Delta r^2) = p_{untreated}(\Delta r^2) - p_{M\beta CD}(\Delta r^2)$, solid circles). Also shown is $\delta p(\Delta r^2)$ low-pass filtered at $500\frac{1}{\mu m^2}$ (red curve). Sum of probabilities out to $\Delta r^2 = 0.02\,\mu m^2$ is $7 \pm 1\%$. (C) Plot of $1 - \frac{MSD_{hop}(t_{lag}=250.8\,ms)}{4D_{micro}\times 250.8\,ms}$ in partially permeable domains as a function of L, using α and D_{micro} obtained from fitting $MSD(t_{lag})$, for untreated and MβCD groups. Here $MSD_{hop}(t_{lag})$ is Eq. 4.4.

Since detector averaging has a noticeable effect on the CDFs at a time lag of 250.8 ms, where t_{lag} is nearly equal to the exposure time $t_{ill} = 250$ ms, we remeasured $P(\Delta r^2)$ at a longer t_{lag} of 1.254 s (Fig. 4.7A and B) where detector averaging would only have a 7% effect on $4D_{micro}t_{lag}$ for Brownian diffusion. Furthermore, at $t_{lag} =$ 1.254 s the time lag is still below $L^2/4D_{micro}$ implied by the average domain size for both groups. Fitting both groups again to Eq. 4.8, we found that the CDF of the untreated group still showed deviations from a monoexponential (CDF rises quicker than the mono-exponential fit, Fig. 4.7A). However, the diffusive portion of the MβCD treated group fit perfectly to a monoexponential (Fig. 4.7B), and the variance of the MβCD data from the fit is over a factor of 10 better than for the untreated fit.

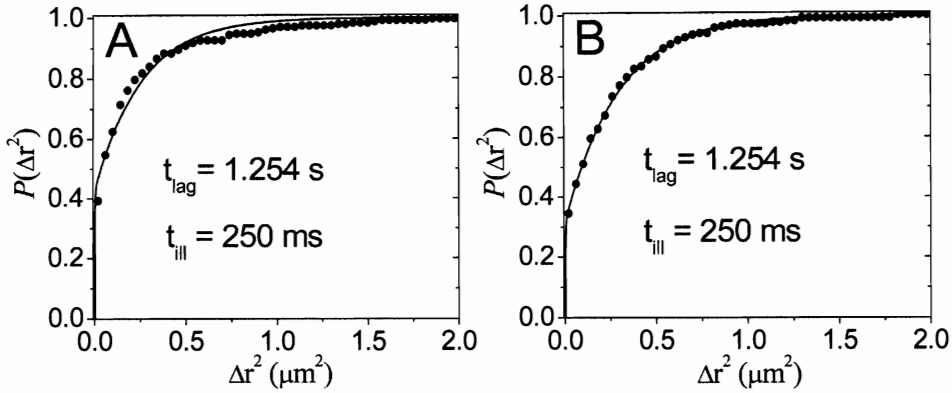

Figure 4.7 : CDF of squared step-size at increased time lag. For both groups, only displacements used to calculate $MSD(t_{lag}=1.254\,s)$ are included. Bin size is $\delta r^2 = 0.04\,\mu m^2$. CDF is shown as solid circles and fit to Eq. 4.8 is shown as black curve. (A) Fit to untreated group gives $r_o^2 - \Delta = 0.250\,\mu m^2$ and $\varepsilon = 0.575$. (B) Fit to MβCD treated group gives $r_o^2 - \Delta = 0.288\,\mu m^2$ and $\varepsilon = 0.685$. Since the diffusive portion of the MβCD group fits perfectly to a single freely diffusive component, it is appropriate to obtain the diffusion constant. We obtain $D = 0.0615\,\mu m^2/s$. The variance of the fit to the MβCD treated group ($S^2 = 2.67 \times 10^{-3}$) is over a factor of 10 smaller than the variance the fit to the untreated group ($S^2 = 2.76 \times 10^{-2}$).

4.4 Discussion

A vast array of studies have demonstrated that the membrane environment cannot be ignored in obtaining a full understanding of prestin function. Various alterations of the native membrane environment influence measurements that characterize prestin function such as motility, charge movement, and V_{pkc}. Biochemical evidence and optical microscopy [Organ and Raphael, 2007, Rajagopalan et al., 2007, 2010, Sturm et al., 2007] strongly suggest that prestin localizes in cholesterol rich, membrane microdomains. Sfondouris et al. [Sfondouris et al., 2008] have shown a linear relationship between membrane cholesterol concentration and both V_{pkc} and prestin associated charge movement in HEK cells. Taken together, these lines of evidence motivate measurement of prestin diffusion to characterize the organization of prestin

in the plasma membrane and its possible interaction with membrane compartments. Previous bulk measurements of prestin diffusion were performed in our lab using FRAP [Organ and Raphael, 2007], however they were unable to definitively identify the existence of membrane confinements or estimate their size since FRAP is an ensemble measurement. In this study, we have characterized the effect of membrane cholesterol on prestin diffusion using SPT to achieve fine resolution on its lateral mobility and organization in the model HEK cell membrane.

We first analyzed the *MSD* of prestin and obtained estimates of domain size, confinement strength, and microscopic diffusion constant for untreated and MβCD treated groups. We measure a relatively small diffusion constant even for D_{micro} compared to a majority of other proteins studied using SPT which typically report diffusion constants on the order of 0.1-1 $\mu m^2/s$ (see for example [Suzuki et al., 2005, Umemura et al., 2008, Wieser et al., 2007a]). However, our low measured value for D is consistent with previous slow estimates using FRAP [Organ and Raphael, 2007] (also unpublished work, [Organ, 2008]). For prestin, slow diffusion has offered us a unique opportunity to measure the full time course of *MSD* describing hop-diffusion thereby enabling precise determination of D_{micro} using a modest time resolution. Our ability to measure the initial rising phase of *MSD* also enabled us to confidently discriminate hop-diffusion from free diffusion. Our observation directly confirms the suspicion in Organ and Raphael [Organ and Raphael, 2007] that prestin undergoes transiently confined diffusion in the HEK cell membrane.

MSD analysis reveals confinement of prestin to domains of average size ($\gtrsim 1\,\mu m$) which is large compared to other studies [Daumas et al., 2003, Suzuki et al., 2005,

Umemura et al., 2008, Wieser et al., 2007a]. Even though L is overestimated because of a broad domain size distribution, the average domain area L^2 is still a proper estimate according to Wieser et al. [Wieser et al., 2007a]. Furthermore, the average size for confinements in the untreated cells are close to the average size reported for lipid microdomains in other cell types [Schaaf et al., 2009, Schütz et al., 2000]. For untreated cells the average domain area is in the range (1.27,1.69) μm^2, and for cells depleted of membrane cholesterol the domain area is increased to be in the interval (3.4,6.1) μm^2. A large domain size is also consistent with observations in prestin transfected HEK cells, from previous studies, of puncta with size clearly resolvable above confocal microscope spatial resolution, some clearly microns in size [Organ and Raphael, 2007, Rajagopalan et al., 2007, 2010, Sturm et al., 2007]. Also well established in these studies is a reversible disappearance of puncta upon depletion of membrane cholesterol [Organ, 2008, Rajagopalan et al., 2007, Sturm et al., 2007]. This is easily understood from our result that depletion of membrane cholesterol reduces the confinement strength of the domains from 11 ± 2 to 2.9 ± 0.3 since as $\hat{\tau} \to 1$ Brownian diffusion is recovered [Wieser et al., 2007a]. For domains of the same size, and large enough to observe with conventional microscopy ($\sim$500 nm), the residence time of prestin in domains within untreated cells would be nearly four times longer than those in MβCD treated cells which would make confocal fluorescence images more diffuse in the latter case.

Analysis of the *MSD* only provides the time evolution for the mean of the distribution of squared displacements. Furthermore, a broad domain size distribution would violate the assumption of a perfectly periodic lattice required for validity of the hop diffusion model [Wieser et al., 2007a]. We therefore analyzed the distribution

in its entirety at select time lags providing a complementary method that contains more detailed information. A fit to the CDF at $t_{lag} = 250.8\,ms$ of both untreated and MβCD treated groups showed deviations from a model describing an immobile component and a freely diffusive component (Fig. 4.5). However, this is to be expected since at $t_{lag} = 250.8\,ms$ the averaging time is nearly 100% of the time lag [Wieser and Schütz, 2008, Wieser et al., 2008].

Recently, the effects of detector averaging on confined diffusion have been well characterized [Destainville and Salomé, 2006, Ritchie et al., 2005, Wieser et al., 2007a] showing that the probability for small displacements appears increased within small confinements. That the diffusion coefficient obtained from the fit to the MβCD treated group was in reasonable agreement with D_{micro} obtained from *MSD* analysis, while that of the untreated group noticeably differed, suggests that cholesterol depletion reduces the density of small domains compared to the untreated group leaving the latter more prone to the effects of detector averaging. This effect is illustrated in Fig. 4.6A which shows that detector averaging effects become rapidly more pronounced for smaller domains. The difference between the probability density distributions (Fig. 4.6B) showed a sharp increase in the effect for the untreated group compared to the MβCD group for squared displacements in a range from zero to $\sim .015\,\mu m^2$ further indicating an increasing shift in average confinement size. This is consistent with the increased average domain size obtained from *MSD* analysis for the MβCD treated group. The closer resemblance to Brownian diffusion for the MβCD CDF is also explained by the 75% reduced confinement strength $\hat{\tau}$ since as $\hat{\tau} \to 1$ free diffusion is recovered [Wieser et al., 2007a]. This is illustrated in Fig. 4.6C which shows that $MSD_{hop}(t_{lag} = 250.8\,ms)$ of the MβCD group is closer to $4D_{micro}t_{lag}$ than

the untreated group, especially for small domain sizes, since it has an α closer to zero.

To reduce the effects of detector averaging, we measured the CDFs at a five times longer time lag of $1.254\,s$ (Fig. 4.7). Minimal effects on the probability density should be seen if the size of the confinements satisfy [Powles et al., 1992, Wieser et al., 2007a, 2008] $L > (4D_{micro}t_{lag})^{1/2} \approx 500\,nm$ for $t_{lag} = 1.254\,s$. Fits to the CDF at this longer time lag showed that deviations remain for the untreated group (Fig. 4.7A) indicating that confinements exist in a size range between than that which would lead to apparent immobility and 500 nm. In contrast, the CDF for the MβCD treated group fit perfectly to an apparently immobile component and a freely diffusing mobile component (Fig. 4.7B). This observation provides strong evidence that depletion of membrane cholesterol produces a gap in the distribution of confinement sizes $\rho(L^2)$, possibly due to removal of cholesterol rich microdomains. We can estimate an upper bound for the size of the small domains remaining after cholesterol depletion by considering the largest domain size for which motion would appear immobile at a time lag of 1.254 s with 250 ms averaging time. By solving $MSD_{hop}(t_{lag} = 1.254\,s; \alpha = 1, L^2) = \Delta$ for L we calculate an upper bound of $142\,nm$. A more realistic estimate for a lower bound on the size of the large confinements is given by $L > (12D_{micro}t_{lag})^{1/2} = 867\,nm$ [Powles et al., 1992].

It is possible that HEK cell membrane focal contacts to the coverslip could produce confinements to prestin. Assuming cell surface contacts of HEK293 cells are similar to that of BKEz-7 endothelial cells, a confinement size on the order of microns might be expected [Stock et al., 2003]. This could account for the average confinement size ($\sim 2\,\mu m$) suggested by MSD at long t_{lag} for cholesterol depleted cells. However, we

are confident that confinements due to focal contacts are not responsible for the domains removed with cholesterol (in a range up to at least $867\,nm$) since if they were present they would have affected the CDF of MβCD treated cells at $t_{lag} = 1.254\,s$ which fit perfectly to free diffusion.

Previous biochemical studies have shown a decrease of prestin in the raft fraction containing flotilin-1 and integrin2α/VLA-2α, known membrane microdomain markers, and relative increase in heavier membrane fractions for depletion of cholesterol using sucrose density gradient fractionation [Rajagopalan et al., 2007, Sturm et al., 2007]. However, they also observed a decrease in the microdomain markers indicating that the reduction of prestin in the raft fraction may be a result of raft removal and concomitant removal of prestin. Furthermore, unpublished work [Organ, 2008] in our group measuring prestin diffusion using FRAP showed no increase in prestin mobile fraction for cholesterol depletion and no decrease for cholesterol loading. In addition, Sfondouris et al. [Sfondouris et al., 2008] have observed that depletion of cholesterol in transfected HEK cells from native levels does not increase prestin associated charge movement in HEK cells even though loading cholesterol reduces charge movement which they attribute to endocytosis of prestin caused by MβCD treatment. Taken together, these results in addition to our observation that small domains remain upon cholesterol depletion tend to rule out removal of prestin from domains and instead point to either a reduction in the number of small domains or a decrease in their size. Both scenarios would increase the area between domains explaining the larger average domain size for the MβCD treated group, extracted from analysis of *MSD* (Fig. 4.4), and our observation of a gap in the distribution of domain sizes (Fig. 4.7). It is interesting that cholesterol depletion preserves a signifi-

cant portion of small confinements, suggesting that many of the small confinements (ones less than 142 nm) may not be part of the detergent resistant membrane fraction and instead may be confinements due to the cytoskeleton. It is worth noting that cytoskeletal confinements to DOPE (a phospholipid probe) $68\,nm$ in size have been found in HEK293 cells using $25\,\mu s$ resolution [Murase et al., 2004] and could be the identity of the small confinements that remain after cholesterol depletion in our study.

Our results have demonstrated that membrane cholesterol is a major source of confinement for prestin in the HEK cell. A possible scenario is that part of the population of prestin is in cholesterol domains or small cytoskeletal confinements (a significant population of small domains remained even after depletion of membrane cholesterol) and another part is confined in the spaces between domains. Removal of cholesterol either makes these domains smaller or reduces their number keeping the size the same. In this scenario, the observed increase in average confinement size after removal of domains would be a result of the increased area between the domains. It is possible that the domains are contained within — or bound to — cytoskeletal fences or that in addition prestin has a direct interaction with the cytoskeleton conforming to either (or both) the anchored-protein picket model or the membrane-skeleton fence model [Kusumi and Sako, 1996, Kusumi et al., 2005, Umemura et al., 2008]. Such interpretations are made more plausible by the recent report that prestin interacts with the microtubule associated protein MAP1S supporting an interaction with the cytoskeleton [Bai et al., 2010]. In addition prestin has recently been shown to bind CFTR [Homma et al., 2010] which in turn associates with PDZ containing cytoskeletal scaffolding proteins [Gray, 2004] via its PDZ binding domain. Furthermore, prestin has a large cytoplasmic domain STAS [Pasqualetto et al., 2010] and it is not

unreasonable to assume that part of the confinement to prestin diffusion post cholesterol depletion involves corralling of STAS with the cytoskeleton. Interestingly, these models generally propose that membrane protein confinement size should usually not be affected by membrane cholesterol [Kusumi et al., 2005] since the confinement is due to the cytoskeleton. That prestin domain size is clearly dependent on cholesterol is still consistent with the anchored-protein picket model since the density of pickets could be cholesterol dependent. Indeed, there exist multiple reports of membrane confinements dependent on cholesterol co-existing with cholesterol-independent confinements [Dietrich et al., 2002, Sharma et al., 2004, Zacharias et al., 2002], and this is likely the case with prestin based on our results.

Interestingly, we found that cholesterol depletion did not change the microscopic diffusion constant of prestin in HEK cells. This is in agreement with unpublished FRAP studies [Organ, 2008] done in our group which also showed no change of effective diffusion constant with cholesterol depletion. Lipid diffusion in HEK cells also shows no change in D upon depletion of membrane cholesterol [Organ and Raphael, 2009]. This is in contrast to OHCs in which lipid lateral mobility is dependent on cholesterol and seems to be tuned to maximize lipid fluidity at native cholesterol concentration [Organ and Raphael, 2009]. This observation partially supports the findings of Sfondouris et al. [Sfondouris et al., 2008] who attributed a decreasing linear shift in both charge density and V_{pkc}, with increases in cholesterol concentration, to decreases in membrane fluidity restricting conformational flexibility of prestin. However, this interpretation is inconsistent with the observation that lipid mobility is actually decreased for cholesterol depletion in OHCs [Organ and Raphael, 2009] since that should cause a hyperpolarizing shift in V_{pkc} while a depolarizing shift is

actually observed [Rajagopalan et al., 2007]. Furthermore, their interpretation is inconsistent with the finding that lipid mobility in HEK cells is insensitive to cholesterol manipulations [Organ and Raphael, 2009] while V_{pkc} shifts remain [Rajagopalan et al., 2007, Sfondouris et al., 2008, Sturm et al., 2007]. In consideration of our results that depletion of membrane cholesterol increases average confinement size, we agree with Sfondouris et al. that depletion of membrane cholesterol could cause depolarizing shifts in V_{pkc} because conformational flexibility is increased, but not because of changes in membrane fluidity. Instead, we propose that conformational flexibility might increase due to reduced crowding of prestin in the increased area between confinement zones.

The interpretation we provided above assumes that only prestin outside cholesterol-rich domains contributes to charge movement. However, prestin residing within lipid rafts could also be functional and may have a different function than prestin outside the domains due either to a direct interaction with cholesterol or with the local environment. Therefore, cholesterol depletion may tune NLC by removing a functionally distinct prestin population from membrane microdomains causing an increased relative importance to prestin outside the domains. Prestin molecules within the DRM fraction could have altered function because: (a) lipid rafts increase or force prestin-prestin interactions that affect function, or (b) prestin within lipid rafts are brought near other raft associated molecules (such as cholesterol or other raft associated proteins) that affect function, or (c) prestin in the lipid rafts have reduced conformational flexibility and would affect V_{pkc} as described above. Scenario (a) is supported by studies that demonstrate prestin oligomerization can effect NLC [Detro-Dassen et al., 2008], and that changes in membrane cholesterol may affect prestin oligomerization

[Rajagopalan et al., 2007]. In addition, the fact that prestin has been shown to bind to CFTR [Homma et al., 2010], which is a raft associated protein[Dudez et al., 2008], directly supports (b) since Homma et al. have shown that activated CFTR increases prestin associated charge movement. The fact that prestin colocalizes with integrin molecules [Rajagopalan et al., 2007, Sturm et al., 2007] and calveolin [Rajagopalan et al., 2010] indirectly supports scenarios (b) and (c) since each are often found as components of large protein-lipid clusters that are likely to have decreased fluidity [Barrantes, 2010, Mayor and Pagano, 2007].

We cannot rule out the occurrence of transient binding of prestin to other slow or immobile proteins in or near the membrane in addition to confinement. The recent report that prestin binds the microtubule associated protein MAP1S [Bai et al., 2010] provides a possible candidate for a binding partner in addition to CFTR as mentioned above. Furthermore, transient binding could explain the unusually low D_{micro} we measure compared to other proteins. However, we can rule out having mistaken transient binding for confinement since the former cannot cause the initial rising phase in *MSD* observed in Fig. 4.4.

The OHC has a unique lateral wall that displays important structural differences from that of the HEK cell membrane. The cytoskeleton of the OHC is a cortical lattice comprising oriented domains composed of actin filaments running almost circumferentially which are crosslinked by spectrin [Wada et al., 2004]. The cortical lattice is bridged to the plasma membrane by pillar structures of unknown origin [Flock et al., 1986]. It is believed that the cortical lattice provides the OHC with its stiffness and unique shape [Wada et al., 2003]. There is likely a dynamically related

interdependence between the cytoskeleton and the membrane in the OHC. OHCs in prestin null mice lack the organized structure of their cytoskeleton suggesting that prestin is required to maintain it [He et al., 2010]. In addition, the domain structure of the cytoskeleton might define membrane domains in the OHC [Santos-Sacchi, 2002, Zhang and Kalinec, 2002]. Hence, the specialized structure of the OHC lateral wall is likely to play important roles in OHC function. However, that prestin still has the same sensitivity to cholesterol manipulations when expressed in HEK cells, which have a very different cytoskeleton from the OHC, suggests that prestin sensitivity to cholesterol is likely not directly related to the organized structure of the OHC cytoskeleton and justifies our measurements in the HEK. There is no reason, however, to expect that domain size and confinement strength in OHCs will be the same as in HEK cells. Our results nonetheless do lead us to predict that cholesterol depletion in OHCs will increase confinement size and decrease confinement strength based on the hypothesis that prestin partitions into cholesterol rich microdomains in the OHC as is suggested in this study for HEK cells.

When trying to discriminate between hop-diffusion and free diffusion, Wieser et al. [Wieser et al., 2007a] have shown that precise determination of the confinement offset CO is required to simultaneously determine D_{micro}, $\hat{\tau}$, and L in cases where the time resolution Δt is greater than τ_{micro}. This requires precise determination of the localization error offset Δ. We have shown that spread in σ_{xy} can cause a significant error in Δ if one simply estimates the average standard deviation in position localization $\bar{\sigma}_{xy}$ and assumes $\Delta = 4\bar{\sigma}_{xy}^2$. In our study we estimated the average localization error to be $19.9\,nm$ with a spread of $8.4\,nm$. Assuming $\Delta = 4\,(19.9\,nm)^2$ would have implied $\Delta = 1.58 \times 10^{-3}\,\mu m^2$. However, we demonstrated using a Monte

Carlo simulation that the actual offset this would produce is $1.88\,\mu m^2$ demonstrating a systematic underestimate of $0.3\,\mu m^2$ (Fig. A.2), nearly four times the statistical error in our measurement of Δ! It is therefore important to measure Δ directly by measuring *MSD* for immobilized particles.

Chapter 5

Voltage dependence of prestin self interactions

5.1 Introduction

As discussed in Chapter 2, the ability of prestin to move charges within the cell membrane has been used as a surrogate to measure OHC motility and commonly accepted as a signature of electromotility [Santos-Sacchi, 1991]. This intramembranous charge movement is displayed as a nonlinear capacitance in OHCs [Huang and Santos-Sacchi, 1993, Santos-Sacchi, 1991, Tunstall et al., 1995] and mammalian cells exogenously expressing prestin [Chambard and Ashmore, 2003, Deák et al., 2005, Iida et al., 2005, Zheng et al., 2000]. The sigmoidal NLC function is interpreted as a mechanistic description of the occupancy probability distribution of the conformational state of prestin. Specifically, prestin is in an expanded state for hyperpolarized potentials and in a contracted state for depolarized potentials, which lead to the use of a Boltzmann function to describe this two state transition [Dallos et al., 1993, Iwasa, 1994, Oliver et al., 2001]. This microscopic description, linking conformational change in prestin as the underlying mechanism of OHC motility and nonlinear charge movement, is a common model but is supported only by indirect measurements. A necessary prerequisite to verify this connection is to directly measure voltage dependent structural changes in prestin.

Förster resonance energy transfer (FRET) has been widely used to detect the

interactions of proteins within living cells [Tsien, 1998]. Due to its short range of interaction ($\sim$ a few nm) which is parameterized by the Förster radius R_o, FRET is a strong indicator for interactions between two proteins [Lakowicz, 1999]. Furthermore, due to the strong dependence of the FRET efficiency (E) on distance (r) and relative orientation (κ^2, where $\kappa^2 \propto R_o^6$) of the molecules (Eq. 5.1, see Sec. 2.3.2),

$$E = \frac{1}{1 + (r/R_o)^6} \tag{5.1}$$

energy transfer is a highly sensitive indicator of changes in molecular interactions [Lakowicz, 1999].

The combined use of FRET based techniques with patch clamp has the potential to be a powerful tool in understanding the conformational changes of voltage sensitive proteins. FRET based techniques in conjunction with patch clamp have proven instrumental in understanding the conformational changes in the voltage gated *Shaker* K^+ channel [Blunck et al., 2004, Cha et al., 1999, Chanda et al., 2005a, Posson et al., 2005] and various other ion channels [Bannister et al., 2005, Kobrinsky et al., 2004, Villalba-Galea et al., 2008, 2009]. In these studies, the use of FRET enabled the estimation of voltage dependent structural parameters such as changes in distance, or improved understanding of the number of voltage dependent conformational states involved in the function of the proteins. In [Villalba-Galea et al., 2008], and [Villalba-Galea et al., 2009], comparisons of structural information were made with voltage-dependent charge movement analogous to charge movement in prestin.

In this study we utilize FRET in combination with whole-cell patch clamp to

characterize voltage-dependent changes in the interaction between prestin C-terminal-fluorophore tags and correlate these voltage-dependent prestin interactions with non-linear charge movement. We hypothesize that the FRET signal should saturate at both extremes of transmembrane potential because a conformational change in the motor, which would change the interactions between the C-terminally located FRET pairs, should also saturate at the extremes. This hypothesis follows from the idea that the motility function parallels the measured charge movement [Ashmore, 1989, Iwasa, 1994, Santos-Sacchi, 1990, 1991], both of which presumably result from a conformational change in the motor [Dallos et al., 1993], and both of which saturate at the extremes of transmembrane potential [Santos-Sacchi, 1991]. We find that FRET decreases with depolarization and we discuss the implications of this voltage dependence.

5.2 Materials and methods

5.2.1 Prestin expression and cell culture

The gerbil-prestin gene (accession number AF230376) was inserted into the multiple cloning site (MCS) of the pECFP-N1 and pEYFP-N1 vectors (Clontech, Mountain View, CA) to create C-terminal fusion proteins (denoted prestin-CFP and prestin-YFP, Fig. 5.1) [Greeson et al., 2006]. The use of prestin fluorescent protein fusions has the advantage of simplicity since they can be expressed in mammalian cells using simple plasmid transfection and since they are well established not to affect prestin function [McGuire et al., 2010]. A positive FRET control was created by amplifying eCFP from pECFP-N1 (forward/reverse primers: 5'-acacggtaccaatggtgagcaagggcgaggagc-3'/5'-caccaccggtcccttgtacagctcgtccatgccgaga-3') and inserting into the KpnI and AgeI

site of the remaining MCS of the prestin-YFP fusion. This resulted in a prestin-CFP-YFP fusion with a short five amino acid sequence (GPVAT) separating the fluorescent proteins (see Fig. 5.11).

HEK293 cells were grown in 6-well plates containing DMEM supplemented with 10% BCS (Invitrogen, Carlsbad, CA), 1% penicillin-streptomycin, 14.3 mM HEPES, and 16.1 mM $NaHCO_3$. Cells below passage 25 were transfected with both prestin-CFP and prestin-YFP plasmids using Fugene 6 transfection reagent (Roche, Indianapolis, IN) according to manufacturer directions. A co-transfection allows sensitivity of the FRET signal to both changes in oligomerization and conformational changes of oligomers containing one or more prestin subunits assuming they contain both FRET pairs (Fig. 5.2). For the positive FRET control a single plasmid, prestin-CFP-YFP, was used. Eight hours after transfection cells were trypsinized and replated onto #1.5 coverslips and then imaged 24-36 hours post transfection in extracellular patch solution (see Sec. 5.2.3) at room temperature. PBS or extracellular patch solution was used to acquire FRET measurements in unpatched cells and is noted in the relevant figures.

5.2.2 FRET microscopy and analysis

FRET measurements were performed on the Zeiss LSM 510 scanning confocal microscope using "multitrack" between donor (CFP) and acceptor (YFP) channels to allow fast switching between PMTs, laser wavelengths, and settings for each channel every scan. This prevented donor emission from entering the acceptor channel. Donor and acceptor are excited with 458 and 514 nm light, respectively, both from an Ar^+ laser. Fluorescence is collected with a 63X, 1.4NA microscope objective. Using

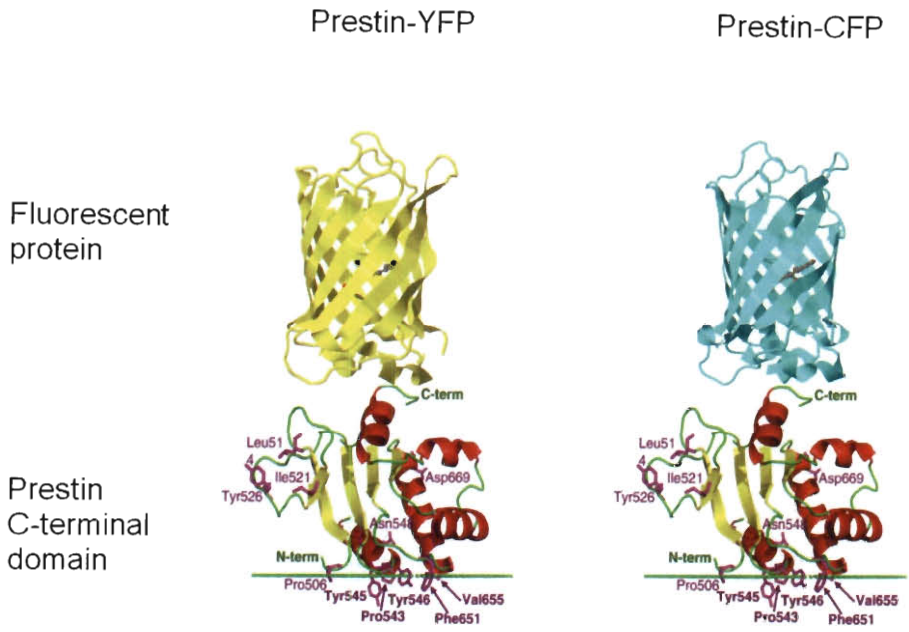

Figure 5.1 : Prestin C-terminal fluorescent protein fusions for co-transfection. Length of barrel for each fluorescent protein is 4.2 nm and width of barrel is about 2.4 nm [Ormö et al., 1996, Rekas et al., 2002, Yang et al., 1996]. The actual crystal structure of the prestin C-terminal domain (STAS) is also depicted (source for STAS image: [Pasqualetto et al., 2010]) on which is fused either eCFP or eYFP. The hydrodynamic radius of the C-terminus is 3.1 nm [Pasqualetto et al., 2010]. Relative sizes of C-terminal domain and fluorescent proteins are drawn roughly to scale based on comparisons using Jmol in Protein Data Bank (For prestin C-terminal domain, http://www.rcsb.org/pdb/explore/jmol.do?structureId=3LLO&bionumber=1; For fluorescent proteins, http://www.rcsb.org/pdb/explore/jmol.do?structureId=2WSN &bionumber=1).

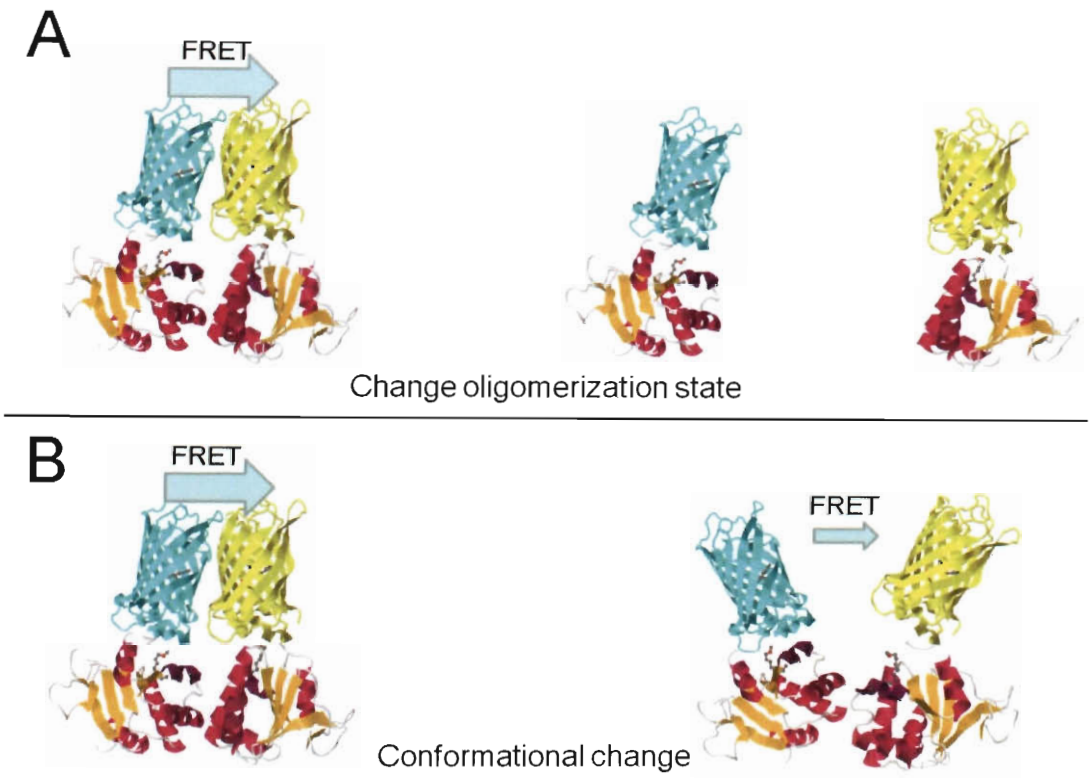

Figure 5.2 : Pathways for changes in FRET efficiency with co-transfection of prestin-CFP and prestin-YFP. A) Depicted is a change in oligomerization scenario that would lead to a reduction in FRET efficiency. A prestin dimer undergoing energy transfer via its C-terminally located FRET pairs dissociates leading to no energy transfer. B) a prestin dimer undergoing energy transfer undergoes a conformational change leading to reduced energy transfer due to either or both increased distance or change in relative orientation between C-terminally fused fluorescent protein FRET pairs.

a secondary dichroic and separate band pass filters for each channel, CFP fluorescence is collected in a band that effectively spans 480-520 nm and YFP fluorescence is collected in a band from 545-590 nm. A pinhole placed in front of the PMT detector, in a conjugate plane to the focal plane of the objective, was set to 2 Airy units.

Only cells with clear membrane localization of prestin-CFP and prestin-YFP fluorescence were patch clamped (see Electrophysiology below). After a stable whole cell patch was established, regions of interest (ROIs) were placed as depicted in Fig. 5.3. Briefly, an approximately 10.5 μm square region, labeled region 1, was placed on a segment of membrane with sufficient and uniform fluorescence. Three circular regions, each with a diameter of approximately 2.9 μm, labeled 2, 3 and 4 (labeled B, C, and bg in Fig. 5.3), were contained within region 1. Region 2, the YFP bleach region, and region 3, the control region, were centered on the cell membrane and region 4 was placed in the background outside the cell, to monitor the background signal in the CFP channel. At the onset of the FRET measurement 40 imaging scans (580 ms/scan) were taken in region 1 to allow CFP fluorescence level to stabilize. After these scans, the acceptors in region 2 were bleached for $\sim$ 9 seconds at high laser power to de-quench the donors in that region only. The transmembrane potential was clamped at the desired test voltage at frame 30, 10 frames prior to the bleach. Finally, 10 additional imaging scans were acquired post bleach (see Fig. 5.4).

The FRET efficiency (E) was determined by measuring the donor fluorescence before (F_{da}) and after (F_d) the bleach using Eq. 5.2 [Lakowicz, 1999]:

$$E = 1 - \frac{F_{da} - BG}{F_d - BG} \tag{5.2}$$

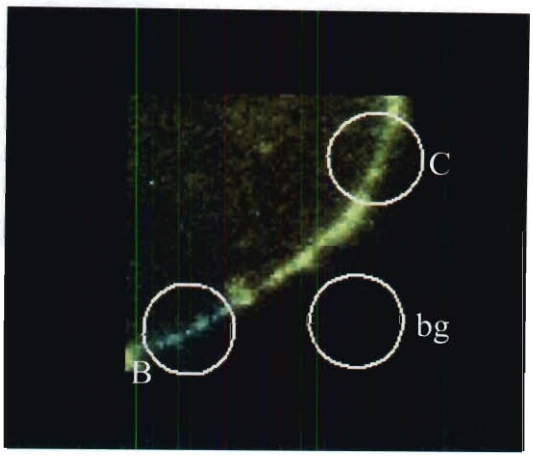

Figure 5.3 : Fluorescence image of a cell expressing prestin-CFP and prestin-YFP. The image shows the bleach (B), control (C), and background (bg) regions of interest (ROIs). Yellow false color represents YFP fluorescence which has been bleached in the bleach region (B) and blue false color represents CFP fluorescence.

where BG is the average background signal in the donor channel in region 4 over the entire experiment. This was done for both the bleach region 2 (B) and the control region 3 (C) and the efficiencies of both were compared as illustrated in Fig. 5.5. In principle the calculated FRET efficiency in the control region should be zero because the donors have not been de-quenched. However, in practice we measure a background control efficiency of about 3%. This is possibly due to donors, that

have not been photobleached by the imaging laser, diffusing into the control region during the 9 second period that the acceptor is being bleached. False positive FRET in the control region may also be caused by donor fluorescent proteins that were not irreversibly photobleached regaining their fluorescence, due to blinking behavior, immediately prior to F_d determination [Garcia-Parajo et al., 2000]. We corrected for these unavoidable, systematic errors by subtracting the control efficiency from the efficiency measured in the bleach region (Fig. 5.5) and reporting the difference on a cell-by-cell basis. Only cells that had control efficiency between -5 and +10% where retained for analysis and the mean FRET was reported for each voltage tested. The FRET versus voltage data was fit to the Boltzmann function shown in Eq. 5.3:

$$E = A_2 + (A_1 - A_2)\frac{1}{1 + e^{(V_m - V_o)/\alpha}} \tag{5.3}$$

where A_1 and A_2 are the hyperpolarized and depolarized asymptotes, respectively; V_o is the potential at half maximal FRET; and α is a parameter describing the width of the FRET versus voltage relationship.

5.2.3 Electrophysiology

2-4 MΩ micropipettes were formed from Kimax-51 capillary tubes (1.5/0.8 mm OD/ID) on a P-97 puller (Sutter, Novato, CA). The patch pipettes and extracellular bath both contained common blocking solutions (Pipette: 130 mM CsCl, 2 mM $MgCl_2$, 10 mM EGTA, 10 mM HEPES; Extracellular: 99 mM NaCl, 20 mM TEA-Cl, 2 mM $CoCl_2$, 1.47 mM $MgCl_2$, 1 mM $CaCl_2$, 10 mM HEPES) to minimize ionic conductance [Deák et al., 2005]. For experiments requiring prestin inhibition 10 mM salicylate was added to both solutions. All solutions were titrated to pH 7.3 and dextrose added to obtain 300±3 mOsm (Osmette A; Precision Systems, Natick, MA). During the experiment

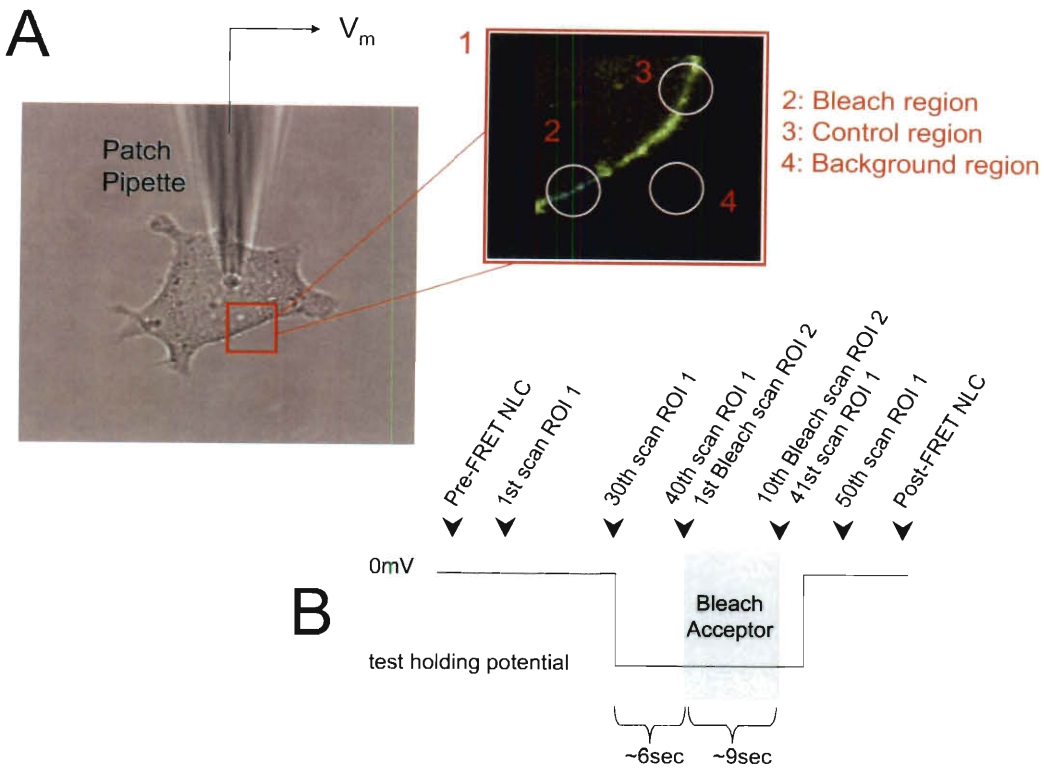

Figure 5.4 : Experimental procedure and timing diagram. A) HEK cells co-transfected with prestin fusion proteins are voltage clamped at various membrane voltages (V_m) using the whole cell patch clamp technique. Shown is a bright field image of a cell under whole cell patch clamp. The patch pipette is visible in the image. Acceptor fluorescence is bleached in region 2 after 40 scans of region 1 to dequench donors in region 2. The acceptors in region 3 (control region) are not bleached. Donor fluorescence measurements in region 3 are used to estimate the degree of false positive FRET efficiency. Background fluorescence and noise in region 4 (background region) is subtracted from the fluorescence in regions 1 and 2 (see Eq. 5.2) before calculating ensemble FRET efficiency E. B) Timing diagram of experiment. Each scan takes $580\,ms$.

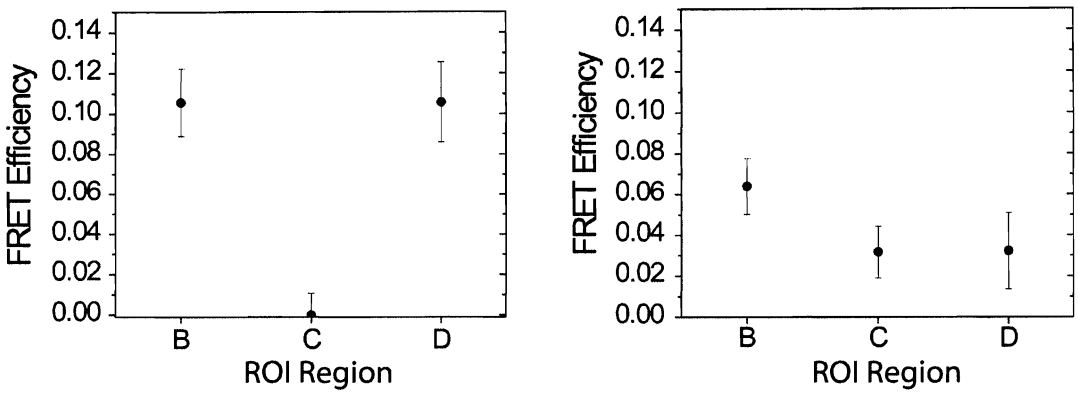

Figure 5.5 : Determination of FRET efficiency. Plots show bleach efficiency (B), control region efficiency (C) and the difference (D=B-C), which is the reported FRET efficiency, for transmembrane potentials of -140 mV (left graph) and +60 mV (right graph).

micropipette placement was controlled using a Burleigh PCS-6200 Micromanipulator (EXFO Life Sciences, Rochester, NY), and pipette pressure monitored and neutralized before recording (PM01R digital pressure meter; WPI, Sarasota, FL). Only healthy, single cells showing suitable fluorescence were attempted. For all experiments GΩ seals were obtained, normal NLC characteristics verified prior to FRET measurement, and membrane resistance monitored to ensure seal integrity during clamped voltage excursion.

Membrane capacitance (C_m) and membrane resistance (R_m) were determined by applying a sinusoidal command voltage at a superimposed DC offset and then determining the real and imaginary components of the admittance, the complex

current response scaled by the command voltage [Lindau and Neher, 1988]. We used a software-based phase sensitive detector implemented in PatchMaster software (HEKA, Mahone Bay, NS) to acquire this information. Specifically we applied an 800 Hz, 10 mV sinewave and measured the current response as DC holding potential was stepped from -140 to +140 mV in 2 mV increments (HEKA EPC 10 Plus Amplifier with 18-bit DAC). At each DC potential four complete sinusoidal voltage cycles occur and discrete capacitance values are calculated from the latter three.

Capacitance-versus-holding potential traces are fit to the first derivative of the two-state Boltzmann function (Eq. 5.4) using MATLAB (the MathWorks, Natick, MA). The first term of the fit represents the nonlinear component, caused by prestin-related charge movement, while the second term (C_{lin}) is linear capacitance derived from the dielectric properties of the membrane and is proportional to cell size. Since variation in cell size causes differences in the maximal charge transfer (Q_{max}), the charge movement is normalized to C_{lin}. This quantity, designated as charge density, has units of fC/pF [Oliver and Fakler, 1999] and was reported along with the voltage at half maximal charge movement ($V_{1/2}$) and valence (z). The fit also contains the following constants: e the elementary charge, k_B Boltzmann's constant, and T the absolute temperature (298 K).

$$C_m = \frac{Q_{max}\left(\frac{ze}{k_BT}\right)}{exp\left[\left(\frac{ze}{k_BT}\right)(V_m - V_{1/2})\right]\left(1 + exp\left[-\left(\frac{ze}{k_BT}\right)(V_m - V_{1/2})\right]\right)^2} + C_{lin} \qquad (5.4)$$

5.3 Results

5.3.1 Voltage dependence of FRET decreases with depolarization

Fluorescence measurements of the FRET signal (see Sec. 5.2) from live mammalian HEK cells co-expressing prestin-C-terminal FRET pairs (prestin-CFP and prestin-YFP, Figs. 5.3 and 5.1) were acquired while simultaneously controlling the membrane voltage using the whole cell patch clamp technique (Fig. 5.4). The NLC fits using Eq. 5.4 from 240 cells yielded a voltage at half maximal charge movement of $V_{1/2}$ = -54.6±0.9 mV and a valence of z = 0.728±0.004 (mean±SEM). The FRET efficiency was measured while holding the cells at transmembrane voltages (V_m) of -140, -90, -55, 0, +30, and +60 mV (Fig. 5.6), which are voltages that span the active range of prestin function [Santos-Sacchi, 1991, Zheng et al., 2000]. In addition, the FRET efficiency in unpatched HEK cells was measured at resting membrane potential (-50±1.6 mV [Fliegert et al., 2007]).

We found that the FRET signal (in a voltage range near peak NLC) is a function of transmembrane voltage and that FRET efficiency decreases with depolarization (Fig. 5.6). The FRET efficiency 0.106±0.020 measured at -140 mV was significantly higher than that measured at +60 mV, 0.032±0.019 ($p < 0.05$) (Fig. 5.5). Our method did not allow us to explore potentials more hyperpolarized than -140 mV or more depolarized than +60 mV, where sustained current flow during the photobleaching phase of the measurement was accompanied by reduced membrane resistance and at times total seal loss. Our analysis only includes FRET data from cells with normal NLC curves both before and after FRET measurement and consistent whole cell membrane resistance in excess of 1 GΩ.

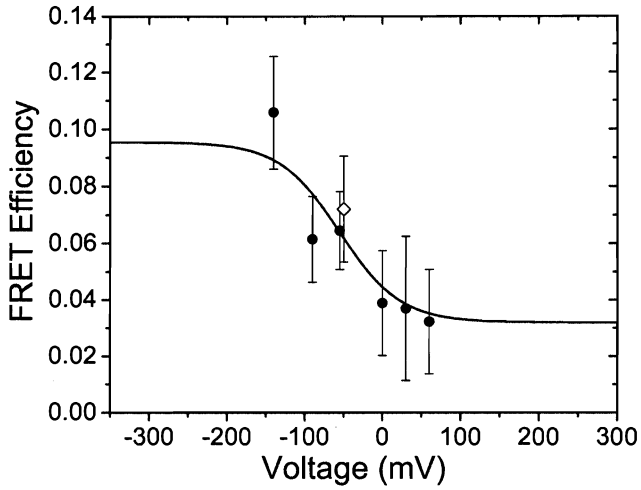

Figure 5.6 : FRET Efficiency decreases with depolarization. The difference between the bleach and control region FRET is plotted versus clamped transmembrane voltage. Solid circles represent groups of cells that are patch clamped. The open diamond represents unpatched cells measured at resting potential (-50±1.6 mV) in PBS [Fliegert et al., 2007]. The number of measurements for each potential, from left to right are 7, 18, 16, 18, 22, 7 and 7. Error bars represent standard error using error propagation. The solid line is a fit to a Boltzmann function of the FRET data (Eq. 5.3) and is weighted by the statistical error bars. The fit is constrained to have an asymptote of A_2=.032 at the depolarized tail, and the center is constrained to be V_o = $V_{1/2}$ = -54.6 mV.

5.3.2 Results of sigmoidal fit to FRET data

To explore the validity of the assumption that nonlinear charge movement parallels a conformational change in prestin, we fit the FRET efficiency versus voltage data with a sigmoidal Boltzmann function (Eq. 5.5, Fig. 5.6). In Fig. 5.7 we compare the derivative of the Boltzmann fit of the FRET data to the mean NLC curve, constructed from the mean Boltzmann parameters (Q_{max}, $V_{1/2}$, and z) acquired from pre-FRET NLC curves (N = 240). The derivative of the Boltzmann fit to the FRET data takes the form:

$$\frac{\partial E}{\partial V_m} = \frac{e^{-(V_m - V_o)/\alpha}}{(1 + e^{-(V_m - V_o)/\alpha})^2} \tag{5.5}$$

where,

$$\frac{1}{\alpha} = \frac{z_{FRET}\, e}{k_B T}. \tag{5.6}$$

The FRET and NLC fits are normalized to a unitless form such that they both have a peak of 0.25 allowing for a direct comparison to each other. The independent fits are quite close to each other. The width (α) of the function is inversely proportional to the dimensionless parameter z_{FRET} (Eq. 5.6) which is analogous to the valence z of the NLC (Eq. 5.4). We find that z_{FRET} differs from z by only slightly more than 10% (Fig. 5.7).

5.3.3 Salicylate eliminates negative voltage dependent FRET trend

Cells co-transfected with prestin-CFP and prestin-YFP are patch clamped in 10 mM salicylate (both pipette and extracellular solutions) and FRET efficiency is measured

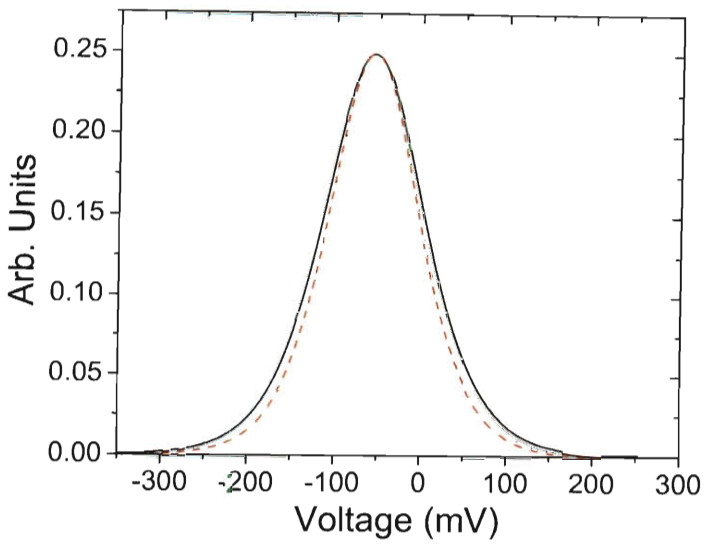

Figure 5.7 : Comparison of fit to FRET data with mean measured NLC. The black curve is the derivative of the Boltzmann fit (Eqs. 5.5 and 5.6) to data from Fig. 5.6. Red dashed curve is average of fits (Eq. 5.4) to measured NLC traces from 240 measurements. Both curves are normalized to a unitless peak of 0.25. The widths differ by only 10% (z_{FRET} = 0.655±0.340 black curve, z = 0.728±0.004 red curve).

at -90 and +60 mV (see Fig. 5.8). As expected, cells show a loss of NLC indicating a loss of prestin function. The FRET efficiency at -90 mV (~7%) remains about the same as the untreated case, while the efficiency at +60 mV is significantly increased from 3.2% to 9.6% ($p<0.5$) indicating departure from the previous trend in Fig. 5.6 where FRET had decreased upon depolarization.

5.3.4 FRET does not depend on prestin expression level

To test whether FRET efficiency is influenced by the amount of prestin expressed in the membrane, FRET was plotted versus charge density (Q_{max}/C_{lin}, obtained from NLC fits using Eq. 5.4) at each holding potential tested. We find no dependence of

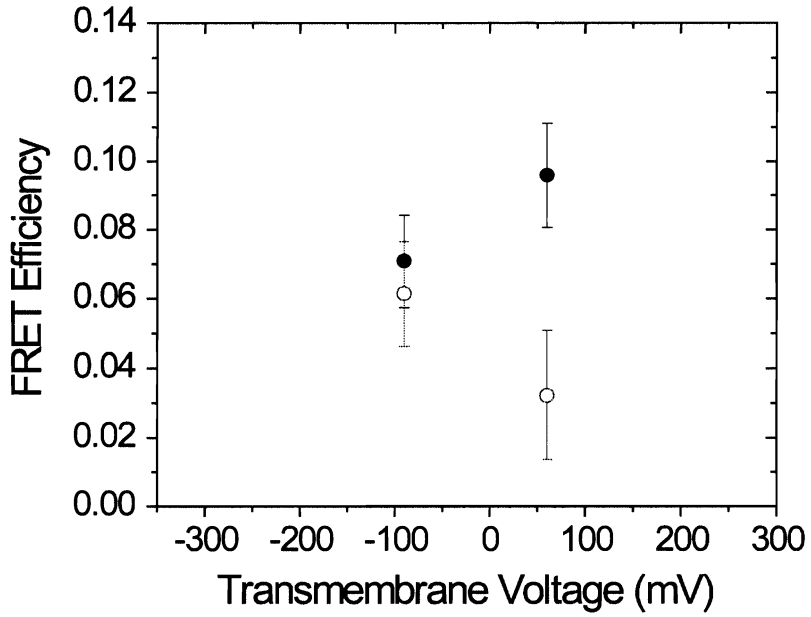

Figure 5.8 : Effects of salicylate on voltage dependent FRET. FRET efficiency is measured in cells co-expressing prestin-CFP and prestin-YFP at -90 mV and at +60 mV under whole cell patch with 10 mM salicylate (solid circles). N=16 and 13 cells, respectively. FRET in untreated cells at -90 mV and +60 mV (from Fig. 5.6) are also plotted for comparison (open circles). Application of 10 mM salicylate eliminates FRET decrease upon depolarization (at +60 mV, FRET in salicylate treated cells is significantly higher than in untreated cells).

FRET efficiency on charge density at all holding potentials. A representative sample of FRET versus charge density at holding potential of -90 mV is displayed in Fig. 5.9 and illustrates no correlation.

5.3.5 Negative FRET control

To test our ability to measure a true zero transfer efficiency, we perform a negative FRET control in unpatched cells expressing only donor molecules (prestin-CFP) in the membrane. We find no significant difference in FRET between bleach and control regions (Figs. 5.10A and 5.10B) resulting in zero FRET. This result confirms that the low FRET measured at 0, +30, and +60 mV in Fig. 5.6 reflect true non-zero FRET measurements.

5.3.6 Positive FRET control

To provide context for our voltage-dependent FRET measurements, we utilized a construct designed to exhibit: 1) a nearly fixed average donor-acceptor distance, 2) relatively high FRET via close donor-acceptor separation, and 3) a situation where all molecules in the sample undergo FRET by virtue of a one-to-one pairing of CFP to YFP. FRET was measured in unpatched cells expressing prestin-CFP-YFP. We observed a relatively large transfer efficiency (around 15%, Fig. 5.10C) compared to that measured from co-expressing prestin-CFP and prestin-YFP. Although the separation and relative orientation of the CFP and YFP in the positive control cannot be known exactly, a rough estimate of the distance between them is made from known structural information about the fluorescent proteins (XFPs) and the intervening amino acids. XFP barrel diameter is roughly 2.4 nm, the barrel length roughly 4.2 nm [Ormö et al., 1996, Rekas et al., 2002, Yang et al., 1996], and the XFP termini

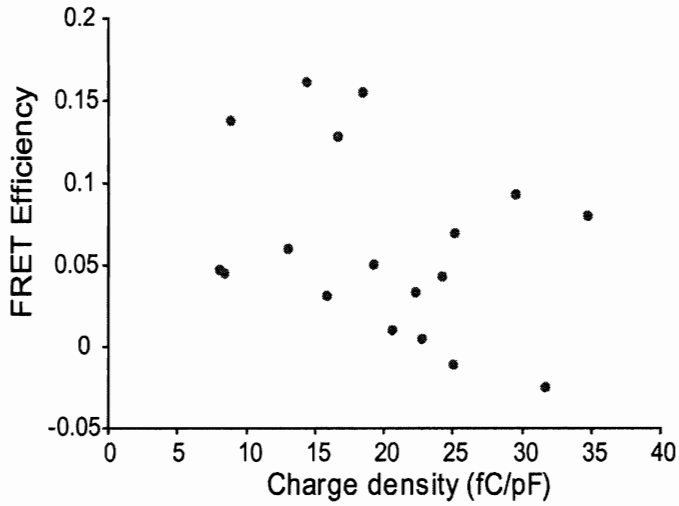

Figure 5.9 : FRET measures do not depend upon prestin charge density. Linear regression of data collected from cells clamped at -90 mV during the FRET measurement shows no correlation between the measured FRET efficiency and amount of prestin in the membrane. The null hypothesis that slope differs from zero cannot be rejected ($p = 0.193037$). All other voltage treatments showed similar results.

adjacent to the linker residues are each 1-1.5 nm (estimated from Fig. 1 published in [Rekas et al., 2002]). We estimate that the distance between the chromophores of the XFPs is at most 9 nm, but likely smaller due to flexibility in the linker region. From the 15% efficiency we measure with the positive control (Fig. 5.10C), we conclude that the average distance between the fluorophores is 6.71 ± 0.24 nm (error calculated from

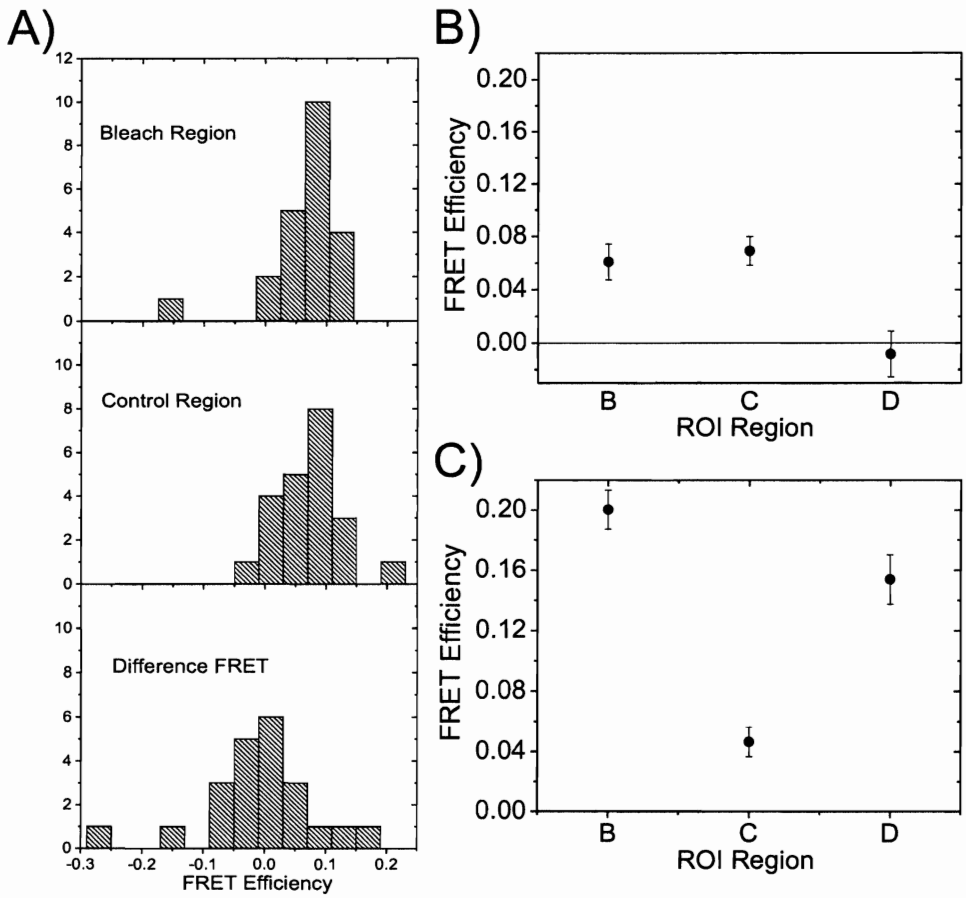

Figure 5.10 : Results of FRET controls. The negative FRET control displays zero measured transfer efficiency, and positive FRET control shows a relatively high measured FRET efficiency. Both measurements were made in PBS. (A) Histograms of measured FRET efficiencies of the negative control (prestin-CFP only; N=22 cells) show normal distributions for the bleach and control regions (top and middle panels, respectively), as well as the difference between the two (bottom panel). (B) Plot showing the average of the three distributions in (A) (mean±SEM) shows zero FRET in the negative control. (C) Plot showing the average efficiency in cells expressing the prestin-CFP-YFP positive control shows high FRET ($E = 0.15 \pm .016$, N = 15 cells).

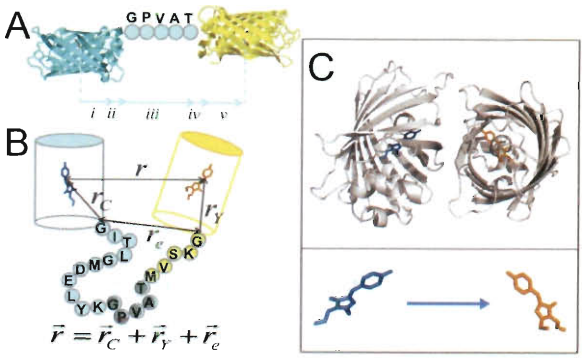

Figure 5.11 : Structural details of positive FRET control. Rough estimates of the maximum possible distance between chromophores within the positive FRET control construct are made from the following structural information. (A) Construct consists of eCFP linked to eYFP via a 5 amino acid linker GPVAT. N-terminus of eCFP is fused to prestin C-terminus. Vectors i-v denote distances relevant to evaluating the inter-chromophore distance assuming a static orientation and using the known crystal structures of the GFP based fluorescent proteins [Ormö et al., 1996, Rekas et al., 2002]. (i) eCFP chromophore to edge of barrel $\sim 2.1nm$, (ii) distance C-terminus in folded state could extend from edge of barrel $\sim 1-1.5nm$ estimated from: 1CV7 RCSB Protein Data Bank (PDB) and [Ormö et al., 1996, Rekas et al., 2002, Yang et al., 1996], (iii) linker region $\sim 1.7\,nm$ assuming it is unstructured and fully stretched and that each amino acid contributes $\ell_c = 0.34nm$ of length (average contour length per amino acid in a β-strand [Ohashi et al., 2007]), (iv) distance from eYFP N-terminus to edge of barrel $\sim 1-1.5nm$ estimated from: 1YFP RCSB PDB and [Ormö et al., 1996, Rekas et al., 2002, Yang et al., 1996], (v) distance from edge of barrel to eYFP chromophore $\sim 2.1nm$. In addition, the diameter of the barrels are $\sim 2.4nm$ [Ormö et al., 1996, Yang et al., 1996]. Adding the sum of vectors i-v in quadrature with the barrel diameter, a maximum inter-chromophore distance of $9.2nm$ is expected. (B) More realistic estimate of maximum inter-chromophore separation is obtained by use of a simple worm-like chain model [Evers et al., 2006, Ohashi et al., 2007, Rivetti et al., 1996, Zhou, 2004] for the linker between the barrels which has been shown to accurately describe end-to-end separations of unstructured peptides. The model treats the peptide as a semi-flexible tube with persistence length $p = 0.45nm$ [Evers et al., 2006]. The mean-squared end-to-end separation is given by $\langle r_e^2 \rangle = 2pL\left\{1 - \frac{p}{L}\left(1 - \exp\left(\frac{-L}{p}\right)\right)\right\}$ where $L = n\ell_c$ is total peptide contour length and $n = 16$ amino acids. n includes: 11 amino acids of eCFP C-terminus, 5 residues of eYFP N-terminus, both of which contain a degree of flexibility [Ohashi et al., 2007, Ormö et al., 1996, Rekas et al., 2002], and 5 residue linker. We obtain $\langle r_e^2 \rangle^{1/2} = 2.454nm$. Adding this to the distance from the peptide endpoints to the chromophores ($r_C = 0.2nm$ and $r_Y = 0.24nm$, see [Evers et al., 2006]) such that all vectors are maximally collinear, we obtain as an estimate for the inter-chromophore separation $r = 6.85nm$. (C) Shown is the structure of the YFP dimer which serves as a structural model for the minimum distance between eCFP and eYFP chromophores, which is estimated to be 24.3 or 25.5 Å [Shi et al., 2007] or 26 Å based on the GFP dimer crystal structure [Kotera et al., 2010]. The highest reported FRET efficiencies between full length CFP YFP chimeric constructs are $\sim 70\%$ [Evers et al., 2006, Zeng et al., 2006].

statistical error in measured FRET and quoted error in R_o from [Tsien, 1998]) using $R_o = 5$ nm [Tsien, 1998]. The R_o estimate assumes a randomized orientation factor of $\kappa^2 = 2/3$, which 1) is quite possible, due to the flexible glycine residue in the linker region, and 2) historically has compared well with experimental results [dos Remedios and Moens, 1995]. Furthermore, because R_o depends only weakly on the sixth root of κ^2, the κ^2 assumption can at most provide 35% error in the calculated distance (for actual κ^2 between 1/9 and 4 [Lakowicz, 1999]). We thus find that the distance we calculate from prestin-CFP-YFP FRET is not unreasonable based on that expected from known structural information. Most importantly, this result demonstrates that there are likely no serious systematic errors entering our measurement of the FRET efficiency (see Fig. 5.11).

5.3.7 "Distance" representation of FRET data

Based on the results of the positive and negative controls, we conclude that the FRET we measure results from specific prestin-prestin interactions and not from unintended sources. Furthermore, if only one donor-acceptor distance contributes to the FRET, as would be possible in the case where an intact prestin oligomeric structure undergoes voltage-dependent conformational change (see Discussion section), we can estimate CFP and YFP separation. Under this assumption, we can solve for r/R_o in terms of E using Eq. 5.1 and replot the data from Fig. 5.6 to obtain an estimate of C-terminal distances (Fig. 5.12). The data is fit to the same Boltzmann form as before (Eq. 5.3) and the fit is superimposed on the data (Fig. 5.12). From the width of the fit, we again obtain the characteristic voltage range of the data, and using an equation analogous to Eq. 5.6 we find that $z_{(r/R_o)} = .681 \pm .285$ which is different by less than 6.5% from z of the NLC. Going from the hyperpolarized to the depolarized asymptote, the

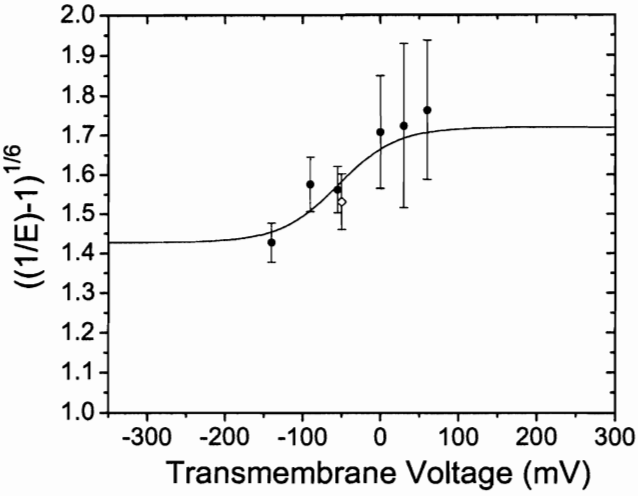

Figure 5.12 : Voltage dependence of $(1/E - 1)^{1/6}$. Solid circles represent cells that are patch clamped and the open diamond represents unpatched cells measured at resting potential in PBS. Data is fit to a Boltzmann function that has the same form as the right hand side of Eq. 5.3. The fit is constrained to have an asymptote of A_1=1.427 on the hyperpolarized end, and the center is constrained to be $V_o = V_{1/2}$ = -54.6 mV. Error bars are calculated by propagating error in E to $(1/E - 1)^{1/6}$.

fit to the data suggests that the voltage induced conformational change causes the distance between the donors and acceptors to change from about 1.4 to 1.7 R_o. This corresponds to a change in distance of 1.5 nm, or including a variation in κ^2 from 1/9 to a possible maximum of 4, a displacement of $\sim$ 1-2 nm.

5.3.8 Positive FRET control revisited

To further examine the voltage dependent conformational change of prestin, we re-measure the FRET efficiency of unpatched cells expressing the prestin-CFP-YFP positive control, but now in extracellular blocking solution (Sec. 5.2.3). The blocking solution should block K^+ channels, which depolarizes the resting potential of the cells to $\sim$ 0 mV, allowing a measurement of the prestin-CFP-YFP FRET at a depolarized

potential. We obtain a significant increase in prestin-CFP-YFP FRET from 15% to 26% (see Fig. 5.13) upon depolarization using blocking solution. This trend is in contrast to that seen for cells co-expressing prestin-CFP and prestin-YFP where E decreases with depolarization.

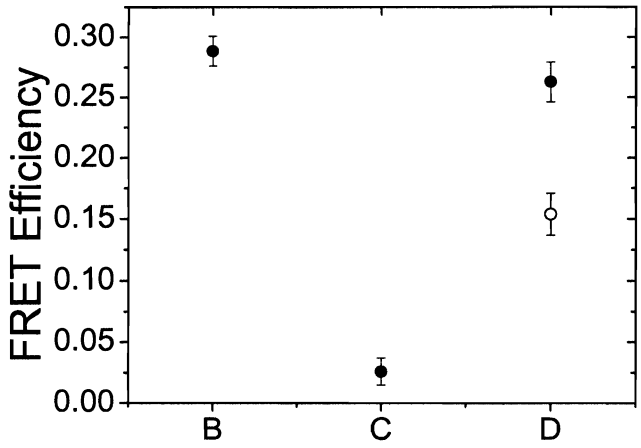

Figure 5.13 : Positive control FRET in extracellular blocking solution. Measured average FRET efficiency (E=0.26 $\pm$ 0.016) of cells expressing presin-CFP-YFP positive control in extracellular blocking solution (solid circle) shows 70% increased efficiency over positive control cells in PBS (shown for comparison,open circle).

5.4 Discussion

Although prestin is well established as the membrane based molecular motor that drives electromotility [Zheng et al., 2000], presumably by undergoing a voltage dependent conformational change, the details of prestin function at the nanoscale level are unknown. The observation of NLC in prestin expressing cells is generally interpreted as charge movement due to voltage dependent conformational changes of prestin that move charged moieties into and out of the membrane [Muallem and Ashmore,

2006, Oliver et al., 2001, Rybalchenko and Santos-Sacchi, 2008]. Reports of electromechanical motion in prestin transfected cells provide evidence that prestin exerts direct mechanical forces on the cell membrane [Zhang et al., 2007, Zheng et al., 2000] and are indirect support that electromotility is driven by a conformational change. Furthermore, [Fang et al., 2008] report that perturbing prestin conformation with thiol-reactive optical switches reversibly effects peak NLC providing evidence linking conformational change in prestin to changes in NLC. However, only one experiment [Gleitsman et al., 2009] similar to this work has observed direct evidence of a conformational change or any other structural change of prestin in response to changes in membrane voltage. They, however, rely predominantly on a high KCl concentration treatment to depolarize the membrane which they report could deplete intracellular chloride concentration calling into question whether the FRET change they measure is due only to changes in voltage since prestin function is sensitive to Cl^- [Oliver et al., 2001]. They also do not measure an absolute FRET but instead a normalized donor fluorescence in contrast to this study. Furthermore, although they do measure normalized donor fluorescence in conjunction with patch clamp, they acquire their signal from TIRF fluorescence (coming only from membrane in close proximity to the coverslip) which is problematic due to voltage drops across the access resistance caused by membrane sealing to the coverslip [Blunck et al., 2004, Gleitsman et al., 2009]. Demonstrating that prestin does in fact undergo a voltage dependent structural change is a requisite for assessing the validity of the common assumption that a conformational change in prestin is the underlying mechanism for electromotility.

Much interest has been placed on what constitutes the functional unit of prestin. The observation of 8-11 nm particles in the OHC membrane and prestin transfected

cells [Gulley and Reese, 1977, Kalinec et al., 1992, Murakoshi et al., 2006] has been used to argue that prestin exists natively as a multimer. Furthermore, several groups have demonstrated that prestin forms oligomers [Detro-Dassen et al., 2008, Mio et al., 2008, Pasqualetto et al., 2008, Rajagopalan et al., 2007, Sturm et al., 2007, Z. et al., 2006] and this is further evidenced by FRET studies showing that prestin interacts with itself [Greeson et al., 2006, Navaratnam et al., 2005, Wu et al., 2007]. However, there is disagreement as to which of these oligomeric states are functional, and it is unknown what role oligomerization might play in the voltage dependent function of prestin. The common model of prestin is a two-state area motor model in which a single functional motor unit changes area between an extended and a compact state [Dallos et al., 1993, Iwasa, 1994, Oliver et al., 2001]. However, a model is also proposed that suggests a possible role for changes in membrane curvature, a phenomena potentially mediated by changes in oligomerization [Raphael et al., 2000, Spector et al., 2006].

5.4.1 Saturation of FRET data at extremes of holding potential

We measure prestin FRET to decrease over a transmembrane potential range going from -140 mV to +60 mV. We were unable to measure FRET outside the range of -140 mV to +60 mV because excessive current flow lead to reduced membrane resistance likely resulting from electropermeabilization [Akinlaja and Sachs, 1998, Navarrete and Santos-Sacchi, 2006]. For this reason we were unable to directly observe saturation at extreme hyperpolarization or depolarization. However, a sigmoidal Boltzmann function (Eq. 5.5) fit to the FRET data is justified because a conformational change in prestin should saturate at the extremes as does motility and nonlinear charge movement.

5.4.2 Possible sources of FRET voltage dependence

From the observation that the FRET efficiency is a monotonically decreasing function of membrane potential, we can propose some molecular level descriptions of potential sources of the voltage dependent FRET. The dependence could arise from one of three scenarios: either 1) a voltage triggered shift in the oligomeric state distribution, 2) a change in conformation within intact oligomers from an unchanging distribution, or 3) a combination of the two. If the voltage dependent structural change is a change in oligomeric state of prestin, this would imply that depolarization causes the distribution of oligomeric states to shift toward lower states. This could be caused by a prestin conformational change that creates steric hindrance at binding sites to other prestin molecules leading to a change of oligomeric states. If however the distribution of oligomeric states remains constant with transmembrane voltage, then this implies that intact oligomeric prestin assemblies undergo a conformational change such that the C-terminal tags get further apart from each other upon depolarization or that the relative orientation of the transition dipole moments are modified to lead to reduced energy transfer. We rule out the possibility that depolarization shifts the oligomeric distribution towards higher states since this scenario would necessarily lead to an increase in FRET efficiency. However, it is possible that lower order oligomers could shift towards higher ones if the conformation of the higher order states leads to decreased distance between fluorescent tags. We also rule out a conformational change in which the C-terminally located FRET pairs get closer together upon depolarization, because this scenario would also lead to an increase in FRET efficiency.

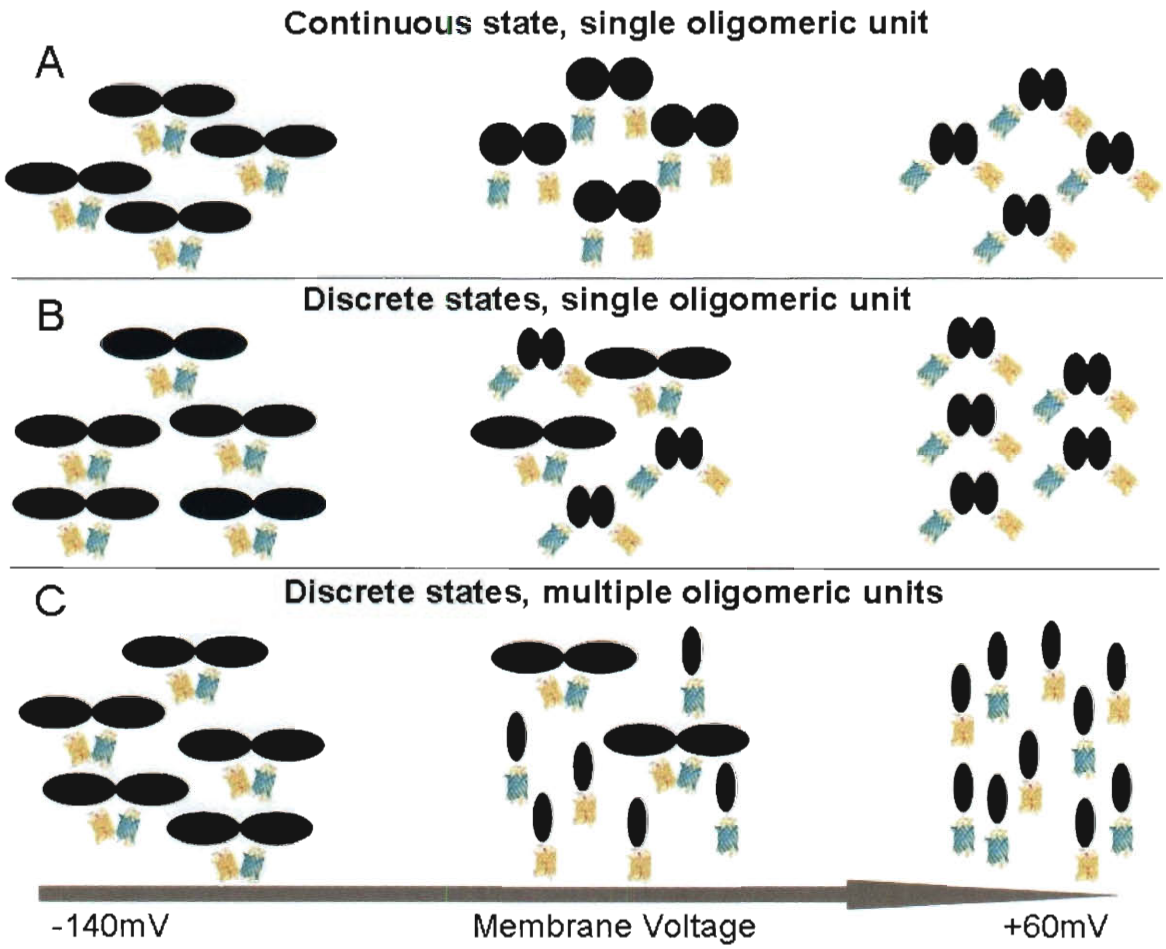

Figure 5.14 : Illustration depicting possible scenarios consistent with FRET voltage trend. Black ovals represent prestin and blue and yellow barrels represent CFP (donor) or YFP (acceptor) fused to prestin C-terminus. (A) Continuous model where all molecules are in the same state at any voltage. (B) Two-state model where state is either: an expanded conformation with high FRET at extreme hyperpolarized potentials, or a contracted conformation with low FRET at extreme depolarized potentials. At intermediate potentials there is a statistical mixture of each state. (C) Two-state model where state is either: a dimer in an expanded state at extreme hyperpolarized potentials with high FRET, or a monomer in a contracted state with low FRET at extreme depolarized potentials. In cases where a single oligomeric state changes conformation, the change in FRET could be due to either or both changes in donor-acceptor distance or changes in relative orientation of donor and acceptor transition dipole orientation.

5.4.3 Relation of FRET to physical quantities

When considering models of electromotility it is more relevant to discuss parameters that directly describe the structural state of the motor as a function of membrane potential. Specifically, we are interested in relating the FRET efficiency to either a distance between fluorescent tags within a motor complex or the fraction of prestin molecules within a particular state.

In the case of the commonly adopted two-state thermodynamic description (i.e. the area motor model [Iwasa, 1994]), the relevant quantity is the fraction of molecules within a particular conformational state. In this model, the FRET changes because the population of molecules in a particular state, with a characteristic FRET, continuously changes with voltage. The microscopic description of the two-state case could be a transition from a high oligomeric state with high FRET to a lower order oligomeric state without FRET upon depolarization (scenario 1). Alternatively, an oligomeric state in a conformation that experiences high FRET may undergo a conformational change to a second state having low FRET while keeping the oligomeric state intact (scenario 2).

In the case that the motor changes its conformational state in a continuous fashion (i.e. the membrane bending model [Raphael et al., 2000, Scherer and Gummer, 2005]) the fluorescent tag distance is the useful quantity to fit to a Boltzmann function. In this model, the FRET changes because the donor-acceptor distance is a continuous function of voltage. Continuous models are compatible with a conformational change of an intact oligomer (scenario 2), but do not provide the discrete states required to explain our voltage dependent FRET through shifts in oligomerization (scenario 1).

The ability to obtain these quantities (tag distance or conformational state probability) from the FRET data is only possible in certain special cases that are explicitly detailed below (see also Appendix B).

5.4.4 Relevance to two-state motor picture

In considering a thermodynamically driven two-state model where the useful quantity is the fraction of motors n_i in a particular state i, the FRET (see Fig. 5.6) is actually directly proportional to the desired quantity, the fraction of donors that are undergoing FRET n_F (see Appendix B). However, this proportionality is strictly true only if a single state exclusively contributes to the voltage dependent FRET signal and the other state provides zero FRET. This could be accomplished by one of the states having a sufficiently large donor-acceptor distance or by the two states consisting of a bound state with high FRET and an unbound state with no FRET. Without the simplification noted above, the measured FRET would be proportional to the sum of the fraction of donors in each state weighted by that state's transfer efficiency (see Appendix B), and in this case we simply do not have sufficient molecular details to evaluate the individual donor fractions.

To remain consistent with the two-state picture, a Boltzmann function (Eq. 5.3) was used to fit the data by fixing the center of the fit function to be equal to the measured voltage of half-maximal charge movement ($V_{1/2}$ of NLC data). From the fit to the FRET data, we extracted the dimensionless parameter z_{FRET}, which is mathematically analogous to the NLC valence. The close agreement between z_{FRET} and z is consistent with our hypothesis that both charge movement and the motility parallel a voltage dependent conformational change in prestin. This idea has long

been suggested and is supported by electrophysiological observations [Santos-Sacchi, 1991]. In contrast, this work provides a correlation of NLC to an optical measure directly sensitive to prestin movement on the molecular level.

5.4.5 Relevance to continuous motor picture

We next consider an estimate of the distance from the FRET which comes from $(1/E-1)^{1/6}$ as is plotted in Fig. 5.12 since this quantity best describes a continuous model for electromotility such as the membrane bending model [Raphael et al., 2000]. The calculated distance is accurate solely in the case that 1) for any voltage there is a single donor-acceptor distance throughout the sample, and 2) 100% of the donors are undergoing FRET (i.e. no donors unpaired with acceptors). Both conditions would presumably be ensured in the positive FRET control experiment if prestin were a continuous motor and all fluorescent proteins folded properly. The case of cotransfection with prestin-CFP and prestin-YFP is far more complicated. However, if we assume the first condition is met and allow for the possibility that only a fraction of donors undergo FRET, the resulting distance calculation overestimates the real distance by a nearly constant systematic shift that depends on n_F as long as r/R_o is greater 1 (see Appendix B) Fig. B.1 and B.2). So under these assumptions the data in Fig. 5.12 is at least proportional to a true distance measurement. Indeed we find that the dimensionless parameter $z_{(r/R_o)}$, calculated from the width of a Boltzmann fit to the data, is in good agreement with the NLC valence z, (slightly better than the agreement z_{FRET} has with z) again providing support for the assumption that prestin associated charge movement parallels a conformational change in the prestin molecule. Furthermore, the calculated 1-2 nm change in distance between the FRET pairs is corroborated by other estimates of the conformational displacement of prestin

[Dallos and Fakler, 2002, Dallos et al., 1993]. Likewise, a 1-2 nm displacement could also easily be supported within the 8-11 nm structures observed from freeze fracture data [Gulley and Reese, 1977, Kalinec et al., 1992], and AFM [Murakoshi et al., 2006] and TEM imaging [Mio et al., 2008] that show similar magnitude, but larger sized prestin containing complexes. We also conclude that conformational changes that could result in a 1-2 nm displacement of C-terminal tags are not inconsistent with published estimates of cross-sectional area changes of 1 to 7 nm^2 [Adachi and Iwasa, 1999, Dong and Iwasa, 2004, Iwasa, 1993].

5.4.6 Salicylate affects prestin conformation

Salicylate is known to inhibit NLC and electromotility in cells expressing prestin [Kakehata and Santos-Sacchi, 1996]. We have shown that application of 10 mM salicylate to prestin transfected cells disrupts the FRET efficiency versus transmembrane voltage trend seen in Fig. 5.6. This further supports a link between prestin function and voltage dependent FRET. The inhibition results suggest that salicylate may allosterically bind to prestin causing a conformational change in the molecule that changes the character of the molecule. In other words, a prestin molecule with salicylate bound to it would have a different conformation, at each voltage, than it had without salicylate. Salicylate may destroy function by inducing a non-functional conformation having increased C-terminal interactions at depolarized transmembrane potentials as evidenced by the increased FRET at +60 mV (Fig. 5.8). This interpretation is supported by fluorescence polarization microscopy studies that suggest a direct interaction of salicylate with prestin [Greeson and Raphael, 2009]. We, however, do not rule out the possibility that salicylate indirectly affects prestin conformation by changing membrane properties. Since we measured FRET in the presence of sali-

cylate at only two potentials, the question remains as to whether salicylate places prestin into a conformation that is voltage independent. However, it is conceivable that prestin with salicylate bound to it can still undergo a voltage dependent conformational change that does not couple charge into the membrane. Such an example is presented by the voltage-dependent phosphatase (Ci-VSP) which has multiple transitions, only some of which induce currents [Villalba-Galea et al., 2008, 2009].

5.4.7 Conformational change involves movement of prestin C-terminus

Prestin has a large C-terminal domain containing a motif STAS that is conserved among the SLC26 family of transporters to which prestin belongs which is important for prestin function [Mount and Romero, 2004, Zheng et al., 2001, 2005]. However, the exact role of the C-terminus for prestin function as well as its involvement in a voltage dependent conformational change are unknown. Zheng et al. have shown that the C-terminus is important for membrane targeting, and that specific mutations in the C-terminus can eliminate NLC while preserving normal membrane targeting. Furthermore, the C-terminal domain of prestin has recently been crystallized, and the authors have identified a hydrophobic spot at its surface [Pasqualetto et al., 2010], composed of five residues, that likely weakly interacts with the lipid bilayer or with the transmembrane domain of prestin. The authors also demonstrate that placing the hydrophobic spot at the membrane would force the C-terminus to point inwards towards the cytosol. Also, the N-terminus of the STAS domain, which is only a few residues away from the last transmembrane domain, would be oriented directly at the lipid bilayer.

We have shown that depolarizing the membrane potential with blocking solution

significantly increases the energy transfer measured in the positive FRET control by over 70%. Since the positive FRET control consists of CFP and immediately YFP fused in tandem to the C-terminus of prestin, the change in FRET must result from a significant change in the relative orientation of the CFP and YFP chromophores which would modify the κ^2 factor buried in R_o in Eq. 5.1. This provides strong evidence that membrane depolarization causes a large movement or reorientation of the C-terminal domain that forces the two fluorescent proteins into a different relative orientation at depolarized potentials. It is possible that a voltage dependent conformational change of the transmembrane domain unbinds the membrane interacting hydrophobic spot [Pasqualetto et al., 2010] in the C-terminal region allowing a lever motion of the C-terminal domain. This would move the tandem fluorescent protein pair closer to or further from the membrane. Near the membrane, the pair of fluorescent proteins would be restricted in their range of relative motion compared to when prestin is in a conformation such that the pair is farther from the membrane which would result in a change in energy transfer. Our observation of a large change in FRET for the positive control construct provides strong evidence of a voltage dependent conformational change in prestin complementary to that provided by voltage dependent FRET of prestin-CFP prestin-YFP co-transfection.

Chapter 6

Conclusions

The following sections in this chapter summarize what we have learned from the three studies reported in this thesis. In addition, the limitations to forming conclusions from the data are presented. Finally, the remaining unknown aspects of prestin interactions with itself and the membrane are employed to motivate future studies.

6.1 Use of single molecule fluorescence to explore prestin oligomerization

In Ch. 3 we used single molecule fluorescence and brightness analysis to determine the stoichiometry of colocalized fluorescently tagged prestin in the cell membrane. We have shown that the intensities of fluorescent signals from colocalized prestin-citrine molecules are found at equally spaced values demonstrating that prestin aggregation likely does not involve interactions with the C-terminus and may instead involve interactions in the transmembrane domain. Due to reduced efficiency for detection of the dimmest signals in background fluorescence, we developed a fitting model that accounts for the effect of background noise on the brightness histogram. This allowed for an accurate accounting of the measured brightness histograms.

Using an analysis of signal brightness, we showed that prestin-citrine colocalizes in the cell membrane. We attempted to determine whether depletion of cholesterol

affects prestin-citrine oligomerization by using brightness analysis as an indicator of relative changes in colocalization. We found no difference between the brightness histograms from untreated cells and cells containing reduced membrane cholesterol concentration. However, it is likely that any differences in the distribution of prestin oligomeric states were masked due to excessive photobleaching prior to analysis.

We modified our initial analysis of measured prestin-citrine signals so that each citrine molecule in the sample that contributed to the analysis had an equal exposure to the excitation laser and therefore an equal probability to be in a fluorescent state. This allowed comparison of the measured distribution of signal brightness stoichiometries to a probabilistic model we developed. The model calculates the total probability to observe a set of brightness stoichiometries, given the distribution of a set of oligomeric states, by unifying the effects of random colocalization and photophysics of citrine. Comparison of the model to the measured distribution of brightness stoichiometries predicts that prestin exists as monomers, dimers, tetramers and possibly 8-mers. The model also predicts that tetramers and dimers are the predominant species with 2-3 times as many tetramers as dimers. The results of this chapter are the first directly measured estimates of prestin oligomeric state distribution *in situ*.

6.2 Diffusion of prestin using single particle tracking

In Ch. 4, we characterized prestin diffusion in the HEK cell in great detail using single particle tracking. Comparison of the full time course of *MSD* with a hop-diffusion model demonstrates that prestin undergoes hop-diffusion in a broad size range of confinements up to an area on the order of several μm^2. Depletion of membrane cholesterol increases the average confinement size and reduces the confinement

strength explaining previous results. Our results support the view that prestin localizes to cholesterol rich microdomains and that membrane cholesterol is a major source of confinement to prestin diffusion. Furthermore, our observations support the growing view that the microscale organization of prestin in the plasma membrane influences prestin function.

An analysis, at more than one time lag, of the statistical distribution of squared displacements (complementary to fitting *MSD* versus time) supports the results of fitting *MSD* to a hop-diffusion model. We find that depletion of membrane cholesterol causes a gap in the distribution of confinement sizes. We attribute the greater average confinement size to prestin to result from either the increased space between cholesterol rich microdomains or from the decrease in number of cytoskeletal "pickets" that corral prestin.

We propose modifications to a prior interpretation on the causal effect of membrane cholesterol on prestin function [Sfondouris et al., 2008]. Namely, the reason that decreases in membrane cholesterol cause a depolarizing shift in V_{pkc} could be because decreased crowding of prestin between domains results in greater conformational flexibility of prestin requiring a smaller membrane potential to induce a conformational change. Alternatively, removal of cholesterol rich microdomains, containing a fraction of prestin that is potentially functionally distinct from prestin outside the microdomains, could alter the overall function of prestin by allowing prestin molecules already outside the domains to assume a relatively increased importance on charge movement.

Finally, we have shown using a simple Monte Carlo simulation that a varying position resolution can cause significant error in determination of localization error offset Δ, and that it is important to measure Δ directly by measuring *MSD* of immobile particles. This error could be important in studies where precise knowledge of confinement offset is required to simultaneously infer domain size, confinement strength, and diffusion constant.

6.3 Voltage dependence of prestin self interactions

In Ch. 5 we provided evidence of voltage dependent prestin-prestin interactions. The decrease in C-terminal FRET with depolarization of transmembrane voltage could arise from either 1) a voltage triggered shift in the oligomeric state distribution, or 2) a change in conformation, within intact oligomers, that does not change oligomeric state. We also do not rule out the possibility that voltage dependent FRET may result from a complicated combination of these two scenarios.

Our data can be interpreted in the framework of either a continuous motor model or by a thermodynamically driven two-state area motor model. Distinguishing between the separate models is not possible here, and in fact it has been shown that distinguishing between a two-state and a multiple state or continuous model is experimentally difficult [Iwasa, 1997, Scherer and Gummer, 2005].

Width parameters of the fits to the data in either model are consistent with the measured valence of nonlinear charge movement ($z_{FRET} \sim z_{(r/Ro)} \sim z$). In addition, the range of membrane potentials over which the FRET efficiency changes is the same as that for nonlinear capacitance. This apparent coupling between charge movement

and the FRET voltage dependence suggests that prestin undergoes conformational changes in response to voltage in such a way that the interactions between their C-termini decrease with depolarization. Furthermore, we have supported the connection between voltage dependent FRET and prestin function by the observation that salicylate both inhibits NLC and disrupts the voltage dependent FRET trend, suggesting that both are a consequence of salicylate affecting the conformation of prestin.

We have also measured a striking 70% increase in FRET efficiency of a prestin construct containing a tandem CFP-YFP FRET pair upon membrane depolarization using blocking solution. We conclude that a molecular level description of the voltage dependent conformational change in prestin must include a significant change in orientation relative to the membrane of the C-terminal domain containing the STAS motif. This finding is particularly interesting in relation to the recently reported crystal structure of the prestin C-terminus showing a likely membrane-interacting hydrophobic spot [Pasqualetto et al., 2010] since it raises the possibility that a conformational change in the transmembrane domain of prestin unbinds the spot from the membrane allowing the C-terminus to change orientation.

Our reporting of voltage dependent FRET provides one of the first direct pieces of evidence that conformational changes in prestin occur in response to changes in transmembrane potential. These results strongly support the widely held view that a prestin conformational change is the underlying mechanism behind membrane based electromotility. Finally, our work supports the possibility of utilizing prestin as a high frequency FRET-based membrane voltage sensor.

6.4 Implications and relevant connections between experiments and between experiments and published results

6.4.1 Oligomerization and voltage dependent FRET

In Ch. 3 we found that the mean intensity of colocalized prestin-citrine populations were equally spaced in multiples of the single molecule intensity. This indicates a low degree of quenching between the citrine tags in colocalized regions. This observation is consistent with the overall low FRET efficiency obtained in the case of prestin-CFP and prestin-YFP co-transfection (Ch. 5). Assuming that the colocalization observed in Ch. 3 was predominantly due to oligomerization, this suggests that the extreme C-terminus of prestin subunits in an oligomer are spaced sufficiently far enough apart that interactions between the FPs are kept to a minimum at depolarized potentials. While speculative, this observation leads us to hypothesize that oligomerization between prestin subunits involves either the hydrophobic transmembrane region or the N-terminus. That the FRET efficiency increased significantly at extreme hyperpolarized potentials suggests that the extreme C-terminal ends of prestin molecules in an oligomer could come closer together as the membrane is hyperpolarized. One can only speculate on a physical picture of how this would translate into membrane area changes and charge movement. One possible picture is that the prestin STAS domains, within an oligomer in a contracted state, might be forced to point outward from the overall center of the molecule due to steric hindrance; and when the transmembrane domains expand space is created for the STAS domains so that they can rotate inward towards each other bringing their extreme C-terminal domains closer. We realize this picture is speculative and others are possible, but it would explain the observed voltage dependence of the FRET, the low amount of quenching in the

brightness analysis, and remain consistent with the idea that the prestin in in an extended state at hyperpolarized potentials.

One other point relating our oligomerization and voltage dependent FRET results is worth mentioning. In our discussion of interpreting the FRET as representing either the fraction of prestin molecules in a particular FRET state or as a separation between fluorescent tags, we emphasized that a single donor-acceptor distance in the sample is required for the connection to be strictly valid. If we accept the results of Ch. 3, namely that prestin can form multiple oligomeric states, then this requirement is clearly not met. We point this out to reiterate that too much emphasis should not be placed on distances or fractions implied by the FRET efficiency in Ch. 5. However, that we have observed a voltage dependence to the FRET at all, using two complementary methods of labeling prestin, still supports our main conclusions from this study that point to a voltage dependent structural change in the prestin molecule as the underlying mechanism behind prestin function.

6.4.2 Colocalization due to confinement

The diffusion results of Ch. 4 suggest an obvious implication relevant to the results of Ch. 3. We found that confinements to prestin of size $<\sim 142\,nm$ could still exist in the HEK cell even after depletion of cholesterol. If the apparently immobile component of the CDF does indeed correspond to such confinements, which would be of sub-diffraction limited size, multiple prestin molecules residing in them would be counted as colocalized in the brightness analysis. Accounting for this fact experimentally would require knowing the positions of individual prestin molecules within such small confinements.

6.4.3 Effect of compartmentalization on FRET

A previous study has reported that depletion of membrane cholesterol reduces the FRET efficiency measured in unpatched HEK cells transfected with C-terminal fusions of prestin with CFP and YFP FRET pairs [Rajagopalan et al., 2007]. In the same study, loading with cholesterol did not significantly change the FRET efficiency from native levels. This observation initially appears at odds with our observations from voltage dependent FRET measurements in Ch. 5. Since depletion of membrane cholesterol shifts the NLC relation in the depolarized direction and since we observe that FRET is higher at hyperpolarized potentials than at depolarized potentials, one might expect that cholesterol depletion should increase the FRET efficiency. There are several factors to consider when trying to reconcile these observations.

In Ch. 4 we found from analysis of *MSD* that the residence time in membrane confinements was reduced by a factor of four and that the average confinement size increased with depletion of cholesterol. The long residence time ($\sim 23\,s$) in confinement zones before cholesterol depletion could account for a portion of the FRET efficiency measured in Ch. 5 by increasing the probability that prestin molecules transiently come in close proximity to each other. The loss of FRET reported in Rajagopalan et al. might be explained by the reduced residence time and reduced number of confinements after cholesterol depletion. By the same token, a positive contribution to the change in FRET efficiency due to increased transient interactions with cholesterol loading might be balanced by a negative change due to the shifting of the voltage dependence. This might explain why increasing cholesterol levels did not significantly change the FRET efficiency [Rajagopalan et al., 2007].

Another important factor must be considered when trying to reconcile these results. It must be kept in mind that a specific FRET efficiency does not necessarily uniquely correspond to a specific conformation of the molecule. Restated, there is not necessarily a one-to-one mapping of FRET efficiency to conformation of the prestin molecule. Similarly, there is not necessarily a one-to-one mapping of charge moved to molecule conformation. Cholesterol could modify the energy profile of the prestin molecule such that different charged species (whether they be anions such as Cl^- or charged residues on the molecule) would be involved in charge movement at any voltage. An example illustrating this issue is provided by noting that an ortholog of prestin in chicken does not evoke somatic motility but does display NLC, albeit weaker than in mammalian prestin [Tan et al., 2011]. Taking into account this consideration, there is no reason to expect *a priori* that the FRET versus voltage relationship in the presence of modified cholesterol levels should be the same as we measured in Ch. 5. In fact, taking this point into consideration together with the observation that FRET is diminished upon cholesterol depletion could lead us to hypothesize that the FRET versus voltage relationship with reduced membrane cholesterol could have the opposite trend, namely FRET could increase with depolarization. As far as we know, the OHC-length versus voltage relationship has not been explicitly determined in reduced cholesterol conditions as it has for NLC. This information, in addition to measuring FRET voltage dependence in reduced cholesterol conditions, will help refine our understanding of how cholesterol manipulations tune prestin voltage sensitivity.

6.5 Limitations of results

6.5.1 Potential differences between HEK cells and OHCs

The unique structure and membrane environment of the OHC is sure to have important functional differences from that of HEK cells. We discussed the importance of the organized cortical lattice of the OHC in Ch. 4. In addition, however, the expression density of prestin by most accounts is higher in the OHC than in transfected cells based on estimates of intramembraneous particle (IMP) density and charge density [He et al., 2010, Iida et al., 2005, Murakoshi et al., 2006]. Estimates of the size of IMPs in OHCs tend to be higher than that in transfected Chinese hamster ovary cells (10-25 nm [Forge et al., 1991, He et al., 2010, Kalinec et al., 1992, LeGrimellec et al., 2002, Sinha et al., 2010] versus 8-12 nm [Murakoshi et al., 2006] respectively). If higher prestin density in OHCs affects the distribution of oligomeric states due to binding kinetics (i.e. K_d), then measurement of the oligomeric state distribution in HEKs may lack some relevance. In addition, OHCs from transgenic mice containing one prestin-null allele, and hence having reduced prestin expression, show a different distribution of IMP sizes and larger areas of membrane devoid of IMPs [He et al., 2010]. This observation has been interpreted to indicate that prestin could partially preclude the presence of other proteins due to the high density of packing, or that reduced expression could lead to different oligomeric state distribution in the OHC [He et al., 2010]. To what extent this is the case in transfected cells and whether it is functionally important remains unknown. The high density of prestin in OHCs may also affect the spatial organization of prestin in the membrane. Autocorrelation analysis of IMPs from AFM images of OHCs showed structural order reminiscent of a hexagonal array [Sinha et al., 2010]. The structure did however noticeably deviate

from a hexagonal array, and the order was only over short range with the spatial distribution being random beyond nearest neighbors. So far, such structure is not apparent from images of IMPs in transfected cells where the spatial distribution appears random. If a short range ordering of prestin is important for function, this aspect is likely missing in our experiments using HEK cells. Differences in the OHC plasma membrane structure could also affect prestin organization differently than in HEK cells. In Ch. 4 we showed that manipulations of membrane cholesterol alter the size of confinements in the HEK cell membrane consistent with prestin participation in cholesterol rich microdomains. Given the strong effect of cholesterol on the size and strength of the confinements, we have proposed that they are possibly the source of prestin sensitivity to cholesterol. However, it is not known whether microdomains enriched in cholesterol exist in OHCs, and estimates of cholesterol content in OHCs appear low [Ermilov et al., 2005, Rajagopalan et al., 2007]. It would therefore be useful to explore whether cholesterol dependent confinements to prestin also exist in the OHC.

6.5.2 Does salicylate "lock" the conformation of prestin?

In Ch. 5 we measured the FRET efficiency in the presence of salicylate at two of the membrane voltages tested without salicylate. The FRET efficiency at a depolarized extreme was significantly increased in the presence of salicylate indicating that a structural change in the molecule occurs in the presence of salicylate. This could mean that salicylate prevents the prestin molecule from undergoing voltage dependent structural changes. However, it could also be the case that the prestin molecule still undergoes voltage dependent conformational changes but that those conformational changes do not couple charge or area changes into the membrane. Since we measured

voltage dependent FRET at only two voltages and since the FRET efficiency was not significantly different between the two we cannot determine whether salicylate "locks" the conformation of prestin. Distinguishing between these scenarios would require measuring the FRET efficiency in the presence of salicylate at multiple membrane voltages to determine whether the FRET efficiency still changes as a function of voltage.

6.5.3 Potential mechanisms beyond oligomerization leading to prestin colocalization

The utility of the method of brightness analysis in Ch. 3 was to provide a method to count the brightness stoichiometries of colocalized fluorescent prestin molecules in the membrane. The precision of the brightness analysis method is limited by detection ability of the single molecule distribution, the number of spots collected, and the width of the single molecule distribution. Furthermore, the probabilistic models used in Ch. 3 are the exact calculation of brightness stoichiometry probabilities given known concentrations of a set of colocalization stoichiometries (which are the quantities ultimately sought), known overall probability of a molecule to be fluorescent, and known size of the region over which two molecules will appear colocalized. Incorporated together, brightness analysis and the probability calculations correct for the effects of photophysics and random colocalization and thereby in principle provide estimates of the real fractions of each colocalization stoichiometry. However, since any molecules localized to a diffraction limited region ($\sim 250\,nm$) are counted as colocalized, the effective spatial resolution of the method is limited to standard microscopic resolution. Furthermore, the method only allows a determination of the degree of colocalization beyond what would be expected purely randomly and there-

fore does not provide the source of the colocalization. While the probabilistic models employed in Ch. 3 assumed colocalization to be due to oligomerization, the observed colocalization could also be due to corralling in confinement zones or due to binding to other proteins. These factors were not taken into consideration when accounting for the observed brightness stoichiometries and must be taken into account to obtain a complete characterization of prestin oligomerization. However, we believe that our method of using brightness analysis still reflects that prestin tends to oligomerize in the membrane since it is hard to imagine how confinement zones could lead prestin monomers to colocalize in stoichiometries of $n = 2$ and $n = 4$ more than $n = 3$. Nonetheless, the fractions of each oligomeric state inferred from the probabilistic models in Ch. 3 could be in error. For example, it could be the case that there are far fewer tetramers than our estimates implied since confinement zones could simply corral dimers into apparent tetramers.

6.5.4 Unknown relationship between oligomerization and confinement

In Ch. 4 we measured the motions of fluorescent signals corresponding to what in most cases are probably single TMR fluorophores which are bound to prestin molecules in the HEK cell membrane. Obtaining a sufficiently low density of fluorescent signals required extensive photobleaching treatments. Each fluorescent signal tracked could correspond to one or to multiple prestin molecules bound together in a complex. Therefore, in using our method of measuring prestin diffusion, information on the oligomeric state of the molecule being tracked has been lost. This raises the question of whether the oligomeric state of prestin affects its diffusion in the HEK cell membrane. If the lipid bilayer were a simple 2-dimensional fluid, the answer would most probably be no. This is because the Saffman-Delbrück equation predicts a weak dependence of

the diffusion constant D on the diffusant size a, $D \sim \log\left(\frac{1}{a}\right)$ [Saffman and Delbrück, 1975]. However in real cell membranes, the environment is heterogeneous and the membrane is compartmentalized. Therefore in many if not all cases in real cells, the Saffman-Delbrück equation is too idealized a description. Even if it were true that on ultra-short timescales there would be little dependence on molecule size, on long timescales the size of a prestin aggregate could influence the strength of confinement within a membrane compartment. However, our present method leaves us unable to test the relationship between prestin oligomeric state and its diffusive behavior.

6.5.5 Limitations of voltage dependent FRET design

The results of Ch. 5 have provided important information supporting a voltage dependent structural change in the prestin molecule. However, we are ultimately interested in a detailed map of what the prestin molecule does as a function of voltage. Some structural design aspects of the fluorescent labeling strategies utilized in our FRET method have partially limited our ability to obtain a detailed and comprehensive description of the voltage dependent structural changes in prestin. Our first strategy employed a cotransfection with a single CFP or YFP on each prestin. While this method offers the advantage of allowing the FRET efficiency to depend on oligomerization, changes in prestin conformation within a single oligomer will also change the FRET efficiency if the process leads to a change in separation between the tags. Therefore, the cotransfection method alone does not allow us to distinguish between the two types of structural changes. Another feature of our method was due to our placement of each fluorescent protein on the prestin C-terminus. This has resulted in a relatively low FRET efficiency at all membrane potentials. While a constant high FRET efficiency at all membrane potentials would not necessarily be any more

useful at determining changes in prestin conformation, a high FRET efficiency using a cotransfection is the optimal configuration for determining changes in FRET due to changes in oligomerization. Perhaps the most limiting aspect of the cotransfection experiment is lack of control over the donor to acceptor expression ratio. As discussed in Ch. 5, this is the dominant source of cell to cell statistical error in the FRET efficiency. Our use of the positive FRET control has helped distinguish conformational changes from changes in oligomerization since both CFP and YFP are on a single prestin. It provides both a high FRET efficiency and a uniform donor to acceptor ratio as advantages. While it has proven useful in demonstrating that the STAS domain undergoes a certain degree of motion as a result of a structural change, since both FPs are in tandem the specific structural details are somewhat ambiguous. Obtaining further details of the voltage dependent structural changes in prestin will require additional labeling configurations.

6.6 Future work

6.6.1 Photoactivatable localization microscopy of prestin

Several of the limitations and remaining questions provided above could be to a large degree resolved by use of the powerful technique known as photoactivatable localization microscopy (PALM) [Greenfield et al., 2009, Hell, 2007]. PALM allows for the ability to obtain high resolution maps of the spatial locations of molecules in cells. By making use of photoactivatable fluorescent protein fusions, low numbers of molecules are stochastically made fluorescent in a controlled manner so that the probability of any two signals residing in close proximity can be made arbitrarily low. This method is therefore not limited by expression level — a crucial advantage to our experiments.

PALM could go a long way in quantifying to what degree corraling affects our determination of colocalization stoichiometries in fixed HEK cells. Whereas in Ch. 3 two prestin molecules $100\,nm$ apart in a membrane confinement would be deemed as colocalized, in a PALM image they would easily be distinguished as spatially separated and therefore could not be subunits in a single oligomer. Not knowing the "on" probability of prestin-citrine was a significant hurdle in Ch. 3. Since in a PALM image all molecules are in principle imaged until they each are photobleached, knowing the "on" probability is unnecessary as is precise quantification of the fluorescence. In this way, PALM images could provide precise measurements of prestin expression density. This measurement, supplemented with measurements of total nonlinear charge movement, would provide estimates of the average amount of charge moved per prestin molecule and would be far less model dependent than current estimates based on IMP density since it is unknown presently what portion of the IMPs are actually composed of prestin. The use of PALM imaging might also provide a visual map that clearly defines domains in which prestin molecules are aggregated into clusters. Qualitative and quantitative changes in the spatial distribution of the prestin molecules due to cholesterol manipulations could be determined. The size of the clusters could be compared to our results in Ch. 4 providing insight into the identity of the confinement zones in each size range both before and after cholesterol depletion. In addition, determining the local spatial density variations of prestin would allow an estimate of the degree to which clustering due to corralling could contribute to our measured FRET efficiency. By determining the frequency with which the fluorescent labels on prestin molecules come within a Förster radius of each other, an upper estimate for the contribution to the FRET efficiency can be estimated.

Using a live cell version of PALM to image the trajectories of prestin, we could further define the structure of membrane compartments [Hess et al., 2007]. Whereas in Ch. 4 long photobleaching treatments were required to obtain a low spatial density of signals, using PALM would allow visualizing the trajectories of many particles in a single cell. This would allow spatial visualization of membrane confinements in relation to each other within individual cells since the combined trajectories of an ensemble of particles would sample the entire area of the membrane.

The use of PALM in OHCs could prove to be particularly powerful. As discussed above (Sec. 6.5.1), it is unclear what fraction of the IMPs are composed of prestin since even OHCs from prestin-null mice contain IMPs of smaller size and since binding partners with prestin have recently been found. PALM in fixed OHCs could determine what portion of the IMPs are composed of prestin and could allow direct estimates of prestin expression density. Furthermore, in OHCs the spatial distribution of the IMPs in some studies appear to have a level of organization [Sinha et al., 2010]. The use of PALM to obtain super-resolution, high density spatial mapping of prestin could confirm this organization in OHCs. As discussed above, it is not known whether prestin exists in microdomains in the OHC. The use of PALM in both live and fixed OHCs, in conjunction with cholesterol manipulations, could determine whether microdomains enriched in cholesterol containing prestin exist in the OHC.

6.6.2 Voltage dependent FRET of prestin with plasma membrane utilizing farsenalated fluorescent proteins

In Ch. 5 we found evidence that a voltage dependent structural change in prestin is accompanied by a movement or rotation of the STAS domain. However, we could only speculate on the structural details of its motion due to our use of tandem FRET pairs. Specifically, does the STAS domain rotate about an axis perpendicular to the membrane or does the axis of rotation have a component parallel to the membrane? The latter would lead to a change in distance between the C-terminus and the membrane. It may even be the case that the STAS domain does not rotate, but that changes in area within the transmembrane domain translate into a modified position of STAS that resulted in changes in the allowed space for relative rotational diffusion of the FP tandem pairs. Changes in the rotational flexibility of the CFP and YFP pairs would result in a change in FRET efficiency due to the angular dependence of the Förster radius. As discussed in Ch. 5, the recent crystal structure of the prestin STAS domain showed that a hydrophobic spot on STAS exists that likely interacts with the membrane [Pasqualetto et al., 2010] raising the possibility that it could unbind as a result of a conformational change. Understanding the voltage dependent motion of the STAS domain is an important goal since STAS has been shown to be critical for prestin function [Mount and Romero, 2004, Zheng et al., 2001, 2005].

To obtain further specific structural details on the motion of STAS as a result of a voltage dependent conformational change, we propose to measure voltage dependent FRET between prestin-CFP and a farsenalated YFP (YFP-F) similar to the approaches performed in Chanda et al. and DiFranco et al. [Chanda et al., 2005b, DiFranco et al., 2007]. The farsenalation tag on the YFP serves as a membrane an-

chor. Measurement of voltage dependent FRET in this configuration would allow an estimate of the separation between the prestin C-terminus and the membrane. This would allow us to discriminate between the different possible motions of the STAS domain. The advantage of the method is that a relatively uniform distribution of donor acceptor separations would exist in the sample. If the FRET efficiency at either extreme of membrane potential were sufficiently high relative to the other extreme, this method would provide the exciting opportunity to make a fast voltage dependent FRET measurement by simply monitoring CFP fluorescence F as a function of holding potential. One could fit the voltage dependence of the fractional change in fluorescence $\Delta F/F$ to a Boltzmann function as performed in Ch. 5 and obtain more precise estimates of parameters relating to prestin function. In addition, one could in principle test the frequency dependence of a prestin conformational change. This configuration offers the possibility of serving as a high bandwidth membrane voltage sensor.

6.6.3 Use of "thinning out clusters while conserving stoichiometry of labeling" (TOCCSL)

Another experimental technique that could solve some of the hurdles in Ch. 3 is the method of "thinning out clusters while conserving stoichiometry of labeling" (TOCCSL) [Brameshuber et al., 2010, Moertelmaier et al., 2005]. The technique is essentially the same as that of the brightness analysis in Ch. 3, however it avoids the necessity of having to account for random colocalization, maximizes the "on" probability, and most importantly can be performed in live cells with high expression density. To perform TOCCSL, a small region of the cell membrane expressing fluorescently tagged protein is selectively bleached with laser light using high intensity, while

proteins outside the region preserve their labeling stoichiometry. Time is allowed for aggregates of protein to diffuse into the region after which they can start being imaged. By adjusting the time after bleaching the region, one can keep the density of protein aggregates low, and since proteins that have not yet been exposed to the laser enter the region, the "on" probability is maximized. The first frame upon imaging provides the information on stoichiometry. In addition, one can track the motions of the molecules in the subsequent frames to generate trajectories. The TOCCSL method could allow us to determine the relationship between prestin oligomeric state and its diffusive behavior.

Bibliography

M. Adachi and K. H. Iwasa. Electrically driven motor in the outer hair cell: effect of a mechanical constraint. *Proc Natl Acad Sci U S A*, 96(13):7244–7249, Jun 1999.

J. Akinlaja and F. Sachs. The breakdown of cell membranes by electrical and mechanical stress. *Biophys J*, 75(1):247–254, Jul 1998.

D. L. Andrews. A unified theory of radiative and radiationless molecular energy transfer. *Chemical Physics*, 135:195–201, 1989.

D. L. Andrews and D. S. Bradshaw. Virtual photons, dipole fields and energy transfer: a quantum electrodynamical approach. *Eur. J. Phys.*, 25:845–858, 2004.

J. Ashmore. Cochlear outer hair cell motility. *Physiol Rev*, 88(1):173–210, Jan 2008.

J. Ashmore, P. Avan, W. E. Brownell, P. Dallos, K. Dierkes, R. Fettiplace, K. Grosh, C. M. Hackney, A. J. Hudspeth, F. Jülicher, B. Lindner, P. Martin, J. Meaud, C. Petit, J. R Santos-Sacchi, and B. Canlon. The remarkable cochlear amplifier. *Hear Res*, 266(1-2):1–17, Jul 2010.

J. F. Ashmore. A fast motile response in guinea-pig outer hair cells: the cellular basis of the cochlear amplifier. *J Physiol*, 388:323–347, Jul 1987.

J. F. Ashmore. Forward and reverse transduction in the mammalian cochlea. *Neurosci Res Suppl*, 12:S39–S50, 1990.

J.F. Ashmore. Transducer motor coupling in cochlear outer hair cells. In D. Kemp and J.P. Wilson, editors, *Mechanics of Hearing*, pages 107–113. Plenum Press, 1989.

D. Axelrod, T. P. Burghardt, and N. L. Thompson. Total internal reflection fluorescence. *Annu Rev Biophys Bioeng*, 13:247–268, 1984.

J. Bai, D. Navaratnam, H. Samaranayake, and J. Santos-Sacchi. En block C-terminal charge cluster reversals in prestin (SLC26A5): effects on voltage-dependent electromechanical activity. *Neurosci Lett*, 404(3):270–275, Sep 2006.

J. Bai, A. Surguchev, Y. Ogando, L. Song, S. Bian, J. Santos-Sacchi, and D. Navaratnam. Prestin surface expression and activity are augmented by interaction with MAP1S, a microtubule-associated protein. *J Biol Chem*, 285(27):20834–20843, Jul 2010.

J. P. A. Bannister, B. Chanda, F. Bezanilla, and D. M. Papazian. Optical detection of rate-determining ion-modulated conformational changes of the ether-á-go-go K^+ channel voltage sensor. *Proc Natl Acad Sci U S A*, 102(51):18718–18723, Dec 2005.

F. J. Barrantes. Cholesterol effects on nicotinic acetylcholine receptor: cellular aspects. *Subcell Biochem*, 51:467–487, 2010.

D. Keith Bevington, Phillip R. Robinson. *Data Reduction and Error Analysis for the Physical Sciences.* McGraw Hill, second edition, 1992.

S. Bian, B. W. Koo, S. Kelleher, J. Santos-Sacchi, and D. S. Navaratnam. A highly expressing Tet-inducible cell line recapitulates in situ developmental changes in prestin's Boltzmann characteristics and reveals early maturational events. *Am J Physiol Cell Physiol*, 299(4):C828–C835, Oct 2010.

G. A. Blab, T. Schmidt, and M. Nilsson. Homogeneous detection of single rolling circle replication products. *Anal Chem*, 76(2):495–498, Jan 2004.

R. Blunck, D. M. Starace, A. M. Correa, and F. Bezanilla. Detecting rearrangements of Shaker and NaChBac in real-time with fluorescence spectroscopy in patch-clamped mammalian cells. *Biophys J*, 86(6):3966–3980, Jun 2004.

M. Brameshuber, J. Weghuber, V. Ruprecht, I. Gombos, I. Horvath, L. Vigh, P. Eckerstorfer, E. Kiss, H. Stockinger, and G. J. Schütz. Imaging of mobile long-lived nanoplatfroms in the live cell plasma membrane. *J Biol Chem*, Oct 2010.

W. E. Brownell, C. R. Bader, D. Bertrand, and Y. de Ribaupierre. Evoked mechanical responses of isolated cochlear outer hair cells. *Science*, 227(4683):194–196, Jan 1985.

D. Cai, K. J. Verhey, and E. Meyhöfer. Tracking single kinesin molecules in the cytoplasm of mammalian cells. *Biophys J*, 92(12):4137–4144, Jun 2007.

A. Cha, G. E. Snyder, P. R. Selvin, and F. Bezanilla. Atomic scale movement of the voltage-sensing region in a potassium channel measured via spectroscopy. *Nature*, 402(6763):809–813, Dec 1999.

J-M. Chambard and J. F. Ashmore. Sugar transport by mammalian members of the SLC26 superfamily of anion-bicarbonate exchangers. *J Physiol*, 550(Pt 3):667–677, Aug 2003.

B. Chanda, O. Kwame Asamoah, R. Blunck, B. Roux, and F. Bezanilla. Gating charge displacement in voltage-gated ion channels involves limited transmembrane movement. *Nature*, 436(7052):852–856, Aug 2005a.

B. Chanda, R. Blunck, L. C. Faria, F. E. Schweizer, I. Mody, and F. Bezanilla. A hybrid approach to measuring electrical activity in genetically specified neurons. *Nat Neurosci*, 8(11):1619–1626, Nov 2005b.

S. Chandrasekhar. Stochastic problems in physics and astronomy. *Rev Mod Phys*, 15: 1–89, 1943.

L. Cognet, F. Coussen, D. Choquet, and B. Lounis. Fluorescence microscopy of single autofluorescent proteins for cellular biology. *C. R. Physique*, 3:645–656, 2002.

M. E. Cuff, K. I. Miller, K. E. van Holde, and W. A. Hendrickson. Crystal structure of a functional unit from Octopus hemocyanin. *J Mol Biol*, 278(4):855–870, May 1998.

P. Dallos and B. Fakler. Prestin, a new type of motor protein. *Nat Rev Mol Cell Biol*, 3(2):104–111, Feb 2002.

P. Dallos, R. Hallworth, and B. N. Evans. Theory of electrically driven shape changes of cochlear outer hair cells. *J Neurophysiol*, 70(1):299–323, Jul 1993.

P. Dallos, X. Wu, M. A. Cheatham, J. Gao, J. Zheng, C. T. Anderson, S. Jia, X. Wang, W. H. Y. Cheng, S. Sengupta, D. Z. Z. He, and J. Zuo. Prestin-based outer hair cell motility is necessary for mammalian cochlear amplification. *Neuron*, 58(3): 333–339, May 2008.

Peter Dallos, Arthur N. Popper, and Richard R. Fay. *The Cochlea*. Springer, 1996.

D. S. Daniels, C. D. Mol, A. S. Arvai, S. Kanugula, A. E. Pegg, and J. A. Tainer. Active and alkylated human agt structures: a novel zinc site, inhibitor and extra-helical base binding. *EMBO J*, 19(7):1719–1730, Apr 2000.

F. Daumas, N. Destainville, C. Millot, A. Lopez, D. Dean, and L. Salomé. Confined diffusion without fences of a G-protein-coupled receptor as revealed by single particle tracking. *Biophys J*, 84(1):356–366, Jan 2003.

J. Boutet de Monvel, W. E. Brownell, and M. Ulfendahl. Lateral diffusion anisotropy and membrane lipid/skeleton interaction in outer hair cells. *Biophys J*, 91(1):364–381, Jul 2006.

L. Deák, J. Zheng, A. Orem, G-G. Du, S. Aguiñaga, K. Matsuda, and P. Dallos. Effects of cyclic nucleotides on the function of prestin. *J Physiol*, 563(Pt 2):483–496, Mar 2005.

Wolfgang Demtröder. *Laser Spectroscopy.* Springer-Verlag, 1998.

N. Destainville and L. Salomé. Quantification and correction of systematic errors due to detector time-averaging in single-molecule tracking experiments. *Biophys J*, 90 (2):L17–L19, Jan 2006.

S. Detro-Dassen, M. Schänzler, H. Lauks, I. Martin, S. Meyer zu Berstenhorst, D. Nothmann, D. Torres-Salazar, P. Hidalgo, G. Schmalzing, and C. Fahlke. Conserved dimeric subunit stoichiometry of SLC26 multifunctional anion exchangers. *J Biol Chem*, 283(7):4177–4188, Feb 2008.

R. M. Dickson, A. B. Cubitt, R. Y. Tsien, and W. E. Moerner. On/off blinking and switching behaviour of single molecules of green fluorescent protein. *Nature*, 388 (6640):355–358, Jul 1997.

C. Dietrich, B. Yang, T. Fujiwara, A. Kusumi, and K. Jacobson. Relationship of lipid rafts to transient confinement zones detected by single particle tracking. *Biophys J*, 82(1 Pt 1):274–284, Jan 2002.

M. DiFranco, J. Capote, M. Quiñonez, and J. L. Vergara. Voltage-dependent dynamic FRET signals from the transverse tubules in mammalian skeletal muscle fibers. *J Gen Physiol*, 130(6):581–600, Dec 2007.

X-X. Dong and K. H. Iwasa. Tension sensitivity of prestin: comparison with the membrane motor in outer hair cells. *Biophys J*, 86(2):1201–1208, Feb 2004.

C. G. dos Remedios and P. D. Moens. Fluorescence resonance energy transfer spectroscopy is a reliable "ruler" for measuring structural changes in proteins. Dispelling the problem of the unknown orientation factor. *J Struct Biol*, 115(2):175–185, 1995.

T. Dudez, F. Borot, S. Huang, B. R. Kwak, M. Bacchetta, M. Ollero, B. A. Stanton, and M. Chanson. CFTR in a lipid raft-TNFR1 complex modulates gap junctional intercellular communication and IL-8 secretion. *Biochim Biophys Acta*, 1783(5): 779–788, May 2008.

C. Eggeling, C. Ringemann, R. Medda, G. Schwarzmann, K. Sandhoff, S. Polyakova, V. N. Belov, B. Hein, C. von Middendorff, A. Schönle, and S. W. Hell. Direct observation of the nanoscale dynamics of membrane lipids in a living cell. *Nature*, 457(7233):1159–1162, Feb 2009.

J. Enderlein. Fluorescence detection of single molecules near a solution/glass interface - an electrodynamic analysis. *Chem Phys Lett*, 308:263–266, 1999.

J. Enderlein, D. L. Robbins, W. P. Ambrose, P. M. Goodwin, and R. A. Keller. The statistics of single molecule detection: an overview. *Bioimaging*, 5:88–98, 1997.

S. A. Ermilov, D. R. Murdock, D. El-Daye, W. E. Brownell, and B. Anvari. Effects of salicylate on plasma membrane mechanics. *J Neurophysiol*, 94(3):2105–2110, Sep 2005.

T. H. Evers, E. M. W. M. van Dongen, A. C. Faesen, E. W. Meijer, and M. Merkx. Quantitative understanding of the energy transfer between fluorescent proteins connected via flexible peptide linkers. *Biochemistry*, 45(44):13183–13192, Nov 2006.

J. Fang and K. H. Iwasa. Effects of chlorpromazine and trinitrophenol on the membrane motor of outer hair cells. *Biophys J*, 93(5):1809–1817, Sep 2007.

J. Fang, T. Sakata, G. Marriott, and K. H. Iwasa. Probing conformational changes of prestin with thiol-reactive optical switches. *Biophys J*, 95(6):3036–3042, Sep 2008.

J. Fang, C. Izumi, and K. H. Iwasa. Sensitivity of prestin-based membrane motor to membrane thickness. *Biophys J*, 98(12):2831–2838, Jun 2010.

R. Fettiplace and C. M. Hackney. The sensory and motor roles of auditory hair cells. *Nat Rev Neurosci*, 7(1):19–29, Jan 2006.

R. Fliegert, G. Glassmeier, F. Schmid, K. Cornils, S. Genisyuerek, A. Harneit, J. R. Schwarz, and A. H. Guse. Modulation of Ca^{2+} entry and plasma membrane potential by human TRPM4b. *FEBS J*, 274(3):704–713, Feb 2007.

A. Flock, B. Flock, and M. Ulfendahl. Mechanisms of movement in outer hair cells and a possible structural basis. *Arch Otorhinolaryngol*, 243(2):83–90, 1986.

A. Forge, S. Davies, and G. Zajic. Assessment of ultrastructure in isolated cochlear hair cells using a procedure for rapid freezing before freeze-fracture and deep-etching. *J Neurocytol*, 20(6):471–484, Jun 1991.

T. Förster. Intermolecular energy migration and fluorescence. *Ann Phys*, 2:55–75, 1948.

G. Frank, W. Hemmert, and A. W. Gummer. Limiting dynamics of high-frequency electromechanical transduction of outer hair cells. *Proc Natl Acad Sci U S A*, 96 (8):4420–4425, Apr 1999.

G. I. Frolenkov, M. Atzori, F. Kalinec, F. Mammano, and B. Kachar. The membrane-based mechanism of cell motility in cochlear outer hair cells. *Mol Biol Cell*, 9(8): 1961–1968, Aug 1998.

T. Fujiwara, K. Ritchie, H. Murakoshi, K. Jacobson, and A. Kusumi. Phospholipids undergo hop diffusion in compartmentalized cell membrane. *J Cell Biol*, 157(6): 1071–1081, Jun 2002.

M. F. Garcia-Parajo, G. M. Segers-Nolten, J. A. Veerman, J. Greve, and N. F. van Hulst. Real-time light-driven dynamics of the fluorescence emission in single green fluorescent protein molecules. *Proc Natl Acad Sci U S A*, 97(13):7237–7242, Jun 2000.

C. Daniel Geisler. *From Sound to Synapse Physiology of The Mammalian Ear.* Oxford University Press, 1998.

K. Giebel, C. Bechinger, S. Herminghaus, M. Riedel, P. Leiderer, U. Weiland, and M. Bastmeyer. Imaging of cell/substrate contacts of living cells with surface plasmon resonance microscopy. *Biophys J*, 76(1 Pt 1):509–516, Jan 1999.

K. R. Gleitsman, M. Tateyama, and Y. Kubo. Structural rearrangements of the motor protein prestin revealed by fluorescence resonance energy transfer. *Am J Physiol Cell Physiol*, 297(2):C290–C298, Aug 2009.

T. Gold. Hearing. II. The physical basis of the action of the cochlea. *Proc R Soc Lond B Biol Sci*, 135:492–498, 1948.

M. Goulian and S. M. Simon. Tracking single proteins within cells. *Biophys J*, 79(4): 2188–2198, Oct 2000.

M. A. Gray. Bicarbonate secretion: it takes two to tango. *Nat Cell Biol*, 6(4):292–294, Apr 2004.

D. Greenfield, A. L. McEvoy, H. Shroff, G. E. Crooks, N. S. Wingreen, E. Betzig, and J. Liphardt. Self-organization of the Escherichia coli chemotaxis network imaged with super-resolution light microscopy. *PLoS Biol*, 7(6):e1000137, Jun 2009.

J. N. Greeson and R. M. Raphael. Amphipath-induced nanoscale changes in outer hair cell plasma membrane curvature. *Biophys J*, 96(2):510–520, Jan 2009.

J. N. Greeson, L. E. Organ, F. A. Pereira, and R. M. Raphael. Assessment of prestin self-association using fluorescence resonance energy transfer. *Brain Res*, 1091(1): 140–150, May 2006.

Jennifer N. Greeson. *Invesigating the Role of the Outer Hair Cell Plasma Membrane in Electromotility and Prestin Function Using Quantitative Optical Microscopy Techniques*. PhD thesis, Rice University, 2008.

O. Griesbeck, G. S. Baird, R. E. Campbell, D. A. Zacharias, and R. Y. Tsien. Reducing the environmental sensitivity of yellow fluorescent protein. Mechanism and applications. *J Biol Chem*, 276(31):29188–29194, Aug 2001.

R. L. Gulley and T. S. Reese. Regional specialization of the hair cell plasmalemma in the organ of corti. *Anat Rec*, 189(1):109–123, Sep 1977.

A. W. Gummer. *Biophysics of the Cochlea from Molecules to Models*. World Scientific, 2003.

G. S. Harms, L. Cognet, P. H. Lommerse, G. A. Blab, H. Kahr, R. Gamsjäger, H. P. Spaink, N. M. Soldatov, C. Romanin, and T. Schmidt. Single-molecule imaging of L-type Ca(2+) channels in live cells. *Biophys J*, 81(5):2639–2646, Nov 2001a.

G. S. Harms, L. Cognet, P. H. Lommerse, G. A. Blab, and T. Schmidt. Autofluorescent proteins in single-molecule research: applications to live cell imaging microscopy. *Biophys J*, 80(5):2396–2408, May 2001b.

D. Z. Z. He, J. Zheng, F. Kalinec, S. Kakehata, and J. Santos-Sacchi. Tuning in to the amazing outer hair cell: Membrane wizardry with a twist and shout. *J. Membrane Biol.*, 209:119–134, 2006.

D. Z. Z. He, S. Jia, T. Sato, J. Zuo, L. R. Andrade, G. P. Riordan, and B. Kachar. Changes in plasma membrane structure and electromotile properties in prestin deficient outer hair cells. *Cytoskeleton (Hoboken)*, 67(1):43–55, Jan 2010.

D. N. Hebert and A. Carruthers. Glucose transporter oligomeric structure determines transporter function. Reversible redox-dependent interconversions of tetrameric and dimeric GLUT1. *J Biol Chem*, 267(33):23829–23838, Nov 1992.

H. Heerklotz. Triton promotes domain formation in lipid raft mixtures. *Biophys J*, 83(5):2693–2701, Nov 2002.

A. A. Heikal, S. T. Hess, G. S. Baird, R. Y. Tsien, and W. W. Webb. Molecular spectroscopy and dynamics of intrinsically fluorescent proteins: coral red (dsRed) and yellow (Citrine). *Proc Natl Acad Sci U S A*, 97(22):11996–12001, Oct 2000.

S. W. Hell. Far-field optical nanoscopy. *Science*, 316(5828):1153–1158, May 2007.

S. T. Hess, T. J. Gould, M. V. Gudheti, S. A. Maas, K. D. Mills, and J. Zimmerberg. Dynamic clustered distribution of hemagglutinin resolved at 40 nm in living cell membranes discriminates between raft theories. *Proc Natl Acad Sci U S A*, 104 (44):17370–17375, Oct 2007.

K. Homma and P. Dallos. Evidence that prestin has at least two voltage-dependent steps. *J Biol Chem*, 286(3):2297–2307, Jan 2011.

K. Homma, K. K. Miller, C. T. Anderson, S. Sengupta, G-G. Du, S. Aguiñaga, M. Cheatham, P. Dallos, and J. Zheng. Interaction between CFTR and prestin (SLC26A5). *Biochim Biophys Acta*, 1798(6):1029–1040, Jun 2010.

M. Howarth, D. J-F. Chinnapen, K. Gerrow, P. C. Dorrestein, M. R. Grandy, N. L. Kelleher, A. El-Husseini, and A. Y. Ting. A monovalent streptavidin with a single femtomolar biotin binding site. *Nat Methods*, 3(4):267–273, Apr 2006.

G. Huang and J. Santos-Sacchi. Mapping the distribution of the outer hair cell motility voltage sensor by electrical amputation. *Biophys J*, 65(5):2228–2236, Nov 1993.

K. Iida, K. Tsumoto, K. Ikeda, I. Kumagai, T. Kobayashi, and H. Wada. Construction of an expression system for the motor protein prestin in Chinese hamster ovary cells. *Hear Res*, 205(1-2):262–270, Jul 2005.

K. H. Iwasa. Effect of stress on the membrane capacitance of the auditory outer hair cell. *Biophys J*, 65(1):492–498, Jul 1993.

K. H. Iwasa. A membrane motor model for the fast motility of the outer hair cell. *J Acoust Soc Am*, 96(4):2216–2224, Oct 1994.

K. H. Iwasa. Current noise spectrum and capacitance due to the membrane motor of the outer hair cell: theory. *Biophys J*, 73(6):2965–2971, Dec 1997.

B. Kachar, W. E. Brownell, R. Altschuler, and J. Fex. Electrokinetic shape changes of cochlear outer hair cells. *Nature*, 322(6077):365–368, 1986.

S. Kakehata and J. Santos-Sacchi. Effects of salicylate and lanthanides on outer hair cell motility and associated gating charge. *J Neurosci*, 16(16):4881–4889, Aug 1996.

F. Kalinec, M. C. Holley, K. H. Iwasa, D. J. Lim, and B. Kachar. A membrane-based force generation mechanism in auditory sensory cells. *Proc Natl Acad Sci U S A*, 89(18):8671–8675, Sep 1992.

A. K. Kenworthy. Imaging protein-protein interactions using fluorescence resonance energy transfer microscopy. *Methods*, 24(3):289–296, Jul 2001.

D. Klostermeier and D. P. Millar. Time-resolved fluorescence resonance energy transfer: a versatile tool for the analysis of nucleic acids. *Biopolymers*, 61(3):159–179, 2001.

M. K. Knowles, S. Barg, L. Wan, M. Midorikawa, X. Chen, and W. Almers. Single secretory granules of live cells recruit syntaxin-1 and synaptosomal associated protein 25 (SNAP-25) in large copy numbers. *Proc Natl Acad Sci U S A*, 107(48): 20810–20815, Nov 2010.

E. Kobrinsky, K. J. F. Kepplinger, A. Yu, J. B. Harry, H. Kahr, C. Romanin, D. R. Abernethy, and N. M. Soldatov. Voltage-gated rearrangements associated with differential beta-subunit modulation of the L-type Ca^{2+} channel inactivation. *Biophys J*, 87(2):844–857, Aug 2004.

I. Kotera, T. Iwasaki, H. Imamura, H. Noji, and T. Nagai. Reversible dimerization of Aequorea victoria fluorescent proteins increases the dynamic range of FRET-based indicators. *ACS Chem Biol*, 5(2):215–222, Feb 2010.

A. Kusumi and Y. Sako. Cell surface organization by the membrane skeleton. *Curr Opin Cell Biol*, 8(4):566–574, Aug 1996.

A. Kusumi, C. Nakada, K. Ritchie, K. Murase, K. Suzuki, H. Murakoshi, R. S. Kasai, J. Kondo, and T. Fujiwara. Paradigm shift of the plasma membrane concept from the two-dimensional continuum fluid to the partitioned fluid: high-speed single-molecule tracking of membrane molecules. *Annu Rev Biophys Biomol Struct*, 34: 351–378, 2005.

Joseph R. Lakowicz. *Principles of fluorescence spectroscopy.* Kluwer Academic/Plenum, 2nd edition, 1999.

R. Lasserre, X-J. Guo, F. Conchonaud, Y. Hamon, O. Hawchar, A-M. Bernard, S. M'Homa Soudja, P-F. Lenne, H. Rigneault, D. Olive, G. Bismuth, J. A. Nunès, B. Payrastre, D. Marguet, and H-T. He. Raft nanodomains contribute to Akt/PKB plasma membrane recruitment and activation. *Nat Chem Biol*, 4(9):538–547, Sep 2008.

G. M. Lee, A. Ishihara, and K. A. Jacobson. Direct observation of brownian motion of lipids in a membrane. *Proc Natl Acad Sci U S A*, 88(14):6274–6278, Jul 1991.

C. LeGrimellec, M-C. Giocondi, M. Lenoir, M. Vater, G. Sposito, and R. Pujol. High-resolution three-dimensional imaging of the lateral plasma membrane of cochlear outer hair cells by atomic force microscopy. *J Comp Neurol*, 451(1):62–69, Sep 2002.

M. Lindau and E. Neher. Patch-clamp techniques for time-resolved capacitance measurements in single cells. *Pflugers Arch*, 411(2):137–146, Feb 1988.

D. Lingwood and K. Simons. Lipid rafts as a membrane-organizing principle. *Science*, 327(5961):46–50, Jan 2010.

J. Ludwig, D. Oliver, G. Frank, N. Klöcker, A. W. Gummer, and B. Fakler. Reciprocal electromechanical properties of rat prestin: the motor molecule from rat outer hair cells. *Proc Natl Acad Sci U S A*, 98(7):4178–4183, Mar 2001.

D. S. Martin, M. B. Forstner, and J. A. Käs. Apparent subdiffusion inherent to single particle tracking. *Biophys J*, 83(4):2109–2117, Oct 2002.

S. Mayor and R. E. Pagano. Pathways of clathrin-independent endocytosis. *Nat Rev Mol Cell Biol*, 8(8):603–612, Aug 2007.

R. M. McGuire, H. Liu, F. A. Pereira, and R. M. Raphael. Cysteine mutagenesis reveals transmembrane residues associated with charge translocation in prestin. *J Biol Chem*, 285(5):3103–3113, Jan 2010.

K. Mio, Y. Kubo, T. Ogura, T. Yamamoto, F. Arisaka, and C. Sato. The motor protein prestin is a bullet-shaped molecule with inner cavities. *J Biol Chem*, 283 (2):1137–1145, Jan 2008.

W. E. Moerner, E. J. Peterman, S. Brasselet, S. Kummer, and R. M. Dickson. Optical methods for exploring dynamics of single copies of green fluorescent protein. *Cytometry*, 36(3):232–238, Jul 1999.

M. Moertelmaier, M. Brameshuber, M. Linimeier, G. J. Schütz, and H. Stockinger.

Thinning out clusters while conserving stoichiometry of labeling. *Appl Phys Lett*, 87:263903, 2005.

D. B. Mount and M. F. Romero. The SLC26 gene family of multifunctional anion exchangers. *Pflugers Arch*, 447(5):710–721, Feb 2004.

D. Muallem and J. Ashmore. An anion antiporter model of prestin, the outer hair cell motor protein. *Biophys J*, 90(11):4035–4045, Jun 2006.

S. Munro. Lipid rafts: elusive or illusive? *Cell*, 115(4):377–388, Nov 2003.

M. Murakoshi, T. Gomi, K. Iida, S. Kumano, K. Tsumoto, I. Kumagai, K. Ikeda, T. Kobayashi, and H. Wada. Imaging by atomic force microscopy of the plasma membrane of prestin-transfected Chinese hamster ovary cells. *J Assoc Res Otolaryngol*, 7(3):267–278, Sep 2006.

K. Murase, T. Fujiwara, Y. Umemura, K. Suzuki, R. Iino, H. Yamashita, M. Saito, H. Murakoshi, K. Ritchie, and A. Kusumi. Ultrafine membrane compartments for molecular diffusion as revealed by single molecule techniques. *Biophys J*, 86(6): 4075–4093, Jun 2004.

S. A. Mutch, B. S. Fujimoto, C. L. Kuyper, J. S. Kuo, S. M. Bajjalieh, and D. T. Chiu. Deconvolving single-molecule intensity distributions for quantitative microscopy measurements. *Biophys J*, 92(8):2926–2943, Apr 2007.

K. Nakajo, M. H. Ulbrich, Y. Kubo, and E. Y. Isacoff. Stoichiometry of the KCNQ1 - KCNE1 ion channel complex. *Proc Natl Acad Sci U S A*, 107(44):18862–18867, Nov 2010.

D. Navaratnam, J-P. Bai, H. Samaranayake, and J. Santos-Sacchi. N-terminal-mediated homomultimerization of prestin, the outer hair cell motor protein. *Biophys J*, 89(5):3345–3352, Nov 2005.

E. G. Navarrete and J. Santos-Sacchi. On the effect of prestin on the electrical breakdown of cell membranes. *Biophys J*, 90(3):967–974, Feb 2006.

P. V. Nazarov, R. B. M. Koehorst, W. L. Vos, V. V. Apanasovich, and M. A. Hemminga. FRET study of membrane proteins: determination of the tilt and orientation of the N-terminal domain of M13 major coat protein. *Biophys J*, 92(4): 1296–1305, Feb 2007.

T. Ohashi, S. D. Galiacy, G. Briscoe, and H. P. Erickson. An experimental study of GFP-based FRET, with application to intrinsically unstructured proteins. *Protein Sci*, 16(7):1429–1438, Jul 2007.

D. Oliver and B. Fakler. Expression density and functional characteristics of the outer hair cell motor protein are regulated during postnatal development in rat. *J Physiol*, 519 Pt 3:791–800, Sep 1999.

D. Oliver, D. Z. He, N. Klöcker, J. Ludwig, U. Schulte, S. Waldegger, J. P. Ruppersberg, P. Dallos, and B. Fakler. Intracellular anions as the voltage sensor of prestin, the outer hair cell motor protein. *Science*, 292(5525):2340–2343, Jun 2001.

L. E. Organ and R. M. Raphael. Application of fluorescence recovery after photobleaching to study prestin lateral mobility in the human embryonic kidney cell. *J Biomed Opt*, 12(2):021003, 2007.

L. E. Organ and R. M. Raphael. Lipid lateral mobility in cochlear outer hair cells:

regional differences and regulation by cholesterol. *J Assoc Res Otolaryngol*, 10(3): 383–396, Sep 2009.

Louise E Organ. *Invesigating the Lateral Mobility of Outer Hair Cell Plasma Membrane Constituents by Fluorescence Recovery After Photobleaching.* PhD thesis, Rice University, 2008.

M. Ormö, A. B. Cubitt, K. Kallio, L. A. Gross, R. Y. Tsien, and S. J. Remington. Crystal structure of the Aequorea Victoria green fluorescent protein. *Science*, 273 (5280):1392–1395, Sep 1996.

M. Parsons, B. Vojnovic, and S. Ameer-Beg. Imaging protein-protein interactions in cell motility using fluorescence resonance energy transfer (FRET). *Biochem Soc Trans*, 32(Pt3):431–433, Jun 2004.

E. Pasqualetto, A. Seydel, A. Pellini, and R. Battistutta. Expression, purification and characterisation of the C-terminal STAS domain of the SLC26 anion transporter prestin. *Protein Expr Purif*, 58(2):249–256, Apr 2008.

E. Pasqualetto, R. Aiello, L. Gesiot, G. Bonetto, M. Bellanda, and R. Battistutta. Structure of the cytosolic portion of the motor protein prestin and functional role of the STAS domain in SLC26/SulP anion transporters. *J Mol Biol*, 400(3):448–462, Jul 2010.

E. J. G. Peterman, S. Brasselet, and W. E. Moerner. The fluorescence dynamics of single molecules of green fluorescent protein. *J Phys Chem*, 103:10553–10560, 1999.

E. M. Phizicky and S. Fields. Protein-protein interactions: methods for detection and analysis. *Microbiol Rev*, 59(1):94–123, Mar 1995.

M. S. Podgorski. *Structural Characterization of the C-terminus of the Cochlear Motor Protein Prestin: Intrinsic Disorder Linked to Voltage Sensor Function.* PhD thesis, University of Tennessee, 2009.

D. J. Posson, P. Ge, C. Miller, F. Bezanilla, and P. R. Selvin. Small vertical movement of a K^+ channel voltage sensor measured with luminescence energy transfer. *Nature*, 436(7052):848–851, Aug 2005.

J. G. Powles, M. J. D. Mallett, G. Rickayzen, and W. A. B. Evans. Exact analytic solutions for diffusion impeded by an infinite array of partially permeable barriers. *Proceedings: Mathematical and Physical Sciences*, 436(1897):391–403, 1992.

S. Preyer, A. Baisch, D. Bless, and A. W. Gummer. Distortion product otoacoustic emissions in human hypercholesterolemia. *Hear Res*, 152(1-2):139–151, Feb 2001.

I. A. Prior, C. Muncke, R. G. Parton, and J. F. Hancock. Direct visualization of Ras proteins in spatially distinct cell surface microdomains. *J Cell Biol*, 160(2): 165–170, Jan 2003.

L. Rajagopalan, J. N. Greeson, A. Xia, H. Liu, A. Sturm, R. M. Raphael, A. L. Davidson, J. S. Oghalai, F. A. Pereira, and W. E. Brownell. Tuning of the outer hair cell motor by membrane cholesterol. *J Biol Chem*, 282(50):36659–36670, Dec 2007.

L. Rajagopalan, L. E. Organ-Darling, H. L., A. L. Davidson, R. M. Raphael, W. E. Brownell, and F. A. Pereira. Glycosylation regulates prestin cellular activity. *J Assoc Res Otolaryngol*, 11(1):39–51, Mar 2010.

Lavanya Rajagopalan, Nimish Patel, Srinivasan Madabushi, Julie Anne Goddard, Venkat Anjan, Feng Lin, Cindy Shope, Brenda Farrell, Olivier Lichtarge, Amy L

Davidson, William E Brownell, and Fred A Pereira. Essential helix interactions in the anion transporter domain of prestin revealed by evolutionary trace analysis. *J Neurosci*, 26(49):12727–12734, Dec 2006.

R. M. Raphael, A. S. Popel, and W. E. Brownell. A membrane bending model of outer hair cell electromotility. *Biophys J*, 78(6):2844–2862, Jun 2000.

A. Rekas, J-R. Alattia, T. Nagai, A. Miyawaki, and M. Ikura. Crystal structure of venus, a yellow fluorescent protein with improved maturation and reduced environmental sensitivity. *J Biol Chem*, 277(52):50573–50578, Dec 2002.

K. Ritchie, X-Y. Shan, J. Kondo, K. Iwasawa, T. Fujiwara, and A. Kusumi. Detection of non-Brownian diffusion in the cell membrane in single molecule tracking. *Biophys J*, 88(3):2266–2277, Mar 2005.

C. Rivetti, M. Guthold, and C. Bustamante. Scanning force microscopy of DNA deposited onto mica: equilibration versus kinetic trapping studied by statistical polymer chain analysis. *J Mol Biol*, 264(5):919–932, Dec 1996.

V. Rybalchenko and J. Santos-Sacchi. Anion control of voltage sensing by the motor protein prestin in outer hair cells. *Biophys J*, 95(9):4439–4447, Nov 2008.

P. G. Saffman and M. Delbrück. Brownian motion in biological membranes. *Proc Natl Acad Sci U S A*, 72(8):3111–3113, Aug 1975.

J. Santos-Sacchi. Fast outer hair cell motility: how fast is fast? In P. Dallos, C.D. Geisler, J.W. Matthews, M.A. Ruggero, and C.R. Steele, editors, *The Mechanics and Biophysics of Hearing*, pages 69–75. Springer-Verlag, 1990.

J. Santos-Sacchi. Reversible inhibition of voltage-dependent outer hair cell motility and capacitance. *J Neurosci*, 11(10):3096–3110, Oct 1991.

J. Santos-Sacchi and H-B. Zhao. Excitation of fluorescent dyes inactivates the outer hair cell integral membrane motor protein prestin and betrays its lateral mobility. *Pflugers Arch*, 446(5):617–622, Aug 2003.

Joseph Santos-Sacchi. Functional motor microdomains of the outer hair cell lateral membrane. *Pflugers Arch*, 445(3):331–336, Dec 2002.

M. J. M. Schaaf, W. J. A. Koopmans, T. Meckel, J. van Noort, B. E. Snaar-Jagalska, T. S. Schmidt, and H. P. Spaink. Single-molecule microscopy reveals membrane microdomain organization of cells in a living vertebrate. *Biophys J*, 97(4):1206–1214, Aug 2009.

M. P. Scherer and A. W. Gummer. How many states can the motor molecule, prestin, assume in an electric field? *Biophys J*, 88(5):L27–L29, May 2005.

T. Schmidt, G. J. Schütz, W. Baumgartner, H. J. Gruber, and H. Schindler. Characterization of photophysics and mobility of single molecules in a fluid lipid-membrane. *Journal of Physical Chemistry*, 99:17662–17668, 1995.

T. Schmidt, G. J. Schütz, W. Baumgartner, H. J. Gruber, and H. Schindler. Imaging of single molecule diffusion. *Proc Natl Acad Sci U S A*, 93(7):2926–2929, Apr 1996a.

T. Schmidt, G. J. Schütz, H. J. Gruber, and H. Schindler. Local stoichiometries determined by counting individual molecules. *Analytical Chemistry*, 68:4397–4401, 1996b.

B. Schuler and W. A. Eaton. Protein folding studied by single-molecule FRET. *Curr Opin Struct Biol*, 18(1):16–26, Feb 2008.

G. J. Schütz, H. Schindler, and T. Schmidt. Single-molecule microscopy on model membranes reveals anomalous diffusion. *Biophys J*, 73(2):1073–1080, Aug 1997.

G. J. Schütz, G. Kada, V. P. Pastushenko, and H. Schindler. Properties of lipid microdomains in a muscle cell membrane visualized by single molecule microscopy. *EMBO J*, 19(5):892–901, Mar 2000.

P. Schwille, S. Kummer, A. A. Heikal, W. E. Moerner, and W. W. Webb. Fluorescence correlation spectroscopy reveals fast optical excitation-driven intramolecular dynamics of yellow fluorescent proteins. *Proc Natl Acad Sci U S A*, 97(1):151–156, Jan 2000.

J. Sfondouris, L. Rajagopalan, F. A. Pereira, and W. E. Brownell. Membrane composition modulates prestin-associated charge movement. *J Biol Chem*, 283(33): 22473–22481, Aug 2008.

P. Sharma, R. Varma, R. C. Sarasij, Ira, K. Gousset, G. Krishnamoorthy, M. Rao, and S. Mayor. Nanoscale organization of multiple GPI-anchored proteins in living cell membranes. *Cell*, 116(4):577–589, Feb 2004.

M. P. Sheetz, M. Schindler, and D. E. Koppel. Lateral mobility of integral membrane proteins is increased in spherocytic erythrocytes. *Nature*, 285(5765):510–511, Jun 1980.

X. Shi, J. Basran, H. E. Seward, W. Childs, C. R. Bagshaw, and S. G. Boxer. Anomalous negative fluorescence anisotropy in yellow fluorescent protein (YFP

10C): quantitative analysis of FRET in YFP dimers. *Biochemistry*, 46(50):14403–14417, Dec 2007.

J. R. Silvius. Role of cholesterol in lipid raft formation: lessons from lipid model systems. *Biochim Biophys Acta*, 1610(2):174–183, Mar 2003.

K. Simons and E. Ikonen. Functional rafts in cell membranes. *Nature*, 387(6633): 569–572, Jun 1997.

S. J. Singer and G. L. Nicolson. The fluid mosaic model of the structure of cell membranes. *Science*, 175(23):720–731, Feb 1972.

G. P. Sinha, F. Sabri, E. K. Dimitriadis, and K. H. Iwasa. Organization of membrane motor in outer hair cells: an atomic force microscopic study. *Pflugers Arch*, 459 (3):427–439, Feb 2010.

A. A. Spector, N. Deo, K. Grosh, J. T. Ratnanather, and R. M. Raphael. Electromechanical models of the outer hair cell composite membrane. *J Membr Biol*, 209 (2-3):135–152, 2006.

R. Steinmeyer, A. Noskov, C. Krasel, I. Weber, C. Dees, and G. S. Harms. Improved fluorescent proteins for single-molecule research in molecular tracking and co-localization. *J Fluoresc*, 15(5):707–721, Sep 2005.

K. Stock, R. Sailer, W. S. L. Strauss, M. Lyttek, R. Steiner, and H. Schneckenburger. Variable-angle total internal reflection fluorescence microscopy (VA-TIRFM): realization and application of a compact illumination device. *J Microsc*, 211(Pt 1): 19–29, Jul 2003.

A. K. Sturm, L. Rajagopalan, D. Yoo, W. E. Brownell, and F. A. Pereira. Functional expression and microdomain localization of prestin in cultured cells. *Otolaryngol Head Neck Surg*, 136(3):434–439, Mar 2007.

K. Suzuki, K. Ritchie, E. Kajikawa, T. Fujiwara, and A. Kusumi. Rapid hop diffusion of a G-protein-coupled receptor in the plasma membrane as revealed by single-molecule techniques. *Biophys J*, 88(5):3659–3680, May 2005.

T. Tadenuma, K. Iida, M. Murakoshi, S. Kumano, K. Tsumoto, K. Ikeda, T. Kobayashi, I. Kumagai, and H. Wada. Functional expression of prestin, the outer hair cell motor protein, using the baculovirus/insect cell system. *Journal of Biomechanical Science and Engineering*, 3:287–298, 2008.

S. Takahashi and J. Santos-Sacchi. Non-uniform mapping of stress-induced, motility-related charge movement in the outer hair cell plasma membrane. *Pflugers Arch*, 441(4):506–513, Jan 2001.

X. Tan, J. L. Pecka, J. Tang, O. E. Okoruwa, Q. Zhang, K. W. Beisel, and D. Z. Z. He. From zebrafish to mammal: functional evolution of prestin, the motor protein of cochlear outer hair cells. *J Neurophysiol*, 105(1):36–44, Jan 2011.

R. E. Thompson, D. R. Larson, and W. W. Webb. Precise nanometer localization analysis for individual fluorescent probes. *Biophys J*, 82(5):2775–2783, May 2002.

F. Tombola, M. H. Ulbrich, and E. Y. Isacoff. The voltage-gated proton channel Hv1 has two pores, each controlled by one voltage sensor. *Neuron*, 58(4):546–556, May 2008.

M. Tomishige and A. Kusumi. Compartmentalization of the erythrocyte membrane

by the membrane skeleton: intercompartmental hop diffusion of band 3. *Mol Biol Cell*, 10(8):2475–2479, Aug 1999.

R. Y. Tsien. The green fluorescent protein. *Annu Rev Biochem*, 67:509–544, 1998.

M. J. Tunstall, J. E. Gale, and J. F. Ashmore. Action of salicylate on membrane capacitance of outer hair cells from the guinea-pig cochlea. *J Physiol*, 485 (Pt 3): 739–752, Jun 1995.

M. H. Ulbrich and E. Y. Isacoff. Subunit counting in membrane-bound proteins. *Nat Methods*, 4(4):319–321, Apr 2007.

Y. M. Umemura, M. Vrljic, S. Y. Nishimura, T. K. Fujiwara, K. G. N. Suzuki, and A. Kusumi. Both MHC class II and its GPI-anchored form undergo hop diffusion as observed by single-molecule tracking. *Biophys J*, 95(1):435–450, Jul 2008.

Robert Michael van Dam. *Solvent-Resistant Elastomeric Microfluidic Devices and Applications.* PhD thesis, California Institute of Technology, 2005.

F. van den Ent, M. Leaver, F. Bendezu, J. Errington, P. de Boer, and J. Löwe. Dimeric structure of the cell shape protein MreC and its functional implications. *Mol Microbiol*, 62(6):1631–1642, Dec 2006.

C. A. Villalba-Galea, W. Sandtner, D. M. Starace, and F. Bezanilla. S4-based voltage sensors have three major conformations. *Proc Natl Acad Sci U S A*, 105(46):17600–17607, Nov 2008.

C. A. Villalba-Galea, W. Sandtner, D. Dimitrov, H. Mutoh, T. Knöpfel, and F. Bezanilla. Charge movement of a voltage-sensitive fluorescent protein. *Biophysical Journal*, 96(2):L19 – L21, 2009. ISSN 0006-3495.

A. Virkamäki, K. Ueki, and C. R. Kahn. Protein-protein interaction in insulin signaling and the molecular mechanisms of insulin resistance. *J Clin Invest*, 103(7): 931–943, Apr 1999.

Hermann von Helmholtz. *On the sensations of tone as physical basis for the theory of music*. Logmans, Green, and Co., 4th. edition, 1912.

Hiroshi Wada, Hiroto Usukura, Michiko Sugawara, Yukio Katori, Seiji Kakehata, Katsuhisa Ikeda, and Toshimitsu Kobayashi. Relationship between the local stiffness of the outer hair cell along the cell axis and its ultrastructure observed by atomic force microscopy. *Hear Res*, 177(1-2):61–70, Mar 2003.

Hiroshi Wada, Kei Kimura, Takashi Gomi, Michiko Sugawara, Yukio Katori, Seiji Kakehata, Katsuhisa Ikeda, and Toshimitsu Kobayashi. Imaging of the cortical cytoskeleton of guinea pig outer hair cells using atomic force microscopy. *Hear Res*, 187(1-2):51–62, Jan 2004.

X. Wang, S. Yang, S. Jia, and D. Z. Z. He. Prestin forms oligomer with four mechanically independent subunits. *Brain Res*, 1333:28–35, May 2010.

W. Weber, V. Helms, J. A. McCammon, and P. W. Langhoff. Shedding light on the dark and weakly fluorescent states of green fluorescent proteins. *Proc Natl Acad Sci U S A*, 96(11):6177–6182, May 1999.

S. Wieser and G. J. Schütz. Tracking single molecules in the live cell plasma membrane-Do's and Dont's. *Methods*, 46(2):131–140, Oct 2008.

S. Wieser, M. Moertelmaier, E. Fuertbauer, H. Stockinger, and G. J. Schütz. (Un)confined diffusion of CD59 in the plasma membrane determined by high-resolution single molecule microscopy. *Biophys J*, 92:3719 – 3728, 2007a.

S. Wieser, G. J. Schütz, M. E. Cooper, and H. Stockinger. Single molecule diffusion analysis on cellular nanotubules: Implications on plasma membrane structure below the diffaction limit. *Appl. Phys. Lett.*, 91:233901, 2007b.

S. Wieser, M. Axmann, and G. J. Schütz. Versatile analysis of single-molecule tracking data by comprehensive testing against Monte Carlo simulations. *Biophys J*, 95(12): 5988–6001, Dec 2008.

X. Wu, B. Currall, T. Yamashita, L. L. Parker, R. Hallworth, and J. Zuo. Prestin-prestin and prestin-GLUT5 interactions in HEK293T cells. *Dev Neurobiol*, 67(4): 483–497, Mar 2007.

F. Yang, L. G. Moss, and G. N. Phillips. The molecular structure of green fluorescent protein. *Nat Biotechnol*, 14(10):1246–1251, Oct 1996.

A. Yildiz, J. N. Forkey, S. A. McKinney, T. Ha, Y. E. Goldman, and P. R. Selvin. Myosin V walks hand-over-hand: single fluorophore imaging with 1.5-nm localization. *Science*, 300(5628):2061–2065, Jun 2003.

J. Z., G-G. Du, C. T. Anderson, J. P. Keller, A. Orem, P. Dallos, and MA. Cheatham. Analysis of the oligomeric structure of the motor protein prestin. *J Biol Chem*, 281 (29):19916–19924, Jul 2006.

D. A. Zacharias, J. D. Violin, A. C. Newton, and R. Y. Tsien. Partitioning of lipid-modified monomeric GFPs into membrane microdomains of live cells. *Science*, 296 (5569):913–916, May 2002.

W. Zeng, H. E. Seward, A. Málnási-Csizmadia, S. Wakelin, R. J. Woolley, G. S. Cheema, J. B., T. R. Patel, A. J. Rowe, and C. R. Bagshaw. Resonance en-

ergy transfer between green fluorescent protein variants: complexities revealed with myosin fusion proteins. *Biochemistry*, 45(35):10482–10491, Sep 2006.

Ming Zhang and Federico Kalinec. Structural microdomains in the lateral plasma membrane of cochlear outer hair cells. *J Assoc Res Otolaryngol*, 3(3):289–301, Sep 2002.

R. Zhang, F. Qian, L. Rajagopalan, F. A. Pereira, W. E. Brownell, and B. Anvari. Prestin modulates mechanics and electromechanical force of the plasma membrane. *Biophys J*, 93(1):L07–L09, Jul 2007.

W. Zhang, Y. Jiang, Q. Wang, X. Ma, Z. Xiao, W. Zuo, X. Fang, and Y-G. Chen. Single-molecule imaging reveals transforming growth factor-beta-induced type II receptor dimerization. *Proc Natl Acad Sci U S A*, 106(37):15679–15683, Sep 2009.

J. Zheng, W. Shen, D. Z. He, K. B. Long, L. D. Madison, and P. Dallos. Prestin is the motor protein of cochlear outer hair cells. *Nature*, 405(6783):149–155, May 2000.

J. Zheng, K. B. Long, W. Shen, L. D. Madison, and P. Dallos. Prestin topology: localization of protein epitopes in relation to the plasma membrane. *Neuroreport*, 12(9):1929–1935, Jul 2001.

J. Zheng, G-G. Du, K. Matsuda, A. Orem, S. Aguiñaga, L. Deák, E. Navarrete, L. D. Madison, and P. Dallos. The C-terminus of prestin influences nonlinear capacitance and plasma membrane targeting. *J Cell Sci*, 118(Pt 13):2987–2996, Jul 2005.

H-X. Zhou. Polymer models of protein stability, folding, and interactions. *Biochemistry*, 43(8):2141–2154, Mar 2004.

Appendix A: Treatment of position uncertainty and detector averaging effects

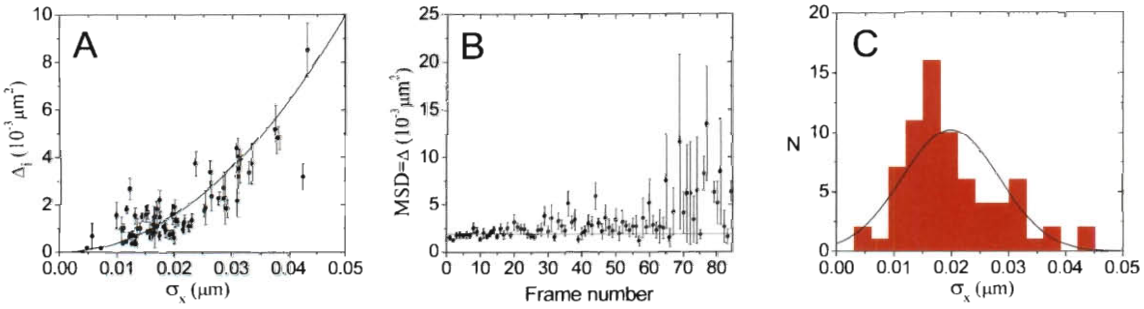

Figure A.1 : (A) Plot of apparent average offset Δ_i against standard deviation in repeated measurement of x-position σ_x of 72 individual immobile fluorescent spots. Solid curve is the relation $\Delta = 4\sigma_{xy}^2$. (B) Plot of *MSD* calculated using Eq. 4.3 in Sec. 4.2.2 of all 72 immobilized trajectories against frame number. Error bars are error of the mean. Data is fit to *MSD*$= \Delta$ and is weighted by error bars. Increased variance at high frame numbers is due to decreased probability of a particle remaining fluorescent at long times. Fit gives $\Delta = 1.91 \pm 0.08 \times 10^{-3}\,\mu m^2$, $\chi_\nu^2 = 1.8$. Measured offset implies localization error $\sigma_{xy} = 22\,nm$. (C) Histogram of measured standard deviations σ_x characterized by sample mean $\bar{\sigma}_x = 19.9\,nm$ and spread $\sigma_{\sigma_x} = 8.4\,nm$. Although obviously skewed, we approximated the distribution by a Gaussian (solid curve) with the measured sample mean $\bar{\sigma}_x$ and standard deviation σ_{σ_x}.

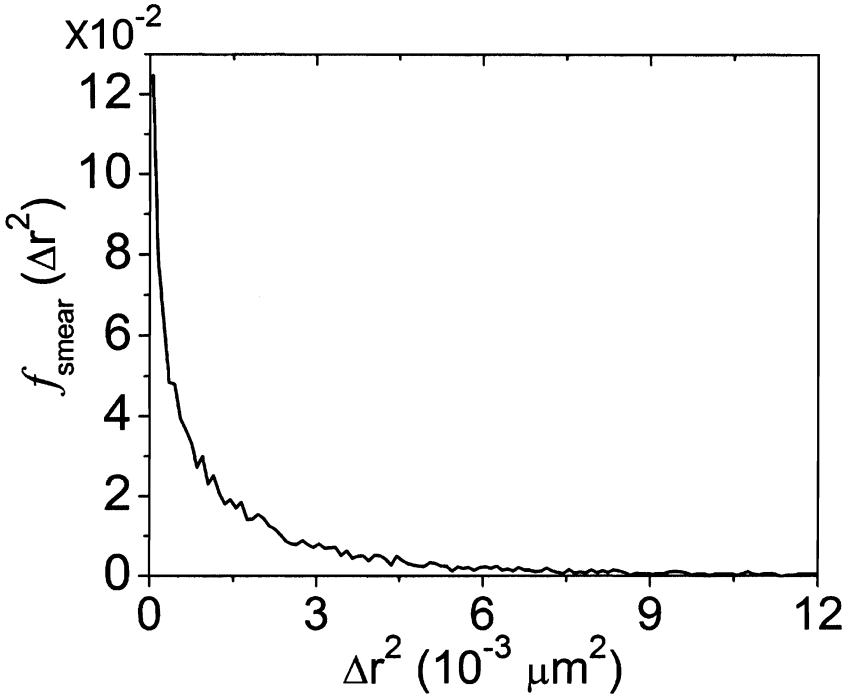

Figure A.2 : Shown is the probability density generated by assuming a Gaussian distribution of immobile particle position uncertainties reported in Fig. A.1. Simulated error is squared distance $|(\vec{r}_2 - \vec{r}_1)|^2$ between two position measurements, $\vec{r}_1 = (\delta x_1, \delta y_1)$ and $\vec{r}_2 = (\delta x_2, \delta y_2)$, where the errors δx_1, δy_1, δx_2, and δy_2 are randomly generated from a Gaussian distribution with zero mean and standard deviation randomly selected from another Gaussian distribution with mean of $19.9\,nm$ and standard deviation $8.4\,nm$. Displayed distribution is a normalized histogram of 30,000 simulations. The mean of the simulated distribution is $\Delta_{simulation} = 1.88 \times 10^{-3}\,\mu m^2$ in excellent agreement with measured $\Delta = 1.91 \pm 0.08 \times 10^{-3}\,\mu m^2$. Assuming $\Delta = 4\bar{\sigma}_x^2 = 4(19.9\,nm)^2 = 1.58 \times 10^{-3}\,\mu m^2$ underestimates $\Delta_{simulation}$ by $0.3 \times 10^{-3}\mu m^2$.

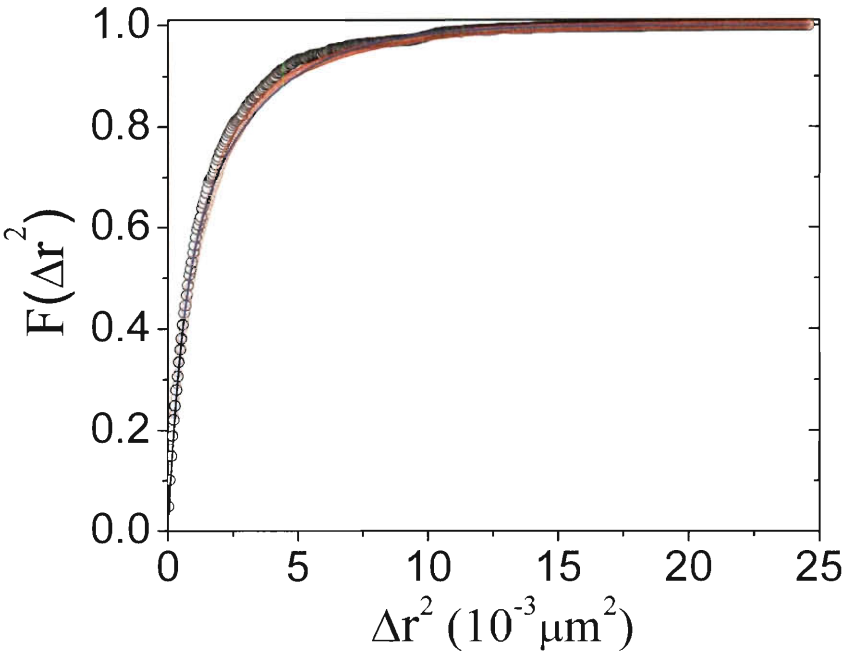

Figure A.3 : Black circles represent the measured CDF of immobile particles. Red circles represent the CDF $F(\Delta r^2)$ generated by assuming a distribution of position errors according to those measured in Fig. A.1. See Results in Ch. 4 for a detailed explanation of its calculation. For the purposes of including $F(\Delta r^2)$ in $P(\Delta r^2)$ (Eq. 4.8 in Sec. 4.2.4), $F(\Delta r^2)$ is approximated by a fit to a bi-exponential ($F(\Delta r^2) = 1 - 0.546542\, e^{-\Delta r^2/.00287\,\mu m^2} + 0.453458\, e^{-\Delta r^2/.00052\,\mu m^2}$ blue curve).

Position uncertainty effect on probability density for Brownian motion

In this section we extend the calculation in performed in Martin et al. to demonstrate the effect of position uncertainty on the PDF of position for a particle diffusing with pure Brownian motion [Martin et al., 2002]. The solution to the diffusion equation in two dimensions for a free particle is

$$P(\vec{r};\vec{r}_o) = \frac{1}{4\pi Dt}\exp(-|\vec{r}-\vec{r}_o|^2/4Dt)\,. \tag{A.1}$$

Specifically, $P(\vec{r};\vec{r}_o)$ is proportional to the probability that a particle starting at $\vec{r}_o$ will be found at $\vec{r}$ after time t given that the diffusion constant is D. If there is random error in the measurement of position, a measurement of $\vec{r}_o$ will result in finding the particle at $\vec{r}_o'$, and a measurement of $\vec{r}$ will result in finding the particle at $\vec{r}'$ after time t. Assuming normally distributed positioning errors $\vec{r}_o-\vec{r}_o'$ and $\vec{r}-\vec{r}'$, the errors can be represented by distribution functions $L(\vec{r}_o,\vec{r}_o')$ and $L(\vec{r},\vec{r}')$ given by

$$L(\vec{r}_o,\vec{r}_o') = \frac{1}{2\pi\sigma^2}\exp(|\vec{r}_o-\vec{r}_o'|^2/2\sigma^2) \tag{A.2}$$

and

$$L(\vec{r},\vec{r}') = \frac{1}{2\pi\sigma^2}\exp(|\vec{r}-\vec{r}'|^2/2\sigma^2) \tag{A.3}$$

where σ is the standard deviation of repeated position measurements of a fixed particle. The goal then is to find the probability density function $P''(\vec{r}',\vec{r}_o')$ that describes the motion in terms of the measured position including localization uncertainty. This

is done by convolving $P(\vec{r};\vec{r}_o)$ with $L(\vec{r}_o,\vec{r}_o')$ and $L(\vec{r},\vec{r}')$ and is written as,

$$P''(\vec{r}',\vec{r}_o') = \int d^2\vec{r}\, L(\vec{r},\vec{r}') \int d^2\vec{r}_o\, P(\vec{r};\vec{r}_o) L(\vec{r}_o,\vec{r}_o')\,. \tag{A.4}$$

Let us tackle the inner integral first and denote it as $P'(\vec{r},\vec{r}_o')$ which is written explicitly using polar coordinates as,

$$P'(\vec{r},\vec{r}_o') = \int_0^\infty r_o dr_o \int_0^{2\pi} d\theta_o \left(\frac{1}{4\pi Dt}\right)\left(\frac{1}{2\pi\sigma^2}\right) \exp\left(\frac{-|\vec{r}-\vec{r}_o|^2}{4Dt} - \frac{|\vec{r}_o-\vec{r}_o'|^2}{2\sigma^2}\right). \tag{A.5}$$

Focusing only on the exponent, we expand to obtain

$$\frac{-r_o'^2}{2\sigma^2} - \frac{(2\sigma^2+4Dt)r_o^2}{2\sigma^2 4Dt} + \frac{2\vec{r}_o\cdot\vec{r}_o'}{2\sigma^2} + \frac{2\vec{r}\cdot\vec{r}_o}{4Dt} - \frac{r^2}{4Dt} \tag{A.6}$$

$$= \frac{-r_o'^2}{2\sigma^2} - \frac{(2\sigma^2+4Dt)r_o^2}{2\sigma^2 4Dt} + \frac{2r_o r_o'}{2\sigma^2}\cos(\theta_o-\theta_o') + \frac{2rr_o}{4Dt}\cos(\theta_o-\theta) - \frac{r^2}{4Dt} \tag{A.7}$$

where the angles θ_o, θ_o', and θ are measured from the x-axis to the respective vectors $\vec{r}_o$, $\vec{r}_o'$, and $\vec{r}$. Now doing the integral over θ_o, only over terms with θ_o dependence, and using trigonometric identities to expand the cosines, we write

$$\int_0^{2\pi} d\theta_o \exp\left[\frac{2r_o r_o'}{2\sigma^2}\cos(\theta_o-\theta_o') + \frac{2rr_o}{4Dt}\cos(\theta_o-\theta)\right] \tag{A.8}$$

$$= \int_0^{2\pi} d\theta_o \exp\left[a\cos\theta_o + b\sin\theta_o\right] \tag{A.9}$$

where factors which are constant with respect to θ_o have been grouped into $a = \frac{4Dt2r_o r_o'\cos\theta_o' + 2\sigma^2 2rr_o\cos\theta}{2\sigma^2 4Dt}$ and $b = \frac{4Dt2r_o r_o'\sin\theta_o' + 2\sigma^2 2rr_o\sin\theta}{2\sigma^2 4Dt}$. The integral in Eq. A.9 can

be found in tables of integrals and gives

$$= 2\pi J_o(i\sqrt{a^2+b^2}) \tag{A.10}$$

where J_o is the Bessel function. After plugging back in the expressions for a and b, and performing some algebraic manipulations, the result of the integral over θ_o becomes

$$= 2\pi J_o\left(i2r_o\frac{\{(4Dtr_o')^2+(2\sigma^2 r)^2+2(4Dtr_o')(2\sigma^2 r)\cos(\theta-\theta_o')\}^{1/2}}{2\sigma^2 4Dt}\right) \tag{A.11}$$

$$= 2\pi J_o\left(\frac{i2|4Dt\vec{r}_o'+2\sigma^2\vec{r}|}{2\sigma^2 4Dt}r_o\right). \tag{A.12}$$

So for $P'(\vec{r},\vec{r}_o')$ we now have

$$P'(\vec{r},\vec{r}_o') = 2\pi\left(\frac{1}{4\pi Dt}\right)\left(\frac{1}{2\pi\sigma^2}\right)e^{-r_o'^2/2\sigma^2}e^{-r^2/4Dt}\int_0^\infty r_o dr_o \exp\left(\frac{-(2\sigma^2+4Dt)}{2\sigma^2 4Dt}r_o^2\right) \times J_o\left(\frac{i2|4Dt\vec{r}_o'+2\sigma^2\vec{r}|}{2\sigma^2 4Dt}r_o\right) \tag{A.13}$$

By comparison to an integral of equivalent form in [Martin et al., 2002] the integral over r_o (independent of prefactors) is

$$= \frac{1}{2}\frac{2\sigma^2 4Dt}{2\sigma^2+4Dt}\exp\left(\frac{1}{2\sigma^2+4Dt}\left(\frac{1}{4}\right)\frac{4|4Dt\vec{r}_o'+2\sigma^2\vec{r}|^2}{2\sigma^2 4Dt}\right). \tag{A.14}$$

So $P'(\vec{r},\vec{r}_o')$ is then

$$P'(\vec{r},\vec{r}_o') = \frac{2\pi}{4\pi Dt}\frac{1}{2\pi\sigma^2}\frac{1}{2}\frac{2\sigma^2 4Dt}{2\sigma^2+4Dt}\exp\left[\frac{-r_o'^2}{2\sigma^2}-\frac{r^2}{4Dt}+\frac{|4Dt\vec{r}_o'+2\sigma^2\vec{r}|^2}{2\sigma^2 4Dt(2\sigma^2+4Dt)}\right], \tag{A.15}$$

which can be simplified to

$$P'(\vec{r},\vec{r}'_o) = \frac{1}{\pi(2\sigma^2+4Dt)}\exp\left(\frac{-|\vec{r}-\vec{r}'_o|^2}{2\sigma^2+4Dt}\right). \tag{A.16}$$

Returning to Eq. A.4, and plugging in the expressions for $P'(\vec{r},\vec{r}'_o)$ and $L(\vec{r},\vec{r}')$, we have the following integral

$$P''(\vec{r}',\vec{r}'_o) = \int_0^{2\pi} d\theta \int_0^{\infty} r dr \left(\frac{1}{2\pi\sigma^2}\right)\frac{1}{\pi(2\sigma^2+4Dt)}\exp\left(\frac{-|\vec{r}-\vec{r}'|^2}{2\sigma^2} - \frac{|\vec{r}-\vec{r}'_o|^2}{2\sigma^2+4Dt}\right) \tag{A.17}$$

running over the final position coordinates. After expanding the exponent, and for the moment isolating only the angular terms, the integral over θ has the same form as in Eq. A.9, however the coefficients of $\cos\theta$ and $\sin\theta$ (a' and b' respectively) are instead

$$a' = \frac{2rr'}{2\sigma^2}\cos\theta' + \frac{2rr'_o}{2\sigma^2+4Dt}\cos\theta'_o \tag{A.18}$$

and

$$b' = \frac{2rr'}{2\sigma^2}\sin\theta' + \frac{2rr'_o}{2\sigma^2+4Dt}\sin\theta'_o. \tag{A.19}$$

The result of calculating the θ integral is of exactly the same form as in Eq. A.10. Plugging in for a' and b' and expanding the argument within J_o we obtain

$$= 2\pi J_o\left(i\left[4r^2\left(\frac{r'^2}{(2\sigma^2)^2} + \frac{r'^2_o}{(2\sigma^2+4Dt)^2} + \frac{2r'r'_o\cos(\theta'-\theta'_o)}{2\sigma^2(2\sigma^2+4Dt)}\right)\right]^{1/2}\right) \tag{A.20}$$

which simplifies to

$$= 2\pi J_o\left(i\frac{2r}{2\sigma^2(2\sigma^2+4Dt)}\left|(2\sigma^2+4Dt)\vec{r}' + 2\sigma^2\vec{r}'_o\right|\right). \tag{A.21}$$

The integral over r (again, independent of prefactors) is

$$\int_0^\infty r dr J_o\left(i\frac{2}{2\sigma^2(2\sigma^2+4Dt)}\left|(2\sigma^2+4Dt)\vec{r}'+2\sigma^2\vec{r}_o'\right|r\right) \times \exp\left(\frac{-4\sigma^2+4Dt}{2\sigma^2(2\sigma^2+4Dt)}r^2\right). \tag{A.22}$$

Again, we recognize the result of the r integral from Martin et al.:

$$\frac{1}{2}\frac{2\sigma^2(2\sigma^2+4Dt)}{4\sigma^2+4Dt}\exp\left(\frac{1}{(4\sigma^2+4Dt)2\sigma^2(2\sigma^2+4Dt)}\left|(2\sigma^2+4Dt)\vec{r}'+2\sigma^2\vec{r}_o'\right|^2\right). \tag{A.23}$$

so we finally have for $P''(\vec{r}', \vec{r}_o')$,

$$P''(\vec{r}', \vec{r}_o') = \frac{1}{\pi}\frac{1}{4\sigma^2+4Dt} \times \exp\left(\frac{1}{(4\sigma^2+4Dt)2\sigma^2(2\sigma^2+4Dt)}\left|(2\sigma^2+4Dt)\vec{r}'+2\sigma^2\vec{r}_o'\right|^2-\frac{r'^2}{2\sigma^2}-\frac{r_o'^2}{2\sigma^2+4Dt}\right). \tag{A.24}$$

However, this equation needs some simplification to make apparent the effect of a finite positional error σ. We consider only the exponent for the moment and expand,

$$\frac{1}{(4\sigma^2+4Dt)2\sigma^2(2\sigma^2+4Dt)}\left\{(2\sigma^2+4Dt)^2r'^2+(2\sigma^2)^2r_o'^2+2\sigma^2(2\sigma^2+4Dt)2\vec{r}'\cdot\vec{r}_o' -(4\sigma^2+4Dt)(2\sigma^2+4Dt)r'^2-2\sigma^2(4\sigma^2+4Dt)r_o'^2\right\} \tag{A.25}$$

which simplifies to

$$\frac{1}{4\sigma^2+4Dt}\left(-r'^2-r_o'^2+2\vec{r}'\cdot\vec{r}_o'\right)=\frac{-\left|\vec{r}'-\vec{r}_o'\right|^2}{4\sigma^2+4Dt}. \tag{A.26}$$

Finally we have the desired result for $P''(\vec{r}', \vec{r}_o')$

$$P''(\vec{r}', \vec{r}_o') = \frac{1}{\pi(4\sigma^2 + 4Dt)} \exp\left(\frac{-\left|\vec{r}' - \vec{r}_o'\right|^2}{4\sigma^2 + 4Dt}\right). \tag{A.27}$$

We see that Eq. A.27 has the same form as Eq. A.1. Therefore, we can see by inspection that the result of a finite position uncertainty σ is to add $4\sigma^2$ to the mean squared deviation ($MSD = \left\langle \left|\vec{r}' - \vec{r}_o'\right|^2 \right\rangle = 4Dt + 4\sigma^2$).

Detector averaging effect on mean squared deviation for Brownian motion

In this section we derive the effect of detector averaging on the measured mean squared deviation of the trajectory for a moving particle. We will then apply the result to a particle undergoing Brownian motion. We start by defining the actual trajectory of the particle as $\vec{R}(t)$ and the apparent position of the particle on a detector (such as a CCD camera) as $\vec{r}(t)$. Suppose that in an experiment we are interested in the displacement the particle makes between a time t and t'. We take snapshots of the particle with the camera such that the time lag between two frames is $t' - t$. If the exposure time Δt_{ill} of the camera is negligible compared to $t' - t$ then the camera measures the true trajectory. What then is the effect on the measured trajectory if the exposure time is not negligible? During the exposure that measures the position of the particle at time t the particle is moving so the measured position $\vec{r}(t)$ is an average of the trajectory over the exposure time:

$$\vec{r}(t) = \frac{1}{\Delta t_{ill}} \int_0^{\Delta t_{ill}} dT\, \vec{R}(t+T)\,, \tag{A.28}$$

and at time t' the measured position is

$$\vec{r}(t') = \frac{1}{\Delta t_{ill}} \int_0^{\Delta t_{ill}} dT\, \vec{R}(t'+T)\,. \tag{A.29}$$

And by definition, $t' \geq t + \Delta t_{ill}$. The squared displacement, in terms of the true trajectory, is then

$$\begin{aligned}\left|\vec{r}(t) - \vec{r}(t')\right|^2 = \left(\frac{1}{\Delta t_{ill}}\right)^2 &\left(\int_0^{\Delta t_{ill}} dT\, \vec{R}(t'+T) - \int_0^{\Delta t_{ill}} dT\, \vec{R}(t+T)\right) \\ &\cdot \left(\int_0^{\Delta t_{ill}} dT\, \vec{R}(t'+T) - \int_0^{\Delta t_{ill}} dT\, \vec{R}(t+T)\right)\end{aligned} \tag{A.30}$$

$$\begin{aligned}= \left(\frac{1}{\Delta t_{ill}}\right)^2 &\left(\int_0^{\Delta t_{ill}} dT\, \vec{R}(t'+T) \cdot \int_0^{\Delta t_{ill}} dT'\, \vec{R}(t'+T') - \int_0^{\Delta t_{ill}} dT'\, \vec{R}(t'+T') \cdot \int_0^{\Delta t_{ill}} dT\, \vec{R}(t+T)\right. \\ &\left. - \int_0^{\Delta t_{ill}} dT\, \vec{R}(t+T) \cdot \int_0^{\Delta t_{ill}} dT'\, \vec{R}(t'+T') + \int_0^{\Delta t_{ill}} dT\, \vec{R}(t+T) \cdot \int_0^{\Delta t_{ill}} dT'\, \vec{R}(t+T')\right)\end{aligned} \tag{A.31}$$

$$\begin{aligned}= \left(\frac{1}{\Delta t_{ill}}\right)^2 \int_0^{\Delta t_{ill}} dT \int_0^{\Delta t_{ill}} dT' \Big[&\vec{R}(t'+T) \cdot \vec{R}(t'+T') \\ &+ \vec{R}(t+T) \cdot \vec{R}(t+T') - 2\vec{R}(t'+T') \cdot \vec{R}(t+T)\Big]\,.\end{aligned} \tag{A.32}$$

Let us rewrite the first two terms in the integrand of Eq. A.32. The first term can be rewritten as

$$\vec{R}(t'+T) \cdot \vec{R}(t'+T') = \frac{1}{2}\left(R(t'+T)^2 + R(t'+T')^2 - \left|\vec{R}(t'+T) - \vec{R}(t'+T')\right|^2\right), \tag{A.33}$$

and the second term as

$$\vec{R}(t+T)\cdot\vec{R}(t+T') = \frac{1}{2}\left(R(t+T)^2 + R(t+T')^2 - \left|\vec{R}(t+T) - \vec{R}(t+T')\right|^2\right). \tag{A.34}$$

Plugging back into $\left|\vec{r}(t) - \vec{r}(t')\right|^2$, performing some algebra and simplifying,

$$\begin{aligned} &= \frac{1}{2}\left(\frac{1}{\Delta t_{ill}}\right)^2 \int_0^{\Delta t_{ill}} dT \int_0^{\Delta t_{ill}} dT' \left(\left|\vec{R}(t'+T') - \vec{R}(t+T)\right|^2\right. \\ &\quad -\left|\vec{R}(t'+T) - \vec{R}(t'+T')\right|^2 - \left|\vec{R}(t+T) - \vec{R}(t+T')\right|^2 \\ &\quad \left. +R^2(t'+T) + R^2(t+T') - 2\vec{R}(t'+T')\cdot\vec{R}(t+T)\right). \end{aligned} \tag{A.35}$$

Since T and T' are dummy variables,

$$\int_0^{\Delta t_{ill}} dT \int_0^{\Delta t_{ill}} dT' R^2(t'+T) = \int_0^{\Delta t_{ill}} dT \int_0^{\Delta t_{ill}} dT' R^2(t'+T') \tag{A.36}$$

and

$$\int_0^{\Delta t_{ill}} dT \int_0^{\Delta t_{ill}} dT' R^2(t+T') = \int_0^{\Delta t_{ill}} dT \int_0^{\Delta t_{ill}} dT' R^2(t+T)\,. \tag{A.37}$$

So after applying Eqs. A.36 and A.37 to Eq. A.35, and taking the ensemble average $\langle\ \rangle$ of both sides, we have for the measured *mean* squared displacement

$$\begin{aligned} \left\langle\left|\vec{r}(t) - \vec{r}(t')\right|^2\right\rangle = \frac{1}{2}\left(\frac{1}{\Delta t_{ill}}\right)^2 \int_0^{\Delta t_{ill}} dT \int_0^{\Delta t_{ill}} dT' \left(2\left\langle\left|\vec{R}(t'+T') - \vec{R}(t+T)\right|^2\right\rangle\right. \\ \left. -\left\langle\left|\vec{R}(t'+T) - \vec{R}(t'+T')\right|^2\right\rangle - \left\langle\left|\vec{R}(t+T) - \vec{R}(t+T')\right|^2\right\rangle\right). \end{aligned} \tag{A.38}$$

For any trajectory $\vec{R}(t)$, Eq. A.38 gives what the measured mean squared deviation would be if sampled on a detector that averages each sampling of the trajectory over a time Δt_{ill}. If the underlying motion is free Brownian, we can replace the terms in the integrand by $4D(t' + T' - t - T)$ for the first term, $4D|T - T'|$ for the second term, and $4D|T - T'|$ for the last term. Integrating over T and T' gives for the mean squared deviation for a particle undergoing simple Brownian motion

$$\left\langle \left|\vec{r}(t) - \vec{r}(t')\right|^2 \right\rangle = 4D(t' - t) - \frac{4}{3} D\,\Delta t_{ill}\,. \tag{A.39}$$

So we see that for Brownian motion, the effect of detector averaging is to subtract a constant $\frac{4}{3} D\,\Delta t_{ill}$ from the mean squared deviation.

Appendix B: Relation of macroscopically measured FRET to microscopic energy transfer

In this appendix, we derive the ensemble FRET efficiency E in terms of a microscopic description. Experimentally, the measured FRET signal is

$$E = 1 - \frac{F_{da}}{F_d} \tag{B.1}$$

where F_{da} is the average fluorescence in the region of interest before bleaching of acceptors, and F_d is the average fluorescence after bleaching of acceptors. For simplicity of calculation, we assume that molecules do not diffuse in or out of the region. We also assume that donor molecules that were non-fluorescent before the bleach do not become fluorescent after the bleach. Likewise, we assume donor particles that are fluorescent before the bleach remain fluorescent after the bleach. These effects are accounted for by subtracting off the measured control efficiency from the efficiency measured in the bleach region as described in the main text. Before the bleach, the measured fluorescence is

$$F_{da} = \sum_i f_{Fi} N_{Fi} + f\, N_{NF} \tag{B.2}$$

where f_{Fi} is the fluorescence of a donor in state i that is undergoing energy transfer, and N_{Fi} is the number of donors undergoing energy transfer in the particular state i. We also account for a possible population of N_{NF} donors that are not paired with an acceptor or are sufficiently far from an accepter that they do not undergo energy

transfer and thus emit the full possible unquenched fluorescence f. Clearly, for any state i the fluorescence $f_{Fi} < f$ because of energy transfer. The total number of donors is $N = \sum_i N_{Fi} + N_{NF}$. After the bleaching of all acceptor molecules, the fluorescence of each donor molecule undergoing energy transfer increases to the full fluorescence level, $f_{Fi} \to f$. So after the bleaching of all acceptors, the fluorescence level is

$$F_d = f \sum_i N_{Fi} + f\, N_{NF} = f\,(N_F + N_{NF}) = f\, N. \tag{B.3}$$

So, the measured FRET efficiency is

$$E = 1 - \frac{\sum_i f_{Fi}\, N_{Fi} + f\, N_{NF}}{f\, N} = 1 - \frac{\sum_i f_{Fi} N_{Fi} + f\,(N - \sum_i N_{Fi})}{f\, N}. \tag{B.4}$$

Now we distribute terms,

$$E = 1 - \frac{\sum_i f_{Fi} N_{Fi}}{f\, N} - 1 + \frac{f \sum_i N_{Fi}}{f\, N}. \tag{B.5}$$

$$\begin{aligned} E &= \frac{\sum_i N_{Fi}}{N} - \frac{\sum_i f_{Fi} N_{Fi}}{f\, N} \\ &= \frac{N_{F1} + N_{F2} + \cdots + N_{FM}}{N} - \frac{f_{F1} N_{F1} + f_{F2} N_{F2} + \cdots + f_{FM} N_{FM}}{f\, N}. \end{aligned} \tag{B.6}$$

And collecting terms,

$$\begin{aligned} E &= \frac{N_{F1}}{N}\left(1 - \frac{f_{F1}}{f}\right) + \frac{N_{F2}}{N}\left(1 - \frac{f_{F2}}{f}\right) + \cdots + \frac{N_{FM}}{N}\left(1 - \frac{f_{FM}}{f}\right) \\ &= \sum_i \frac{N_{Fi}}{N}\left(1 - \frac{f_{Fi}}{f}\right). \end{aligned} \tag{B.7}$$

And by definition $\left(1 - \frac{f_{Fi}}{f}\right) = \left(\frac{1}{1+(r_i/R_o)^6}\right)$ so, $E = \sum_i \frac{N_{Fi}}{N}\left(\frac{1}{1+(r_i/R_o)^6}\right)$, and defining $n_{Fi} \equiv \frac{N_{Fi}}{N}$ which is the fraction of all donor molecules that are undergoing FRET in the state i we write,

$$E = \sum_i n_{Fi}\left(\frac{1}{1+(r_i/R_o)^6}\right). \tag{B.8}$$

In the special case that the sample contains only one species undergoing energy transfer, corresponding to only one donor-acceptor distance, the equation reduces to a useful form,

$$E = n_F\left(\frac{1}{1+(r_i/R_o)^6}\right), \tag{B.9}$$

and demonstrates that the donor-acceptor distance can only be know if 100% of the donors undergo energy transfer unless n_F is known *a priori* which is generally not the case. (r/R_o) is plotted versus E for various n_F in Fig. B.1. From the plot (Fig. B.1) it can be observed that for any n_F, for all but the smallest energy transfers the curves differ from each other by a systematic shift as long as r/R_o somewhat greater than 1. This is made more obvious by plotting the error you make in estimating r/R_o from $\left(\frac{1}{E} - 1\right)^{1/6}$ as a function of E as shown below (Fig. B.2, curves are parameterized by n_F).

These results are relevant to our experiment because of our use of a cotransfection, which on average is designed to express equal amounts of donor and acceptor, and ensures that n_F will be less than 1. In the simplest possible case that prestin forms only dimers and that there is an equal population of donors and acceptors, statistically 1/2 of all donor labeled molecules will be paired with acceptor molecules and 1/2 will be paired with other donor molecules assuming there was an initially large population of donor and acceptor labeled molecules. By utilizing the curve labeled with $n_F = 1/2$

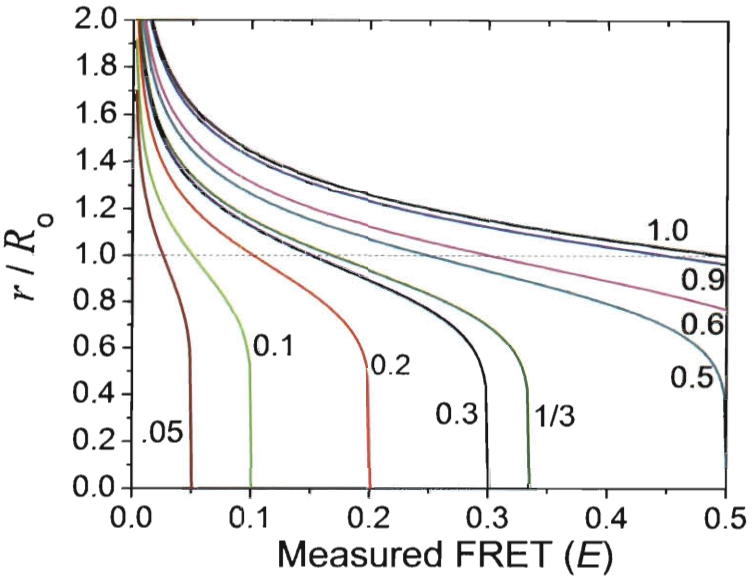

Figure B.1 : Donor-acceptor distance versus measured FRET efficiency parameterized by the fraction of donors undergoing FRET. Assumes only one donor-acceptor distance enters the problem.

in Fig. B.2, this implies that all distance measurements must be off by at least $0.18\,R_o$. However, since the highest FRET we measure is around 10%, as long as $n_F \gtrsim 0.2$ (which ensures that $r/R_o > 1$), estimates of r/R_o will differ from the true values by a constant amount. So under the assumptions that only one donor-acceptor distance in the sample contributes to the FRET signal and that the fraction of donors undergoing energy transfer $n_F \gtrsim 0.2$, then estimates of changes in donor-acceptor distance remain valid even though absolute donor-acceptor distances do not.

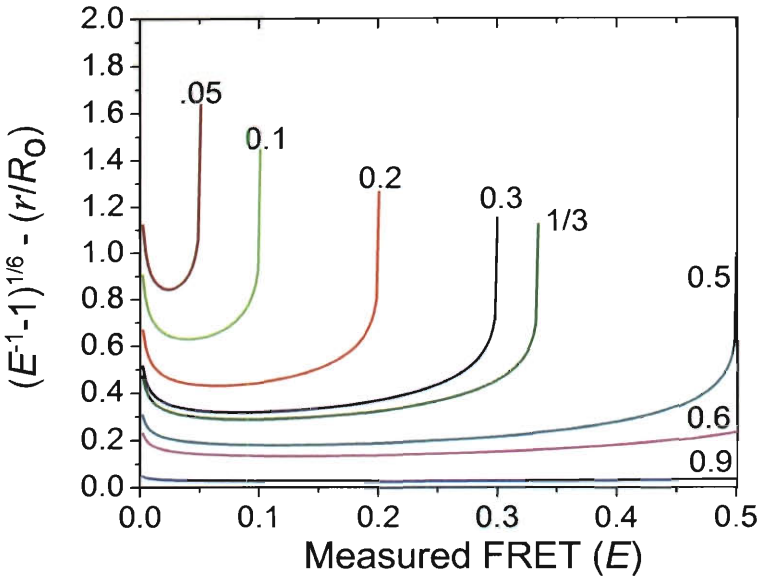

Figure B.2 : Error one makes in estimating the donor-acceptor distance from the measured FRET efficiency if there exist unpaired donors. Curves show that the error is nearly constant over a large range of FRET values. As the condition that all donors are paired with an acceptor is met, $\left(\frac{1}{E}-1\right)^{1/6} \rightarrow r/R_o$, the macroscopically measured FRET is equal to the microscopic FRET, and no error is made.